ABSTRACT

ROUXELIN, PASCAL NICOLAS. Reactor Physics Uncertainty and Sensitivity Analysis of Prismatic HTGRs. (Under the direction of Dr. Kostadin Ivanov and Dr. Maria Avramova).

The growing capabilities of high-fidelity multi-physics, the new features of reactor physics relative to neutronics and depletion simulations necessitate the prediction of uncertainties. The efforts of the international scientific community to establish extensive sets of nuclear data libraries coincide to the appeal to measure and model both sensitivities and uncertainties for HTGR applications. The objective of this Ph. D thesis is to investigate, develop and improve the uncertainty quantification methods in the field of reactor physics applied to prismatic HTGRs. This work was motivated by the International Atomic Energy Agency (IAEA) that started a Coordinated Research Program (CRP) for the continued elaboration of safety and design attributes of High Temperature Gas-cooled Reactors (HTGR). The Idaho National Laboratory and the North Carolina State University participated to the IAEA CRP and funded this research.

Introductory concepts unveil the MHTGR-350, HTTR and VHTRC general specifications pertinent throughout the study, and lists the challenges of HTGR design and simulation. The analysis starts with the elaboration of a methodology to prepare collapsed, problem-dependent cross sections with KENO and TRITON/NEWT during depletion calculations. The methodology demonstrates an automated algorithm to obtain the flux-weighted cross sections for both pebble-bed and prismatic configurations.

A second part applies T-NEWT-generated cross sections in AMPX format to initiate PHISICS/RELAP5-3D multi-physics, core calculations. Super cell models are compared to traditional fuel block lattices defined in the IAEA CRP for HTGR. This analysis assesses the

effects of the neutron spectra on multi-physics core predictions for four lattice cells. The influence of the flux-weighted cross sections in the subsequent PHISCS/RELAP5-3D solution proves that the choice of the lattice model impacts the spatial power density of the MHTGR core by ~4 % to 7%. Comparable super cell lattices were utilized to demonstrate the adaptive sampling capabilities of RAVEN associated with NEWT and PHISICS. The sequence, applied to an HTTR two-dimensional core, performs automatic investigations on few-group structures using RAVEN's Limit Surface Search and Reduced Order Model capabilities. Six-group structures were derived. An interface was produced to ensure the cooperative work between the nuclear codes (NEWT, PHISICS) and the probabilistic software.

SCALE 6.2.0's SAMPLER/T-NEWT code evaluates the uncertainties on nuclide inventories during burnup calculations in two MHTGR lattice cells. The code demonstrated that the cross section uncertainties (input) govern entirely the uncertainties on the actinide inventories (output). The fission yield uncertainties (input) influence primarily the fission product uncertainties (output). The cross section uncertainties bring a non-negligible contribution to the fission product's uncertainty component. About 12 % of the total uncertainty varied as a function of the spectrum effects originating from the lattice models.

The last section of the analysis transitioned to VHTRC modeling. The perturbation capabilities of the RAVEN/PHISICS sequence were applied to replicate the manufacturing uncertainties stipulated in the VHTRC experimental report. RAVEN/PHISICS predicted output uncertainties for the three VHTRC cores at six temperatures. Although a good agreement is found between the simulations and the experiment, the study highlights the challenges of approaching the non-specificity of input uncertainties.

Reactor Physics Uncertainty and Sensitivity Analysis of Prismatic HTGRs

by
Pascal Rouxelin

A thesis submitted to the Graduate Faculty of
North Carolina State University
In partial fulfillment of the
requirements for the degree of
Doctor of Philosophy

Nuclear Engineering

Raleigh, North Carolina
2019

APPROVED BY:

Maria Avramova Co-Chair of Advisory Committee	Kostadin Ivanov Co-Chair of Advisory Committee
Jason Hou	Arkady Kheyfets

BIOGRAPHY

Pascal Rouxelin received his doctorate in Nuclear Engineering from the North Carolina State University in Raleigh. He started his doctorate at the Pennsylvania State University after obtaining a Master's degree in Nuclear Engineering at the National Institute of Nuclear Sciences and Technologies (INSTN) at the French Atomic Energy Commission and Alternative Energies (CEA) and in Mechanical Engineering at the Ecole Polytechnique Universitaire of Marseille. His principal area of focus is reactor physics in gas-cooled systems with an emphasis on uncertainty quantification.

ACKNOWLEDGEMENTS

Firstly, I would like to express my deepest appreciation to Andrea Alfonsi who accessed my almost-constant requests for PHISICS code developments, tolerated my empty pull requests on GITHUB and provided, more importantly, invaluable advice throughout my stay at INL, always in an all-Italian good humor. His guidance helped me greatly completing my thesis.

I would like to extend my gratitude to Gerhard Strydom, my mentor at INL, who provided me technical advice, great HTGR-related literature for bed-time reading and very pleasant company at work.

I am extremely grateful to Dr. Kostadin Ivanov who has been supervising my work since the beginning, continuously supported me over the years and given me multiple professional opportunities. The trust he lent me as a teacher assistant were greatly appreciated as well.

I would like to express an equally great appreciation to Dr Maria Avramova for her very nice support, her advice and her professionalism throughout my thesis.

I am deeply indebted to Dr. Winfried Zwermann for his exceptional knowledge, his tremendous insights and his supervision.

I would like to extend my sincere thanks to Alex Aures and Dr. Jason Hou, who patiently and promptly helped me clarifying scientific problems.

Finally, I would like to thank my insightful colleagues Friederike Bostelmann – for her cooperation with HTGR CRP work - , Alex Bennett – study buddy and lab mate - , Mike Mankosa – valued roommate and lab mate, Mario Milev – my administrative vigilante -.

TABLE OF CONTENTS

LIST OF FIGURES

LIST OF TABLES

LIST OF ACRONYMS

BEPU	Best Estimate Plus Uncertainty
BNL	Brookhaven National Laboratory
BOC	Beginning Of Cycle
BP	Burnable Poison
BWR	Boiling Water Reactor
CANDU	CANadian Deuterium Uranium
CI	Code Interface
CR	Control Rod
CRP	Coordinated Research Program
CSV	Comma-Separated Values
DBRC	Doppler Broadening Rejection Correction
DNBR	Departure from Nucleate Boiling Ratio
ENDF	Evaluated Nuclear Data File
EOC	End Of Cycle
EC	External Code
EXI	External code's Input
GPT	General Perturbation Theory
HFP	Hot Full Power
HTGR	High Temperature Gas-Cooled Reactor
HTTR	High Temperature Test Reactor
HZP	Hot Zero Power
IAEA	International Atomic Energy Agency
IDW	Inverse Distance Weight
IHX	Intermediate Heat Exchanger
INET	Institute of Nuclear and new Energy Technology
INL	Idaho National Laboratory
IPyC	Inner Pyrolitic Carbon
JAERI	Japanese Atomic Energy Research Institute
KI	Kurchatov Institute

LANL	Los Alamos National Laboratory
LSS	Limit Surface Search
LWR	Light Water Reactor
MHTGR	Modular High Temperature Gas-cooled Reactor
MG	Multi-Group
MoC	Method of Characteristics
MOX	Mixed OXide
NEA	Nuclear Energy Agency
NEWT	New ESC-based Weighting Transport code
NTE	Neutron Transport Equation
OECD	Organization for Economic Co-operation and Development
OPP	Output Post-processor
OPyC	Outer Pyrolitic Carbon
ORNL	Oak Ridge National Laboratory
PBR	Pebble-Bed Reactor
PDE	Partial Differential Equation
PDF	Probability Density Function
PWR	Pressurized Water Reactor
RBMK	High-power Channel Reactor
RCCS	Reactor Cavity Cooling System
RI	Raven Interface
ROM	Reduced Order Model
RPT	Reactivity-equivalent Physical Transformation
SB	Single Block
SC	Super Cell
SiC	Silicon Carbide
SFR	Sodium Fast Reactor
TP	TRISO Particle
TRISO	TRI-Structural ISOtropic
UAM	Uncertainty Analysis Modeling
VHTRC	Very High Temperature Reactor Critical Assembly

VVER	Water-Water Energetic Reactor
XS	Cross section

CHAPTER 1

MOTIVATION OF THE WORK AND CONTRIBUTIONS

1.1 The IAEA Coordinated Research Program on HTGRs

The Organization for Economic Co-operation and Development (OECD) initiated the Uncertainty Analysis Modeling (UAM) project in 2006 to promote the quantification of uncertainties in Light Water Reactors (LWRs). In the wake of the OECD UAM, the IAEA launched a Coordinated Research program (CRP) (see summary of results in section 3.4) on High Temperature Gas-cooled Reactors (HTGR) [1] to investigate uncertainty propagations and ensure the continuation of method and simulation development of HTGRs. The project applies unified cooperation of participants to assess safety margins complemented with quantified uncertainties. This approach provides more complete and peer-reviewed estimates of reactor safety. An HTGR international benchmark also appeals the scientific community because it can accelerate the licensing process. Similarly to the LWR UAM benchmark, the HTGR benchmark defines multiple exercises aiming to propagate the root input uncertainties (nuclear data and manufacturing uncertainties) across increasingly complex scales and if possible through multi-physics models.

In a separate effort, the OECD Nuclear Energy Agency (NEA) Modular High Temperature Gas-cooled Reactor (MHTGR)-350 MW benchmark [2] was launched at Idaho National Laboratory (INL) in 2012 to provide a best-estimate code-to-code verification data set for the development of HTGR computational tools. This benchmark, comparatively to the approach explained in the previous paragraph, defines various phases and exercises corresponding to the typical MHTGR cells, lattices and core. The CRP on HTGRs utilizes most of the MHTGR-350 design information specified in the OECD/NEA MHTGR-350 benchmark for the cell and lattice phases, except for small changes made to the fuel specification that is based on the latest Advanced Gas Reactor (AGR) fuel irradiation program at INL. The core models developed for the OECD/NEA benchmark are therefore applied to the simulation of the CRP Phase II and III problems.

The first Phase of the HTGR UAM focuses on neutronics calculations, ranging from lattice cell (Exercise (Ex.) I-1a/b) to single block (Ex. I-2a/b) and supercell (Ex.I-2c) calculations.

The attention is oriented towards the impact of nuclear data (such as cross-sections, fission yields etc.) and manufacturing uncertainties on the neutron flux, power and eigenvalue obtained for these lattice models, but also a comparison of the cross section libraries generated in Phase I for use in the Phase II core models. This scope is extended to burn-up calculation problems, induced by the complex evolution of the core's intrinsic key parameters.

1.2 Ph.D. Contribution

This work contributed to the development of methodologies in neutronics calculations applied to HTGRs.

A first fragment of the work demonstrated two proof-of-concepts for the generation of cross sections in (a) KENO/NEWT for PBR and MHTGR lattices and (b) with NEWT/PHISICS for the MHTGR, High Temperature Test Reactor (HTTR) and Very High Temperature Reactor Critical assembly (VHTRC) lattices. Method (a) consists in an automatic data-handling sequence written in PERL language to homogenize and collect cross sections carried over XSUSA/KENO depletion calculations. In method (b), the capabilities of PHISICS were enhanced to let the transport code support disadvantage factors along with the microscopic cross sections to perform core calculations from T-NEWT lattice cells. An accurate use of AMPX cross sections from SCALE 6.1 T-NEWT passed to PHISICS was demonstrated. The AMPX format relative to SCALE 6.2 functions correctly as well.

The second fragment of the thesis concentrated on the development of RAVEN interfaces for the code PHISICS to allow uncertainty analysis. Interfaces now exist for (a) RAVEN/PHISICS, (b) RAVEN/MRTAU standalone (the depletion module of PHISICS), (c) RAVEN/PHISICS/RELAP5-3D to fulfill coupled neutronics calculations, and (d) RAVEN/NEWT/PHISICS. Each interface was created from scratch and can interact based on the RAVEN driver inputs. The interfaces (a), (b) and (c) were released on the INL HPC resources for internal use. The study established suitable HTTR and VHTRC lattices to create PHISICS core models. An uncertainty analysis was carried out on a VHTRC assembly as verification process of the interface RAVEN/PHISICS, using the manufacturing uncertainties (validation). Additional capabilities were implemented within PHISICS to achieve cross section perturbations. The development of uncertainty studies with RAVEN/PHISICS stimulated the implementation of additional features in PHISICS, with the cooperation of Andrea Alfonsi. The code is now capable of

recognizing identical isotopes belonging to different lattice model's mixtures (capability developed by Andrea Alfonsi to improve the fidelity of the NEWT-to-PHISICS results, in CHAPTER 5). This feature ensures a better assimilation of the self-shielded cross sections and evidenced more accurate transport solutions. The code PHISICS is now qualified to admit perturbation factors as an input and can modify the self-shielded cross sections accordingly (with, again, the cooperation of Andrea Alfonsi). A user's manual unveils the RAVEN/PHISICS and RAVEN/PHISICS/RELAP5-3D capabilities.

Finally, a state-of-the-art sequence that accomplishes autonomous searching of energy group structures was created with RAVEN/NEWT/PHISICS and demonstrated with an HTTR model. The sequence utilizes NEWT to generate on-the-fly cross sections for PHISICS, while the adaptive sampling capabilities of RAVEN orientate and accelerate the energy group search.

1.3 Outline of the Thesis

The study starts with a global description of HTGR systems. The specification emphasizes on three prismatic cores that are modeled in the following chapters. The section also reports the codes utilized to simulate the HTGR cores, and the key concepts of neutron transport, resonances, cross section self-shielding and burnup calculations. CHAPTER 3 outlines the sensitivity and uncertainty analysis methodologies developed for nuclear engineering applications, and summarizes the main results obtained from the Uncertainty Analysis Modeling on LWRs and the IAEA CRP on HTGRs. CHAPTER 4 proposes an approach to collect few-group, homogenized cross sections to carry out in a second step stochastic samplings in burnup calculations with XSUSA. CHAPTER 5 investigates the effect of lattice cross sections on multi-physics core solutions with the codes T-NEWT and PHISICS/RELAP5-3D. CHAPTER 6 focuses on the output uncertainties obtained on nuclide inventories over depletion calculations, using SAMPLER/T-NEWT. The spectral effects on the output uncertainties are estimated. CHAPTER 7 concentrates on the verification of the RAVEN/PHISICS interface and the analysis of input and output uncertainties obtained from a VHTRC core. CHAPTER 8 exposes a methodology to obtain few-group structures with surrogate models constructed with RAVEN/NEWT/PHISICS. CHAPTER 9 concludes the work and suggests the future directions of the research on the topics exposed.

CHAPTER 2

INTRODUCTION ON HTGR SYSTEMS AND NUCLEAR CODES RELEVANT TO HTGR ANALYSIS

CHAPTER 2 provides a general background on the HTGRs, regarding the designs and historical aspects. An attempt is done to draw the broad lines of the neutronics such as neutron transport, self-shielding and burnup calculations. This chapter also outlines the codes used in the following sections to carry out the simulations.

2.1 The General Aspects of the High Temperature Gas-cooled Reactors

The most commonly operated reactors are nowadays LWR systems, constituted by either Pressurized Water Reactors (PWR) or Boiling Water Reactors (BWR). These reactors represent about 80 % of the total number of nuclear power plants in the world. Other designs include, amongst others, Sodium Fast Reactors (SFR), light water graphite reactors (RBMK), pressurized heavy water reactors (CANDU) or HTGRs. Specific features characterize all these previously cited systems, for instance the type of moderator (if present), the coolant, the lattice geometry, the fuel type and fuel enrichment, the neutron spectrum, the temperature of operations etc.

The concept of HTGR has appeared in the late 1950s in United Kingdom, and has started being developed in the 1960s. Inherently safe and presenting a high thermal efficiency (~40%), the HTGRs promote flexibility to the designer. The HTGR sets itself apart from common reactors such as PWRs or BWRs by its high thermal inertia, making it intrinsically safe [3].

Two branches of operational HTGRs exist: the Pebble Bed Reactor (PBR) and the prismatic type. Table 1 summarizes these two styles of reactors that were tested under the form of experimental and industrial reactors. The plants have demonstrated the successfulness of the coated particle design and the helium as a coolant. The Peach Bottom reactor encountered a bright success. The fuel kernels in the Peach Bottom reactor were originally coated with pyrolitic carbon. The regular failures of the fuel coatings encouraged the development of BISO and

TRISO particles for safety purposes. Despite successful fuel behaviors, other reactors have faced difficulties in the design and operation. For instance, one of the AVR's issues was the absorption of fission products in the graphite dust. The Fort St. Vrain Reactor faced mechanical difficulties, for instance in the helium circulators and the reactivity control systems [4].

Table 1. A few characteristics of High Temperature Gas-Cooled Reactors built in the history

Reactor	*Criticality/shutdown*	*Power (MWt)*	*Type*	*Country*
Dragon	1964/1975	20	Prismatic	England
Peach Bottom	1966/1974	115	Prismatic	USA
AVR	1966/1988	40	Pebble	Germany
Fort Saint Vrain	1974/1989	840	Prismatic	USA
THTR-300	1983/1989	750	Pebble	Germany
VHTRC	1985/-	-	Prismatic	Japan
HTTR	1998/-	30	Prismatic	Japan
HTR-10	2000/-	10	Pebble	China
HTR-PM	2018/-	250	Pebble	China

After the mixed results reported from the HTGRs in the 1970s and 1980s, a renewed interest in gas-cooled systems stemmed from the co-generation capacities, in terms of hydrogen production [5] and desalination process [6]. The recent need in small, modular reactors in newcomer countries also reaffirms the attentiveness.

The pebble-bed design consists in a short-necked funnel-shaped vessel containing tennis-ball-sized pebbles. The pebbles, mostly made of graphite, encompass the fuel. The bottom end of the vessel discharges continuously the pebbles to test the integrity of the elements. About ten percent of the controlled pebbles are disposed while the rest re-enters the top of the core, in addition to fresh pebbles for reactivity sustainability. The pebble-bed core can operate in a continuous fashion. The prismatic-type HTGRs are more conventional: they consist in hexagonal blocks stacked together with the fuel dispatched in fuel pins placed within hexagonal compacts. A particular attention is drawn to the prismatic models, namely the MHTGR (section 2.1.1), the HTTR (section 2.1.2) and the VHTRC (section 2.1.3).

2.1.1 The Modular High Temperature Gas-cooled Reactor

The MHTGR is a General Atomic design originating from the eighties [7]. The plant is a graphite-moderated, helium-cooled core. The fuel, embedded in TRI-structural ISOtropic (TRISO) particles (see Section 2.2), provides a thermal power of 350 MWt. Helium transports the heat to a steam generator vessel, where a heat exchanger superheats the steam. The net efficiency of the plant is evaluated to 38.4%, with a core power density of 5.9 $W.cm^3$ and an equilibrium fuel burnup estimated at 82.4 GWd/MTHM. Key safety features that characterize the MHTGR are inherent to HTGRs:

- The graphite structure across the core has a high heat capacity, which induces slow temperature changes within the core in case of power increases and transients;
- The TRISO particles (see Section 2.2) are temperature and pressure resilient;
- The mechanical integrity of graphite is preserved beyond 2,760 °C;
- The core has a strong negative power coefficient, meaning that an increase of power decreases the neutron flux through Doppler Effect and moderator temperature effect, leading ultimately to a decrease in the power. This feature provides a passive power control (so-called negative feedback);
- The decay heat can be removed passively (i.e. even in case of malfunction of the coolant pumps);
- A passive Reactor Cavity Cooling System (RCCS) removes the heat through conduction and radiation in case of a pump failure. The RCCS uses outside air that circulates inside panels around the pressure vessel.

One of the appeals of the MHTGR is the modular aspect of the design, encouraging the addition of modular units according to the demand.

2.1.2 The High Temperature Test Reactor

The Japanese Atomic Energy Research Institute (JAERI) established the application for installation of the High Temperature Test Reactor (HTTR) in 1989 to ensure continuous improvements of HTGR designs and promote the production of hydrogen through HTGRs. The bibliography ([8], [9]) provides the full specification of the HTTR and the two-dimensional representation of the core design.

The HTTR is made of a 30 MWt core cooled by two different cooling circuits. The first cooling circuit is a serial association of an intermediate helium/helium heat exchanger (IHX) followed by a secondary pressurized water cooler. The second cooling circuit consists in one single pressurized water cooler. The heat collected by the IHX is passed to the secondary helium circuit for heat utilization purposes such as hydrogen generation. The two pressurized water coolers fulfill pure cooling functions. An air cooler removes the heat extracted by the pressurized water from the primary helium. The average power axial power density ranges from 2.0 $W.cm^{-3}$ at the top of the core to 9.0 $W.cm^{-3}$ at the bottom with an average at 2.5 $W.cm^{-3}$.

The reactor pressure vessel is 5.5 m in diameter and 13.2 m in height. It includes the reactor core, replaceable graphite reflector and permanent graphite reflector. Helium circulates downward at an inlet temperature of 395 °C to cool down the reactor core. The coolant outlets from 850 °C to 950 °C in seven hot plenum blocks. A mixing plate ensures the homogenization of the helium temperature from the seven hot plenum blocks into a single hot plenum before the heat exchangers.

The active core is 2.3 m in diameter and 2.9 m in height. It contains 30 fuel columns and seven control rod (CR) columns. The reactivity is controlled through the CRs that are inserted in specific control channels located in the replaceable reflector and fuel region. The CR guide blocks have three holes. Two holes are allocated to rod insertion. Additional negative reactivity can be inserted as back up via B_4C/graphite pellets into the third hole located in the CR columns.

TRISO particles (see section 2.2) scattered within a graphite matrix encapsulate the fuel. Fuel rods embed the TRISO particles and matrix. Graphite prismatic compacts enclose the rods. The combination of fuel compacts and CR compacts constitute fuel blocks of 36.0 cm in flat-to-flat distance. A cluster of either 33 or 31 fuel compacts composes a fuel block. The fuel blocks also contain 3 slots allocated for Burnable Poison (BP) compacts located under dowel pins. One out of three BP compact is kept empty. The dowels are positioned at the top of the rods and connected at the bottom by sockets. Handling holes top the fuel rods. The fuel blocks are stacked axially to form columns. Uranium dioxide enriched from 3 % to 10 % ^{235}U with an average of 6 % constitutes the fuel. Twelve fuel enrichments are used in the core, increasing from top to bottom axially and from inner layer to outer layer radially. Two BP enrichments are available. Residual ^{10}B models the

impurities in the replaceable graphite, permanent graphite and graphite sleeves. A gap exists between the core's graphite blocks to tolerate the thermal expansion and effect of irradiation. Figure 1 gives an overview of the HTTR model from reference [8].

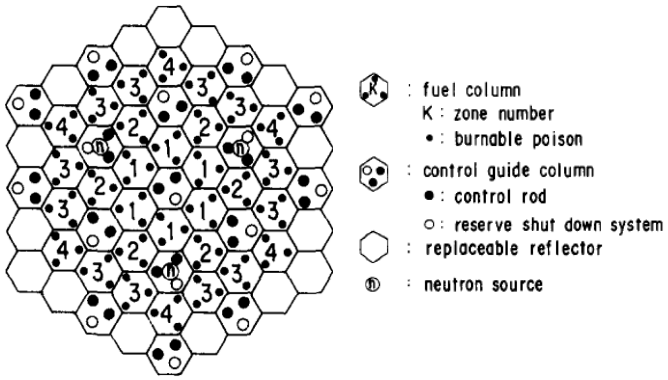

Figure 1. Radial representation of the HTTR (Ref. [8])

2.1.3 The Very High Temperature Reactor Critical Assembly

This section briefly describes the VHTRC. Interested readers can refer to the detailed specifications of the VHTRC in reference [10]. The VHTRC experiment was conducted to collect neutronics data applicable to the closely-related HTTR. The first criticality of the reactor was achieved in May 1985. The VHTRC core consists in two identically-shaped hexagonal assemblies. The first half is fixed while the second moves along one spatial degree of freedom. Figure 2 provides a bird's eye view of the VHTRC system.

The panels include 40 electric heaters to study the temperature effects on the neutronics characteristics. The core contains six types of rods dispatched in the graphite blocks:

- Two fuel rods "B-4 type" and "B-2 type" characterized by different UO_2 enrichments;
- Graphite rods;
- Heater rods;
- Control rods;
- BF_3 counters;

Radially, prismatic compacts embed the rods. A cluster of compacts constitutes a block. The fuel rods are hollow cylinders made of five concentric layers. Helium fills the innermost layer, which is surrounded by a region made of approximately 20,000 BISO particles containing the fuel. A graphite matrix hosts the randomly-distributed BISO particles. A helium gap circles

the fuel/matrix ring, which is enclosed by a graphite sheath followed by another layer of helium gap. Figure 3 depicts a radial cut of a fuel compact. The dimensions of the helium gaps are not represented on the sketch for clarity: the innermost gap thickness is 0.025 cm and the outermost gap thickness is 0.020 cm.

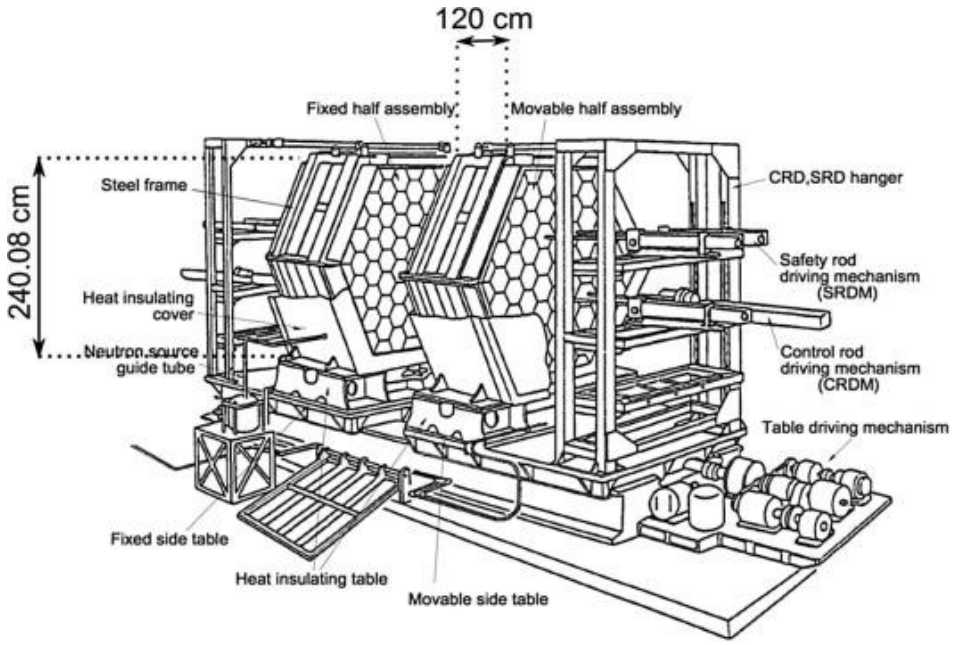

Figure 2. Bird's eye view of the VHTRC (NEA, [10])

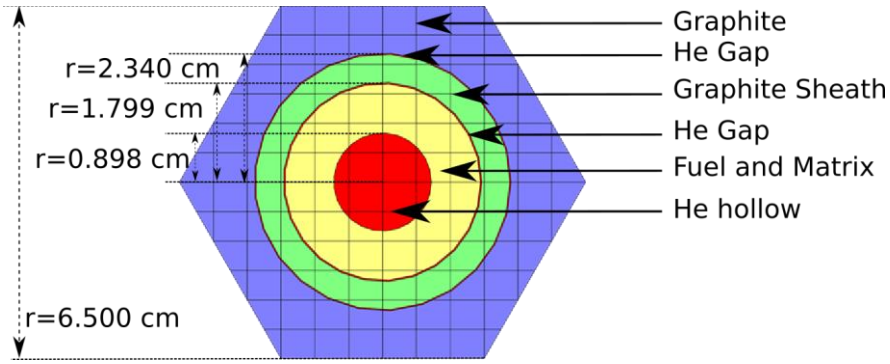

Figure 3. Radial representation of a VHTRC B-4 fuel compact

One panel comprises fifty-five prismatic blocks while the outermost layer is populated with eighteen trapezoidal-shaped blocks to give a hexagonal shape to the halves. Three types of blocks exist across the assemblies: one-holed, six-holed, and nineteen-holed blocks. The one-

holed blocks contain either a heater rod or a graphite rod at the center. The six-holed blocks contain three large graphite holes and three regular graphite holes. The nineteen-holed blocks contain eighteen slots allocated to either fuel or graphite rods. The central hole, slightly larger, is designated to CR insertion and instrumentation. The outermost trapezoidal elements contain a graphite rod at their center. The fuel blocks are stacked together to form 72.0 cm-long column in each panel. The radial combination of the fuel blocks, one-holed graphite blocks, three-holed blocks and heater-host blocks lead to three loading pattern named HP, HC-I and HC-II (

Figure **4**). The HP core reached criticality at 25.5°C and the effects of the temperature on the reactivity were measured at 71.2 °C, 100.9 °C, 150.5 °C and 199.6 °C, while the HC-I and HC-II cores reached criticality at 8.0 °C and 200.3 °C respectively. The temperature distribution was flattened at the beginning of each experiment and the control rods were pulled to a fully-withdrawn position.

In the experiment, a "pulsed neutron method" measures the multiplication factor: a neutron source generates 10^8 neutrons per pulse at 14 MeV. Each assembly hosts two BF_3 counters (four counters total) to tally the neutron production.

The counters determine the area ratios of the prompt neutron A_p and delayed neutron A_d modes. A_p and A_d originate from the point-kinetics equations.

$$\frac{A_p}{A_d} = \frac{-\rho}{\beta} \qquad \text{Equation 2-1}$$

This method disregards the higher modes and the kinetic distortions. A theoretical correction factor is used to calibrate the reactivity values [11]. The areas relative to the prompt neutron and delayed neutron modes are obtained experimentally after the following pre-processing steps [12]:

- Evaluation of the decay curve at the temperatures chosen for the experiment;
- Correction of the decay curve to take into consideration the detector's dead time;
- Least-square fitting of the corrected decay curve with a data-processing code;
- Another correction is carried out on the prompt-to-delayed area ratio A_p/A_d to screen out the higher modes. The correction factor is calculated from broad-group constants generated with the diffusion code CITATION;

- The Equation 2-1 provides the final reactivity, using the averaged value from the four detectors.

The steps described above are listed here to better understand the uncertainties derived in the VHTRC experiment (treated in CHAPTER 7).

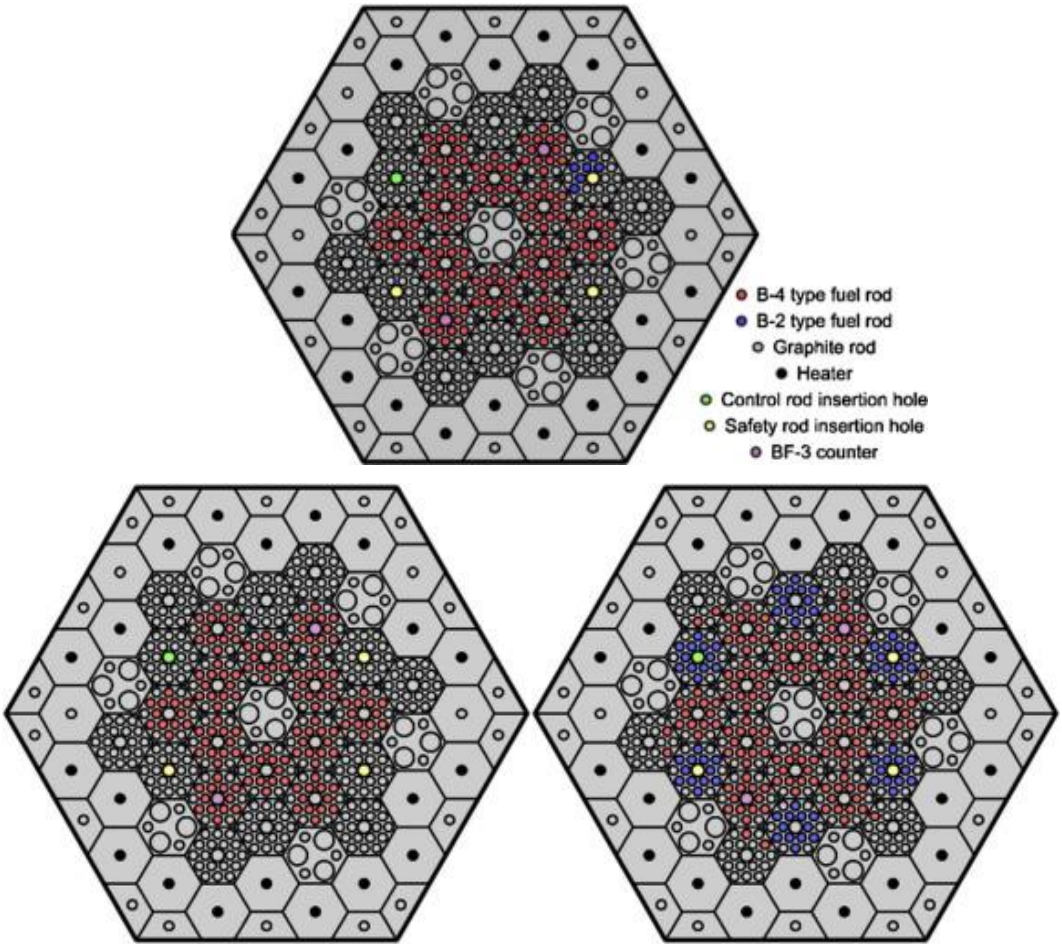

Figure 4. The VHTRC loading patterns HP (top) HC-I (bottom left) and HC-II (bottom right) (NEA, [10])

2.2 Coated Particles and double heterogeneity

2.2.1 Design of the TRISO and BISO Particles

Regardless of the design and features of the HTGRs, the multi-layered spherical grains called TRISO and BISO particles embed the heavy metal (usually UO_2, but also UCO or UCN). A graphite matrix contains these particles to constitute either the so-called pebbles, surrounded

with pure graphite, or the so-called prismatic compacts put in hexagonally-arranged graphite blocks. Therefore, the resulting models are in a doubly heterogeneous state, the first heterogeneity being the lattice of TRISO or BISO particles (grains) within the graphite matrix. The lattice of pebbles or fuel rods constitutes the second heterogeneity.

The BISO fuel is simply made of two pyrolitic carbon layers to enclose the fuel kernels. Five layers compose the TRISO particles (Figure 5):

- Fuel kernel;
- Porous Carbon Buffer;
- Inner Pyrolytic Carbon (IPyC);
- Silicon Carbide (SiC);
- Outer Pyrolytic Carbon (OPyC).

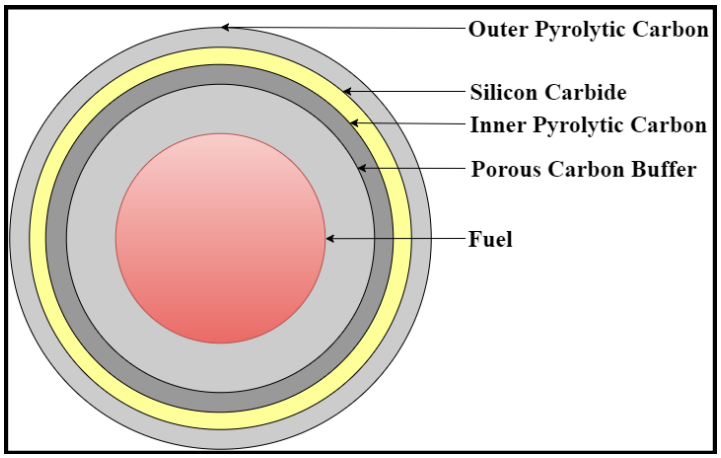

Figure 5. Two-dimensional cut of a TRISO particle

The particles' prime job resides in the high-efficiency sealing of the fission products, while withstanding the high pressures created by the fission product gasses. A TRISO particle diameter ranges around ~1 mm, which implies there are about $\sim 10^{11}$ TRISO particles in a full-sized reactor core. A grain must guarantee a leak-tight barrier to fission products and the mechanical integrity of the fuel under irradiation over the cycle. The fuel kernel contains the fissile material and thus the fission source. The low-density carbon buffer serves as storage space to collect both the gaseous fission products released after the fission events and the chemical products originating from the reactions between the carbon and oxygen (contained in the uranium oxide). It also

supports the fuel kernel swelling induced by temperature changes and facilitates the fission product retention. The buffer puts up the recoil energy of fission products to protect the IPyC and SiC layers from damages. The high density IPyC provides an appropriate surface to deposit the silicon carbide on. The inner pyrolitic carbon protects the SiC from chlorine attacks during the manufacturing. It finally prevents the attack of carbon monoxide (produced mainly by UO_2 fuel) on the silicon carbide. The SiC is the major barrier to the fission products. It is also designed to supply the mechanical support required to resist to the internal gas pressure. Under accident circumstances involving temperature increases up to 2000 °C, the SiC is the dominant channel of mechanical failure. The outer pyrolitic carbon layer offers an adequate compression to the silicon carbide lying underneath. It bonds the particle with the matrix, protects the SiC from external chemical reactions and acts as a fission product barrier.

2.2.2 Fission Product Transport in TRISO Particles

Several transport mechanisms are observed in a particle. They include, not exhaustively, the recoil mechanism after a fission event, the motion through the interconnected porosities in the kernel, chemical reactions at the interface kernel – buffer, thermal diffusion (buffer), cracking (buffer), trapping (IPyC and OPyC) etc. Those mechanisms depend on the irradiation status of the particles and the temperature and thus vary over the cycle. The mechanical integrity of the particles can severely change under accident conditions. Overall, the krypton, xenon, silver and cesium are the isotopes characterized by the largest diffusion capabilities [13] [14]. Because of these safety concerns, those isotopes were retained as figure of merit in CHAPTER 6 while tracking the uncertainties on the isotopes' number densities as a function of the burn-up.

2.2.3 Migration Area in HTGRs

The effective multiplication factor is defined as the ratio of the number of neutrons produced to the number of neutrons absorbed from one generation to another. The power distribution and the neutron multiplication factor are determined by three fundamental values:

- the product of the average number of neutrons generated after a fission event and the fission cross section: $\nu\Sigma_f$;
- the absorption cross section: Σ_a;
- the total cross section Σ_t.

$\nu\Sigma_f/\Sigma_a$ settles the ratio of the neutron reproduction after a fission versus the number of absorptions. The migration area (M^2, in cm^2) establishes the elementary path of neutrons from emission to absorption, accounted for through the total cross section. The migration area also comprises the number of diffusions experienced between apparition and disappearance of neutrons, and finally, in the framework of the transport theory, it models the anisotropy of scattering through the transport cross section Σ_{tr}. The migration area is defined as $1/\sqrt{6}$ of the average crow-flight distance between the neutron's birth (as a fast neutron) to the neutron's absorption (as a thermal neutron). In mono-energetic theory (also referred to as "one-group theory"):

$$M^2 = \frac{1}{3\Sigma_a\Sigma_{tr}} \qquad \text{Equation 2-2}$$

$$\Sigma_{tr} = \Sigma_t - \mu\Sigma_s \qquad \text{Equation 2-3}$$

μ is the cosine of the average angle of deviation after a scattering event and Σ_s is the scattering cross section. M^2 *de facto* depends on the nature of the moderator. The migration area indicates the size of a core neutronically speaking, and hence demonstrates how unit cells (or assemblies) are coupled to each other.

The deterministic nuclear code SCALE6.2/T-NEWT (detailed in section 2.6.2) is chosen to simulate a compact cell (typical HTGR unit cell) and a PWR pin cell to compare the differences between the respective migration areas in one-group theory. The HTGR compact is a 0.9398 cm side-to-side hexagonal and contains TRISO particles in a graphite matrix. A thin layer of helium coolant circles the fuel rod that is moderated with graphite (Figure 6). The entire cell is at 1,200 K. CHAPTER 5 details the complete specifications relative to the compact. The PWR pin cell is 1.275 cm wide. The fuel is 2.35 % ^{235}U in uranium dioxide form at 900 K, surrounded by a 0.10 cm thick layer of ziraclloy-4 at 600 K and moderated with light water of density equal to 750 $g.cm^{-3}$ (Figure 7). Table 2 compares the migration areas of the two models.
r is defined as the crow-flight distance between neutron's birth and absorption:

$$r = \frac{1}{\sqrt{6}} M \qquad \text{Equation 2-4}$$

Table 2 proves that neutrons "travel" longer distances in a HTGR system than PWR, which demonstrates in other words that HTGR blocks are more tightly coupled than LWR assemblies.

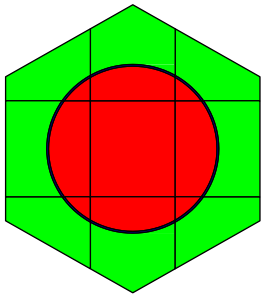

Figure 6. Compact unit cell, made of fuel (red), helium (blue) and graphite (green)

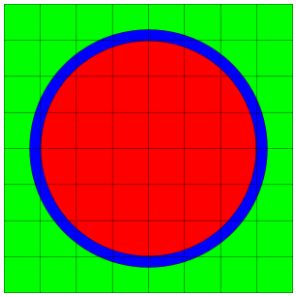

Figure 7. PWR unit cell, made of fuel (red), zircalloy-4 (blue) and light water (green)

Table 2. Migration area of a HTGR compact and PWR pin cell

Type of cell	Σ_a (cm^{-1})	Σ_{tr} (cm^{-1})	M^2 (cm^2)	*r* *(cm)*
HTGR	3.9775 E-03	3.1108E-01	269.4	40.2
PWR	2.1208E-02	2.5970E-01	60.5	19.0

2.3 Nuclear Data and Cross Sections

Most of the fission reactions in nuclear reactors involve a target neutron with a given energy and a target fissile nucleus. The target nucleus undergoing the fission reaction produces two fission product nuclei, a few resulting neutrons, fission gamma rays and neutrinos. The resulting interaction between an incident neutron and a target nucleus may as well be, not exhaustively, an elastic scattering, an inelastic scattering, or a radiative capture event. The fission outcome may also occur spontaneously, or with high-energy gamma rays. The reaction of a particle on a target nucleus is evaluated with a probability of interaction. The cross section data establish the number of reactions happening between a flux of particles and the target.

The fission neutrons appear at energies ranging about 2-10 MeV. Fission events occur typically at ~1 eV in thermal reactors, hence the cross sections must be evaluated on a broad energy spectrum. A non-linear profile over the energy spectrum characterizes the cross sections partly because of resonances. Resonances originate from the existence of discrete levels of excited states. An incident neutron and a target nucleus enter a short-lived excited state after the collision called compound nucleus. The formation of a compound nucleus state requires that the sum of the incident neutron energy (sum of the kinetics energy and the binding energy) and the energy of the nucleus at ground state is equal to compound nucleus energy. This will result in a large increase in the cross section value at this given energy. In addition, the energy difference between two resonances (i.e. two energy levels) decreases with increasing atomic number. The number of possible excited state increases with increasing atomic number. Eventually, smooth cross section profiles characterize the light nuclei because of the few resonances levels over their energy spectrum. Heavy nuclei's several resonances result in chaotic cross section profiles (Figure 8).

The large energy spectrum and the resonance peaks complicate the estimation of the cross section data. The cross sections are evaluated experimentally in the smooth regions and through correlations in the absorption regions. Thus, the experimental evaluation of the cross sections is subject to measurement uncertainties. The neutron cross sections are nowadays measured as a function of cross section standards.

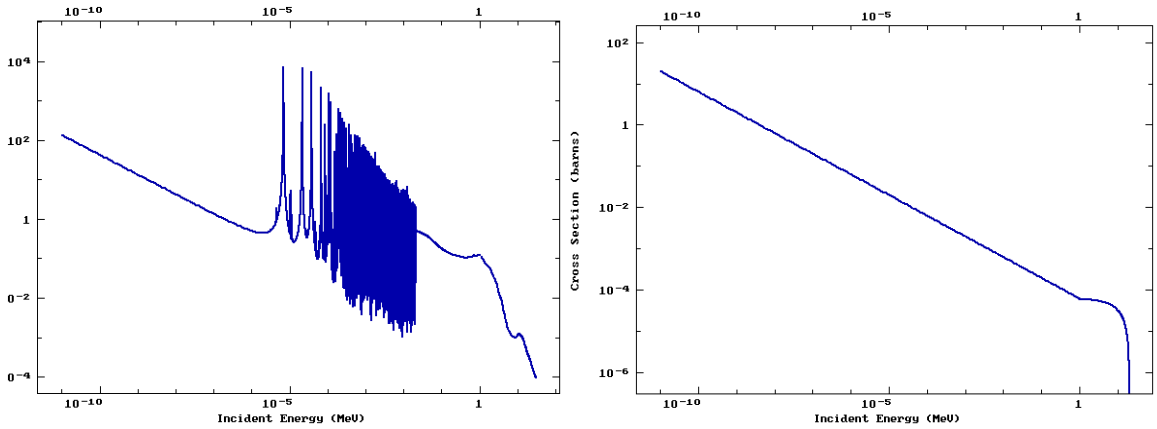

Figure 8. ^{10}B capture cross section (left) and ^{238}U capture cross section (right) from the ENDF/B-VII.1 library

The rate of a standard detector is defined as:

$$R_s = \varepsilon_s \Phi N_s \sigma_s \quad \text{Equation 2-5}$$

ε_s is the efficiency of detection of a given reaction type, Φ is the neutron flux; *N* is the number density of the sample and σ_s the microscopic cross section that is measured. The relative cross section can be measured as:

$$\sigma_m = \frac{R_m \varepsilon_s N_s}{R_m \varepsilon_m N_m} \sigma_s \quad \text{Equation 2-6}$$

m is the subscript relative to the measured values. The use of a standard detector cancels out the neutron flux parameter previously explicit in Equation 2-5 [17].

Such experimental processes are also required to determine the decay constants, delayed neutron fractions and fission yields [18], [19], [20] to eventually compile them into standardized nuclear data libraries [21]. The values measured for all the nuclear data come with an uncertainty attributed to the experimental process. Hence, the nuclear data libraries should rather be interpreted as the best estimate values among a range of values described by a Probability Density Function (PDF).

Covariance matrices give the amount to which nuclear reactions are correlated to each other for each group of discretized energy. Significant efforts have been dedicated into the development of the covariance data libraries to obtain a robust set of data for various applications [22]. The covariance data have been included as sub-modules in the traditional nuclear data libraries. The accuracy and validation of nuclear data and the nuclear covariance data has been investigated since the early stages of the nuclear engineering industry and remains a continuously studied [23], [24]. Because discrepancies between the Evaluated Nuclear Data File ENDF/B-

VII.0 and ENDF/B-VII.1 were evidenced even for major isotopes, it is reasonable to assume some discrepancies linger in the newest covariance data libraries and covariance data from other sources. For example [25], some inconsistencies have been demonstrated for the ^{240}Pu or ^{241}Pu. Low-fidelity covariance are associated to several fission products and minor actinides. Efforts are now concentrated onto the development of quality assurance codes to perform systematic verification of covariance data, dedicated to rule out unrealistically low or high uncertainties as well as adjusting mathematically incorrect covariance matrices. It has also been shown that different sets of covariance data lead to different uncertainty results [26].

The SCALE 6.2 covariance data library [27] is used in the study to perform uncertainty quantification with the sequence SAMPLER. Section 3.2 provides more information on SAMPLER and stochastic sampling. The following sources compose the SCALE 6.2 covariance library:

- 187 nuclides originate straight from the ENDF/B-VII.1;
- 215 nuclides, missing in the ENDF/B-VII.1, were conserved from the previous version of SCALE (6.1) and from ENDF/B-VII.0;
- A low-fidelity component created cooperatively by Oak Ridge National Laboratory (ORNL), Brookhaven National Laboratory (BNL) and Los Alamos National Laboratory (LANL) was also appended.

The high-fidelity covariance data are evaluated through a rigorous procedure based on regression algorithms set to tweak the nuclear physics parameters. It is aimed ultimately to fit experimental results. The high-fidelity covariance data are derived from the evaluation of the cross sections themselves. If such rigorous methodology cannot be achieved, the uncertainty evaluation is decoupled from the experimental measurement of the cross sections and approximations must be introduced. Low-fidelity covariance information are completely independent from experimental measurements. They are derived from the absolute uncertainty of the resonance integral parameters [28], the measured value and the value computed from ENDF/B-VII. The SCALE 6.2 covariance data are used in CHAPTER 6 to perform uncertainty quantification of nuclide inventories.

The COMMARA-2.0 covariance data is also suggested in the future work of CHAPTER 7 as input uncertainty for cross section perturbation with RAVEN/PHISICS (see sections 2.6.8 and 2.6.5). The panel of experts participating to the CRP (see CHAPTER 1 for additional details)

on HTGRs suggested a greater variety in the codes, tools and methods chosen for uncertainty quantification. Such directive is motivated by the fact that there are no exact evaluations of uncertainties for nuclear data, which means there are no defined procedures to measure or derive the reliability of the uncertainty values (see also CHAPTER 7).

2.4 Neutron Transport Equation and Discretization Schemes for Nuclear Code Applications

The distribution of neutrons within a reactor is determined by neutron transport, i.e. the way neutrons stream in media throughout the system. The equation governing the motion of neutrons in their environment is referred to as Neutron Transport Equation (NTE). The NTE (Equation 2-7) is obtained by a heuristic derivation, by summating the gain and loss mechanisms of neutrons in an arbitrary control volume.

$$\frac{1}{v(E)}\frac{d\phi(\mathbf{r},E,\hat{\mathbf{\Omega}},t)}{dt}+\hat{\mathbf{\Omega}}.\nabla\phi(\mathbf{r},E,\hat{\mathbf{\Omega}},t)+\Sigma_t(\mathbf{r},E)\phi(\mathbf{r},E,\hat{\mathbf{\Omega}},t)$$
$$=\int_{4\pi}d\hat{\mathbf{\Omega}}'\int_0^{\infty}dE'\Sigma_s(E'\rightarrow E,\hat{\mathbf{\Omega}}'\rightarrow\hat{\mathbf{\Omega}})\phi(\mathbf{r},E',\hat{\mathbf{\Omega}}',t)$$
$$+\frac{\chi(E)}{4\pi}\int_{4\pi}d\hat{\mathbf{\Omega}}'\int_0^{\infty}dE'\nu(E')\Sigma_f(E')\phi(\mathbf{r},E',\hat{\mathbf{\Omega}}',t)$$
$$+s_{ext}(\mathbf{r},E,\hat{\mathbf{\Omega}},t)$$

Equation 2-7

v is the neutron speed;

ϕ is the angular neutron flux;

r is the neutron position (three-dimensional);

E is the neutron energy;

$\hat{\mathbf{\Omega}}$ is the solid angle of the direction of the neutrons (two-dimensional);

t is the time variable;

Σ_t is the macroscopic total cross section;

Σ_s is the double differential scattering cross section;

χ is the fission spectrum;

Σ_f is the macroscopic fission cross section;

s_{ext} is any external source;

The first term on the left-hand side of Equation 2-7 is the rate of change of the neutron flux. The second term is the leakage contribution while the third term is the collision term. The right hand side represents the source (gain) contributions, from (a) scattering, (b) fission and (c) external sources.

The space, angle, energy and time represent the seven independent variables relative to neutron transport. In nuclear reactor analysis, classical engineering techniques treat the space variables (for instance finite difference method or finite element method). The time discretization is performed by separating the neutronics calculations into a succession of steady states. The refinement of the time grid as well as the algorithms required for the time discretization depend on the type of transients analyzed. Rod ejection accidents take ~0.1 second to occur, while isotopic build-up over an entire fuel cycle can be studied over years of neutron exposure (see section 2.7). Nuclear codes discretize the energy variable as groups of small-ranged energy bins. Some codes can treat the energy continuously (See Section 2.6.4). CHAPTER 8 treats in detail the energy discretization and energy collapsing methods. Finally, the nuclear codes discretize the angle parameter. Codes such as SCALE6.2/NEWT are programmed with discrete ordinate angle discretization.

Discrete ordinates [29], or S_N methods, consists in discretizing the angle variables into a set of discrete possible directions of motion. In two-dimensional codes such as NEWT, in Cartesian geometry, the steady state transport equation is written:

$$\widehat{\boldsymbol{\Omega}}.\boldsymbol{\nabla}\phi\left(\mathbf{r},\mathrm{E},\widehat{\boldsymbol{\Omega}},\mathrm{t}\right)+\Sigma_{\mathrm{t}}(\mathrm{r},\mathrm{E})\phi\left(\mathbf{r},\mathrm{E},\widehat{\boldsymbol{\Omega}},\mathrm{t}\right)$$

$$=\int_{4\pi}\mathrm{d}\widehat{\boldsymbol{\Omega}}'\quad\int_{0}^{\infty}\mathrm{dE}'\;\Sigma_{\mathrm{s}}\left(\mathrm{E}'\rightarrow\mathrm{E},\widehat{\boldsymbol{\Omega}}'\right.$$

$$\left.\rightarrow\widehat{\boldsymbol{\Omega}}\right)\phi\left(\mathbf{r},\mathrm{E}',\widehat{\boldsymbol{\Omega}}',\mathrm{t}\right) \qquad \text{Equation 2-8}$$

$$+\frac{\chi(\mathrm{E})}{4\pi}\int_{4\pi}\mathrm{d}\widehat{\boldsymbol{\Omega}}'\int_{0}^{\infty}\mathrm{dE}'\nu(\mathrm{E}')\Sigma_{\mathrm{f}}(\mathrm{E}')\phi\left(\mathbf{r},\mathrm{E}',\widehat{\boldsymbol{\Omega}}',\mathrm{t}\right)$$

$$+\mathrm{s}_{\mathrm{ext}}\left(\mathbf{r},\mathrm{E},\widehat{\boldsymbol{\Omega}},\mathrm{t}\right)$$

The polar angle θ is the angle between the neutron direction $\widehat{\Omega}$ and the x-axis. The transport equation in a two-dimensional system within the discrete ordinate formulation is:

$$\left[\mu_{\mathrm{n}}\frac{\partial}{\partial\mathrm{x}}+\eta_{\mathrm{n}}\frac{\partial}{\partial\mathrm{y}}\right]\phi\left(\mathbf{r},\mathrm{E},\widehat{\boldsymbol{\Omega}_{\boldsymbol{n}}},\mathrm{t}\right)+\Sigma_{\mathrm{t}}(\mathrm{r},\mathrm{E})\phi\left(\mathbf{r},\mathrm{E},\widehat{\boldsymbol{\Omega}}_{n},\mathrm{t}\right)$$

$$=\mathrm{q}(\mathbf{r},\mathrm{E},\widehat{\boldsymbol{\Omega}_{\boldsymbol{n}}}) \qquad \text{Equation 2-9}$$

μ and η are the direction cosines at the n^{th} level.

The major problem related to S_N methods is its general inapplicability to non-orthogonal or highly non-symmetric systems. The S_N code NEWT (section 2.6.2) dodges this issue by approximating impractical shapes into arbitrary polygons and operating the systems in two-dimensional Cartesian grids.

In a discrete ordinate approach, the spatial discretization is performed *via* a so-called diamond difference scheme. This approach links the volume-averaged angular fluxes to the surface-averaged fluxes to ensure the heredity of the iteration sweeps based on the scattering source. The methodology may produce negative fluxes if the source is highly anisotropic.

The Method of Characteristics (MoC) is an alternative to the treatment of the spatial variable. Such method solves the transport equation along characteristic directions in a given cell system, defined by NEWT through the previously discussed arbitrary polygon treatment. An s-axis oriented towards the direction of motion $\widehat{\Omega}$ is created to solve the angular flux in the first term of Equation 2-9. The transport equation becomes:

$$\frac{d\Phi(s,E)}{ds} + \Sigma_t(s,E)\Phi(s,E) = q(s,E) \qquad \text{Equation 2-10}$$

Equation 2-10 is written in one given energy group and is repeated for each energy group accounting for the coupling between energy groups. The energy dependence is omitted in the notation from this point on. The solution of this differential equation is Equation 2-11.

$$\Phi(s) = \Phi_0 + \frac{q}{\Sigma_t}(1 - e^{-\Sigma_t s}) \qquad \text{Equation 2-11}$$

Φ_0 is the flux at s=0.

NEWT treats the total cross section and the source term as constant within a unit cell defined by the grid, ridding these two terms of their *s* dependence. Such assumption is exact for infinitesimally small cells and increases in error as the cell size increases. A study on the iterative convergence and effects on the neutron flux as function of the cell size is carried out in CHAPTER 5.The flux in Equation 2-11 is constant along all the known sides of a given cell. The set of characteristic directions is determined by the quadrature set chosen. The angular fluxes originating from the possible characteristic directions are numerically computed and integrated to generate the scalar fluxes. The use of the sides of the polygon length and the direction cosines μ and η provide the angular fluxes on the unknown sides. Overall, the entire system partitioned into cells is swept from the system boundary (that has known boundary conditions), following one given characteristic direction. It is then possible to compute the cell-averaged flux within each cell, for a given direction. The process is repeated for each characteristic direction considered. The flux crossing an unknown side of the cell is only dependent on the angular flux in one of the known side, the distance between them, the material's total cross section, the fission source and the length of the sides [31]. The angular fluxes combined to the numerical quadrature provide the scalar flux in each cell. The scalar flux provides then the average neutron source q (fission and scattering). The source is updated in Equation 2-11, and the process of angular flux calculation for a given direction is repeated, until convergence of the neutron sources and scalar fluxes.

The drawback of S_N methods is the possible apparition of so-called "ray effects". It consists in unphysical oscillations of the scalar flux and neutron source over the iteration process. Such effect appears typically in small-dimensioned problems, containing materials characterized

by a total-cross section-to-scattering ratio close to one. The graphite having a small absorption cross section, the scattering cross section is close to the total cross section and therefore the graphite-moderated systems are candidates to generate a ray effect, especially in compact cells. A representation of the scalar flux in a 5 × 5 cm cell, graphite-moderated and fueled with Mixed OXide (MOX) illustrates the ray effect in Figure 9. The energy group 11 (fast group) in a 252-group structure is represented on the plot. This scalar flux map generated by NEWT shows a high neutron flux in energy group 11 within the MOX pellet (red cylinder). One should expect a smooth change of color from warm to cold colors, as a spatial region (i.e. a squared cell) of interest is far from the MOX cell (the fuel). On the contrary, there are flux oscillations, depicted here by alternation of blue (low amounts of neutrons in energy group 11) and green (moderate amounts of neutrons in energy group 11) regions. Figure 10 shows the scalar flux in the same energy group, in an identical cell where the graphite moderator was replaced by light water moderator. The total-cross-section-to-scattering-cross-section ratio consequently shifts further away from 1, which annihilates the ray effect. Figure 11 displays the iterations on the multiplication factor as a function of the iterations number for both a graphite-moderated cell and a light-water-moderated cell. The peak at the beginning of the iterations corresponds to the user-input guess on the multiplication factor. The ray effect induces oscillations in the k_{inf} iterations and slows down the convergence, which impacts the preparation of the moderator cross sections (CHAPTER 5 and CHAPTER 8). The HTGR block-sized lattice cells have a sufficient fuel-to-moderator ratio to prevent such effect to occur. The increase in the S_N order can also lower the magnitude of the ray-effect but increases the computational cost and consequently the cost of the cross section generation. The computational efficiency will have a significant importance in random sampling sequences (see section 3.2) treated with NEWT in CHAPTER 6 and CHAPTER 8.

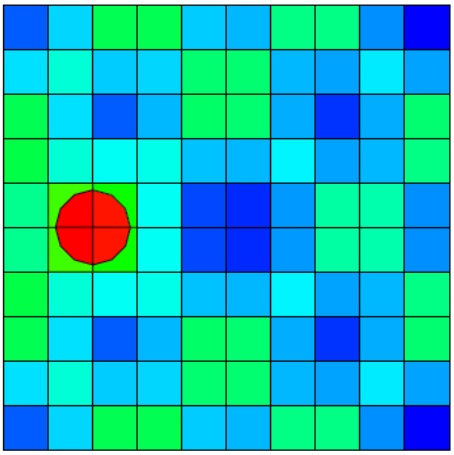

Figure 9. Ray effect on the scalar flux in discrete ordinate methods (NEWT plot) in a MOX, graphite-moderated cell

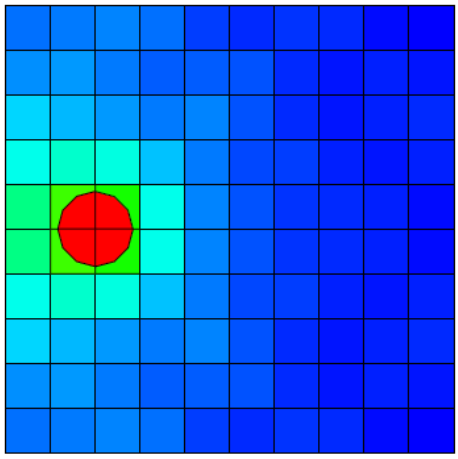

Figure 10. Absence of ray effect on the scalar flux in discrete ordinate methods (NEWT plot) in a MOX, light-water-moderated cell

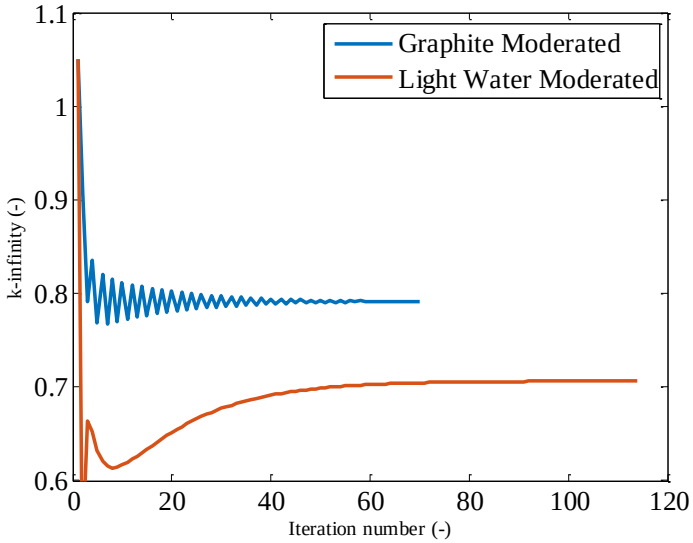

Figure 11. k_{inf} convergence in an LWR versus small-sized HGTR affected by ray effect

2.5 Multi-Group Treatment in Doubly-Heterogeneous States

Section 2.3 assesses the origin and the importance of nuclide resonances. Section 2.4 summarized the parameter discretization techniques appropriate for the resolution of the NTE. The generation of multi-group libraries handles the treatment of the energy variable. The neutron

cross sections relative to a nuclide *n* in an energy group *g* for a reaction *x* is averaged over the energy bin:

$$\sigma_{x,g}^{(n)} = \frac{\langle \sigma_x^{(n)} \phi_\infty(E) \rangle}{\langle \phi_\infty(E) \rangle} \qquad \text{Equation 2-12}$$

Φ_∞ is a generic function representative a neutron flux in a non-multiplying (i.e. without absorption) infinite medium. The reactor physics codes contain tabulated problem-independent nuclear data at a reference temperature. The isotopic inventory and the geometrical configuration establish the leakage, absorption and resonance specific to the system. For instance, enhanced leakage will soften the generic Maxwellian function allocated to the thermal spectrum. The resolution of the fine-group structure usually accounts properly for such effect, however, the fine-energy resolution of the resonances triggers flux variations within ranges lower than 1 eV. Significant discrepancies may appear between the generic function and the problem-specific neutron flux in the resonance range. The neutron flux's weighting function governing the cross section calculations, as theorized in Equation 2-12, requires approximations at the early stages of a transport calculation. Prior investigations have implemented approaches to determine the problem-, cross section- dependent neutron flux spectrum. In CHAPTER 4, CHAPTER 5, CHAPTER 7 and CHAPTER 8, the neutron cross section generation is administered in SCALE by the TRITON module. The sections 2.6.2 and 2.6.3 detail the files produced from TRITON. This section explores succinctly how SCALE derives the problem-dependent cross sections [31].

The nuclear data libraries exist as problem-independent tables in the codes and compel preliminary operations to obtain problem-dependent data. An accurate consideration of the resonances in the multi-group data is of essence to replicate the reactor physics within the multi-group simulations. The spectral calculations are subdivided into three categories.

- The unresolved resonance range (high neutron energies) is treated with the Bondarenko self-shielding method through the SCALE 6.2's BONAMI sequence. The narrow resonance approximation derives an analytical expression of the flux in a given material region *m.* The narrow resonance approximation depends on the generic flux Φ_∞, the total cross section of the material *m* and the background cross section. The background cross

section $\sigma_0^{(n)}$ relative to a nuclide *n* accounts for the relative density of the isotope *n* as compared to the macroscopic cross section of the other nuclides within the mixture:

$$\sigma_0^{(n)} = \frac{1}{N^{(n)}} \sum_{i \neq n} N^{(i)} \sigma_t^i \qquad \text{Equation 2-13}$$

The shielding factor associated with a nuclide *n* in a group *g* for a reaction type *x* stands as the ratio of the neutron cross section of the isotope *n* in group *g* for a reaction *x* normalized to the same cross section evaluated at an infinitely-dilute configuration.

$$f_{x,g}^{(n)} = \frac{\sigma_{x,g}^{(n)}(\sigma_0, T)}{\sigma_{x,g}^{(n)}(\sigma_0 \to \infty)} \qquad \text{Equation 2-14}$$

- In the range 0.001 eV to 20 keV, the SCALE 6.2's CENTRM code solves the simplified Continuous-Energy (CE) NTE in the lattice cell(s) representative of the system.
- CENTRM performs a Multi-Group (MG) lattice calculation to approximate the neutron flux for the rest of the neutron spectrum.

Section 2.2 highlights that the doubly-heterogeneous topology of the fuel in HTGR requires special neutronics treatments. The disseminated spherical particles compel three-dimensional lattice cell calculations, whereas two-dimensional spectral calculations suffice in single-heterogeneity. The neutronics of the doubly-heterogeneous state is decomposed into grain-to-grain interactions in a first step and classic fuel-element-to-fuel-element interactions in a second step. A point-wise flux distribution and disadvantage factors arise from the first stage of the spectral calculations. The disadvantage factors correct the spatial self-shielding after volume-averaging the grains with the matrix. Omission of the disadvantage factor yields to an artificial parasitic spread of absorbing nuclides such as ^{238}U across the volume that encapsulates the matrix and the grains. Spectral calculations supplemented with the newly-obtained cell-averaged cross sections are repeated for the second heterogeneity to derive the final MG data.

Regardless the number of heterogeneities, the SCALE self-shielding calculation is completed in a "black box" fashion. A common reflex to contend the doubly-heterogeneous paradigm

is to homogenize the graphite matrix and the TRISO particles into one mixture prior the beginning of the self-shielding sequence. However, this approach fails to replicate the neutron behavior in the medium. Getting around the two-step self-shielding sequence with a volume-averaged homogenization of the fuel/matrix region decreases significantly the resonance escape probability of the neutrons, which artificially hardens the neutron flux.

Prior researches confirm that volume-averaged homogenization is too approximate to model the TRISO particles. In the literature, Reactivity-equivalent Physical Transformation (RPT) methods were employed, tested [32] [33] on the multiplication factor for both steady state and burn up calculations. The RPT consists in homogenizing the TRISO fuel with the matrix while calibrating the radius of the smeared out mixture r_{rpt}. The artificial radius corrects the decrease of the resonance escape probability introduced by the homogenization and hence calibrate the multiplication factor. The application of this approach in 2-D geometries remains challenging. The verification and validation of all spectrum effects is a vast topic. For instance, the investigation in reference [33] falls short of addressing the ^{10}B burnable poison in coated particles. The approach evidenced ~0.00150 difference with explicit TRISO particle models in criticality and burnup calculations. The work presented in the next chapters avoids approximated approaches that skirt the doubly-heterogeneous particles. Efforts are invested in the methodologies to ensure explicit self-shielding treatments of the problem's lattice cell(s).

The concepts evoked in this section influence directly the methods detailed in the following chapters. CHAPTER 4, CHAPTER 5 and CHAPTER 7 and CHAPTER 8 necessitate spectral calculations on one or more lattice cells to construct few-group cross sections. Disregarding the cross section self-shielding leads to erroneous nominal results and sensitivity evaluations. Regarding CHAPTER 6, one can beneficiate from the exclusive application of the BONAMI sequence to perform the spectral calculations, rather than BONAMI plus CENTRM, to accelerate the burn up calculations, although this approach was not chosen to carry out the study.

2.6 Nuclear Codes for uncertainty analysis, burn-up and eigenvalue calculations

2.6.1 AMPX system

The AMPX code system [34] generates MG neutron cross sections, MG gamma cross sections and MG gamma yields relevant for neutron production through gamma interactions.

AMPX outputs MG neutron cross sections suitable for other reactor physics codes. The AMPX sequences return the nuclear data from ENDF-B/VII.0 or ENDF-B/VII.1 in SCALE 6.2. The work presented in the next chapters does not employ the AMPX code *per se*, because the codes embedded in the SCALE 6.2 suite have already yielded AMPX-processed libraries. The cross sections resulting from the various SCALE codes materialize in AMPX binary format. The cross section format may govern the choice of post-treatment codes (in this study, PHISICS, outlined in section 2.6.5) and the development of specific data-handling methodologies.

2.6.2 NEWT (New ESC-based Weighting Transport code)

The ORNL developed the SCALE 6.2's NEWT transport solver. NEWT can compute the problem eigenvalues, and create flux-weighted, few-group, AMPX-formatted cross-section libraries for ulterior full core solutions. The cross sections may be produced in microscopic or macroscopic format depending on the user's need. NEWT provides along with the broad-group energy data the neutron flux spectrum in the desired collapsed group structure. It relies on S_N ordinates methods and Extended Step Characteristic Approach (see section 2.4) to handle polygon-shaped surfaces in two-dimensional geometry. NEWT runs in general hand in hand with the control module TRITON for reactor physics calculations. The generation of problem-dependent cross sections followed by the transport solution emerges as the main appeal of the TRITON/NEWT (abbreviated into T-NEWT) pair. The TRITON/XSDRN's T-XSEC sequence fulfills the spectral calculation task (section 2.6.3). T-NEWT offers two execution options:

- The automatic sequence consisting in spectral simulations followed by the transport solution ensured by T-NEWT or;
- The manual sequence combining T-XSEC in a first run followed by NEWT in a second step.

The need for burnup prediction capabilities has also shaped T-NEWT into a depletion analysis code.

NEWT cannot perform Continuous-Energy (CE) transport solutions, and hence relies on the SCALE 6.2's 56- or 252-group energy libraries, originating from the primary nuclear data ENDF/B-VII.1. For legacy purposes, NEWT can apply transport calculations with the ENDF/B-VII.0 library in the SCALE 6.1's 238- or 44-group structure. In the version 6.2, the collapsing

features rely on the pre-existing, most refined group structures. In other words, a collapsed structure must be a sub-set of the SCALE 252-group structure.

Section 2.5 emphasized how the SCALE 6.2 codes, including T-NEWT, handle doubly-heterogeneous state of TRISO fuels. Section 2.6.7 details the SAMPLER/T-NEWT sequence relevant for uncertainty quantification purposes.

2.6.3 T-XSEC

In reactor physics calculations, T-XSEC may operate collaboratively with NEWT in the sequence called T-NEWT to successively prepare the problem-dependent cross sections and estimate the transport solution. In most applications, convenience points to the T-NEWT option. In some isolated applications, the cross section preparation apart from the transport calculations promotes advantages. CHAPTER 8 (section 8.2) details an example of such situation.

T-XSEC accounts for the spatial and energy self-shielding effects to provide appropriate microscopic cross section libraries. Among others and aside from the main output, T-XSEC generates relevant libraries and files for further transport calculations:

- The pre-mixed macroscopic cross section libraries in the fine-group structure (ft04f001);
- The master microscopic library in the fine-group structure (ft44f001). In the decoupled T-XSEC/NEWT progression, the NEWT problem mock-up requires additionally the *premix* and the *xnlib* flags, set to *no* and *44* respectively;
- The problem-dependent ASCII-formatted mixing table (ft92f001). It specifies the number densities of each isotope in each region of the problem. In the version 6.2.2 of SCALE, T-XSEC generates erroneously the mixing table in doubly-heterogeneous systems. Section 2.5 assesses the spectral calculation algorithm on the grain level (first heterogeneity). T-XSEC carries out a first spatial homogenization, leading to volume-averaged number densities within the matrix and the TRISO particles. The resulting medium appears then in a self-shielded single-heterogeneous fashion. A second spectral calculation follows, before accomplishing the transport iterations. In the SCALE 6.2.2 version and previous, the first volume-averaging step is executed over the entire prismatic volume instead of the fuel rod volume (which includes solely the TRISO particles and the matrix). Thus, the volume-averaged number densities originating from a doubly-heterogeneous system require manual corrections. As a simple verification, either to convince oneself

the mixing tables do not corroborate with the T-XSEC original input or to verify the performances of the SCALE's newer versions, it is suggested to implement a dummy compact cell in which the TRISO coatings are all made of pure ^{235}U as well as the matrix. This "trick" simulates a model characterized by volume-averaging factors equal to 1.0 in the matrix, the coatings and the fuel. The net result equivales to a single-heterogeneity problem. Hence, the number densities in the mixing table must remain equal to the number densities in the T-XSEC problem input.

2.6.4 KENO-VI and Serpent-2.1.27

KENO-VI is the SCALE 6.2 Monte Carlo code for eigenvalue neutronics and shielding analysis. KENO-VI can model three-dimensional systems for criticality analysis and neutron flux calculations in both MG and CE with ENDF/B-VII.0 or ENDF/B-VII.1. The TRITON reactor physics module can integrate the KENO-VI code for burnup predictions. In this analysis, KENO-VI is used to verify the Serpent-2.1.27 and T-NEWT models in CHAPTER 6. The cross section generation plus burn-up sequence detailed in CHAPTER 4 employs KENO-VI as depletion code. KENO-VI (CE) can treat explicitly the coated particles, under the condition they are modeled explicitly (i.e. manually) in the input deck. The code allows explicit modeling of burnable poison particle, which remains impossible in T-NEWT.

The section 6.7 evidences that the SAMPLER/KENO-VI code malfunctions for uncertainty quantification applied to burn-up calculations within the version 6.2.0 of SCALE. The later versions have not been tested on that issue.

The VTT Technical Research Center of Finland developed the Serpent-2.1.27 Monte Carlo code. Serpent is a CE three-dimensional code with multi-purpose reactor physics capabilities. Serpent 2.1.27 is used in CHAPTER 5 to verify the eigenvalues and neutron flux data obtained with the T-NEWT and KENO-VI codes. Serpent-2.1.27 generates a reference spectrum in the MHTGR core with explicit modeling of the TRISO particles.

2.6.5 PHISICS

The Idaho National Laboratory implemented the transport code PHISICS [35] in 2011. Recent updates coupled PHISICS to RELAP5-3D to provide a flexible platform that copes with the challenges of coupled-neutronics/thermal-hydraulic for HTGR core simulations. PHISICS

displays two- and three- dimensional geometrical modeling features. Its capabilities break down into a nodal and semi-structured spherical-harmonics-based transport core solver (INSTANT) for steady state and time-dependent problems, a depletion module (MRTAU), and a cross-section mixer-interpolator (MIXER) module.

In CHAPTER 5, CHAPTER 7 and CHAPTER 8, PHISICS handles the few-group transport calculations consecutive to the TRITON/NEWT cross section preparation. The treatment of the TRISO particles in PHISICS does not raise issues because PHISICS calculates the transport solution with flux-weighted homogenized microscopic cross sections characteristic of the TRISO fuel. The disadvantages factors, derived from the lattice cell's mixture-wise scalar fluxes, control the spatial self-shielding. The current version of PHISICS identifies identical isotopes from different regions which allows accurate spatial self-shielding modeling. PHISICS also supports cross section perturbation factors for uncertainty analysis purposes.

2.6.6 RELAP5-3D

INL coupled the neutron transport code PHISICS to the INL-developed thermal-hydraulics RELAP5-3D code [35]. RELAP5-3D is relevant for best estimate transient simulations of light water reactor systems during postulated accidents. The generic modeling approach allows HTGR simulations. In this study, the PHISICS/RELAP5-3D "ring" model of the MHTGR-350 design [36] supplied a constant isothermal temperature of 1,200 K to the neutronics module for the steady-state solution.

2.6.7 SAMPLER

The SCALE6.2/SAMPLER sequence is used in CHAPTER 6 to predict the uncertainty in the multiplication factor and nuclide concentration stemming from cross section and fission yield input uncertainties. SAMPLER relies on the creation of a perturbed input vector. This input vector originates from pre-defined PDFs included in the SCALE nuclear data covariance library (section 2.3). The SAMPLER sequence must be wrapped around other SCALE 6.2 modules to generate perturbed inputs. The process of generating perturbed vectors with PDFs is repeated N times over an analysis to collect the scatter in the output response (standard deviation and correlation coefficients) induced by the perturbed input data. Hence, a stochastic sampling can be applied to the SCALE codes to resolve criticality calculations, shielding and burn up problems No

adjoint calculations are required for such stochastic approach. The data from the input vector are perturbed simultaneously, hence providing a global uncertainty response, as opposed to the first order perturbation theory that provides individual sensitivity coefficient on the output response.

The covariance data were folded into pre-computed perturbation factors which are stored in the SCALE libraries. Those factors are utilized for the perturbation of cross sections and other parameters (fission yields, decay constants) during the SAMPLER execution.

SAMPLER collects the infinitely-dilute 1-D cross sections in MG format and passes them to the module MEDUSA. Using the nuclear data covariance libraries, MEDUSA generates pre-compiled perturbation factors. The flux-weighted cross-sections generated by BONAMI and CENTRM/PMC (the SCALE cross section processing modules) must agree with the perturbations operated on the infinitely-dilute 1-D cross sections. It has been shown [37] that the perturbation factors corresponding to the infinitely-dilute 1-D cross sections are suitable for the perturbation of the Bondarenko factors and the CE cross sections, both necessary to perform the problem-dependent spectral calculations. After the generation of the perturbed inputs, the classic SCALE6.2 module starts simulating the model following the normal process.

Section 2.5 broke down the spectral calculation steps implemented in the MG approach. By default, the modules BONAMI (unresolved range) and CENTRM cover the neutron spectrum, but the BONAMI module, based on the Bondarenko method, may be chosen exclusively. BONAMI runs faster than CENTRM so the sole use of BONAMI to produce the spectral calculation can relieve the running of SAMPLER/T-NEWT or SAMPLER/KENO simulations. The BONAMI/CENTRM sequence was chosen in this analysis to perform the spectral calculations for SAMPLER/T-NEWT simulations.

2.6.8 RAVEN

INL also created RAVEN, a software environment relevant for statistical analysis built around a system's response [38]. RAVEN was programmed to work collaboratively with any external code via Python interfaces. The development of an interface ensures efficient data interactions between RAVEN and the external code, which facilitates the input variable definition and the output uncertainty processing. RAVEN's built-in post-processing capabilities enable sensitivity and uncertainty analysis, but the software supports other powerful post-processing options,

such as data mining, adaptive sampling, data classifying etc. The next sub-sections outline the RAVEN's features applied in CHAPTER 7 and CHAPTER 8.

2.6.8.1 Sensitivity and Uncertainty Analysis in RAVEN

As mentioned at the beginning of section 2.6.8, a Python interface links RAVEN to a complex system. Section 2.6.8.4 addresses the architecture of RAVEN's generic interfaces. A RAVEN interface recognizes the input(s) relative to the external code, for example the number density in a PHISICS input, and generates new perturbed values with respect to user-defined distributions (uniform, Gaussian, Poisson etc.). The repetition of N perturbed simulations representative of a system modeled through the external code serves as foundation to elaborate the statistical analysis. After the execution of N perturbations, RAVEN post-processes automatically the code outputs and generates a statistical report that includes (among others) the standard deviation, the Pearson coefficients, the mean values, the input/output covariances, the sensitivity coefficients etc. CHAPTER 7 utilizes this approach within the RAVEN/PHISICS framework to simulate the VHTRC's manufacturing uncertainties.

2.6.8.2 Reduced Order Model in RAVEN

RAVEN can construct Reduced Order Models (ROM) to calculate fast solutions of an advanced problem. A ROM is a mathematical model representative of a given problem built from a training process. The training routine relies on the sampling of the parameters of interest relative to the physical model and the associated system responses. The algorithm that constructs the surrogate model receives the outcome of the sampling phase, so the ROM can shape itself to imitate the results obtained from the training.

Among the various classes of ROM supported by RAVEN, the *Neighbor class* classifies the outcome of a result into binary categories. At the beginning of a sampling sequence, RAVEN constructs a grid corresponding to the input phase space. Leaning on the trained database, the algorithm allocates a binary label to all the points of the grid. The classification scheme used in CHAPTER 8 relies on the k-closest neighbor(s) evaluated in the training process. The number of closest neighbors k is an integer defined by the user *a priori*. The distance, usually Euclidian, between the k-nearest neighbors to the query (i.e. the evaluated point) materializes as a weight

function in the decision-making process. The k-nearest neighbor embraces problems with a large input space in which the output tolerates a binary-classifying system.

Consider the input space in Figure 12. The green dots symbolize data points collected from previous queries classified as “successful”. The red dots represent data collected from previous queries that were labelled “failure”. The green and red dots embody the database of trained points. The user-defined three-neighbor approach evaluates which category a query (black dot) falls into. In a G-dimensional space, Equation 2-15 calculates the Euclidian distance between the query point Q and the trained points T_i.

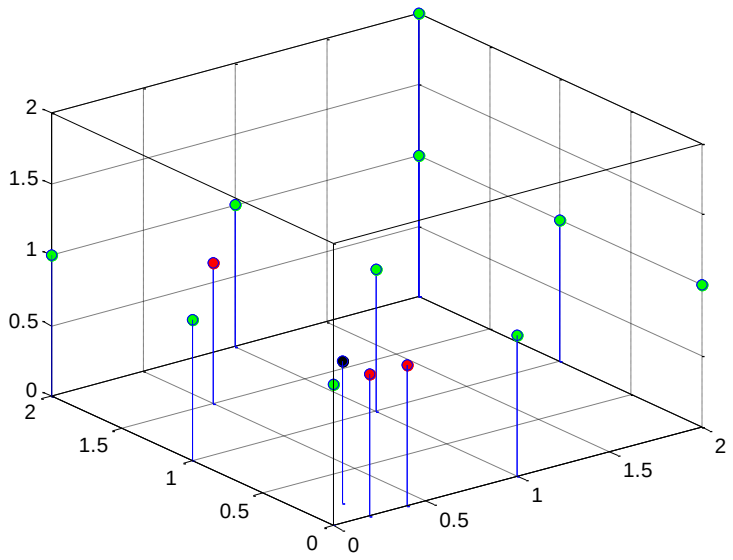

Figure 12. New query in a three dimensional input space

$$d_i(Q, T_i) = \sqrt{\sum_{g=1}^{G} (q_g - t_{ig})^2} \qquad \text{Equation 2-15}$$

$q_1, q_2, \ldots, q_g, \ldots, q_G$ denote the coordinates of the query Q and $t_{i1}, t_{i2}, \ldots, t_{ig}, \ldots, t_{iG}$ designate the coordinates of a trained point T_i. In Figure 12, the three closest trained points are T_1 (0;0;1) green, T_2 (0.2;0;1) red and T_3 (0.4;0;1) red. Table 3 gives the distance from the trained points to Q.

Table 3. Three-nearest neighbor example

Point	*Coordinate G_1*	*Coordinate G_2*	*Coordinate G_3*	*Distance to Q*
T_1	0	0	1	0.28
T_2	0.2	0	1	0.20
T_3	0.4	0	1	0.28
Q	0.2	0.2	1	0.00

An Inverse Distance Weight (IDW) deduces the amount of proximity from Q to the nearest neighbors. A coefficient u = 1 is assigned to a successful training point and u = -1 to a failure training point.

$$\mathrm{IDW} = \frac{\sum_{i=1}^{k} w_i u_i}{\sum_{i=1}^{k} w_i} \qquad \text{Equation 2-16}$$

$$\mathrm{w_i} = \frac{1}{\mathrm{d_i}} \qquad \text{Equation 2-17}$$

The sign of the IDW determines the query's label. In the example, the query's IDW is negative which associates it into the category of "failure" points.

2.6.8.3 Limit Surface Search as an Adaptive Sampling Technique in RAVEN

RAVEN's adaptive sampling function performs a "smart" survey of the input space to minimize the number of simulations. This type of approach fits problems characterized by infinite input spaces. The simulation of such systems remain time and computationally expensive, even with Message Passing Interface (MPI) capabilities, invalidating the possibility to examine the entire input space. The adaptive sampling strategy maximizes the amount of information collected while minimizing the simulation load. The workflow (a) gathers a few outcomes from a simulation *via* forward samplings, (b) constructs a ROM as described in section 2.6.8.2 to model the simulation space and (c) generates new samples based on the ROM's database to define a "limit surface". The Limit Surface Search (LSS) identifies the boundary between the acceptable solutions defined by constraints, and the unacceptable solutions. The ROM approach detects the

set of input variables associated with a response in the transition zone. The new simulations enhance the ROM that progressively shapes itself closer to the actual model. In CHAPTER 8, the k-nearest neighbor algorithm predicts the shape of the limit surface after each transport simulation. Based on the prediction, a limit surface region is determined. The algorithm converges when the shape of the limit surface is not modified after *P* consecutive samplings. The sampling is called "adaptive" because the future input points to be labelled represent the most relevant points that would define the limit surface. Those points are clustered around the limit surface line. Two mechanisms intervene then: the transport solution highlights the true label of a sampled input, and the prediction algorithm (e.g. the k-nearest neighbor) guesses the labels of the input points that have not yet been surveyed.

Figure 13 sketches three snapshots of the sampling evolution: It shows how the sampling progresses towards populating input values around the boundary success/failure.

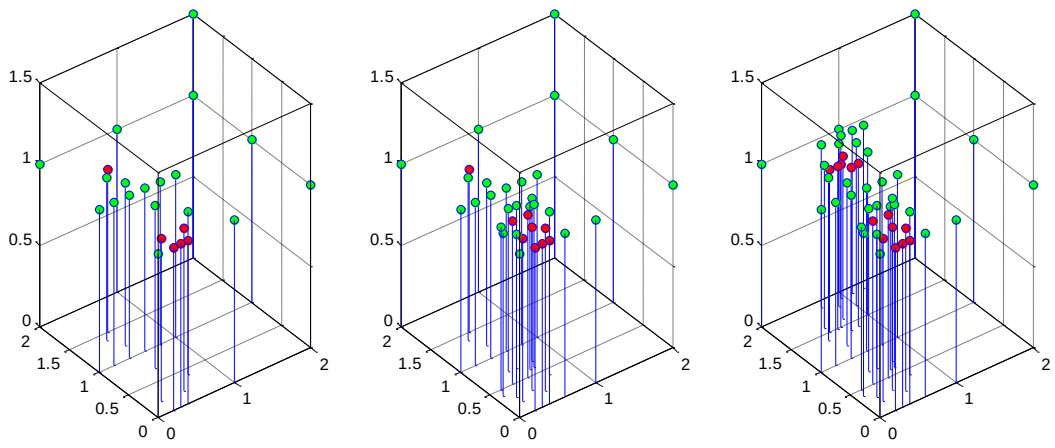

Figure 13. Snapshots of the evolution of the sampling in a limit surface search

In an N-variable problem, the limit surface is drawn on an N-dimensional Cartesian grid in the uncertain domain. The threshold separating the successful hyper-volume to the failure hyper-volume is not a "surface" *per se* but the N-dimensional layer of nodes bounding the 0-to-1 transition. Each node on the N-dimensional grid corresponds to a set of N values from the uncertain input space. Figure 14 depicts a simple limit surface line: the continuous hyper-volume (in

this case, N=2 so the hyper-volume is a surface) of nodes crossed by the limit surface line establishes the limit surface bounding. In other words, the limit surface boundaries are the "shell" surfaces between the green and the red line in Figure 14.

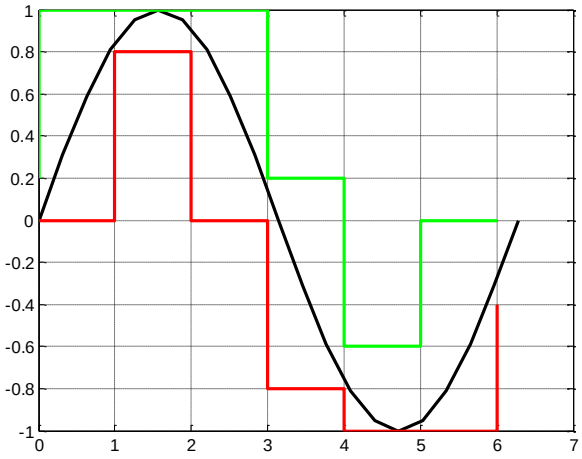

Figure 14. Limit surface bounding

The error in the limit surface definition depends on the N-dimensional Cartesian grid defined by the user in RAVEN. A fine grid needs to be implemented to obtain a fine hyper-volume "shell" boundary. The grid also settles the discrete values taken by the uncertain inputs in each dimension, starting from their PDF defined in the RAVEN input. A fine grid prevents from shadowing input space regions on the Cartesian grid. In the iterative scheme, the convergence of the limit surface is attained once the location of the limit surface does not change after *P* consecutive samplings, hence the refinement of the grid significantly influences the convergence speed. Interested readers can refer to reference [39] for more information about the limit surface search, the convergence of the iterative process and acceleration techniques.

2.6.8.4 Code interfaces in RAVEN

RAVEN's pre- and post-processing capabilities entails the implementation of a code interface between the simulation code and RAVEN. This section outlines the general workflow while CHAPTER 7 and CHAPTER 8 respectively will clarify the code-specific details of the RAVEN/PHISICS and the RAVEN/NEWT/PHISICS architectures. The RI, EXI and EC denote respectively the RAVEN Input file, the External code's Input file(s) and the External Code.

- The RI constitutes the emerged part of the iceberg from the user point of view. The user does not interact with the Code Interface (CI) and specifies the input variables in the RI, the variable distributions, the EXI(s), the executable(s), the working directory, the post-processed variable(s), the plotting options and the samplers;
- The EXI includes all the files expected to be run successfully the EC;

The CI between RAVEN and an EC encompasses three major subsets of interfaces, namely the interface, the parsers and the Output Post-Processor (OPP). All these programs are coded in Python and interact with each other.

- The interface distributes the data contained in the RI to the other subsets (parsers, OPP and EXI) and drives the sequence. The interface also detects job failure(s) after the code execution and verifies the consistency of the flags in the EXI;
- The parsers receive the perturbed inputs defined in the RI and replace the nominal values by the perturbed values in the EXI. The parsers must recognize the variable entries in the RI to substitute the appropriate parameters in EXI. The parsers do not return anything to the interface, but merely modify the EXI in a new folder. The interface proceeds to the code execution after the parsing step.
- After the code execution, the OPP dissects the output file(s) generated by the EC and gathers the data in a Comma-Separated Value (CSV) file. RAVEN utilizes the CSV file to carry out the statistical analysis of the sequence.

Figure 15 summarizes the workflow of the RAVEN-to-EC interaction through the CI.

2.7 Burn-Up Calculations in SCALE 6.2.0

Fuel depletion relates to the long-term behavior of the core under normal operation. The changes undergone by the core stem from the exposure to a neutron flux and gamma rays which results in fission products, decays and isotope activations. The mechanisms implicated in the burn-up process all have their particularities. The build-up of fission products starts immediately after the beginning of the power generation. Complex equilibrium related to fission products' decay into new actinides, neutron absorption leading to transmutations and isotope apparition through fission events can take seconds, hours, days and sometimes months. 500+ isotopes lie permanently in a reactor core, which encourages the selective targeting of nuclides with respect to the discipline of nuclear engineering considered. In radiation protection, the analyst will give a

close look to long lived isotopes, high-energy gamma ray emitters, volatile fission products, isotopes easily absorbed by the human body etc. Such isotopes are for example iodine, cesium, xenon, krypton etc. In neutronics, the analyst will investigate the fission products that poison the neutron multiplication such as ^{135}Xe, ^{149}Sm, burnable poisons (^{10}B, ^{154,155,156,157,158,160}Gd etc.). The build-up of the actinides (e.g. ^{239,240,241,242}Pu) and the ^{235}U depletion appeals the research community. The time scale of each isotope production or loss varies in order of magnitude. The ^{135}Xe build-up (~few hours), the burnable poisons disappearance (~few days or weeks) the plutonium build-up (~months) highlights these time scales, hence the study of the fuel cycle ranges from the first seconds after the start-up to hours after the shutdown.

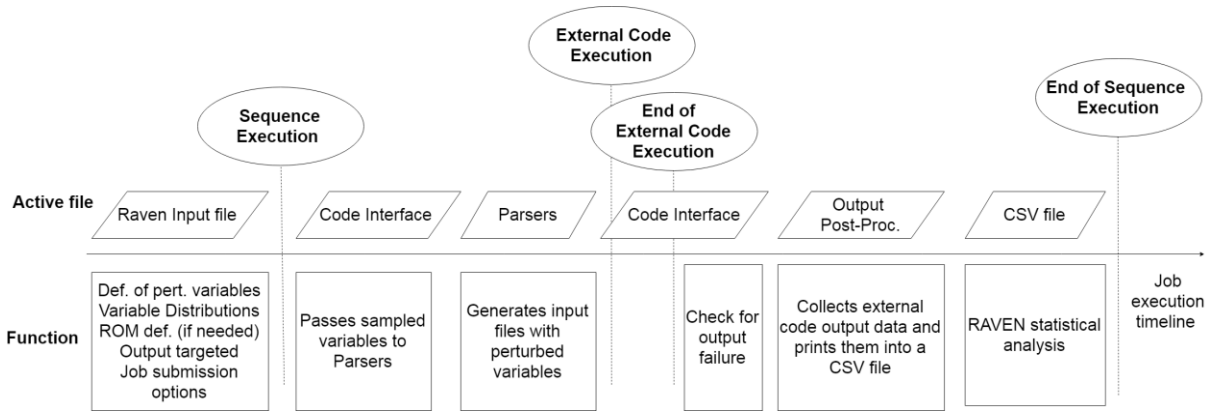

Figure 15. Code interface dynamic in RAVEN

In HTGRs, the design of TRISO particles raises different challenges as compared to traditional LWRs regarding the fission product containment. As detailed in section 2.2.1, each coating justifies its existence with specific mechanical, thermal, neutronics, chemical and fission product retention properties. Reference [13] analyzes exhaustively the transport mechanisms of the fission products in TRISO particles. In general, the largest diffusion coefficients are attributed to the Pd, Eu, Ag, Cs, I and Xe isotopes. Test accidents after long fuel exposure and elevated temperatures prove high releases of silver (Ag) across the TRISO particles [14]. Hence, CHAPTER 6 emphasizes the uncertainty quantification of ^{235,238}U, ^{238,239,240,241,242}Pu, ^{10}B, ^{107,109,110m,111}Ag, ^{131}I, ^{135}Xe, ^{137}Cs, ^{149,151}Sm and ^{102,104,105,106,107,108,110}Pd number densities.

In burnup simulations, the number of reactions and the number of isotopes in the core challenges the derivation of analytical solutions. The task is delegated to nuclear codes such as

CASMO, PHISICS or SCALE/TRITON, SERPENT (etc.). In SCALE/TRITON, series of steady states with fixed nuclide inventories subdivide the burn-up cycle. For each interval, SCALE/TRITON predicts the nuclide inventory at the middle of a given time point and bases its spectral calculation on the predicted isotopic inventory. The expected self-shielding gives an estimate of the neutron flux and cross sections for the given interval, which yields to the isotopic composition at the end of the interval. This new isotopic inventory contributes to the prediction of the inventory at mid-point for the next time interval and repeats the previous steps until the end of the simulation. Thus, the time grid influences the mid-point inventory. The closeness between the beginning of the time step to the mid-point conditions the neutron flux and the self-shielded cross sections and consequently the fidelity of the entire time step. The modeling error made at the begin of a cycle propagates throughout the time intervals.

A second major assumption in SCALE/TRITON resides in the choice of the flux level. The prediction in the nuclide inventory depends on the user-input amplitude of the flux and the normalization scheme. The user specifies for each burn step a specific power P (in megawatts day per metric ton of initial heavy metal) and a time length (in days). The following algorithm defines the flux level and the normalization:

(a) Define the material to be depleted (fuel and BP in the MHTGR);

(b) Optionally, the input specific power P can be imposed in the depleted materials. If disregarded, total system-averaged power is equal to P;

(c) Define the flux level used to deplete the material: the flux is either determined based on the specific power within the material (“deplete by power” option) or the flux is taken straight from external power sources (“deplete by flux” option). The specific power P is known through the calculation, so it is in general more appropriate to select the depletion by power option. The depletion by flux is justified in non-multiplying mixtures (i.e. BP in the MHTGR).

A concrete example highlights the options exposed in the algorithm, to prove the influence of the burnup step refinement and the deplete-by-power versus a deplete-by-flux calculation. The concentration in ^{10}B and the k-infinity are evaluated for different options. From (a), the fuel and the BP are depleted in a graphite-moderated block. Let’s consider the following configurations implemented in the system. In the four examples below, the first statement involves the definition of the power and the second statement defines the flux in the depleted materials:

1- The system-averaged power matches *P*; both materials are depleted-by-power.
2- The power in the fuel matches *P*; both materials are depleted-by-power.
3- The system-averaged power matches *P*; the fuel is depleted-by-power and the BP is depleted-by-flux.
4- The power in the fuel matches *P*; the fuel is depleted-by-power, and the BP is depleted-by-flux.

The time steps are broadened at t > 150 days. The results on the ^{10}B concentration (Figure 16) and k-infinity (Figure 17) show large discrepancies between deplete-by-power (Single Block (SB) 1 and SB 2) and deplete-by-flux (SB 3 and SB 4). CHAPTER 5 discusses in-depth the design of the MHTGR lattice models. Figure 29 depicts the fuel block modelled in this section.

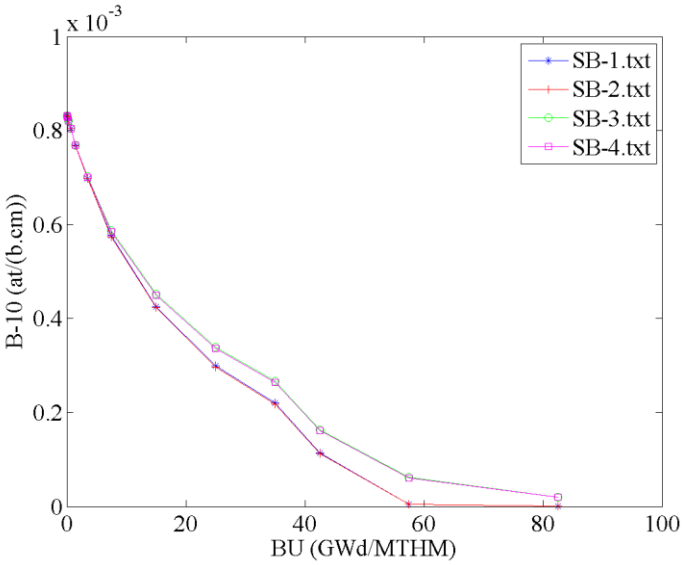

Figure 16. ^{10}B concentration for the four depletion options selected; broad burn steps

The reduced time steps result in more coherent predictions of the nuclide inventories. In Figure 18, Figure 19 and Figure 20, the time steps shrunk down to 30.93 days after the fifth day of operation. This investigation advances that fine time steps alleviate the effect of the depletion options on the number densities.

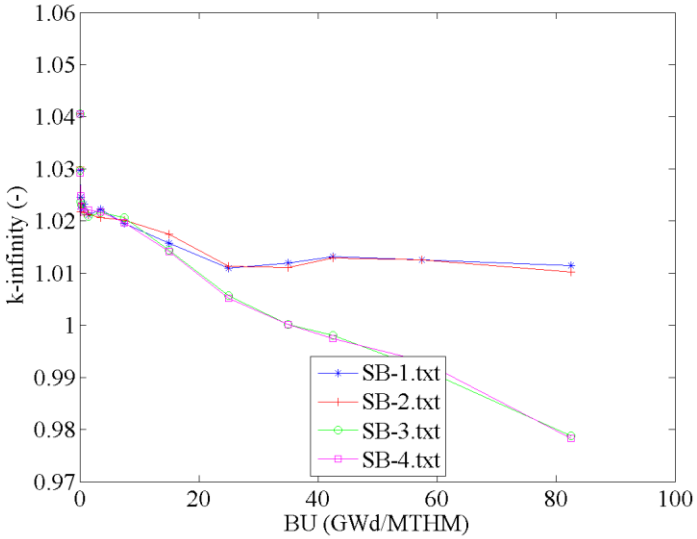

Figure 17. k-infinity for the four depletion options selected; broad burn steps

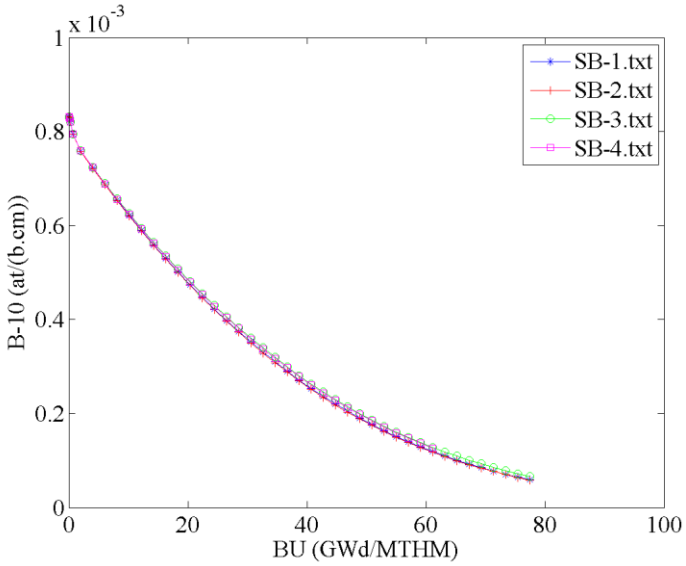

Figure 18. ^{10}B number density for the four depletion options; refined burn steps

The infinite multiplication factor still shows discrepancies between the deplete-by-flux and deplete-by-power options, because the ^{10}B and plutonium isotopes, among others, still manifest low disparities between the deplete-by-flux and deplete-by-power options.

Unless mentioned otherwise, the fission materials will be depleted-by-power, the non-multiplying media will be depleted-by-flux and the power in the fuel will match the user-defined specific power *P*. This configuration corresponds to SB 3.

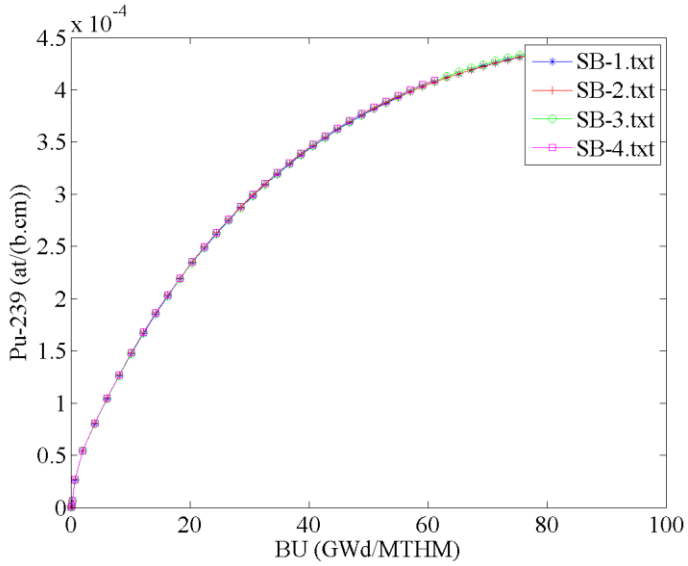

Figure 19. ^{239}Pu number density for the four depletion options; refined burn steps

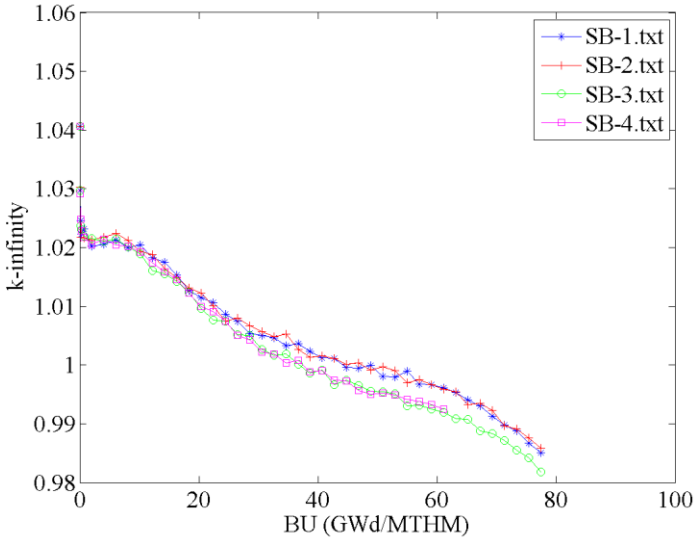

Figure 20. k-infinity for the four depletion options; refined burn steps

CHAPTER 3

SENSITIVITY AND UNCERTAINTY ANALYSIS IN NUCLEAR ENGINEERING

This chapter compiles the origins of uncertainties, the methods implemented to model them and appraises the appeal related to uncertainty analysis. Section 3.3 and 3.4 overviews briefly the results obtained in the previous years on that matter.

3.1 Conservative and Best Estimate Plus Uncertainty Approaches

The uncertainties originating from scientific computing arise from the following sources:

- Input uncertainties: These uncertainties stem from lack of information on the input data necessary to compute the output responses. The nuclear data, for example, are sources of input uncertainties;
- Model uncertainties: The transition from a physical model to a mathematical model entails assumption(s), which engenders model uncertainties;
- Manufacturing uncertainties: The physical components of a system are manufactured with a given tolerance (dimension, concentration, weight etc.) which contributes to the uncertainty response of the simulation;
- Numerical uncertainties: they are caused by the discretization of the Partial Differential Equations (PDE) in the mathematical model.

In nuclear engineering, the safety analysis relies on a conservative approach. The conservative methodology yields disproportionate and pessimistic assumptions to evaluate the safety margins. The responses measured in the nuclear power plants preserve the integrity of the fuel to avoid at any cost a meltdown. The limiting values are defined as the values that the exceeding of which leads to a failure. Those limiting values are not known accurately and thus regulatory acceptance criteria are established. A safety margin quantifies the deviation from the acceptance criteria value (in absolute or relative value) that a parameter of safety concern is constrained to, to its estimated value. An exceeding of the acceptance criteria would not necessarily lead to a

system failure. The safety margins presume the limiting value and the actual value of operation are sufficiently conservative to anticipate several unexpected penalties even under severe accident conditions.

Overall, the conservative approach benefits from a large international experience, and widely-documented sources after many years of operation under this approach. The procedures applied to this methodology have also the advantage to remain clear and simple. On the negative side, the conservative approach may lead to unrealistic behaviors, or subvert the chain of events. In transients, a conservative value (i.e. pessimistic) for a parameter can become not conservative (i.e. optimistic on a safety point of view) at the end of the transient. Although the conservative values result from sensitivity calculations, expert judgement may contribute to the evaluation. The sensitivity calculations are usually decoupled to each other, accentuating the need of user's choice, and then leading to possible user's mistakes.

Over the past few years, the Best Estimate Plus Uncertainty (BEPU) approach challenged the conservative approach to evaluate the safety margins, allowing more reasonable safety requirements to operate the nuclear power plants [40]. Figure 21 sketches the benefits from the BEPU approach as compared to the conservative method. The BEPU methodology relies on the examination of the nominal values with realistic input but accompanied with uncertainty. Thus, conservative assumptions still feature the BEPU approach, but unlike the conservative method, realistic input data with uncertainties are utilized. Hence, the best estimate methodology is free of unrealistic events caused by surpassing input data, and mostly rids of expert-judgment-based decisions. Another powerful advantage of the BEPU resides in the consideration of the joined contribution of the input parameters. The major disadvantage of the BEPU approach is the increased number of simulations necessary, leading to time-consuming, computationally-hungry simulations and heavy data pre- and post-processing. The lack of experience in the development of BEPU tools can limit the user's capabilities and demands enhanced developer's work force. In addition, experimental values (if any) are recommended to validate the measures. One of the key requirements for the development of BEPU methods lies in international agreements on validation methodologies. Prescriptions in the literature [41] encourages the BEPU scheme to implement:

- Available and affordable high-fidelity tools;
- Benchmark models based on available and affordable experimental data.

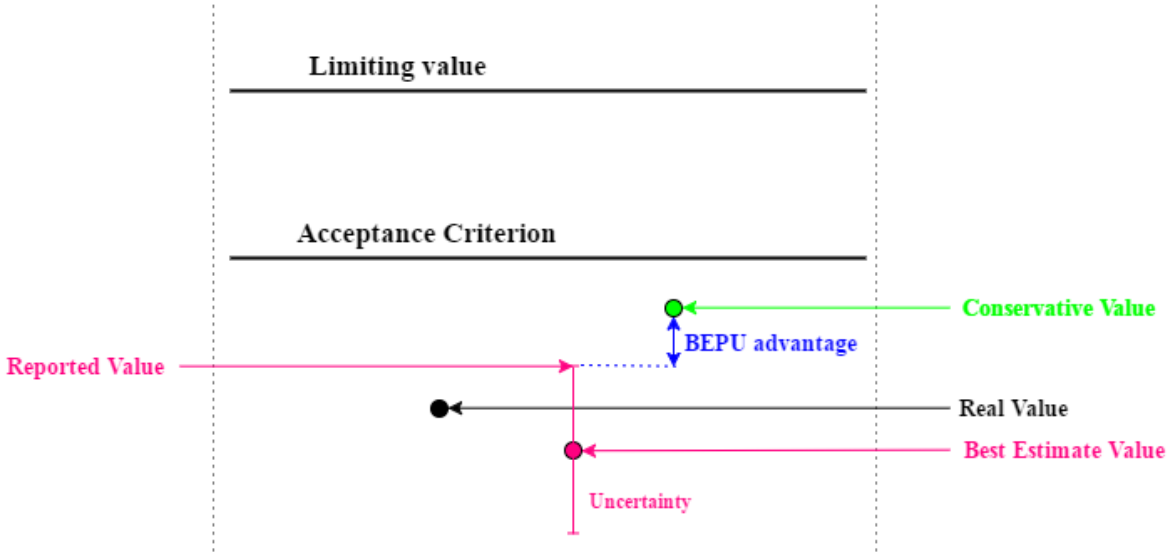

Figure 21. BEPU versus conservative approach diagram

3.2 Uncertainty Analysis Methods

3.2.1 Deterministic and Statistical Methods

The academic community has extensively explored the sensitivity and uncertainty analysis methodologies. This section overviews the methods available currently along with the advantages and drawbacks.

A sensitivity analysis focuses on elaborating the contribution of each input parameter on the output uncertainty [42]. Concretely, a sensitivity analysis derives a list of priority among the output variables with respect to the input variables. The number of uncertain input parameters may be reduced by ruling out the least important variables contributing to the total uncertainty. A wide variety of engineering disciplines pioneered sensitivity analysis techniques [43]. If all the sensitivities are known, so if the output parameters' deviation as a function of all input parameters is determined, an uncertainty on the output parameters can be performed.

The uncertainty analysis does not unveil, in general, the sensitivities of the output parameters towards each input parameter. The uncertainty quantification propagates uncertainties from the model's input parameters. Such analysis is sub-divided into two families of methods, the statistical methods [44] and the deterministic methods [45].

Deterministic methods are based on the first-order perturbation theory, which has the disadvantage to require small perturbations that are properly represented by first order (linear relationship between input and output) Taylor expansions. It also involves the derivation of an adjoint solution of the problem, which, under the condition the adjoint solution exists, codes may not necessarily perform. For instance, first order perturbation is not suitable to model rapid changes of the neutron flux in the vicinity of burnable absorbers. The second drawback of the approach remains the possible unavailability of the adjoint operator, which is the case for example in the code SCALE 6.2 for coupled neutronics and depletion sequences. The first order perturbation theory relies on a "brute force" calculation of sensitivity coefficients for a targeted output response. The calculation of forward and adjoint transport solutions for each targeted output response yields to the system's sensitivity coefficients. The first order perturbation theory has the advantage to provide a simple analytical example, applicable to diffusion or transport theory in one-group or MG. The perturbation method applied to nuclear cross sections relies on a single calculation requiring the following steps:

1- Generation of the self-shielded cross sections from the cross section libraries;
2- Generation of covariance library;
3- Calculation of the sensitivity coefficients for the response of interest with the transport solver, using the cross section generated in step (1);
4- The covariance data (2) are folded with the sensitivity coefficients from (3) for each energy group to estimate the uncertainties.

The method is limited by the type of perturbation that can be applied in step (3), leading potentially to underestimated uncertainty responses.

Several statistical sampling methods were implemented for advanced reactor analysis [46]. The basic statistical sampling consists in the determination of the uncertainty of an input parameter through PDFs. The code simulates N samples associated with the uncertain input space generated with respect to the PDF. The evaluation of the PDF is ideally based on experimental data or on expert judgement otherwise. The sampling method applied to cross sections relies on the following steps:

1- Evaluation of *a priori* input uncertainties from the covariance data. XSUSA or SAMPLER use such guidance, for instance;

2- The input parameter(s) are sampled *N* times following a normal distribution. Step (1) dictates the width of the Gaussian curve;
3- Transmit the *N* inputs to the transport code.

The process is computationally expensive, but it results in a complete evaluation of the output uncertainties (if all the uncertain parameters are perturbed). Prior researches compared perturbation methods versus sampling methods [47] showing acceptable agreements.

The random sampling codes available for nuclear engineering applications all have their peculiarities. XSUSA [48] can vary the elastic, (n,2n) and inelastic scattering, the capture and fission cross section, nu-bar and the fission spectrum, the decay and fission yield, while NUDUNA [49] cannot perturb the fission yields but can perturb for example the thermal scattering data. XSUSA perturbs the cross sections after the spectral calculations and then assumes that the implicit effects (i.e. the effects of self-shielding calculations on the cross section generation) are linear, while SAMPLER performs the perturbations before the spectral calculation and thus accounts for the implicit effects. For burn up calculations, XSUSA performs a reference spectral calculation for each burnup step with the reference nuclide inventory, which prevents from performing self-shielding computation efforts for the *N* perturbations, then requiring only the nominal case's spectral calculations. This method does not account for the propagation of the nuclide inventory uncertainties caused by nuclear data, and thus does not account for the flux spectrum uncertainty induced by the nuclear data uncertainties.

Large covariance matrices result from such methodology to account for all the possible correlations between all the possible reactions for each isotope. With the increase in the computational power, several sampling-based codes have been developed recently, for instance the Oak Ridge National Laboratory sequence SAMPLER (detailed in [37] and section 2.6.7), TMC [50], the GRS sequence XSUSA [51], the Areva code NUDUNA [49] (etc.).

3.2.2 Confidence intervals

The uncertainty evaluation originating from Monte Carlo sampling depends on the population (*N*), the population mean (μ) and the standard deviation (σ). The population mean calculated through multiple samplings varies as a function of *N*. The repetition of the same experiment or perturbed simulations is characterized by a true (unknown) population mean with a given un-

certainty reported usually as the standard deviation of the population sampled. A confidence interval accompanies the mean and standard deviation as a complementary information on the uncertainty result. It specifies the statistical plausibility of the results. The confidence interval comes with a pre-defined confidence level α (usually 95%). α represents the frequency at which future confidence intervals, yet non-observed, will contain the true value (of the mean or standard deviation). It does not represent the frequency at which the current interval will contain the future predictions of the value (mean or standard deviation) [52]. An α % confidence interval does not contain α % of the values sampled.

Matlab® was used to illustrate the confidence interval with an example. A normal distribution of a variable *k* is defined by an average of μ = 1.05 and standard deviation of σ = 0.10. For N = 15 different sample populations, 100 points are randomly drawn from the normal distribution. The sample mean is represented along with the sample's α = 95% confidence interval. The true mean is assumed to equal μ. Figure 22 sketches the results. On the plot, black dotted lines point out the range of the first sample's confidence interval. As discussed in the previous paragraph, the confidence interval indicates the frequency at which the confidence intervals of a simple *i* (i=2, 3 … N) contains the true value μ is 95%. It does not signify that the mean values k_i relative to the samples will lie within the first samples' CI. In fact, the N_i studies are unbiased and independent, so the chances of having the next samples' mean value lying within the first samples' CI is lower than 95%..

For a given α, the confidence interval will naturally decrease as sample size augments because the enhanced number of samples raises the "confidence" in the output value obtained through the multiple simulations. For a given model and sample size, the confidence interval is wider as α increases. Typically, a 95% confidence interval is broader than a 90% confidence interval.

The confidence interval on the mean value is:

$$\left[\alpha_{down}^{\mu} = \bar{x} - \frac{z^{*}\sigma}{\sqrt{N}};\ \ \alpha_{up}^{\mu} = \bar{x} + \frac{z^{*}\sigma}{\sqrt{N}}\right] \qquad \text{Equation 3-1}$$

Where α^{μ}_{down} and α^{μ}_{up} are the lower and upper boundaries of the confidence interval relative to the mean, $\bar{x}$ is the population mean, σ is the population's standard deviation and *N* is the number of samples. The confidence interval on a standard deviation is:

$$\left[CI^{\sigma}_{down} = \sigma\sqrt{\frac{N-1}{\chi^2_{\frac{\alpha}{2},N-1}}};\ \ CI^{\sigma}_{up} = \sigma\sqrt{\frac{N-1}{\chi^2_{1-\frac{\alpha}{2},N-1}}}\right] \qquad \text{Equation 3-2}$$

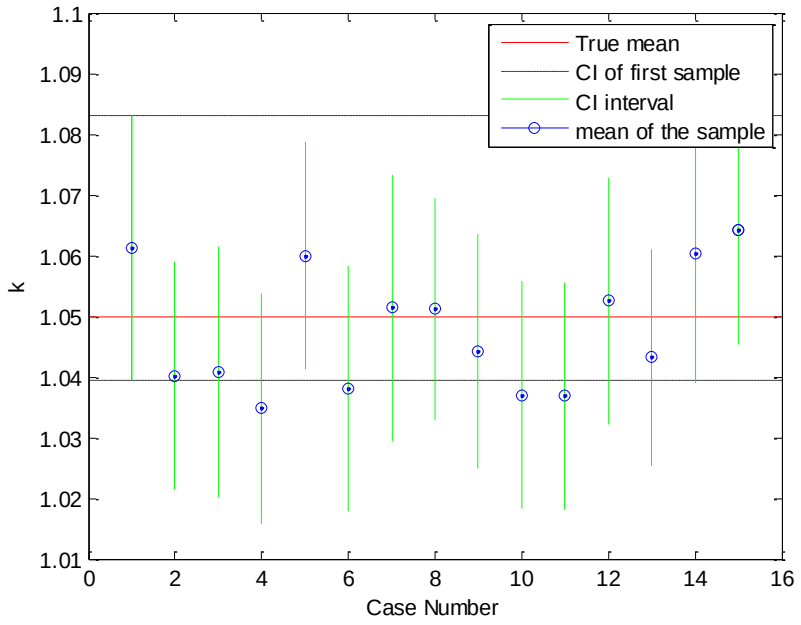

Figure 22. Illustration of confidence interval interpretation

In relative values:

$$\left[CI^{\sigma\%}_{down} = \sqrt{\frac{N-1}{\chi^2_{\frac{\alpha}{2},N-1}}};\ \ CI^{\sigma\%}_{up} = \sqrt{\frac{N-1}{\chi^2_{1-\frac{\alpha}{2},N-1}}}\right] \qquad \text{Equation 3-3}$$

The term N-1 is called the degree of freedom of the sample. χ^2 is given by the χ^2-distribution relative to a pair [degree of freedom; confidence defined *a priori*]. The χ^2-distribution is a non-symmetric distribution positively skewed. It varies in shape with the degree of freedom of

the sample. It is always positive and its integral is equal to 1. Table 4 summarizes a few χ^2 values relative to a 95% confidence interval for typical degrees of freedom used in the following chapters (calculated with the *chi2inv* function in Matlab®).

The standard deviations will be complemented, if possible, with the corresponding confidence intervals in the next chapters.

Table 4. Typical χ^2 values at 95% confidence interval

Degrees of freedom (N-1)	$\chi^2_{\alpha/2}$ *95% lower confidence interval*	$\chi^2_{1-\alpha/2}$ *95% upper confidence interval*
99	1.284E+02	7.361E+01
249	2.946E+02	2.072E+02
499	5.628E+02	4.390E+02
999	1.088E+03	9.133E+02

3.3 Review of the Results Related to Uncertainty Analysis Modeling obtained on LWRs

The NEA and the OECD developed a benchmark to enhance the improvement and validation of uncertainty analysis applicable to nuclear engineering [53]. The benchmark focuses on UAM applied to LWR analysis. Comparatively to the OECD/MHTGR benchmark, the tasks are separated into various exercises, among which phase I is oriented towards the propagation of nuclear data uncertainties throughout steady state standalone neutronics. The analysis incorporates three thermal, water-moderated systems: a PWR, a BWR and a Water-Water Energetic Reactor (VVER). A depletion analysis component supplements the stand-alone exercises. The benchmark suggests increasing level of geometrical complexity with advancing exercises, going from pin cell models, to assemblies and cores. The results in [54] are obtained with SCALE 6.0 covariance library [55].

The results contend that the ^{238}U (n,γ) reaction contributes majorly to k_{inf} uncertainty, followed by $^{235}U(\bar{\nu})$ (average number of neutrons emitted after fission by ^{235}U). The large amount (in mass) of the ^{238}U isotope justifies the contribution, combined to its high capture cross section in both fast and thermal range. Consequently, the shift in the neutron spectrum contributes in the

uncertainty: the scatter in the predictions tends to increase with hardening spectrum. Thus, increasing temperatures tend to amplify the uncertainty in the multiplication factor. Hence, the uncertainty on the multiplication factor is greater, in general but not always, at Hot Full Power (HFP) than Hot Zero Power (HZP). The use of sub-models (i.e. small lattice cells) can yield over-estimated uncertainties, considering the lattice cells have harder spectrum than the actual core models. The presence of plutonium isotopes in MOX fuels or irradiated cells also raises the uncertainty on the multiplication factor. The effect is two-fold: the ^{239}Pu has a relatively high capture cross section and the uncertainties on the plutonium nuclear data are intrinsically higher than the one relative to the major uranium isotopes.

The relative standard deviations in the Peach Bottom Unit-2 BWR are equal to 0.603 %Δk/k (HZP) and 0.680 %Δk/k (HFP) in pin cells, 0.519 % Δk/k (HZP) and 0.471 % Δk/k (HFP) in an assembly, 0.548 %Δk/k (HFP) in the core. The three major contributors to the k_{eff} uncertainty are the microscopic absorption cross section of ^{238}U, the average number of neutrons emitted after a fission of ^{235}U, and the microscopic absorption cross section of ^{235}U.

The relative standard deviation of a PWR pin cell depleted to 60 GWd/MTHM is equal to 0.891 % Δk/k, in which ^{239}Pu(nu-bar) substitutes ^{238}U(n,γ) as the top-ranked contribution. The relative uncertainty on the major actinides' concentration (^{235}U, ^{238}U, ^{239}Pu, ^{240}Pu) does not exceed 1.5 % in relative standard deviation and increases for the fission products, going up to 16.3 % for ^{149}Sm for instance. Few conclusions were drawn on the manufacturing uncertainties.

The UAM activities:

- Encouraged the re-evaluation of nuclear data uncertainties (cross sections, covariance, kinetics parameters);
- Stimulated the refined quantification of input uncertainties regarding the manufacturing variables, boundary conditions and the modeling specifications;
- Triggered the development of new uncertainty and sensitivity quantification methods (deterministic, stochastic, hybrid and reduced order models).

3.4 Review of the Results Related to the IAEA CRP on HTGR uncertainty

The results obtained from the UAM on LWRs promoted efforts on comparable activities towards HTGRs. CHAPTER 1 outlines the motivations of the IAEA CRP on HTGRs while this section aims to summarize the contributions observed since the beginning of the project.

The CRP on HTGR uncertainties officially started in 2013. At this time, the participants surveyed the needs regarding the HTGR uncertainties and drafted the main axes for the future meetings:

- Development of decay heat uncertainties applicable to the HTR-PM model (see section 2.1);
- Investigation of the covariance data and their relevance for PBR applications;
- Estimate in the pebble flow uncertainties;
- Influence of the heavy metal load.

The tools available for HTGR uncertainties were scarce if not non-existent at the time. The sequence XSUSA (GRS) generated promising results for LWRs but doubly-heterogeneous fuel challenged the compatibility of the code with the pebble or prismatic designs. The SAMPLER sequence was under development at ORNL (released finally in 2015), while the sensitivity analysis code TSUNAMI could not support double-heterogeneous states. The Korean Atomic Energy Research Institute (KAERI) initiated efforts to implement few-group cross section uncertainties from the code CAPP in association with DECART. The codes' capabilities at the time could not achieve uncertainty quantifications.

Over the years, the software incorporated new methods to address the uncertainties in HTGR systems. The code VSOP can calculate the effect of pebble's random travel throughout a PBR core *via* a mixing coefficient. Stochastic sampling methods were added to the VSOP code to compare uncertainty output values induced by cross section perturbations. The GRS code XSUSA enhanced its capabilities to tolerate cross section perturbations of HTGR fuel for criticality and depletion calculation [56] (see CHAPTER 4). GRS also verified that the implicit effects, disregarded by the XSUSA sequence, approximated weakly the uncertainty quantifications. The Institute of Nuclear and new Energy Technology (INET) proposed a method to evaluate the uncertainty on the rod worth from the cross section uncertainties. KAERI developed the MUSAD code, based on General Perturbation Theory (GPT), and compared the performances of the Seoul National University MCCARD with the DECART/MUSAD sequence. KAERI also proposed a two-step approach for uncertainty calculation with DECART/MUSAD for core models. INL and INET evaluated the contribution of the random TRISO packing in MHTGR-350 and pebble-bed lattice cells, respectively, as modelling uncertainties. Kurchatov Institute (KI) derived a methodology to generate covariance matrices from the SCALE modules CADILLAC and

COGNAC, to apply the covariance in the WIMS code. KI's sequence SUW (Sensitivity and Uncertainty in WIMS) produced manufacturing uncertainties evaluated at 0.049 %Δk/k in the MHTGR-350. KAERI estimated the uncertainty on the multiplication factor from the manufacturing uncertainties to be around 0.140 %Δk/k in a pebble-bed lattice cell.

Lattice cell results [57] collected from the participants agreed to conclude that the contribution of the cross sections to the k_{inf} uncertainty ranges around 0.6 % Δk/k at HFP, and decrease down to around 0.5 Δk/k at HZP. $^{238}U(n, \gamma)$, $^{235}U(\bar{\nu})$ and $^{235}U(n,\gamma)$, C(el) and ^{238}U(inel) (inelastic scattering) contribute the most the k_{inf} uncertainty in fresh fuel. Irradiated fuel's contributors were not evaluated. KAERI assessed that the uncertainty on the multiplication factor calculated with an infinite lattice's spectrum versus a critical spectrum did not introduce additional uncertainties. GRS estimated the random packing effect on the k_{inf} nominal values (compact cells and fuel blocks) at 0.00300 as compared to regularly-arranged TRISO particles. The literature evaluated this effect at ~0.00100 to 0.00200 in HTTR lattices [58]. Finally, Figure 23 compares the GRS results obtained with XSUSA and SAMPLER with the ENDF/B-VII.0 (238 groups, 44-group covariance) and ENDF/B-VII.1 (252 groups, 56-group covariance) in a compact cell. The results summarize that:

- The uncertainty on the k_{inf} is lower at HZP than HFP in HTGR lattice cells;
- XSUSA and SAMPLER achieve equivalent results (the confidence interval is assessed at roughly ±10 %);
- The covariance library and/or the number of groups in the covariance library influence the results.

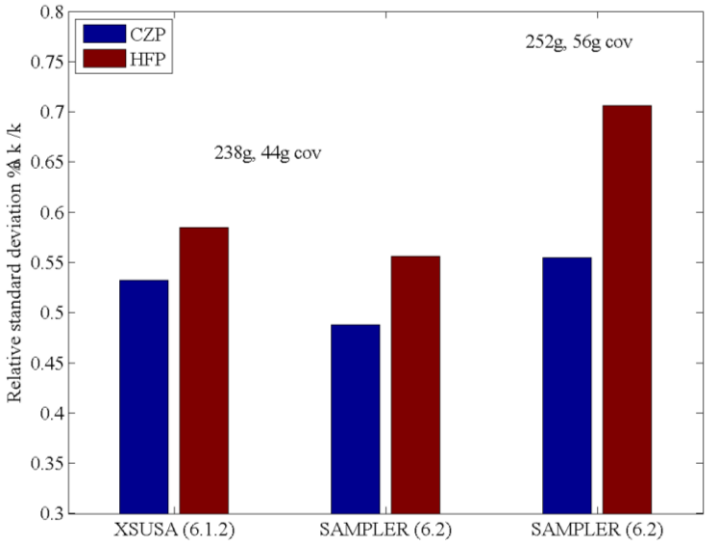

Figure 23. GRS results comparing XSUSA and SAMPLER with ENDF/B-VII.0 and ENDF/B-VII.1 [59]

CHAPTER 4

PREPARATION OF FEW-GROUP CROSS SECTIONS FOR SCALE/XSUSA BURNUP CALCULATIONS IN HTGR LATTICES

4.1 Methodology

As the uncertainty analysis fits more and more safety and design calculations, several tools have been developed to fulfill this task, such as for instance, the control modules TSUNAMI or SAMPLER in the SCALE suite. The sampling-based XSUSA methodology is aimed to elaborate uncertainty and sensitivity analysis on the OECD/NEA HTGR depletion benchmark. XSUSA embraces the propagation of cross section uncertainties in criticality and depletion calculations. The key idea of the methodology is to impose slight perturbations on nuclear data by using Gaussian distributions and correlations between the input parameters and implement them to execute *N* perturbed simulations. For either burn-up or criticality solutions, the variations of cross sections are processed after the spectral calculations. Thus, the XSUSA methodology initially depends on the determination of the collapsed group structure after the spectral calculation (typically, two-group configuration for LWRs, possibly more for HTGRs).

The double heterogeneity challenges the cross section generation process for both criticality and burnup calculations (see section 2.5). This chapter formulates an automatized routine to prepare and collect few-group cross sections at each time step of the burnup, using different modules from the SCALE 6.1 suite.

A 238-group structure that originates from the ENDF/B-VII.0 library is chosen for reference procedure. The resulting collapsed cross sections are in a two-group configuration. The scheme operates regardless the input and output group structure. Considering the spherical topology of the pebble-bed fuel type, transport and depletion calculations are performed throughout a three-dimensional model. The TRITON sequence of SCALE 6.1 is exploited to run the burn-up calculations as a first step, utilizing the Monte Carlo code KENO-V as a solver. KENO-V (or

KENO-VI, see section 2.6.4) cannot generate cross sections in a collapsed form, so the SCALE 6.1 two-dimensional code NEWT (see section 2.6.2) must accompany KENO-V.

The scheme achieves (a) the burnup solutions with TRITON/KENO-V. The TRISO particles in the graphite matrix are automatically homogenized by TRITON (more details in section 2.5), which results in the creation of a fuel mixture. Each time step produces a nuclide inventory, self-shielded cross sections (ft04f001 library) and mixing tables (ft92f001). NEWT follows strictly the same scheme as KENO-V to perform the spectral calculations, inducing repetitions of the methodology. Figure 24 summarizes the successive TRITON/NEWT and TRITON/KENO-V sequences. The self-shielded cross sections resulting from the TRITON/KENO-V lattice are conserved at each step. (b) These libraries are implemented in a stand-alone 1-D XSDRN calculation to perform the homogenization and spatial self-shielding. This XSDNR step provides the homogenized mixture's flux-weighted cross sections in a 238-group structure. The mixture embeds the fuel/matrix pre-mix, the graphite outer layer and the surrounding coolant in the pebble's pitch. (c) With a given nuclide inventory and mixing table, a final NEWT calculation in a homogenized 2-D medium (which is in fact 1-D, considering the homogenization), provides the collapsed few-group cross sections. To conduct properly the transport solution, NEWT requires a prepared mixing table that describes the homogenized medium, additionally to the XSDRN-prepared cross sections. These mixing tables are pre-generated by TRITON/KENO-V (ft92f001 file) at the beginning of each time step to prepare the appropriate cross sections. Because TRITON/KENO-V accomplishes only partial homogenization of the fuel plus the matrix region and does not handle the complete homogenization of the cell, a special care to weight the TRITON/KENO-V mixing table with respect to the volume is mandatory. In other words, weighting coefficients must correct the number densities of the three-region (fuel mixture, graphite, helium) model. These weighting coefficients are merely defined as the ratio of the volume of a mixture over the total volume of the pebble. Table 5 gathers the three weighting coefficients; they do not change over the cycle and depend only on the volume of the different mixtures in the model. Figure 25 summarizes the proposed sequence.

For the prismatic geometry, the methodology a simplified methodology is suggested. (a) At each time step, the burnup calculations are executed with KENO-V to generate the nuclide inventories, mixing tables and weighted cross sections. (b) Cylindrical rods compose the prismatic configuration, and therefore a two-dimensional representation suffices. The mixing tables

are immediately utilized for the NEWT calculations without preliminary XSDRN calculations. Figure 26 sketches the various steps of this pattern.

Table 5. Weighting coefficients for the mixing tables in the pebble bed

	Radius/Width (cm)	*Volume (cm^3)*	*Weighting Coefficient (-)*
Fuel mixture	2.5	65.450	0.3030086
Graphite	3.0	47.647	0.2205902
Helium	6.0	102.903	0.4764012
Total	6.0	216.000	1.0000000

4.2 Verification of the results

A verification analysis compares the KENO-V/XSDRN/NEWT sequence versus a straight KENO-V burn-up calculation. The evolution of the multiplication factors as a function of time, obtained with the actual heterogeneous geometry from KENO-V and the homogenized mixture from NEWT, are evaluated in Table 6 and Table 7. The k_{inf} corroborate for both pebble bed and prismatic configurations. The difference between the multiplication factors computed by the two codes is within the KENO standard deviation for the pebble bed model and two standard deviations for the prismatic geometry. The NEWT k-infinity convergence criterion is set to the SCALE default value (10^{-5}). Figure 27 and Figure 28 respectively illustrates the results from Table 6 and Table 7.

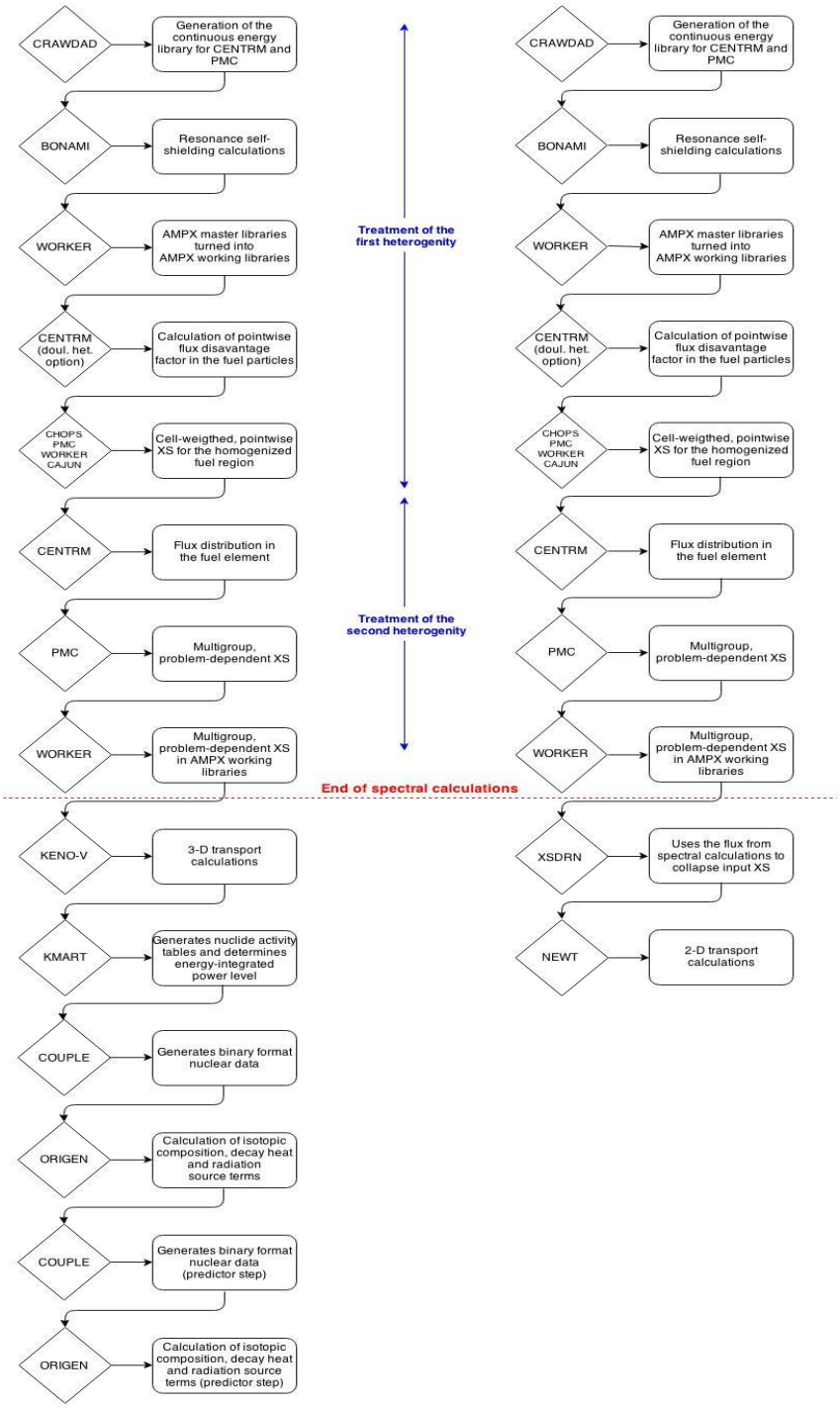

Figure 24. Doubly-heterogeneous treatment in TRITON/KENO sequence (left) and TRITON/NEWT sequence (right)

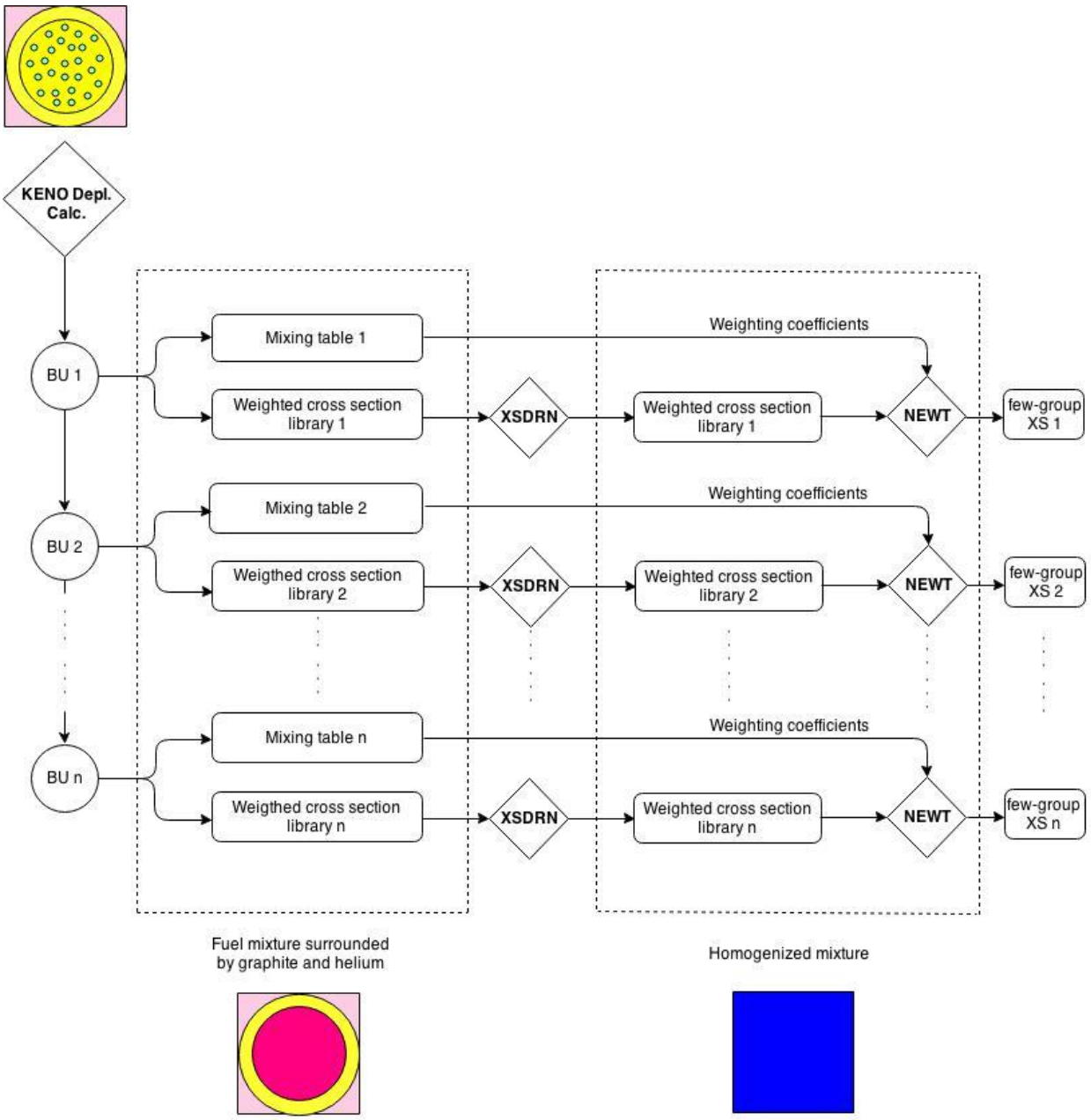

Figure 25. Overview of the Few-group cross section generation for pebble-bed model with NEWT

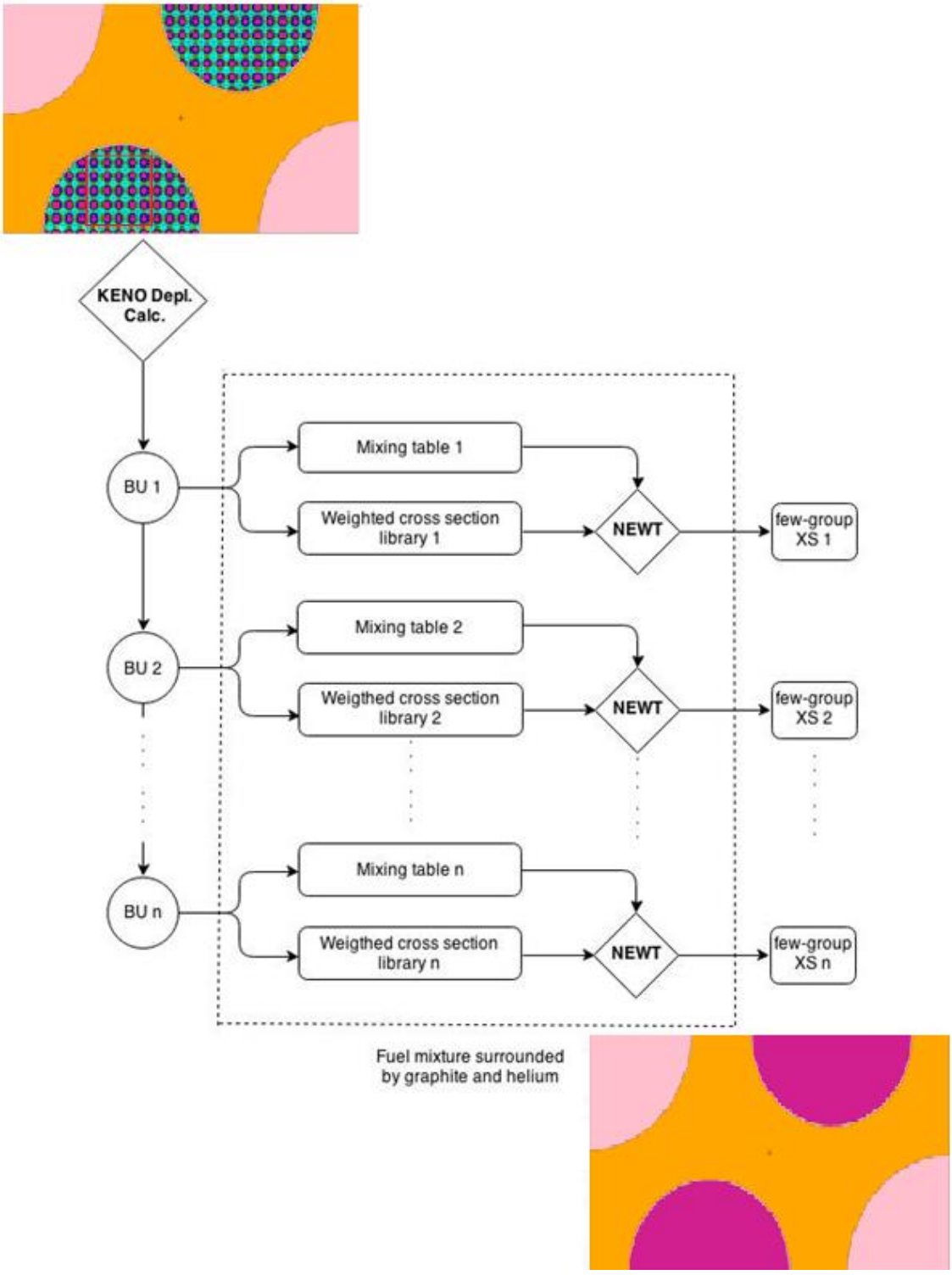

Figure 26. Overview of the few-group cross section generation for prismatic model with NEWT

Table 6. Comparison of infinite multiplication factors for equivalent KENO-V/XSDRN/NEWT (noted KXN) and KENO-V calculations in a pebble-bed lattice

Time (days)	*Sequence KXN*	*KENO-V*	*Difference ($\times 10^{-5}$)*	*KENO-V std dev. ($\times 10^{-5}$)*
0	1.51527	1.51516	11	130
4	1.4594	1.45845	95	120
28	1.44327	1.44241	86	140
68	1.4306	1.43071	-11	110
108	1.41781	1.41752	29	120
132	1.41002	1.40977	25	110

Table 7. Comparison of infinite multiplication factors for equivalent KENO-V/NEWT (noted KN) and KENO-V calculations in a prismatic lattice

Time (days)	*Sequence KN*	*KENO-V*	*Difference ($\times 10^{-5}$)*	*KENO-V std dev ($\times 10^{-5}$)*
0	1.4756	1.47636	-76	71
4.03	1.42118	1.42272	-154	62
44.35	1.39885	1.39965	-80	62
116.93	1.37321	1.37459	-138	65
319.89	1.29578	1.29697	-119	62

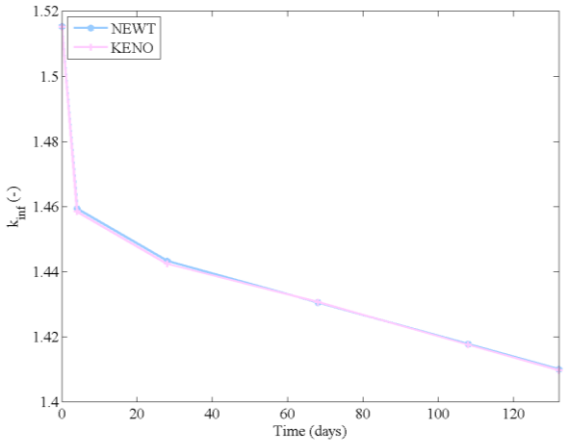

Figure 27. k_{inf} = f(t) for equivalent homogenized NEWT and heterogeneous KENO-V depletion calculation (pebble lattice)

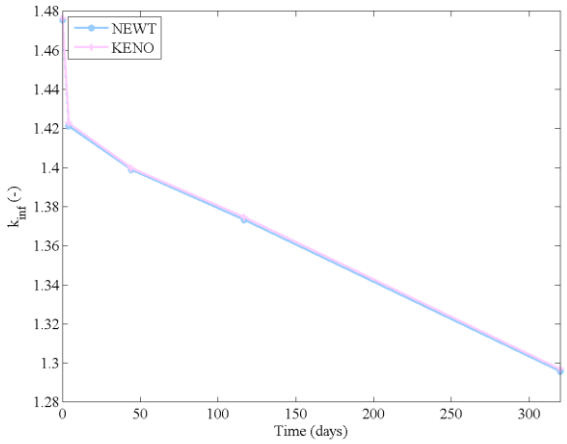

Figure 28. k_{inf} =f(t) for equivalent homogenized NEWT and heterogeneous KENO-V depletion calculation (prismatic lattice)

CHAPTER 5

SENSITIVITY STUDY ON PHISICS/RELAP5-3D MHTGR-350 CORE CALCALCULATIONS WITH VARIOUS LATTICE SETS

The response of lattice model uncertainties to the neutron cross section uncertainties dominates the first phase of the CRP. The SCALE 6.2.0 two-dimensional lattice code TRITON/NEWT assembled best-estimate results for the prismatic fuel block (Ex. I-2a) and super cell models (Ex. I-2c). A reference spectrum was obtained with Serpent 2.1.27 for the single block, super cell and core models. The flux spectrum in the system influences the quantification of uncertainties that are stimulated by cross sections. In this work, the T-NEWT's flux-weighted cross sections obtained for Ex. I-2a and various models of Ex.I-2c are utilized to perform a sensitivity analysis of the MHTGR-350 core power densities and eigenvalues. The PHISICS/RELAP5-3D code provides the core solutions. It is observed that axial shape of the core power density does not vary significantly with the various lattice cell libraries utilized. The use of cross section libraries originating from super cells induces changes of the core power density by 1% to 10% radially as compared to the Ex.I-2a cross sections. The magnitude of these variations increases as the moderator-to-fuel ratio increases in the lattice models. A lattice spectrum resembling the core spectrum is recommended for correct predictions in nodal core calculations.

5.1 Description of the Model

The first phase of the CRP benchmark proposes a super cell model along with a single fuel block. This study evaluates the effects of neutron spectra's weighting methodology in different lattice models for the generation of the few-group cross sections. The ENDF/B-VII.1 252-group self-shielded cross section libraries collapsed into a 26-group format are applied to the neutronics/thermal fluid steady state core solutions. PHISICS/RELAP5-3D (section 2.6.5 and 2.6.6) utilizes the collapsed library to perform the core calculations. The PHISICS/RELAP5-3D

axial and radial power profiles serve as figure of merit to measure the effect of the various flux-weighted cross section sets on the core solutions.

Coolant channels are distributed in the prismatic configuration to remove the heat out of the fuel. Six burnable poison (BP) compacts are located at the corners of the fresh fuel blocks. Graphite moderator surrounds the fuel, coolant and burnable poison rods. Figure 29 depicts an MHTGR-350 fuel block. The 2-D nature of T-NEWT does not provide the capability to model the BP coated particles explicitly, so the particles have been homogenized over the volume of the BP rod for the generation of the cross section data. This approximation introduces significant modeling errors, but does not defeat the purpose of the analysis, which concentrates on analyzing the effect of identical lattice cells whose cross sections were collapsed in a different spectrum environment.

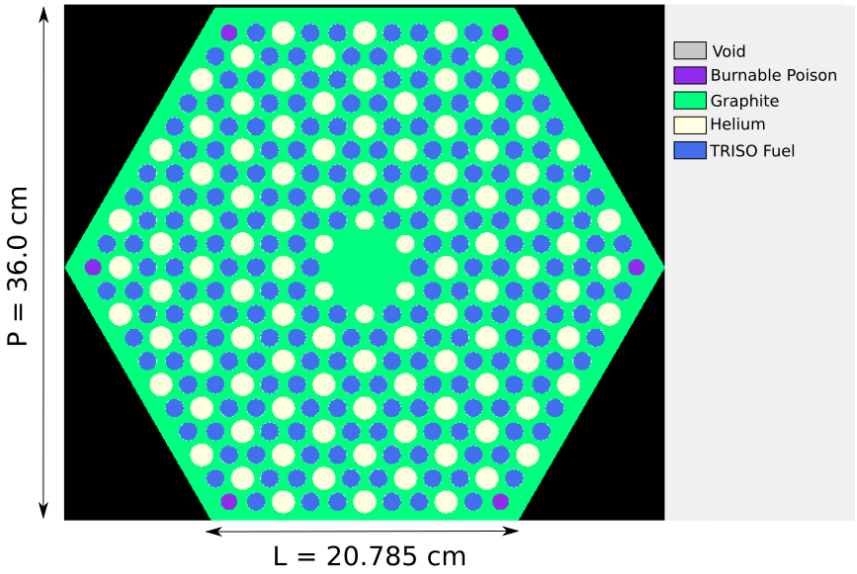

Figure 29. Radial representation of a fresh prismatic fuel block

A second lattice model has been developed in the form of a seven-block "super cell" to substantiate the spectral effects more accurately over the central fuel block. It consists in a central heterogeneous block (identical to Figure 29) surrounded by homogenized blocks representative of a sub-region in the fuel loading pattern of the core [60]. Figure 30 illustrates the super cell geometry as defined in the MHTGR-350 benchmark.

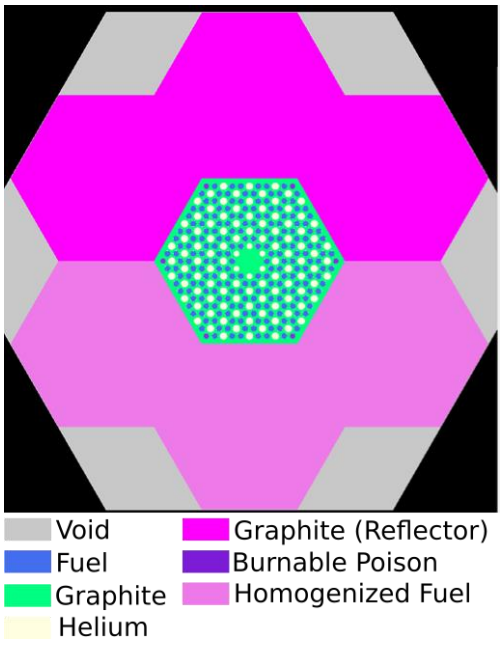

Figure 30. Design of a super cell model (Ex. I-2c)

Such model aims to generate more accurate cross section data for the central block by accounting for the local effects of the neutron flux spectra induced by the fuel/reflector interfaces in the MHTGR-350 core. The cross sections collected from several of these representative super cells are implemented as inputs to the corresponding fuel blocks in the 1/3rd core symmetry models.

It is intended for example to investigate the neutron flux effects at the periphery of the fuel ring (i.e. blocks 8-13, blocks 23-26 and block 28-31 in Figure 31) versus the neutron flux in the central fuel ring in the core (blocks 14-21). Only the nuclear data related to the central block are collected from the super cell, and not the cross sections characterizing the entire super cell.

Overall, in a case of a mixed core made of burned and fresh blocks, a set of about fifteen super cells can be constructed [61]. This study only highlights the results from the fresh-fueled super cells. An additional reflector cell represents the inner, outer and replaceable reflector blocks. As explained in section 2.4, the reflector cell needs to be modeled with a sufficient amount of fuel and enhanced number of discrete ordinate to avoid the ray effect in the numerical scheme. Reflective boundary conditions surround the fuel block (Exercise I-2a) in the benchmark specifications, as depicted in Figure 29. Exercise I-2a stands as a reference to

compare the super cell models, since this is the most basic (and for most historical applications the default) lattice representation.

Figure 31. MHTGR-350 one-third core model representation. Blocks 1-7 , 22, 27 and 32-91 are reflector blocks. Blocks 8-21, 23-26 and 28-31 are fuel blocks

A set of four super cells represents the second lattice, each with a fresh fuel block at the center (see Figure 32). Figure 33 illustrates the equivalent reflector cell. In Figure 32 and Figure 33, the plain pink blocks symbolize the homogenized fuel (labelled "*F*") and the striped pink blocks denote the heterogeneous fresh fuel. The black blocks represent the reflector (labelled "*R*").

The four super cells are identified as super cell *k* (three graphite blocks), super cell *l* (two graphite blocks), super cell *m* (one graphite block) and super cell *i* (fuel blocks only). A homogenized variant of cell *k* is referred to as Ex. I-2c in the benchmark specifications.

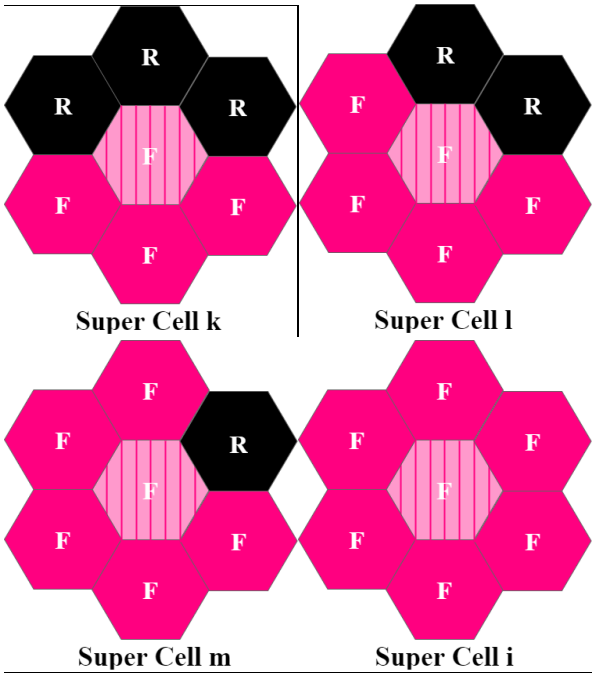

Figure 32. Representation of the Ex. I-2c super cells *k*, *l*, *m* and *i* (fuel)

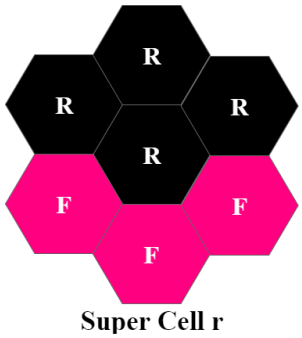

Figure 33. Representations of the Ex. I-2c super cells *r* (reflector)

5.2 Convergence of the Models

A convergence study on the P_N order, the number of discretized azimuthal angles and the spatial mesh grid was evaluated on super cells *i* (least thermal spectrum), *k* (most thermal spectrum) and the fuel block. The goal was to estimate the settings in NEWT required to obtain acceptable eigenvalues compared to KENO-VI or Serpent, and evaluate the global running time if a large number of perturbed cells is necessary in a later analysis (SAMPLER, RAVEN). Table

8 summarizes the effect of the spatial mesh grid, the scattering order (P_N) and the number of discretized azimuthal angles (N_{AZ}) on the k_{inf}. The mesh grid corresponds to number of spatial regions defined in the two-dimensional geometry. P_N corresponds to the number of Legendre moments in the scattering cross section expansion. This parameter is modified for all the materials simultaneously except the coolant. N_{AZ} is the number of equally-spaced azimuthal directions in the product quadrature set. N_{AZ} is set to three by default and is coupled to three polar angles. The grid, Legendre order and the number of azimuthal directions all increase the cost of the calculations to some degree.

In Ex. I-2a, the main unit (i.e. the entire system) is refined systematically. The parametric study on the mesh grid in the super cells is concentrated on the neighboring blocks. Super cell *i* is selected for the analysis to evaluate to what extent the homogenized fuel is impacted by the discretization settings. The six surrounding blocks are systematically refined in super cell *i*. The parametric study focuses entirely on the graphite blocks in super cell *k*. The data relative to the central block are set with the following values: 24 × 24 grid and $P_N = 1$ for each material in the super cells.

Table 8 proves that the NEWT multiplication factor tends to the KENO-VI best estimate as the discretization and convergence parameters are refined. NEWT's inability to process a finer grids or a greater number of angles without modifying the defaulted grid explains the empty cells in Table 8. The running time severely increases with the number of azimuthal angles and the refinement of the mesh grid, while the P_N order remains relatively inexpensive. The super cell *k* with six azimuthal angles approaches ~80 hours of running time (Figure 34).

The three systems do not respond similarly to the type of refinements. The spatially large systems (super cells) have more severe responses to a grid refinement than the small systems (single block). The widely heterogeneous systems (single block) respond more severely to the number of direction angles than the hybrid systems, which have homogeneous and heterogeneous regions (super cell). The amount of non-absorbing media (in this case, graphite) in the super cell significantly slows down the convergence of the iterations. This effect is paired with an increased sensitivity of the multiplication factor to the amount of non-absorbing media in the system. With a mesh grid eight times finer, the k-infinity in super cell *i* augments by 19×10^{-5}, while k-infinity in super cell *k* decreases by 340×10^{-5}. The effect is even more sensitive when

one considers that the six homogenized fuel blocks are refined in super cell *i* while only the three graphite blocks are refined in super cell *k*.

Table 8. NEWT convergence results related to discretization parameters in the single block, super cell *i* and super cell *k*

Discretization	*Ex. I-2a*	*Super cell i*	*Super cell k*
12 × 12	-	1.18549	
24 × 24	1.02011	1.18576	1.25946
48 × 48	1.02013	1.18590	1.25703
96 × 96	1.02001	1.18595	1.25606
192 × 192	1.02000	-	-
$P_N = 1$	1.02011	1.18576	1.25946
$P_N = 3$	1.02014	1.18577	1.25945
$P_N = 5$	1.02014	1.18577	1.25945
$N_{AZ} = 3$	1.02011	1.18576	1.25946
$N_{AZ} = 6$	1.02054	1.18568	1.25949
$N_{AZ} = 9$	1.02107	1.18572	-
KENO ref.*	1.02242	1.18677	1.25523

*The results are given with a 16 pcm standard deviation or less

The criticality calculations do not occupy a central place in this study. The effect of neutron flux on the cross sections motivates the work, so the change in neutron spectra as a function of the discretization parameters is estimated. The average difference per energy group in the single block's flux spectrum between N_{AZ}= 3 and N_{AZ}= 6 is 0.09 % (maximum of 0.28% in the most thermal energy group 26). The average relative difference is equal to 0.12% (maximum of 0.39 % in energy group 26) between N_{AZ} = 3 and N_{AZ} = 9. The refinement of the reflector's mesh grid induces an average flux difference in the super cell *k* equal to -0.03% between a 24 ×24 and

a 48 × 48 mesh grid, and -0.05% between a 24 × 24 and a 96 × 96 mesh grid. Lower differences are observed in the single block. The P_N order does not change the flux spectrum at all in any of the models.

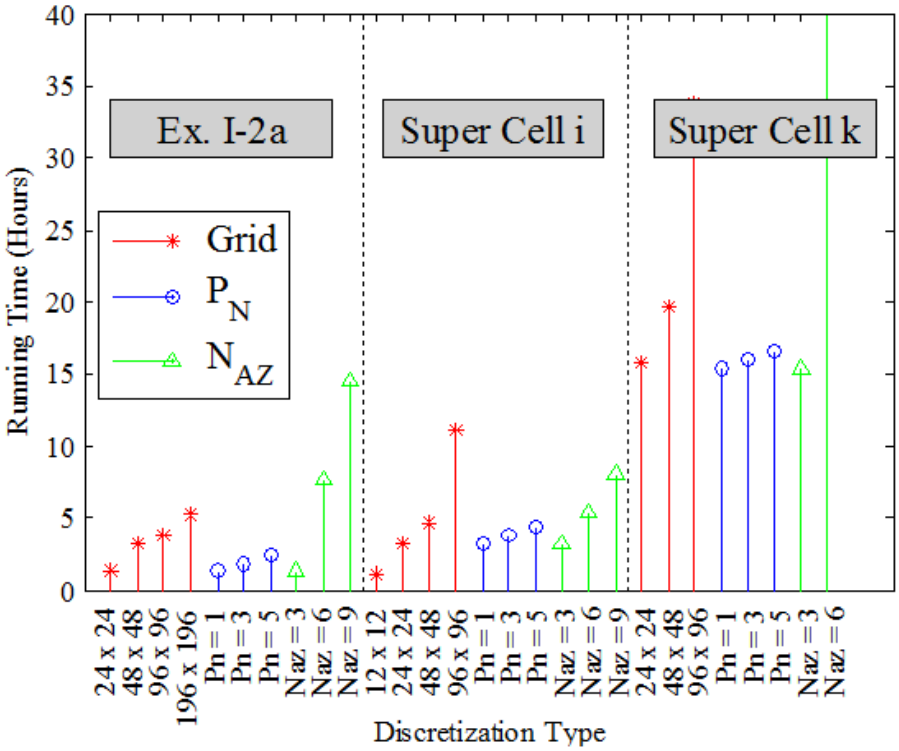

Figure 34. NEWT's running time as a function of the discretization type in super cell *i* and *k and* the fuel block Ex I-2a.

In summary, a sensitivity study determined the NEWT discretization parameters that will produce accurate problem-dependent nuclear data libraries, using a reasonable compromise between the converged multiplication factors, the neutron spectra and the running time. Table 9 recapitulates the convergence parameters chosen for each region. Table 10 indicates the multiplication factor obtained in NEWT as compared to KENO-VI using these parameters.

5.3 Neutron Flux Reference

This section establishes (a) the consistency of the NEWT collapsed flux and (b) a reference core flux spectrum based on Serpent-2.1.27.

Figure 35 sketches a compact cell from a fuel block. Figure 36 compares the neutron fluxes between NEWT and Serpent-2.1.27 in a compact cell and the MHTGR core.

Table 9 Final discretization settings chosen in NEWT

Region	*Discretization*
Heterogeneous block	24 × 24 grid
Homogenized fuel	24 × 24 grid
Graphite	48 × 48 grid
P_N order	1
N_{AZ}	3

Table 10. Infinite multiplication factor compared between NEWT and KENO-VI

Model	k_{inf} *NEWT*	k_{inf} *KENO-VI* (*std dev* $\times 10^{-5}$)	*Absolute diff.* ($\times 10^{-5}$)
Ex. I-2a	1.02011	1.02242 (15)	-231
Super cell *i*	1.18576	1.18677 (13)	-101
Super cell *m*	1.25710	1.25730 (16)	-20
Super cell *l*	1.33136	1.33063 (14)	73
Super cell *k*	1.25703	1.25523 (14)	+180

Figure 37 compares the neutron flux spectra from a fuel block and the core with NEWT and Serpent. Identically, Figure 38 juxtaposes the neutron flux spectra from the super cell *k* and the core. Figure 39 overviews the spectra from the various spatial models (compact, block, super cell and core levels). The fluxes from NEWT and Serpent corroborate within less than 0.1%. A harder spectrum characterizes the compact as compared to the core spectrum. The fuel block

spectrum is softer than the compact spectrum but still harder than the core spectrum, while the spectrum in the super cell *k* remains much softer than the core. Those results were expected considering the relative moderation of each model.

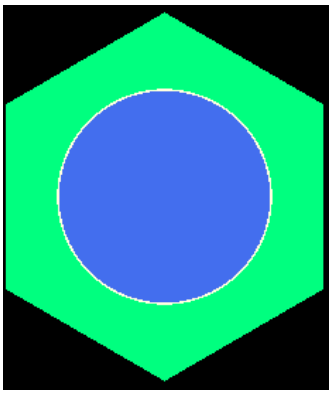

Figure 35 Radial representation of a compact cell

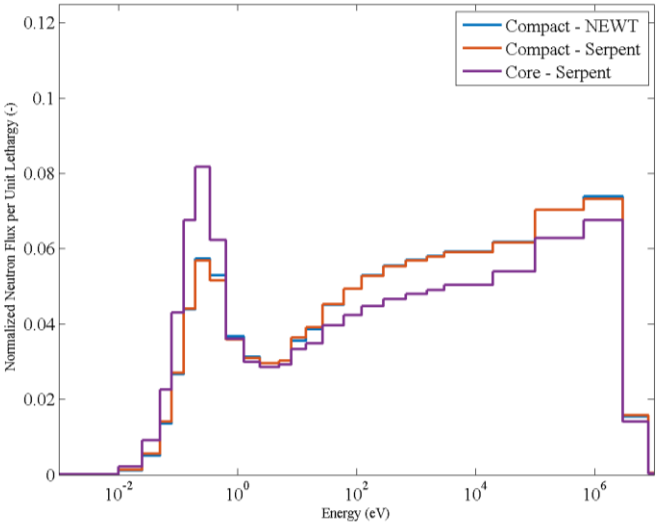

Figure 36. Flux spectra in a compact cell (NEWT and Serpent) compared to the reference core spectrum (Serpent)

5.4 Neutron Flux across the Core Fuel Rings

The neutron flux spectrum is analyzed in deeper details across the spatial regions of the core. As shown in [62] and explained in section 2.2.3, the neutron flux across a fuel block varies

smoothly compared to a light water reactor. The neutron flux is evaluated in two distinctive regions of the core. The first region corresponds to the inner and outer layers of the fuel blocks that are in contact with the reflector. The spectrum in this region is expected to be relatively thermal. The second region corresponds to the central ring in the fuel region and a faster spectrum can be anticipated. Figure 40 shows how the two regions are defined.

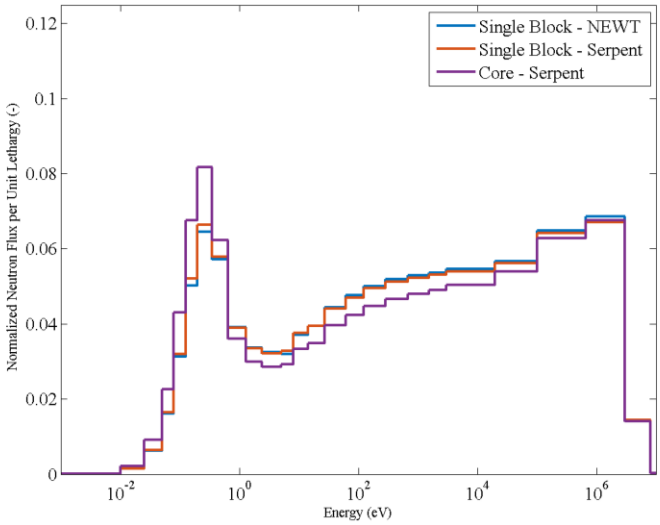

Figure 37. Flux spectrum in the fuel block compared to the MHTGR core spectrum

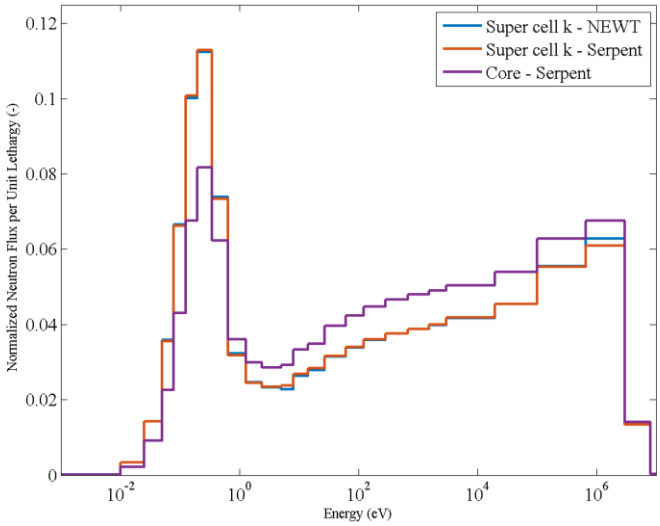

Figure 38. Flux spectrum in the super cell *k* compared to the MHTGR core spectrum

Figure 41 displays the neutron fluxes in the two regions. Radially, the neutron flux is significantly softer on the edge of the core than the center. This plot points to the potential importance of using a super cell model versus a single block model to generate HTGR cross section data in core analysis. It also raises the questions of the most representative way to model the core with a super cell.

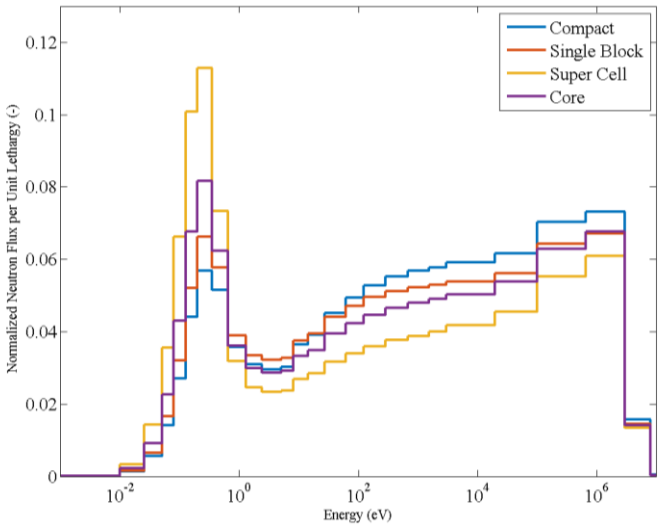

Figure 39. Overview of the neutron flux spectra in the compact cell, fresh fuel block, highly-moderated super cell (*k*) and full core models (Serpent)

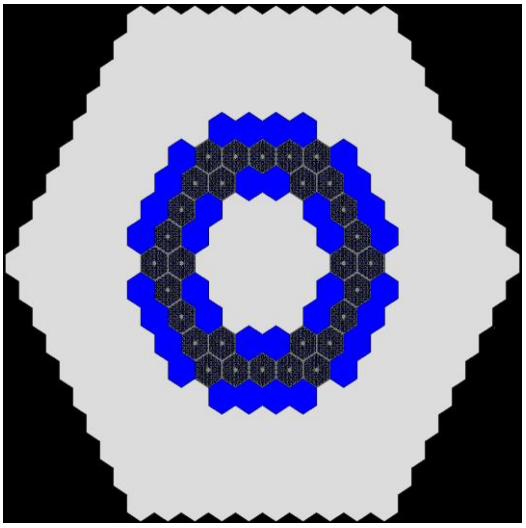

Figure 40. Separation of the core region: the blue blocks correspond to the fuel's inner and outer region; the remaining dark blocks correspond to the central ring of fuel blocks; the cream-white zone symbolizes the graphite blocks. The black region on the corners is vacuum.

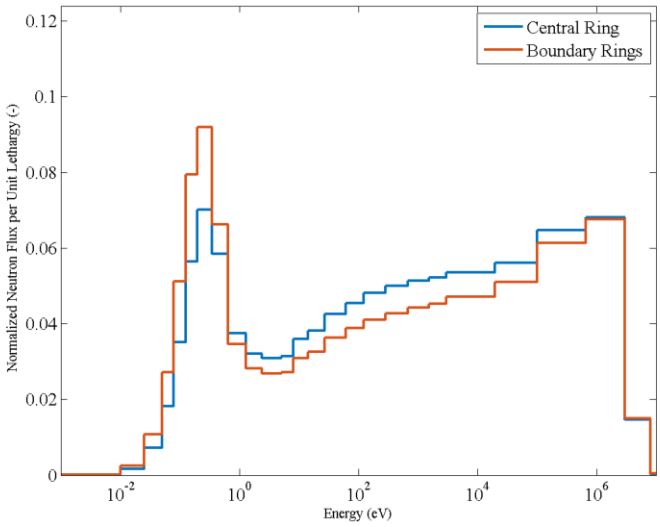

Figure 41. Comparison of the neutron fluxes across fuel/reflector boundaries and the central fuel ring of the core

5.5 Neutron Flux across the Central Block in the Super Cells

Figure 42 gives the normalized neutron flux per unit lethargy across the central block of the super cells *i*, *m*, *l* and *k*. Figure 43 emphasizes on the thermal peaks. A 26-group structure

characterizes the neutron flux [63]. The super cell *k* contains the local region that has highest moderation achievable in this core design, thus providing the softest (most thermal) spectrum. The single block (Ex. I-2a) does not have additional reflector blocks in the vicinity and thus represents the lowest moderator-to-fuel ratio. The flux spectrum at the center of a super cell becomes softer as the amount of graphite increases in the neighboring regions. Reference [61] demonstrated that the topology of the homogenized regions (fresh or depleted) around the heterogeneous central block does not influence the neutron flux spectrum at the center of the super cell. Thus, the use of homogenized fuel blocks as represented here is justified.

Figure 44, Figure 45 and Figure 46 illustrate neutron flux maps of the fuel block, super cell *i* and super cell *l*. They highlight differences between the cells' flux in group 3 (the fast group with the highest χ) in the 26-group structure. It should be noted that the color scale is relative to each model, i.e. one should not cross-compare the color scale between Figure 44, Figure 45 and Figure 46. NEWT bases its color scheme on the minimum, the maximum and average neutron fluence, and those parameters varies significantly from one model to another. Thus, the neutron flux appears (artificially) softer in the heterogeneous portion of super cell *l* as compared to Ex. I-2a, since there are fewer neutrons from group 3 transported from the fuel region to the graphite region of the cell, which implies that group 3 is well represented throughout the central block as compared to the northern region (graphite). The super cell *i* and the fuel block I-2a have the same isotopic composition, since the single block boundaries are reflective, which explains the closeness of the spectra.

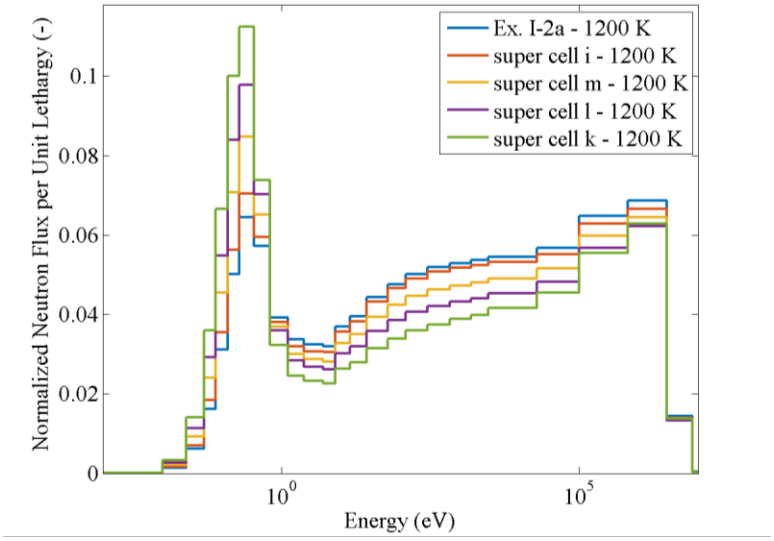

Figure 42. Normalized neutron flux per unit lethargy in a 26-group structure for Ex. I-2a and Ex. I-2c super cells *i, m, l* and *k*

Figure 42, Figure 44 and Figure 46 prove the spectral effect induced by the neighboring blocks in super cell *l*: the spectrum in the northern section of the heterogeneous block is harder than the southern section. This suggests that the fission rate is greater at the top than the bottom part of the super cell because of the locally improved moderation. The flux perturbations induced by the super cell's composition lead to a modification the collapsed cross sections.

Figure 47 shows the product of the normalized neutron flux per unit lethargy and the homogenized macroscopic fission cross section (i.e. the total fission reaction rate). This fission rate is evaluated only in the central block region. Figure 47 confirms that the fission reaction rates originating from thermal regions (at the periphery of the core) are significantly different to the fission rates at the center of the core where the neutron flux is harder.

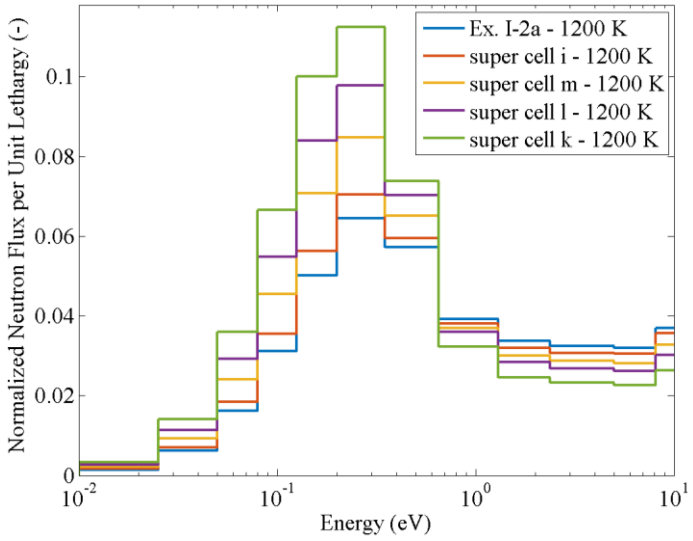

Figure 43. Normalized neutron flux in a 26-group structure for Ex. I-2a and Ex. I-2c super cells *i, m, l* and *k (*Close-up on the thermal peak)

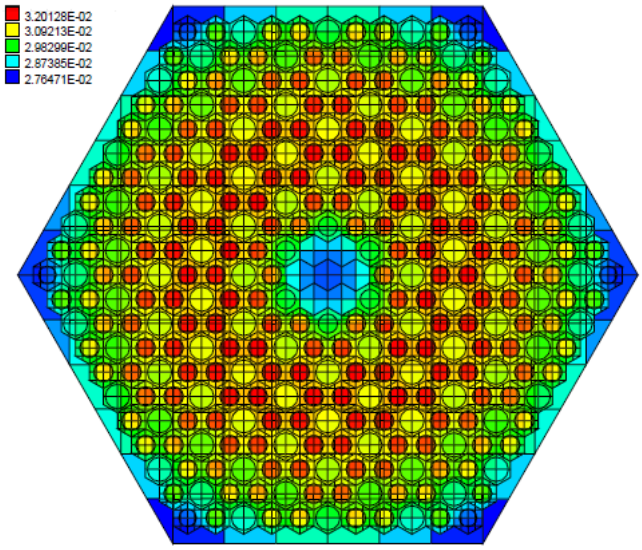

Figure 44. Group 3 neutron flux map for Ex. I-2a

5.6 PHISICS/RELAP5-3D Core Calculations

In this section, the 26-group data sets are implemented in the PHISICS/RELAP5-3D core calculations. The effect of the various flux-weighted cross sections originating from the super cells on the core power density is evaluated.

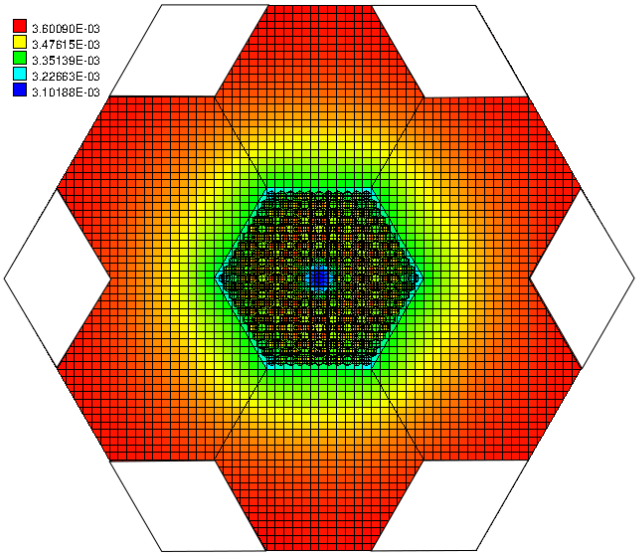

Figure 45. Group 3 neutron flux map for Ex. I-2c (super cell *i*)

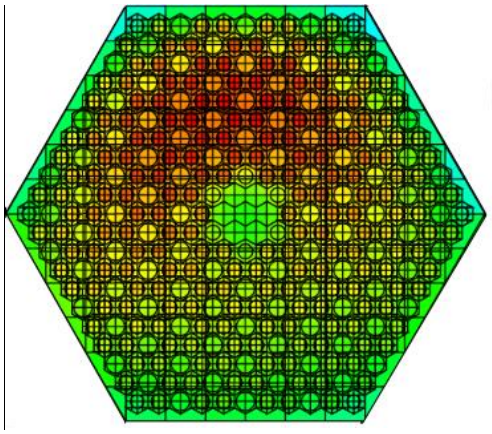

Figure 46. Group 3 neutron flux map for super cell *l* (close-up on the central block).

5.6.1 Description of the Model

The flux-weighted 26-group cross sections are propagated as input to the one-third core model on a homogenized block-by-block basis. Figure 49 exposes the PHISICS/RELAP5-3D core model constructed with the cross sections generated from the block cell (Ex. I-2a, hereafter referred to as "core *2a*"). Core *2a* is used as a reference case for comparison with more complex core configurations. This core represents the simplest link between the lattice and core simulation phases, as it only utilizes cross sections generated by a single infinitely-reflected fuel block.

It is intended to estimate the effects induced by the implementation of the cross sections that were generated previously (Section 5.5) according to their spectral environment. For instance, the super cell *k*'s cross sections are utilized at the periphery of the core. Figure 48 illustrates the arrangement of the core $\{i-k-l-m\}$. The same reflector's cross sections are implemented throughout the core's reflector regions.

The results obtained for six PHISICS/RELAP5-3D 1/3rd cores are reported in this study. It includes:

(1) a core loaded with the cross sections from cell *2a* (reference, core *2a*);

(2) a core loaded with the cross sections from cell *i* (core *i*);

(3) a core loaded with the cross sections from cell *m* (core *m*);

(4) a core loaded with the cross sections from cell *l* (core *l*);

(5) a core loaded with the cross sections from cell *k*. This is the core with cross section data that are flux-weighted with the most thermal neutron flux (core *k*);

(6) a core mixing the cross sections sets *m* and *2a* (core $\{m-2a\}$);

(7) a core mixing the cross sections sets *l* and *2a* (core $\{l-2a\}$);

(8) a core mixing the cross sections sets *k* and *2a* (core $\{k-2a\}$);

(9) the most refined core using the cross sections generated from the cells *i*; *k*; *l*; *m* (core $\{i-k-l-m\}$).

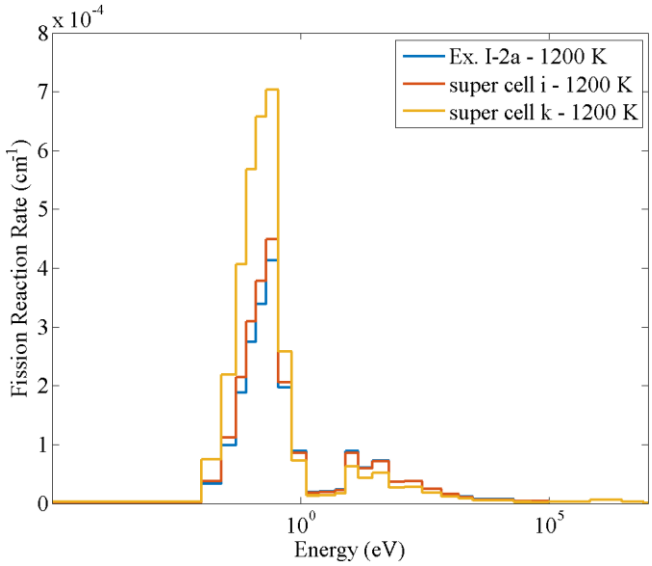

Figure 47. "Normalized" total reaction rates for Ex. I-2a, super cells *i* and *k*.

The 26-group NEWT microscopic cross sections are collapsed from the SCALE-6.2.0 252-group structure and stored in AMPX format. The disadvantage factors relative to the homogenized mixtures are calculated from the NEWT mixture's fluxes and are passed to PHISICS. The PHISICS input is constructed with the block-homogenized isotopic inventory to perform transport iterations. Table 11 provides the k_{eff} computed by PHISICS for each of these cores. The multiplication factor increases as the neutron flux softens in the NEWT models. The k_{eff} difference between the core *2a* and the core *i* is relatively small (0.00381). The single block is an infinite lattice, hence the lattice *i* is the super cell representation of a single fuel block. The homogenization of the outer blocks of the super cell *i* causes slight changes in the few-group cross sections, which justifies the reactivity difference in core *2a* and core *i*. The multiplication factors from the other super cells cannot be analyzed with the single block's k-effective, because the graphite-to-fuel ratio is modified in comparison to Ex. I-2a. It is important to emphasize that the number densities are strictly identical in all the PHISICS core constructed, hence the change in the multiplication factor between the different models is only induced by the cross section effects during the NEWT calculations. Note that NEWT calculates the infinite multiplication factor of the user-defined homogenized region (i.e. the entire central fuel block). In a "dummy" core, cross sections from cell *i* replaced the reflector. Reflective boundary conditions were applied on this dummy configuration. The core becomes an infinite lattice of homogenized blocks. The two

models are then perfectly equivalent, and a perfect agreement was obtained between NEWT and PHISICS (0.2×10^{-5}), guarantying the correctness of the transition methodology between NEWT and PHISICS.

From the comparison of an integral parameter such as k_{eff}, it cannot be concluded whether the more complex lattice representations were worth the effort, since a detailed investigation of the spatial reaction rates and flux distributions would typically be required to fully assess the impact of these different cross section sets. In this study, the integral effects on the power density profiles are compared in Section 5.6.2.

5.6.2 Axial Power Density Profiles

Table 12 indicates the coordinates of four points in the core. The axial power density profiles are evaluated at these radial locations (Figure 49).

Figure 50 shows the power density profiles in core *2a*. The inner parts of the fuel ring contain the highest power densities. The points 2 (yellow line with dotted markers) and 3 (purple line with circled markers) presented in Table 12 overlap in Figure 50. The reflector regions do not generate power. A slight peak is observed at the axial fuel-to-moderator interface. The locally higher moderator-to-fuel ratio justifies this extremum. This effect is more pronounced at points 2 and 3, where the fuel blocks are located next to the graphite blocks radially.

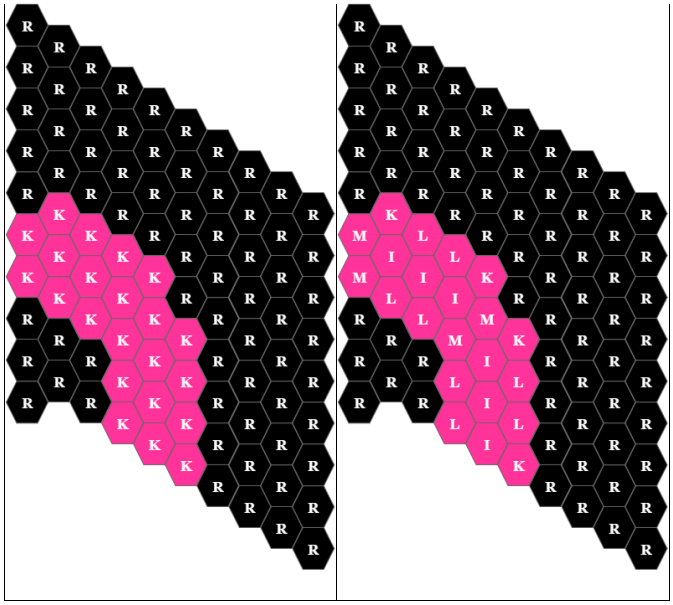

Figure 48. PHISICS/RELAP5-3D one-third core models constructed with Ex. I-2a and Ex. I-2c super cell *k* (left) and cells *k*; *l*; *m* and *i* (right) cross sections

Figure 51 compares the axial power density profiles in the cores *2a*, $\{i-k-l-m\}$, *k, m, l* and *i* at the periphery of the system (x = 126.0 cm; y = 31.1 cm, northernmost green dot in Figure 49). Cores $\{k-2a\}$ and *m* are left over for clarity. The figure emphasizes only the peak power density because of the small changes in the profile.

A difference of 1.2% is observed in the peak power density between cores *2a* and *i*. The difference between the core $\{i-k-l-m\}$ and the core *2a* in the peak power density goes up to 6.4%. Note that the material number densities are identical for all the cores considered here. Therefore, the difference of about 0.2 W/cm^3 between core *2a* and *k* is induced by the cross sections that are flux-weighted during the TRITON/NEWT sequence.

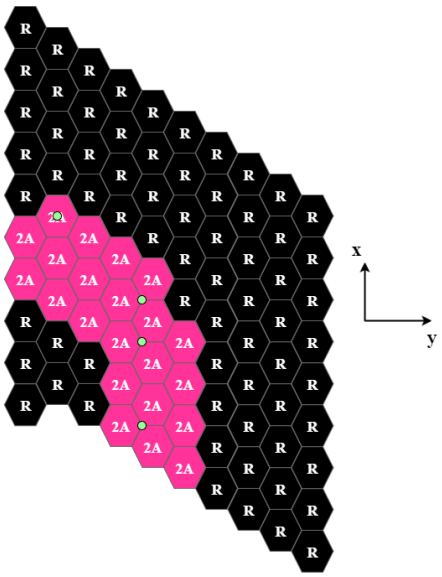

Figure 49. PHISICS/RELAP5-3D third core packed with Ex. I-2a cross sections

Table 11 PHISICS's k_{eff} with various sets of NEWT microscopic cross sections

Core loadings	*k-effective*	*Absolute Difference* ($\times 10^5$)
2a	1.00093	(reference)
i	0.99712	-381
m	0.98603	-1,490
l	0.97348	-2,745
k	0.96034	-4,059
m – 2a	0.99041	-1,052
l – 2a	0.98146	-1,947
k – 2a	0.97215	-2,878
i – k – l - m	0.97855	-2,238

Table 12 Radial coordinates of the points selected for the comparison of axial power density profile

Point number	*x-coordinates (cm)*	*y-coordinates (cm)*
1	54.0	93.53
2	126.0	31.17
3	90.0	93.53
4	-18.0	93.53

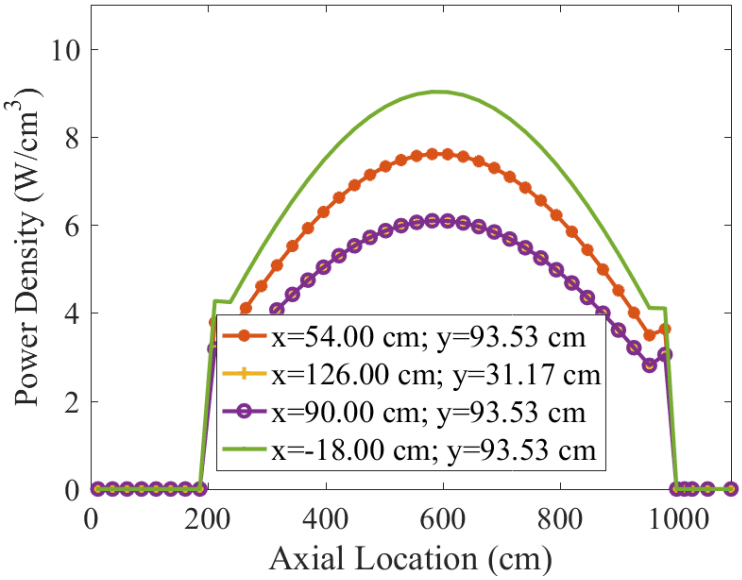

Figure 50. Axial power density profile for Core *2a*

5.6.3 Radial Power Density Distribution Obtained with RELAP5-3D/PHISICS

In this section, the radial power densities are compared (in relative values) to the reference core *2a* at the axial location z = 607.9 cm, corresponding to the axial peak power density. PHISICS/RELAP5-3D computes the power density for each of the homogenized fuel blocks, i.e. the power is calculated per assembly and not as a pin-by-pin basis.

Figure 52 compares the core loaded with the cross sections *2a* with the core loaded with the cross sections *i.* The differences range from 0.1 % on the peripheral blocks to 1.7 % on the central blocks. The flux-weighting of the cross sections are almost equivalent between super cell *i*. Figure 53 maps the power density between core *2a* and core *m*. Figure 54 compares core *k* and core *2a* and demonstrates the implementation of the cross section sets originating from a softer flux raises the power density at the central ring of the core. The magnitude of the differences between core *m* and core *2a* are predicted from 0.4% to 1.9%. Those results are comparable to the differences between core *i* and core *2a*. The magnitude of the differences between core *k* and core *2a* are valued from 1.1% to 3.4%. Note that those differences are positive, which means the raise of the peak power density is balanced by a negative power peak at the top and the bottom of the core, resulting in a less flat axial power profile. The higher power density at the central ring as compared to the inner and outer fuel rings can be explained by either (a) an increased fission reaction rate at the central fuel ring and/or (b) the increased absorption reaction rate at the inner and outer fuel ring. The core *i*, core *m* and core *k* do not account for the actual spectral environment of the core, as demonstrated in section 5.4. They are merely an attempt to evaluate the pure effects of the cross sections from the lattice cells. Those core configurations confirm that core power density behaves correlatively with the graphite-to-fuel ratio chosen in the lattice cells, and hence the local environment of the lattice cells. Figure 45 confirmed that only the first neighbor influences immediately the central cell.

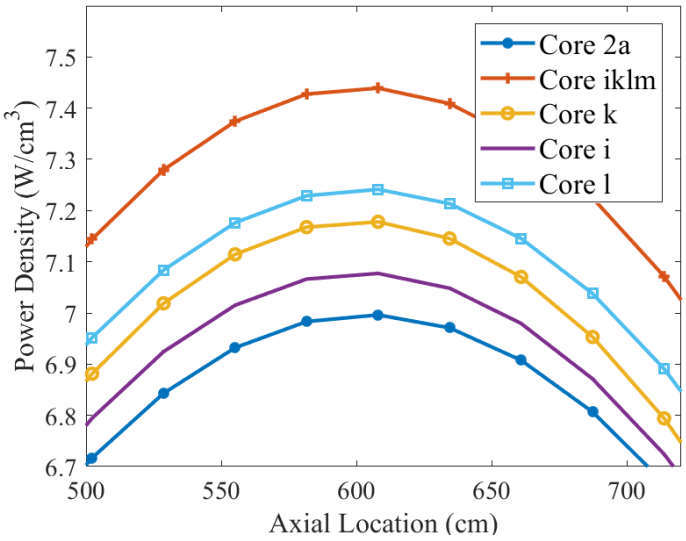

Figure 51. Comparison of the axial power density profiles between core *2a*; {*i-k-l-m*}; *k* and *i* at the radial coordinates x = 126.00 cm; y = 31.17 cm

Figure 55 shows that a raise in the power density affects the mixed core $\{k-2a\}$ (NEWT's cross section *k* on the edges of the core and NEWT's cross section *2a* at the central ring). Figure 55 also emphasizes a power density decrease at the inner and outer fuel rings. The range of the changes with core *2a* are -1.3%; 6.4% radially throughout the core. This means that the power gradient between the corner blocks and the central fuel ring is caused by the implementation of the "soft" cross sections from super cell *k*. Such effect is also observable with a core $\{l-2a\}$ with a range of -2.0%; 3.5% radially throughout the core, and core $\{m-2a\}$ with a range of 0.2 %; 1.2 % radially throughout the core. Figure 57 provides a comparison between core $\{k-2a\}$ and core $\{l-2a\}$. The nodes at the central fuel ring are filled with the NEWT cross section *2a.* Those blocks have a power density noticeably increased to maintain the total power normalization at 350 MW. Note that the power density gradient is more pronounced throughout the core as the moderation in the lattice cells increases, as it was observed previously in core *m* (Figure 53) and core *k* (Figure 54). The refinement of the core loading into a $\{i-k-l-m\}$ configuration (Figure 48) evidences a comparable trend to the core $\{k-2a\}$, $\{l-2a\}$ and $\{m-2a\}$. The power density at central fuel ring increases while the inner and outer fuel rings observe a decrease of the power density. The range of the difference with the reference core *2a* are -9.0 %; 8.4 %. The statements made for core $\{k-2a\}$ can be confirmed by comparing core $\{i-k-l-$

m} in Figure 56*,* where the power density increases accordingly to the softness of the super cell's spectrum used at each location. Figure 58 collates core $\{i-k-l-m\}$ and core $\{l-2a\}$ and proves that the two configurations remain apart by a range of 1.6% to 7.6% (average: 3.8% difference). Table 13 summarizes the minimum and maximum relative differences of the core loadings *i*, *k*, $\{k-2a\}$, $\{l-2a\}$, $\{m-2a\}$ and $\{i-k-l-m\}$ as compared to the reference core *2a.* Table 13 highlights that the use of one single set of cross section set raises the power density peak. The use of a refined core $\{i-k-l-m\}$ redistributes radially the power density. The average variation of the radial power density remains low (about 1.0 %), which induces that the axial power shape remains only slightly affected by the cross section changes.

The use of the libraries *i* in the core $\{i-k-l-m\}$ still results in about 8 % power density difference, although these cross sections do not change the power distribution in the core *i* as compared to core 2a. This implies that the use of cross sections flux-weighted with a soft spectrum (super cell *k* or *l*) leads to a flux redistribution, and the power decrease induced at the periphery of the core is balanced with an increase at the center region.

Table 13. Relative difference (%) in the power density between the reference core *2a* and six core configurations

Core loading	*Lower bound of the range (%)*	*Upper bound of the range (%)*	*Average (%)*
i	0.1	1.7	0.9
m	0.4	1.9	1.1
k	1.1	3.4	2.3
m – 2a	0.2	1.2	0.6
k – 2a	-1.3	6.4	0.9
l – 2a	-2.0	3.5	0.6
i – k – l – m	-9.0	8.4	1.0

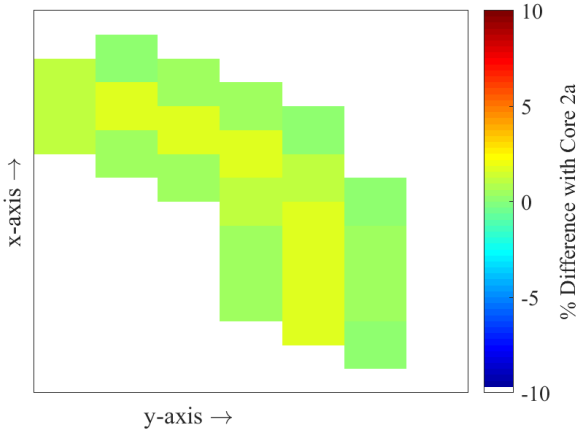

Figure 52. Relative difference (%) in the power density between core *i* and core *2a* (reference)

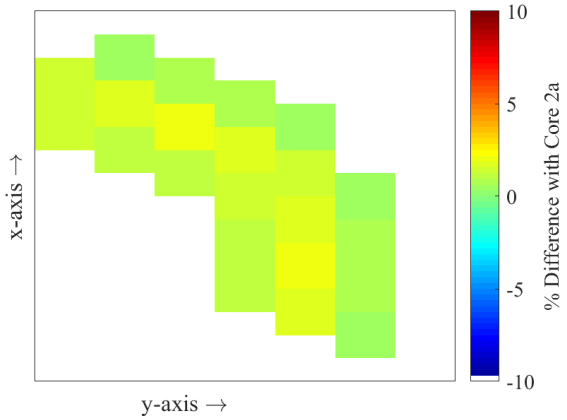

Figure 53. Relative difference (%) in the power density between core *m* and core *2a* (reference)

The overall trend between the core $\{i-k-l-m\}$ and the core $\{k-2\text{a}\}$ or $\{l-2a\}$ remains significant, although the power reduction is down to -0.8% in the case of core $\{k-2a\}$. This suggests that the most complex set of cross sections $\{i-k-l-m\}$ only leads to a slight modification of the power density distribution, and that core *k* or $\{k-2a\}$ is probably sufficient to capture the power distribution.

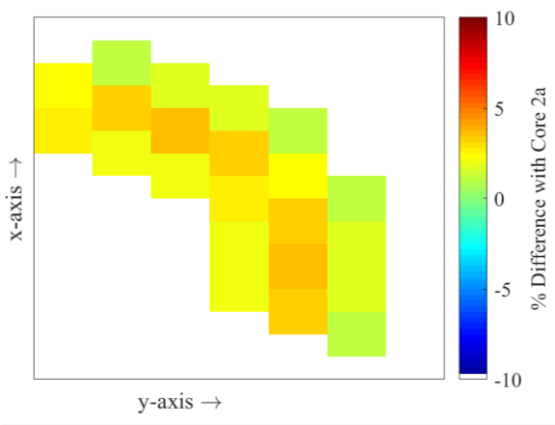

Figure 54. Relative difference (%) in the power density between core *k* and core *2a* (reference)

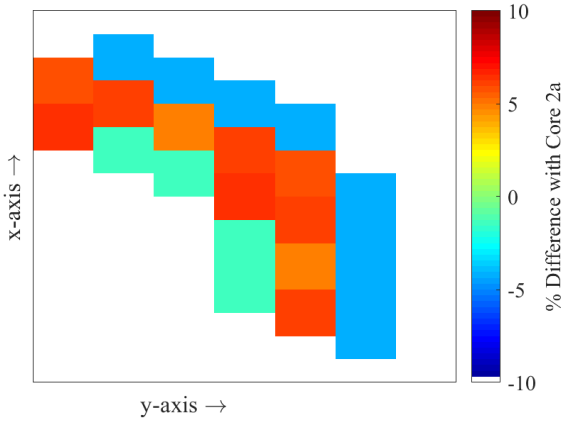

Figure 55. Relative difference (%) in the power density between core $\{k - 2a\}$ and core *2a* (reference)

5.6.4 Conclusions

The neutron flux spectrum in HTGR super cells is strongly influenced by the amount of graphite in the system and the burnable poison in the neighboring blocks. The softening effects of the graphite are spatially effective on a block-size scale. Thus, the graphite in the neighboring blocks strongly influences the neutron flux spectrum in heterogeneous regions, and in turn impacts the flux-weighted, collapsed cross sections obtained from these lattice models. This study shows however that the subsequent use of the cross section from a super cell lattice's central block in PHISICS/RELAP5-3D MHTGR-350 core calculations has an impact on the full core's multiplication factor, which can go up to thousands of pcm. The radial power density profiles are subject to significant redistributions using super cell cross sections versus single block cross sections. The radial power density can change spatially by up to +9.0% and -8.6% when compared to a reference core loaded with the cross sections originating from an infinitely-reflected single fuel block (Ex I-2a). The magnitude of the changes is closely related to the softness of the neutron flux spectrum utilized to collapse the super cells' cross sections.

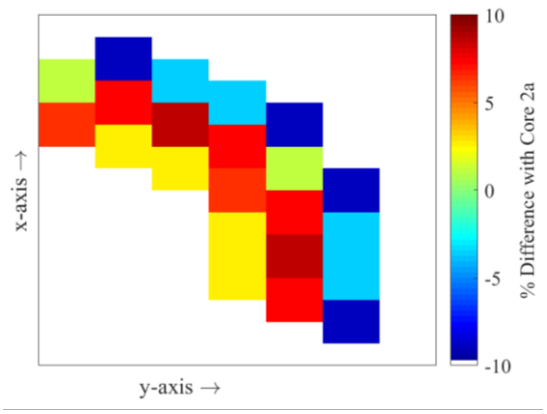

Figure 56. Relative difference (%) in the power density between core $\{i-k-l-m\}$ and core $2a$ (reference)

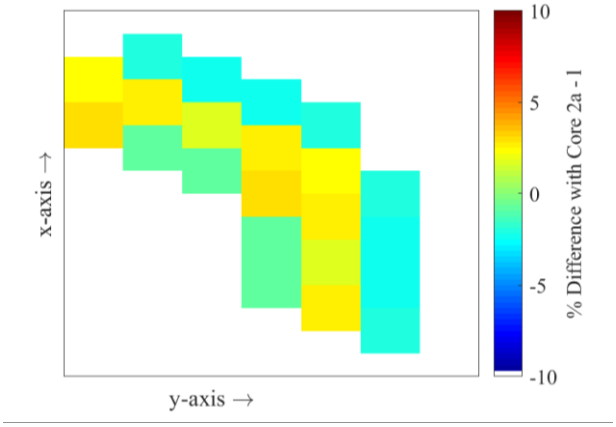

Figure 57. Relative difference (%) in the power density between core $\{k-2a\}$ and core $\{l-2a\}$

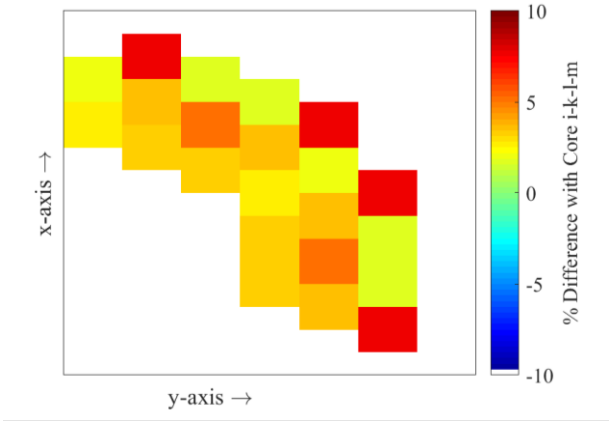

Figure 58. Relative difference (%) in the power density between core $\{i-k-l-m\}$ and core $\{l-2a\}$

The use of lattice cell cross sections in nodal HTGR core calculations must account for the immediate block neighbors to obtain spatially refined power densities. One possibility is the use of traditional single block lattice cells for the nodal calculations at the central ring of the core, where the fuel blocks are only surrounded by other fuel blocks. The lattice cells used to fill the slots on the edges, on the inner and outer ring of the core must account for the presence of

graphite in the neighboring environment. Super cells can account for such settings. Only the central block of the super cell generates the self-shielded cross sections to conserve identical isotopic inventory to the single block. A super cell made of two graphite blocks and four fuel blocks fills the core's peripheral fuel blocks (super cell denoted "*l*" in the analysis), at the interface fuel/reflector. A fuel-only super cell is also valid to model the central ring of the core (super cell denoted "*i"* in the analysis). It must however be kept in mind that these conclusions are based on the current 26-group structure selected for use in these PHISICS calculations, and that a lower number of groups (e.g. less than 8) could lead to more significant spectral differences between these models.

CHAPTER 6

UNCERTAINTY QUANTIFICATION APPLIED TO DEPLETION CALCULATIONS IN THE MHTGR-350

6.1 Scope of the Work

This chapter evaluates the uncertainty of nuclide inventories and multiplication factor over depletion calculations with the SCALE-6.2.0/SAMPLER sequence. The models representative to the MHTGR-350 exposed in CHAPTER 5 are assessed to understand to what extent the neutron flux influences the nuclide inventory's uncertainty. CHAPTER 5 showed that a fuel block, a super cell and a core from the MHTGR specifications have different neutron spectrum. The results related to UAM for LWRs (Section 3.3) proved that the neutron flux spectrum plays a role in the quantification of uncertainties. The goal of this chapter is two-fold:

- Presenting uncertainty associated to a nuclide inventory over a MHTGR cycle;
- Comparing those uncertainties between a single block and a super cell, two lattices representative of the MHTGR system.

As a preliminary study, KENO-VI and Serpent depletion simulations establish the burnup parameters desired for SAMPLER/T-NEWT uncertainty quantification. This chapter also conducts an analysis on the statistical convergence of the two models (fuel block and super cell). The SAMPLER/KENO sequence originally achieved the uncertainty study, but section 6.7 invalidates the simulations. T-NEWT remains the only option to perform the uncertainty quantification on nuclide inventories with SAMPLER in the version of SCALE at the time available (2017).

6.2 Geometrical Representation of the Model

Figure 29 represents the single block (Ex I-2a, also referred to as SB) depleted in this chapter. Figure 59 depicts the initially super cell (Ex-I-2c, also referred to as SC) initially considered and Figure 60 the full core model. KENO-VI generated those plots after execution. Reflective boundary conditions characterized the fuel block and super cell. The core has vacuum

boundary conditions. Table 14 gives the equivalences of the material numbers printed in the KENO-VI legend.

TRITON homogenizes the fuel rigorously with the two-step self-shielding approach described in section 2.5. The homogenized burnable poison channels include the BP particles smeared out with the graphite matrix in the burnable poison rods. An explicit representation of the burnable poisons is chosen in Section 6.6.3 to evaluate the homogenization effects of the BP. The graphite that compounds the fuel blocks is the same as the graphite used as reflector in the core model and super cell model.

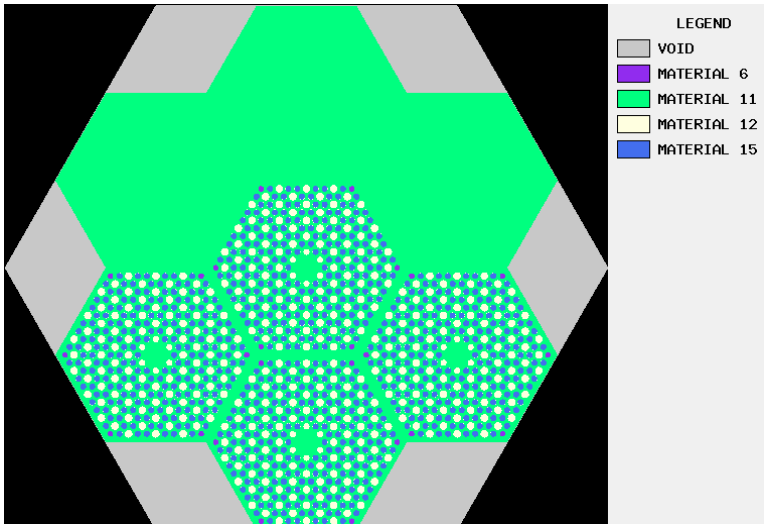

Figure 59. Radial representation of a prismatic super cell

Table 14. Material correspondences in Figure 59

KENO-VI material number	*Description*
6	Homogenized burnable poisons
11	Graphite reflector and matrix
12	Helium
15	Homogenized fuel

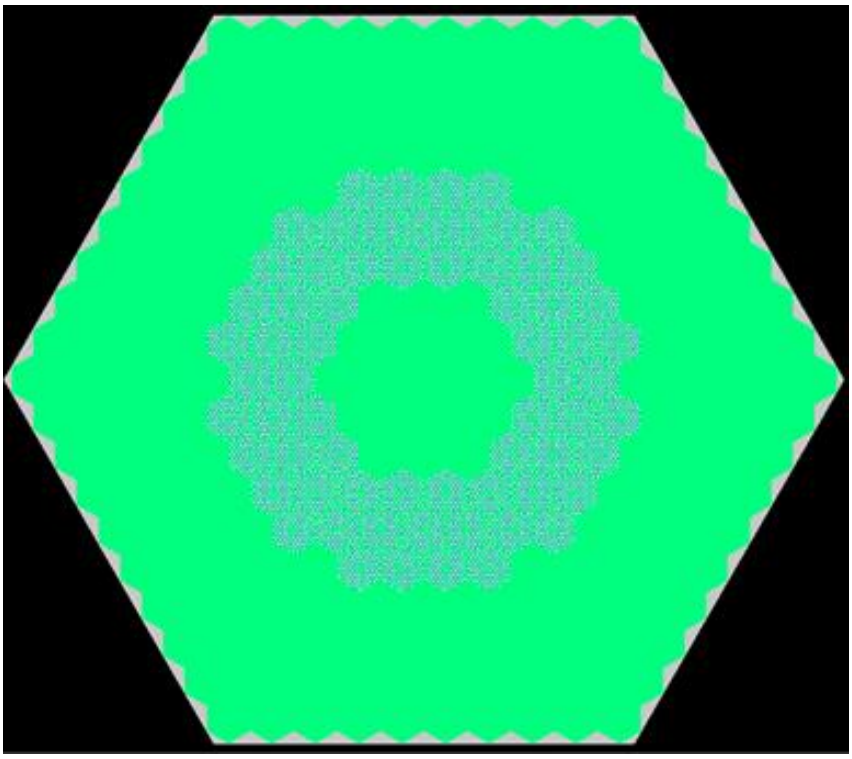

Figure 60. Radial representation of the MHTGR core

6.3 Statistical Convergence

A brief statistical convergence is achieved as the function of the number of neutrons sampled. The total number of neutrons is referred to as the number of neutrons per generation times the number of generations. The default value in KENO-VI is 203,000 neutrons (203 generations, 1000 neutrons per generation and 3 skipped generations). The number of skipped generations is increased up to 20 in the calculations. The standard deviation is evaluated at the Beginning Of Cycle (BOC) and at the end of cycle (EOC), for each model, varying the number of generations per cycle from 100,000 to 2,000,000 neutrons. The EOC burnup equals to 78.4 GWd/MTHM. Figure 61 represents the standard deviation (associated to KENO-IV's best estimate of the infinite multiplication factor) as a function of the total number of neutrons. Figure 62 sketches the execution time as function of the number neutrons sampled in the single block, super cell and core model. The calculations were performed on 1 node and 1 processor.

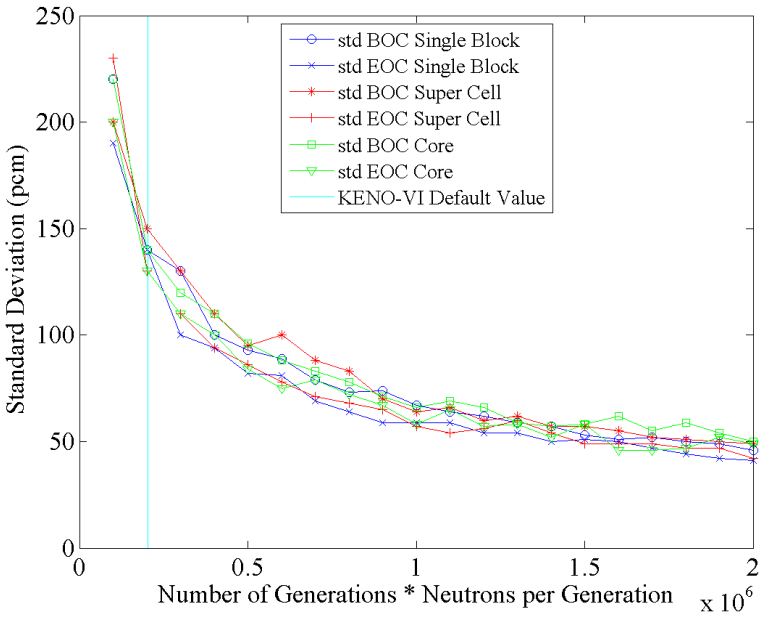

Figure 61. Standard deviation as a function of the total number of neutrons sampled at the BOC and EOC for the single block, super cell and core models

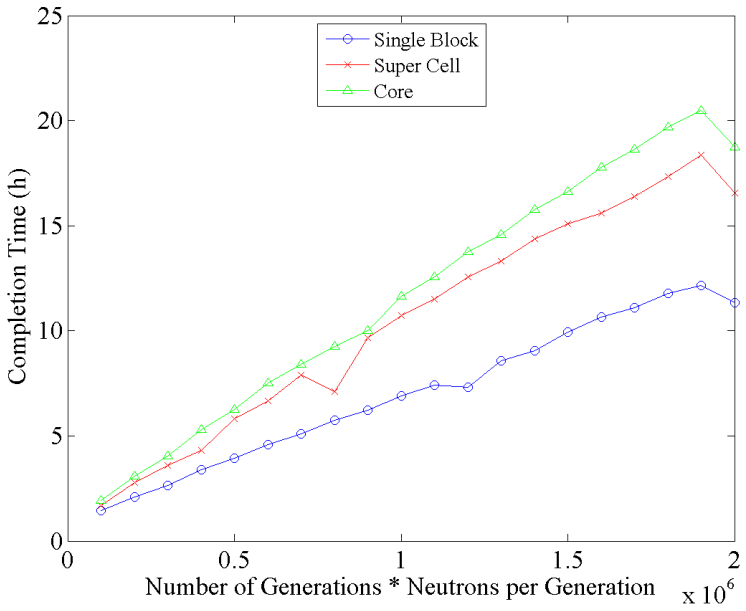

Figure 62. Execution time as the function of the total number of neutrons sampled for depletion calculations of the single block, super cell and core models

6.4 Burn Step Definition

Following the preliminary study performed in Section 2.7, the burn steps must be sufficiently refined to obtain accurate neutron flux and nuclide inventories over each burnup step. It is chosen to have short burn time for the first 5 days to model properly the xenon build-up and have then 30.93-day long burnup steps, corresponding to 2.0 GWd/MTHM. Section 6.5 derives the power density from the MHTGR specifications. Table 15 details the burnup steps considered in the study.

Figure **63** displays the ^{235}U concentration for the (a) single block, (b) super cell and (c) core model.

Table 15. Refined burn steps implemented in KENO-VI for uncertainty analysis

Added time (d)	*Cumulated time (d)*	*Cumulated burn up (MWd/MTHM)*	*Added time (d)*	*Cumulated time (d)*	*Cumulated burn up (MWd/MTHM)*
1.52	1.52	100	30.93	602.85	39728
0.76	2.28	150	30.93	633.78	41766
2.28	4.56	301	30.93	664.71	43804
10.62	15.18	1000	30.93	695.64	45843
30.93	46.11	3039	30.93	726.57	47881
30.93	77.04	5077	30.93	757.5	49919
30.93	107.97	7115	30.93	788.43	51958
30.93	138.9	9154	30.93	819.36	53996
30.93	169.83	11192	30.93	850.29	56034
30.93	200.76	13230	30.93	881.22	58072
30.93	231.69	15268	30.93	912.15	60111

Table 15 (continued)

30.93	262.62	17307	30.93	943.08	62149
30.93	293.55	19345	30.93	974.01	64187
30.93	324.48	21383	30.93	1004.94	66226
30.93	355.41	23422	30.93	1035.87	68264
30.93	386.34	25460	30.93	1066.8	70302
30.93	417.27	27498	30.93	1097.73	72340
30.93	448.2	29536	30.93	1128.66	74379
30.93	479.13	31575	30.93	1159.59	76417
30.93	510.06	33613	30.93	1190.52	78455
30.93	540.99	35651	30.93	1221.45	80494
30.93	571.92	37690			

6.5 Core Power Density

SCALE 6.2 requires a user-input power density (in Giga-Watt per metric ton of heavy metal) to determine the flux level at each burnup step during the depletion calculations. This section derives the power density from the MHTGR-350 core specifications.

The power density is given by the initial mass of heavy metal normalized to the thermal power generated in the core. The energy emitted per fission is assumed to be equal to 200 MeV ($3.20405 \ .10^{-11}$ J) regardless of the fissionable atom that reacts. The data required to calculate the power density of the MHTGR-350 core are given in Table 16.

The derivation neglects the energy deposited through decay heat and gamma ray attenuation; therefore only fission processes are assumed to generate power in the core. Referring to Table 16, the total volume of fuel UCO in the core is:

$$V_F = \frac{4}{3}\pi r_T^3 N_T N_c \frac{H_{core}}{H_b} N_{b,rad} = 5.75 \ .10^5 \ cm^3 \qquad \text{Equation 6-1}$$

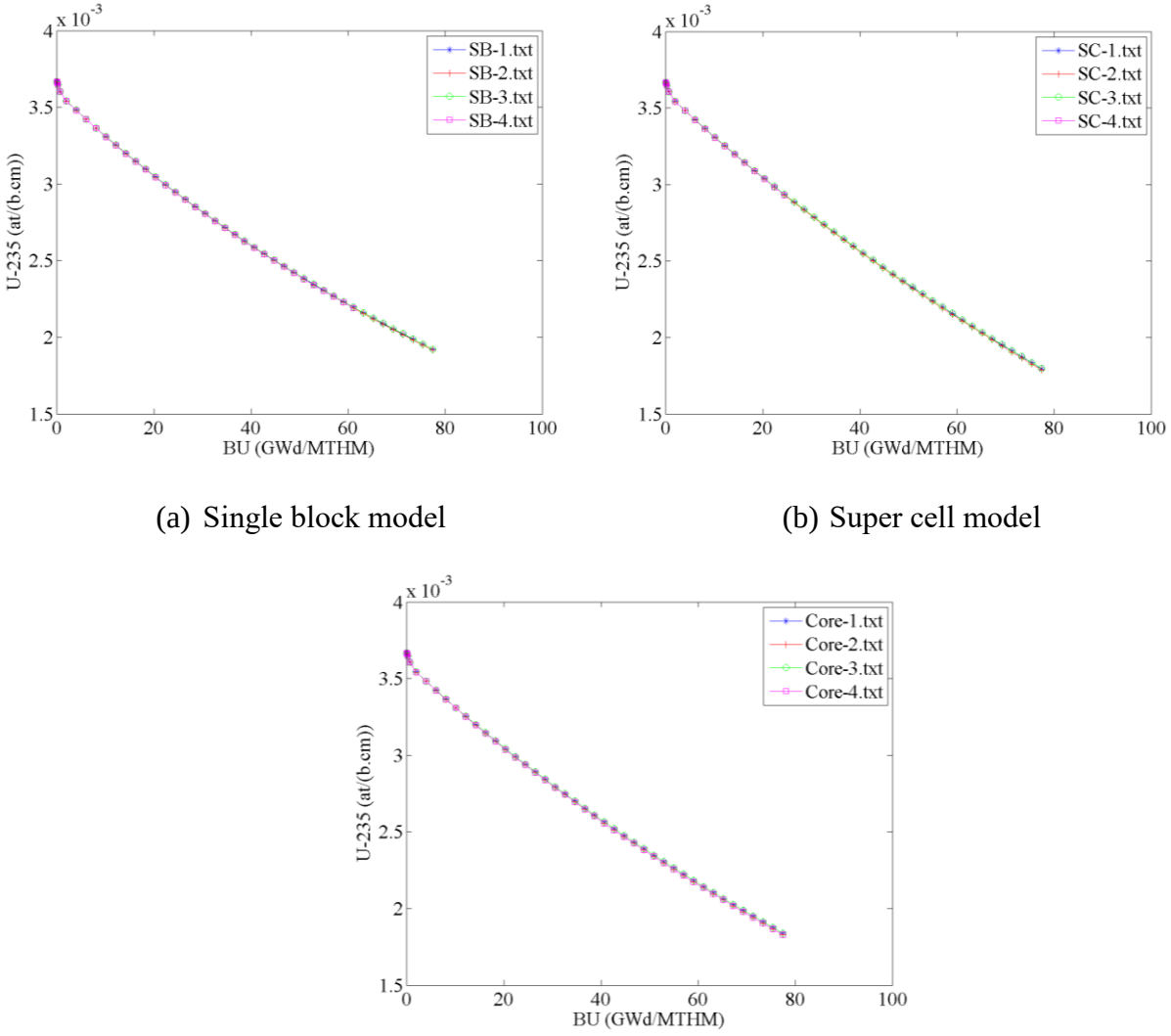

(a) Single block model

(b) Super cell model

(c) Core model

Figure 63. ^{235}U concentration in the (a) single block, (b) super cell and (c) core models considering the depletion options available in KENO-VI; section 2.7 defines the depletion options 1 through 4

The total mass of uranium in the core is:

$$m_U = \frac{1}{N_A}(M_{^{235}U} n_{^{235}U} + M_{^{238}U} n_{^{238}U}) V_F = 5.312 \ .10^6 \ g \qquad \text{Equation 6-2}$$

M_{235U} and M_{238U} are the molar masses of ^{235}U and ^{238}U respectively ($g.mol^{-1}$);

N_A is Avogadro's constant. The total power density is:

$$P_d = \frac{P_t}{m_U} = 65.9 \ \ MW_t.tHM^{-1}$$ Equation 6-3

Table 16. MHTGR-350 fuel and core properties

Parameter	*Units*	*Value*	*Variable*
Fuel kernel radius	cm	0.02125	r_T
TP* packing	-	0.35	N_T
TP per compact	-	6416	
Number of compacts per block	-	210	N_c
Core height	cm	793	H_{core}
Block height	cm	4.928	H_b
^{235}U number density	at.b^{-1}.cm^{-1}	3.67E-03	n_{235U}
^{238}U number density	at.b^{-1}.cm^{-1}	1.97E-02	n_{238U}
Number of blocks (radially)	-	66	$N_{b,rad}$
^{235}U enrichment	% wt	0.155	
^{238}U enrichment	% wt	0.845	
Core power	MWt	350	P_t

*TP = TRISO Particle

6.6 Comparison of KENO-VI and Serpent-2.1.27 calculations with the ENDF/B-VII.1 library

The section predicts the evolution of the ^{10}B number density, ^{239}Pu number density and k_{inf} with Serpent 2.1.27 and KENO-VI. The ENDF/B-VII.1 library provides the cross section data in both codes and the total number of neutrons generated is increased up to 1,200,000, while the number of skipped generations remains fixed at 20. The thermal scattering libraries at 1,200 K in the Serpent 2.1.27 do not function, so the use of the thermal scattering libraries in both KENO-VI and Serpent was turned off in Section 6.6 to obtain models as equivalent as possible between the two codes. The thermal scattering is turned back on in Section 0 to perform the uncertainty analysis. The differences in the infinite multiplication factor are firstly evaluated with homogenized BP model, then the differences between the codes and the models in the number

densities listed above are cross-compared with fully heterogeneous BP model. KENO-VI executes both CE and MG simulations to compare to Serpent CE and the error induced by the MG mode.

6.6.1 Compact Model

This section involves comparisons of a 4.928 cm high compact (Figure 35) filled with 4,616 TRISO particles and surrounded by reflective boundary conditions. This side exercise is simulated to verify that the number of particles, the volumes, and the masses between KENO-VI and Serpent are matching, since compacts represents unit cells over the fuel block, super cell and the core. The Doppler Broadening Rejection Correction (DBRC) is turned off in Serpent as KENO-VI 252MG does not support such feature in the SCALE 6.2.0 version. The graphite around the rod does not contain traces of boron. Table 17 (Serpent), Table 18 and Table 19 (KENO-CE) collate the volumes and masses of each model. Table 20 provides the mass verification in KENO-252MG. The two codes report in the output masses and volumes based on built-in estimators. The data calculated by the estimators are reported in the tables and compared to the theoretical values.

Table 21 compares the infinite multiplication factor of KENO-CE, KENO-252MG and to Serpent.

Table 17. Volume comparison in a compact cell in Serpent

Material	*Theoretical volume (cm^3)*	*volume estimator (cm^3)*	*Relative difference (%)*
UCO	0.25788	0.25733	-0.21
Porous C	0.56228	0.56176	0.09
PyC*	0.89294	0.89204	-0.10
SiC	0.38660	0.38622	-0.10
Matrix	3.89956	3.90163	0.05
Graph. block	8.83496	8.83583	0.01
Helium-4	0.24335	0.24342	0.03

*Includes the two layers of PyC incorporated in the TP

Table 18. Volume comparison in a compact cell in KENO-CE

Material	*Theoretical volume (cm^3)*	*volume estimator (cm^3)*	*Uncertainty (cm^3)*	*Falls within uncertainty?*
UCO	0.25788	0.25776	0.00299	Yes
Porous C	0.56228	0.56374	0.00474	Yes
PyC 1	0.35697	0.35462	0.00367	Yes
SiC	0.38660	0.38405	0.00406	Yes
PyC 2	0.53596	0.53254	0.00440	Yes
Matrix	3.89956	3.90237	0.00936	Yes
Graph. block	8.83496	8.82004	0.01314	No
Helium-4	0.24335	0.24602	0.00325	Yes

The multiplication factor between KENO-CE and Serpent shows a good agreement of 57 $\times 10^{-5}$ between the two codes. KENO-252 MG shows a discrepancy of 1,262 $\times 10^{-5}$. The large difference between the multi-group and continuous energy calculations can be explained by the explicit modeling of the TRISO particles within the CE codes as opposed to the implicit modeling imposed in MG to compute the self-shielding. The thermal scattering kernel $S(\alpha,\beta)$ induces a difference of -212 $\times 10^{-5}$ as compared to the free-gas model in KENO-252MG.

6.6.2 Criticality Calculations of Homogeneous Burnable Poison Model

The heterogeneous modeling of the BP particles becomes challenging for two-dimensional reactor physics codes. This section evaluates the discrepancies induced by the homogenization of the BP yet keeping the fuel in a heterogeneous fashion. It stands as an intermediary step to verify the number densities, geometry etc. have been correctly implemented in Serpent and KENO-VI.

Table 22 (fuel block), Table 23 (super cell) and Table 24 (core) gives the criticality results obtained with KENO-CE, KENO-252MG and Serpent-CE. Identically to section 6.6.1, the free-gas theory models the thermal scattering in both KENO and Serpent, and the DBRC option was disabled.

Table 19. Mass comparison in a compact cell in KENO-CE

Material	*Theoretical mass (g)*	*Mass estimator (g)*	*Uncertainty (g)*	*Falls within uncertainty?*
UCO	2.682E+00	2.681E+00	3.116E-02	Yes
Porous C	5.904E-01	5.914E-01	4.975E-03	Yes
PyC 1	6.782E-01	6.732E-01	6.980E-03	Yes
SiC	1.233E-00	1.224E+00	1.294E-02	Yes
PyC 2	1.018E+00	1.011E+00	8.367E-03	Yes
Matrix	5.654E+00	5.653E+00	1.357E-02	Yes
Graph. block	1.634E+01	1.630E+01	2.429E-02	No
Helium-4	3.978E-05	4.022E-05	5.320E-7	Yes

Table 20. Mass comparison in a compact cell in KENO-MG

Material	*Theoretical mass (g)*	*mass estimator (g)*
Fuel Mixture*	1.1856E+01	1.1865E+01
Block Graphite	1.6344E+01	1.6344E+01
Helium-4	3.9789E-05	3.9796E-05

*KENO-252MG homogenizes the TP with fuel matrix to produce a fuel mixture

Table 21. Criticality calculations on a compact model in KENO-CE, KENO-252MG and Serpent

Model	k_{inf} *best estimate*	*Standard Deviation* $(\times 10^{-5})$	*Absolute difference* $(\times 10^{-5})$
Serpent-CE	1.25772	22	Reference
KENO-CE	1.25829	64	57
KENO-252MG	1.24567	61	1262

Table 22. Single block's eigenvalue with homogeneous BPs in KENO-CE, KENO-252MG and Serpent-CE

Model	k_{inf} *best estimate*	*Standard deviation* $(\times 10^{-5})$	*Absolute difference* $(\times 10^{-5})$
Serpent-CE	1.04874	7	Reference
KENO-CE	1.04884	74	10
KENO-252MG	1.04496	53	-378

The CE results are in better agreement than the MG results, as expected. The multi-group calculations tend to underestimate the multiplication factor. The Serpent and KENO-CE simulations agree within two standard deviations.

6.6.3 Criticality Calculations of Heterogeneous Burnable Poison Model

This section establishes the comparison of the single block, super cell and core model with explicit modeling of the BP particles. Criticality calculations are carried out for each model for

KENO-CE, KENO-252MG and Serpent. The ^{10}B nuclide inventories are compared afterwards, to evaluate the agreement between the two codes. The differences observed with a homogenized BP model are assessed as well. Table 25 (single block), Table 26 (super cell) and Table 27 (core) summarize the infinite multiplication factor obtained in KENO-CE, KENO-252MG and Serpent.

Table 23. Super cell's eigenvalue with homogeneous BPs in KENO-CE, KENO-252MG and Serpent-CE

Model	k_{inf} *best estimate*	*Standard deviation* $(\times 10^{-5})$	*Absolute difference* $(\times 10^{-5})$
Serpent-CE	1.08670	7	Reference
KENO-CE	1.08813	70	143
KENO-252MG	1.08362	58	-308

Table 24. Core's eigenvalue with homogeneous BPs in KENO-CE, KENO-252MG and Serpent-CE

Model	k_{inf} *best estimate*	*Standard deviation* $(\times 10^{-5})$	*Absolute difference* $(\times 10^{-5})$
Serpent-CE	1.03260	81	Reference
KENO-CE	1.03123	71	137
KENO-252MG	1.02781	70	-479

The results between the CE codes show a good agreement, within one or two standard deviations. The MG energy mode shows again an under-estimation of ~400 $\times 10^{-5}$ compared to KENO-

CE. The agreement between the models ensures that the modeling of the geometry and material composition is correct. The comparison of Table 25, Table 26 and Table 27 to Table 22, Table 23 and Table 24 demonstrates that homogenizing the burnable poisons induces an average difference of -1,732 $\times 10^{-5}$ in the single block, -3,447 $\times 10^{-5}$ in the super cell and -3,482 $\times 10^{-5}$ in the core. Serpent, KENO-CE and KENO-252MG agree very well on effect of the homogenization (12×10^{-5}, 38×10^{-5} and 94×10^{-5} standard deviation for respectively the single block, the super cell and the core).

Table 25. Single block's eigenvalue with heterogeneous BPs in KENO-CE, KENO-252MG and Serpent-CE

Model	k_{inf} *best estimate*	*Standard deviation* $(\times 10^{-5})$	*Absolute difference* $(\times 10^{-5})$
Serpent-CE	1.06605	7	Reference
KENO-CE	1.06632	73	27
KENO-252MG	1.06213	62	-392

Table 26. Super cell's eigenvalue with heterogeneous BPs in KENO-CE, KENO-252MG and Serpent-CE

Model	k_{inf} *best estimate*	*Standard deviation* $(\times 10^{-5})$	*Absolute difference* $(\times 10^{-5})$
Serpent-CE	1.12129*	9	Reference
KENO-CE	1.12208*	22	79
KENO-252MG	1.11849*	65	-280

*The BP traces in the graphite have been removed

Table 27. Core's eigenvalue with heterogeneous BPs in KENO-CE, KENO-252MG and Serpent-CE

Model	k_{inf} *best estimate*	*Standard deviation* ($\times 10^{-5}$)	*Absolute difference* ($\times 10^{-5}$)
Serpent-CE	1.06641*	22	Reference
KENO-CE	1.06732*	70	91
KENO-252MG	1.06237*	67	404

*The BP traces in the graphite have been removed

The homogenization of the BPs enhances spatial self-shielding effect in the vicinity of BP rods, which increases the capture rate in the BP region and decreases the multiplication factor. The ^{10}B isotope is a burnable absorber at thermal energies (see Figure 8). The spectrum in the fuel block is harder than the super cell and core; hence, the ^{10}B absorbs less neutrons in the fuel block than other models. Thus, the multiplication factor decreases less severely in the single block model. Figure 64 provides a comparison of the ^{10}B burn out in KENO-CE and KENO-252MG in case of heterogeneous and homogeneous modeling in the single block. The relative difference between the homogeneous BP and heterogeneous BP is given in Figure 65 for both KENO-CE and KENO-252MG. Note that in the post-processing of the data, the boron number density in the homogeneous case is multiplied by the volume ratio r = 0.038883841 to convert the number density into heterogeneous-equivalent value.

As expected, the ^{10}B depletion occurs faster in the homogenized case. Figure 66 sketches the absolute difference in the multiplication factor. The spatial self-shielding effect is predominant until 40 GWd/MTHM. As the BPs burn out, the spatial self-shielding effect fades away but the reactor breeds ^{239}Pu (see Figure 67), which can explain the reversed trend of the multiplication factor at the EOC.

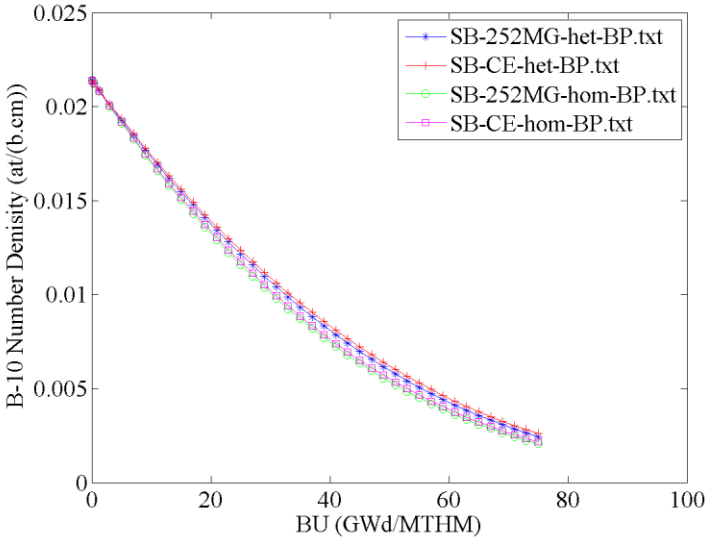

Figure 64. Comparison of the ^{10}B depletion with KENO-CE and KENO-252MG as the function of the BP topology (homogeneous versus heterogeneous)

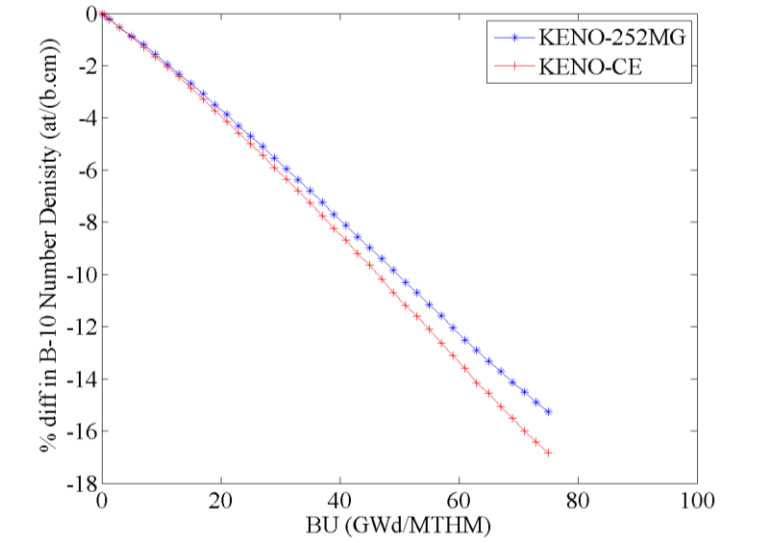

Figure 65. Relative difference between homogeneous and heterogeneous ^{10}B number density in KENO-CE and KENO-252MG

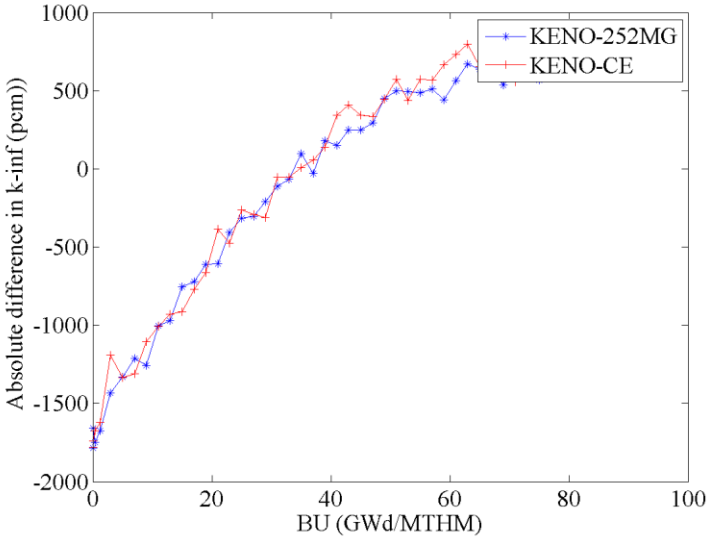

Figure 66. Absolute difference in the multiplication factor induced by homogenization of the BPs

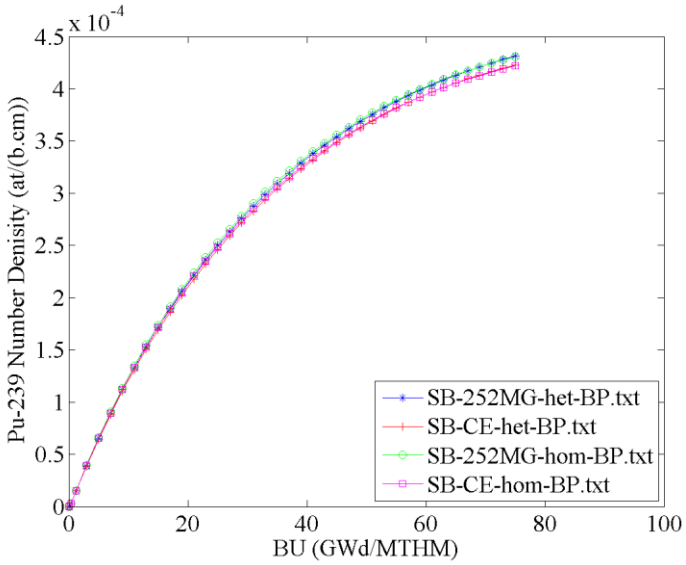

Figure 67. Comparison of the ^{239}Pu build-up with KENO-CE and KENO-252MG as the function of the BP topology

6.7 SAMPLER/KENO-VI Code malfunction

SAMPLER/KENO-VI perturbs 150 samples in which decay constants, cross sections and fission yields are set as variables (resulting in three batches of 150 samples). Another simulation perturbs the three variables together. Figure 68 illustrates the spread of the k_{inf}'s best estimates along with the standard deviation. A [-10.1%; 12.7%] confidence interval complements the standard deviation relative to the predictions. In SAMPLER/KENO-VI, the standard deviation drops after the initial fresh fuel step from 0.55 % Δk/k to around 0.16 % Δk/k. The perturbation of the fission yields, the cross sections and the three variables combined leads to about the same flat profile. The decay perturbation results in no propagation of uncertainty. A few comments:

- Regarding the decay constant, the flat negligible uncertainty profile over the cycle may translate into a negligible influence of the decay constants on the k_{inf} uncertainty, a code malfunction or both.
- The early stages of the depletion prove the fission yields contribute to the multiplication factor uncertainty so one would expect a raise of the output uncertainty in response to the actinide build-up.
- The behavior of the cross section uncertainty challenges the results' logic because an increment of 0.100 GWd/MTHM induces a drop from 0.55 to 0.16 % Δk/k.

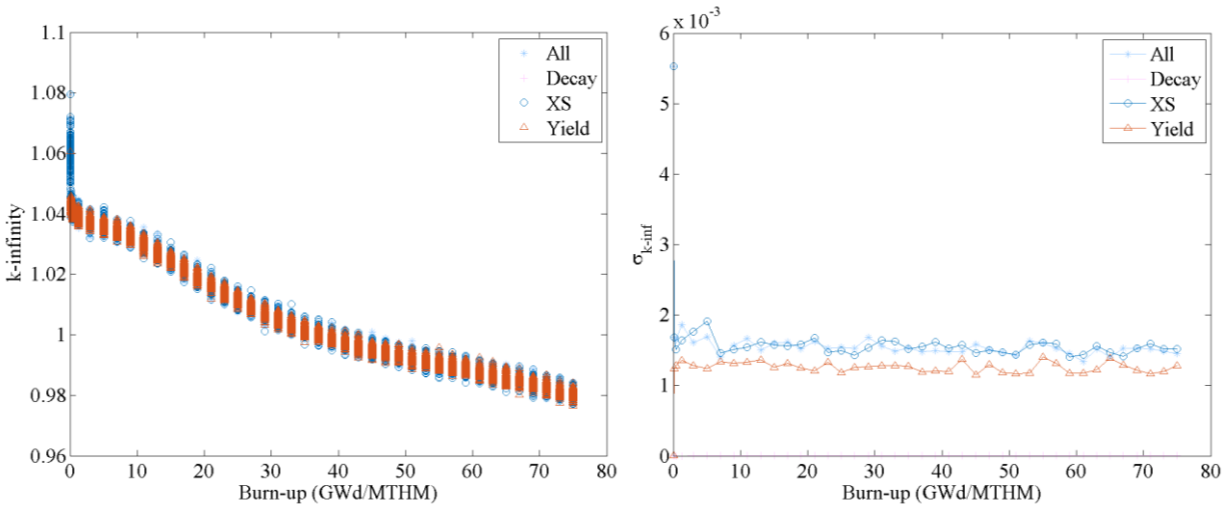

Figure 68. k_{inf} spread (left) and associated standard deviation (right) caused by perturbation of (a) decay constants, (b) cross sections, (c) fission yields and (d) the three combined in SAMPLER/KENO-VI over a depletion sequence for a MHTGR-350 fuel block

As a verification process, a compact cell is modeled with SAMPLER/ T-NEWT and SAMPLER/KENO-VI. An artificial two-dimensional model is implemented in KENO-VI, in which the compact's axial boundary conditions are reflective. T-NEWT imposes a 2-D modeling so the burnable poisons must be homogenized in T-NEWT and KENO-VI for comparison purposes. Thus, the KENO-VI model replicates exactly the NEWT features. The cross sections perturbed by SAMPLER yield to the results presented in

Figure **69**. The first burn step substantiates the results between SAMPLER/KENO-VI (0.730 %Δk/k) and SAMPLER/ T-NEWT (0.735 %Δk/k) but the remaining burnup steps evidence discrepancies between the transport code (0.680 %Δk/k) versus the Monte Carlo code (0.180 %Δk/k).

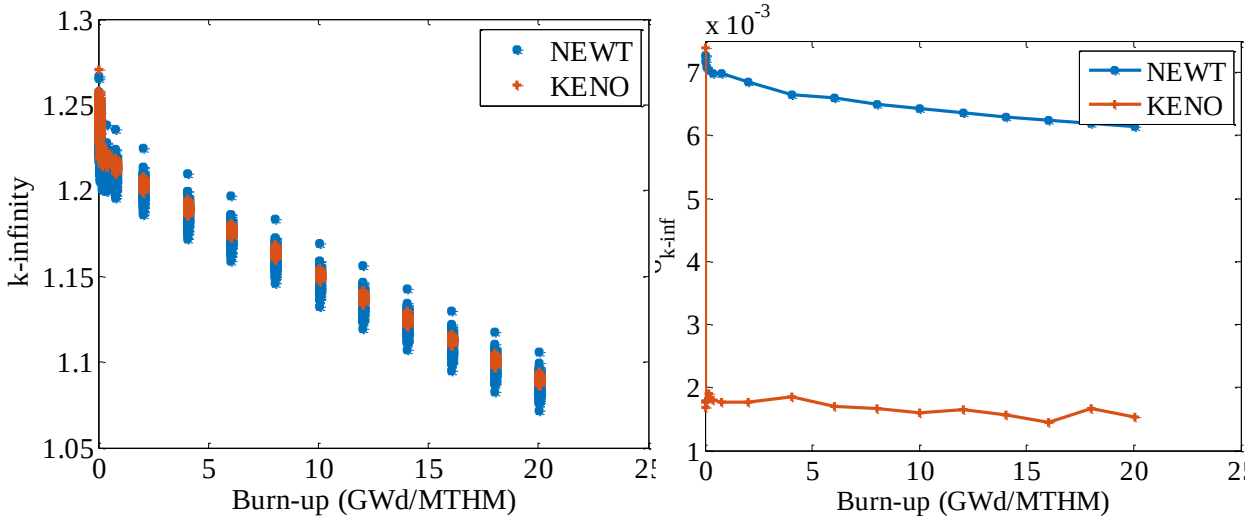

Figure 69. k_{inf} spread (left) and associated standard deviation (right) caused by perturbation of cross sections in SAMPLER/ T-NEWT compared to SAMPLER/KENO-VI over a depletion sequence for a MHTGR-350 compact cell

Another four-step methodology confirms the discrepancies in KENO-VI:

- Replicating the KENO-VI burnup simulations (without SAMPLER);
- Collecting the nuclide inventory at an arbitrary burnup (12.5 GWd/MTHM);
- Implementing the nuclide inventory in a SAMPLER/ T-NEWT and in a SAMPLER/KENO-VI criticality input with cross section perturbation;
- Evaluating the output uncertainty on the infinite multiplication factor (Table 28).

Table 28. k_{inf} relative uncertainty caused by perturbation of cross sections in SAMPLER/NEWT compared to SAMPLER/KENO-VI over a depletion sequence (12.5 GWd/MTHM) and criticality sequence for a MHTGR-350 compact cell

Sequence	*Code*	*Uncertainty k_{inf} (%Δk/k)*
Criticality	T-NEWT	0.599
Criticality	KENO-VI	0.596
Depletion	T-NEWT	0.629
Depletion	KENO-VI	0.160

SAMPLER/ T-NEWT estimates the output uncertainties in the next sections of CHAPTER 6. T-NEWT cannot implement the core and super cell designed in Figure 59 and Figure 60 for performance reasons. CHAPTER 5 demonstrated that the spectrum in the super cells denoted "*l*" and "*m*" resembled the core's flux. Figure 70 illustrates the homogenized region around the central block simplified into one single region. Figure 71 compares the spectrum relative to cells *m* (fuel blocks plus one graphite block in the homogenized region), *l* (four fuel blocks and two graphite blocks in the homogenized region) from T-NEWT to the core spectrum from Serpent. The cell *m* shows the closest agreement to the core spectrum and is carried over the next sections as super cell model.

6.8 Uncertainty Quantification of the nuclide inventory

The SAMPLER/T-NEWT sequence perturbs 150 single block cells and 150 super cells with respect to cross sections, fission yields and both. The relative confidence interval of the uncertainties lies within [-10.1 %; 12.7 %]. The cross sections and fission yields are perturbed independently to evaluate the effect of each perturbation on the isotope concentrations over the cycle. The third case estimates the global uncertainty on the number densities. The decay constants are not perturbed because SAMPLER/TRITON does not handle this capability in SCALE 6.2.0.

On a general basis, 224 isotopes originating from the SCALE 6.2 TRITON depletion module are investigated to ensure no major contributor to uncertainties is ruled out of the study. All those isotopes are produced in the fuel by the fission, decay or transmutation process. The ^{10}B in the burnable poison particles represents the 225th entry in the list.

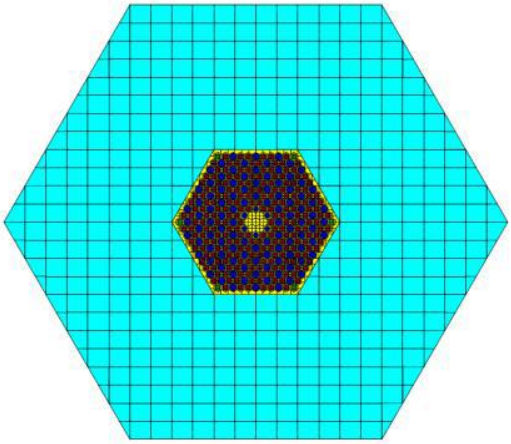

Figure 70. Radial representation of a one-region super cell

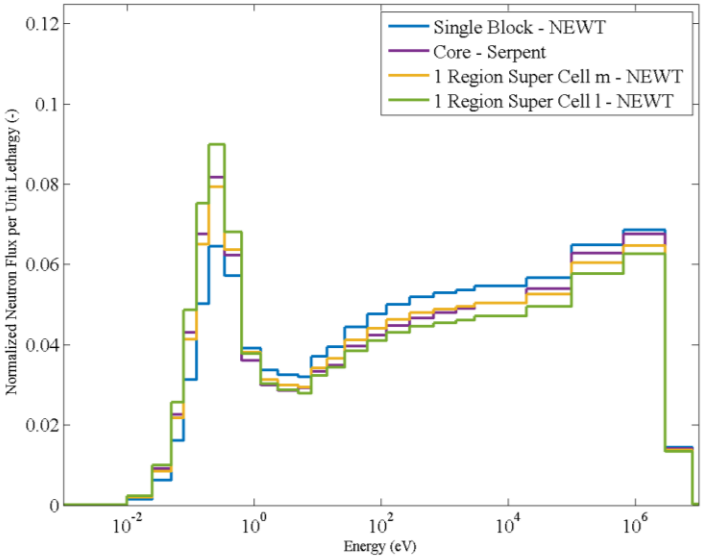

Figure 71. Neutron spectrum in one-region super cells compared to the core's spectrum

The number of isotopes combined with the number of steps, for two different models (SBor SC) and three perturbed variables requires to quantify around 55,000 data points. The results take the form of figures for major isotopes described in section 2.2.2. More integral parameters quantify the uncertainty associated to the other isotopes. The relative standard deviation for each isotope is normalized with respect to the nominal (not the mean value) isotope's concentration at the burnup step considered. The relative deviations obtained over the cycle are integrated with respect to the burnup to derive a cycle-averaged uncertainty. This uncertainty is complimented with a BOC and EOC uncertainty. The BOC and EOC uncertainties are respectively averaged over the first three and last three burnup steps. This process is repeated for the three types of perturbations. As a reminder, Table 15 specified the time length of the burnup steps. Finally, the cycle-averaged standard deviation for each isotope is compared between the single block and the super cell models. The one standard deviation for the following isotopes is reported for each time step: $^{102, 104, 105, 106, 107, 108, 110}$Pd; $^{107, 109, 110m, 111}$Ag, ^{131}I, ^{135}Xe, ^{137}Cs, ^{149}Sm, ^{151}Sm (referred to as "poisons" on the figures);$^{151, 152, 153, 154, 155, 156, 157}$Eu;$^{235, 238}$U;$^{238, 239, 240, 241, 242}$Pu.

The multiplicative perturbation factors are sampled using the covariance libraries relative to the independent yield uncertainties. A so-called isotope's independent yield is defined as the proportion of an isotope produced after a fission event but before this isotope experiences delayed neutron fission, beta or radioactive decay. The cumulative yield is defined as the production of an isotope by the combination of fission event plus a succession of decay events. The combination of independent yields and decay constants must agree with the cumulative yields. The yield uncertainties contained in ENDF/B-VII.1 library do not include correlations between the fission products. The yield uncertainties are only constrained to two conditions:

- The sum of all the yields must be equal to two;
- The uncertainties in the independent yields must agree with the uncertainties in the cumulative yields.

Correlations between the yields only exist for ^{235}U, which means that the uncertainty data on fission events originating from plutonium isotopes or ^{238}U are uncorrelated.

6.8.1 Multiplication Factor

Figure 72 sketches the scatter in the k-infinity's best estimate of the single block model. Figure 73 represents the associated relative standard deviation. It appears the perturbation of the

cross sections dominate the uncertainty on the multiplication factor. The fission yields bring a negligible contribution. The fission yields and the cross sections contribute independently to the k_{inf} uncertainty. The uncertainty on k_{inf} in the super cell was not estimated because the parasitic homogenized region would contribute largely to the results. Although, interested readers can evaluate the central block's contribution by defining (artificially) a collapse block within NEWT in 252 group structure, and collect the infinite multiplication factor provided in the output's collapsed block. This method does not apply in KENO-VI.

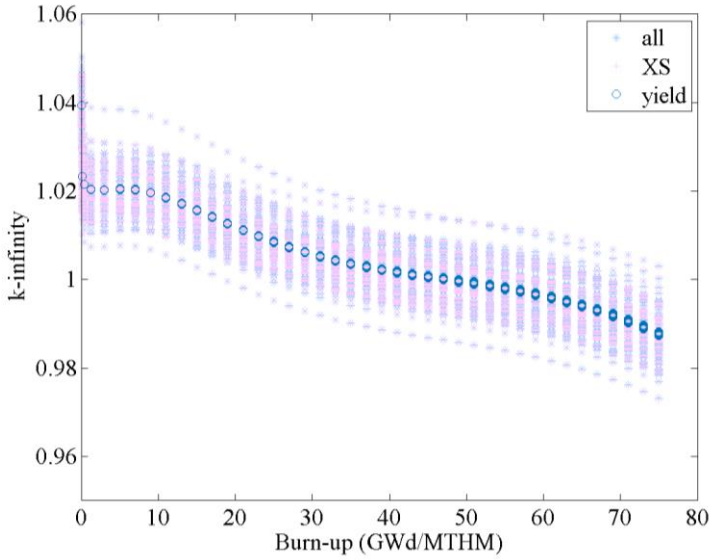

Figure 72. k_{inf} scatter of the single block model for different perturbations

6.8.2 Nuclide Inventory

Table 29 maps the figure numbers to the corresponding isotope/perturbation. The plots compare qualitatively the uncertainties in the single block versus the super cell. The trends are identical in shape. The uncertainties relative to the fission products tend to reach a maximum at the BOC and a steady state after about 20 GWd/MTHM. Some isotopes experience a local minimum between the xenon equilibrium and 20 GWd/MTHM (^{102}Pd, ^{109,110m,111}Ag, ^{151}Sm). The uncertainties of the depleted materials (uranium and boron) and the actinides monotonically increase over the cycle. The fission yield contribution governs in general the fission products' uncertainties although the cross sections may regulate the total uncertainty (for the ^{135}Xe and ^{149}Sm). In some rare occasions, both mechanisms contribute equally (^{151}Sm, ^{114}Sn) while the cross section contribution

dominates the actinides and BP uncertainties. The uncertainty of the uranium isotopes doubles from the single block to the super cell, which means that the harder spectrum (single block) yields to higher $^{238, 235}$U uncertainties. The combined participation of cross sections and fission yields is estimated only for the fission products because the fission yields do not participate to the actinides' uncertainty (the sole cross section component would have sufficed). It was verified that an uncertainty inferior to 0.01 % for the uranium and plutonium isotopes if the fission yields are perturbed independently. The effect of the fission yield uncertainties on the actinides was predictable because the fissionable elements never yield to actinide elements. The marginal uncertainty induced by the fission yield perturbation on the actinide concentration is an implicit effect. The perturbation of the yields induces a perturbation of the fission product inventory, which modifies the neutron spectrum. The perturbed neutron spectrum modifies the fission, capture and breeding regime of the system, which explains the negligible uncertainties found on the actinide concentrations.

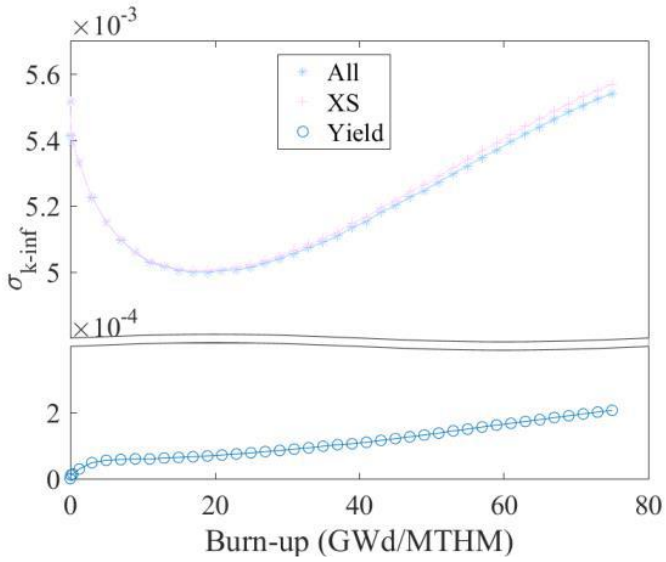

Figure 73. k_{inf} uncertainty of the single block model for different perturbations

Table 30 extracts the relative uncertainty attributed to 213 nuclides (no uncertainty was allocated to ^{96}Ru, ^{124}Xe, ^{175,176}Lu, ^{181}Ta, ^{182,183,184,186}W, ^{185,187}Re, ^{197}Au by SAMPLER). The table confirms that the fission yields contribute almost exclusively to the fission product uncertainty and the cross sections influence entirely the actinides. The integrated relative standard deviation

with respect to burnup is normalized to obtain an average relative standard deviation over the cycle. Bold captions highlight the dominant effect (fission yield or cross section) to the total uncertainty in Table 30. The BOC and EOC mean σ, calculated from the first three and last three burnup steps, accompany the cycle's mean σ to indicate the evolution of the uncertainty with burnup. Table 31 identifies the differences in the uncertainties produced by the SB and the SC models. No trend appears clearly in the profiles: the super cell (softer spectrum) may over- or under-evaluate the uncertainty as compared to the single block, depending on the isotope considered. The average deviation between the two models is 12 % (the deviations from the two models is measured in absolute value).

Table 29. List of figures leading to isotope nominal concentration over the cycle and the isotope relative uncertainties

Atom	*Type of perturbation*	*Relative uncertainty (1σ)*	
		Fuel block	*Super cell*
Pd	Cross section + Yield	Figure 74	Figure 75
	Cross section	Figure 86	Figure 87
	Yield	Figure 94	Figure 95
Ag	Cross section + Yield	Figure 76	Figure 77
	Cross section	Error! Reference source not found.	Figure 89
	Yield	Figure 96	Figure 97
Poisons	Cross section + Yield	Figure 78	Figure 79
	Cross section	Figure 90	Figure 91
	Yield	Figure 98	Figure 99
Eu	Cross section + Yield	Figure 80	Figure 81
	Cross section	Figure 92	Figure 93
	Yield	Figure 100	Figure 101
U	Cross section + Yield	Figure 82	Figure 83
Pu	Cross section + Yield	Figure 84	Figure 85
^{10}B	Cross section + Yield	Figure 102	-

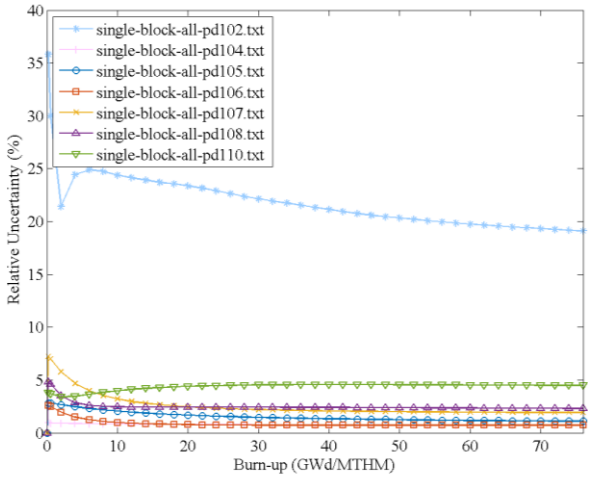

Figure 74. Pd relative uncertainty – XS and yield perturbed in the single block

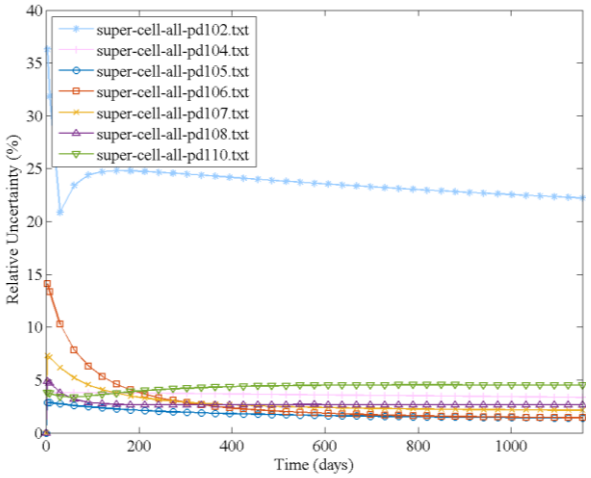

Figure 75. Pd relative uncertainty – XS and yield perturbed in the super cell

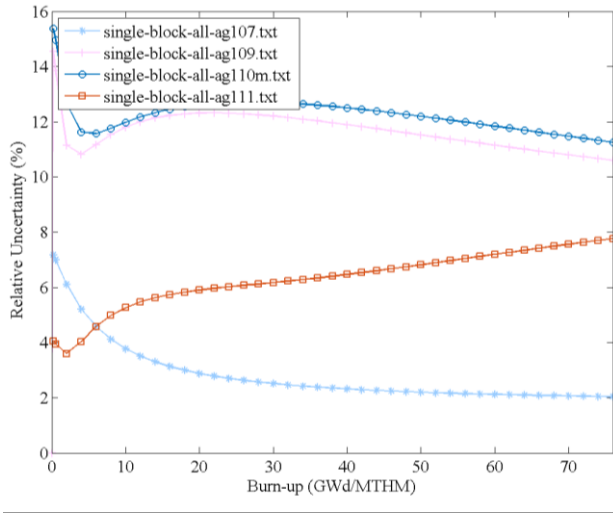

Figure 76. Ag relative uncertainty – XS and yield perturbed in the single block

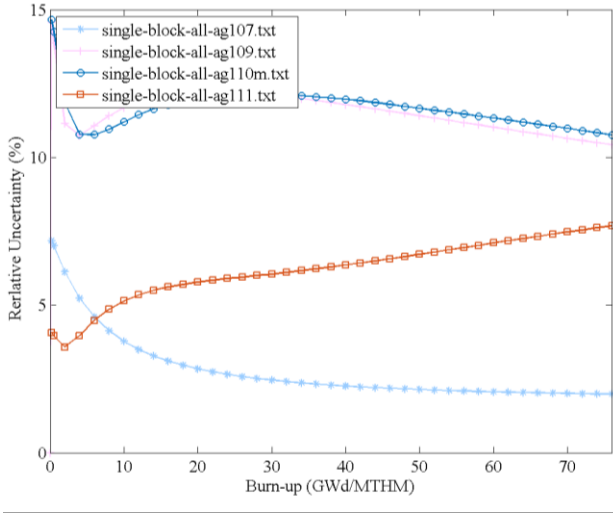

Figure 77. Ag relative uncertainty – XS and yield perturbed in the super cell

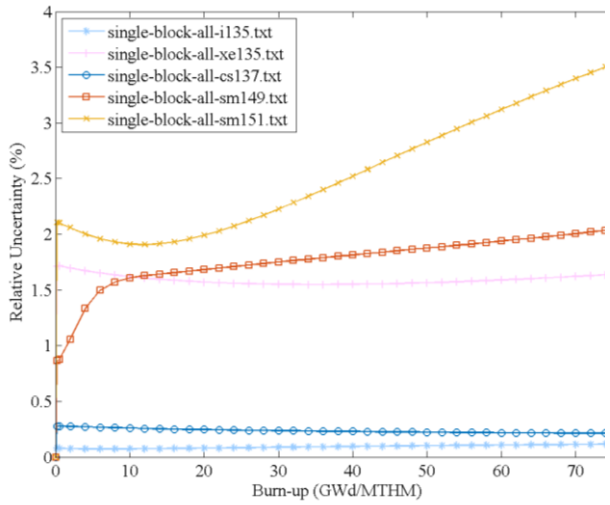

Figure 78. Poisons relative uncertainty – XS and yield perturbed in the single block

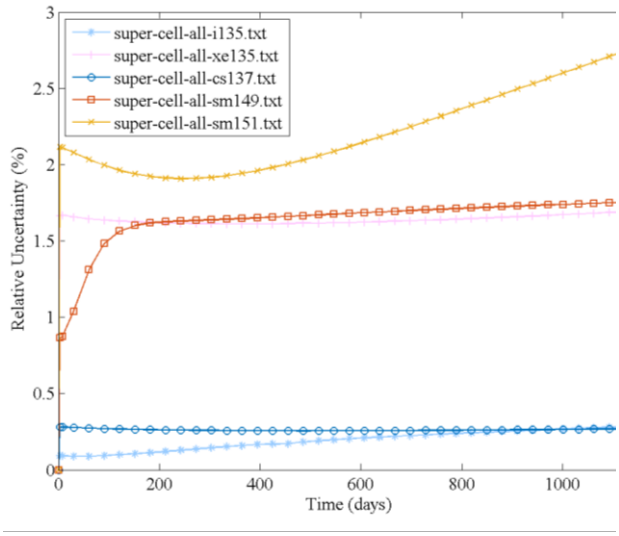

Figure 79. Poisons relative uncertainty – XS and yield perturbed in the super cell

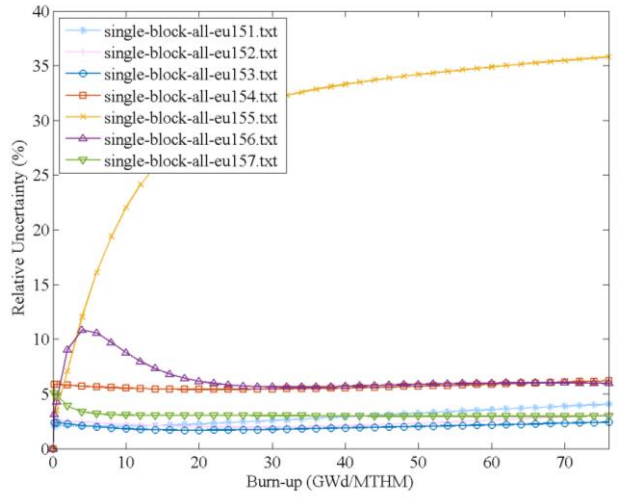

Figure 80. Eu relative uncertainty – XS and yield perturbed in the single block

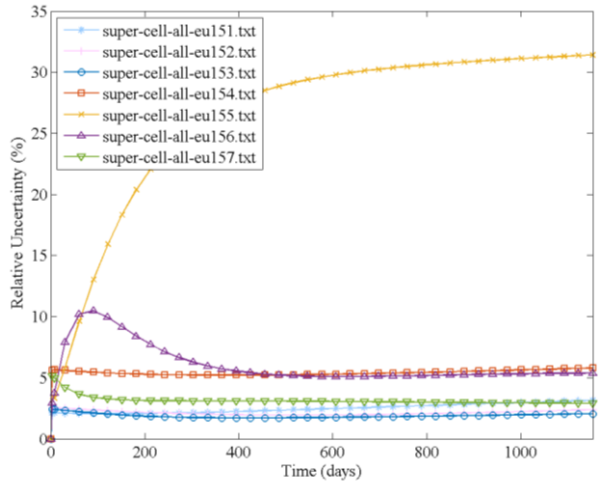

Figure 81. Eu relative uncertainty – XS and yield perturbed in the super cell

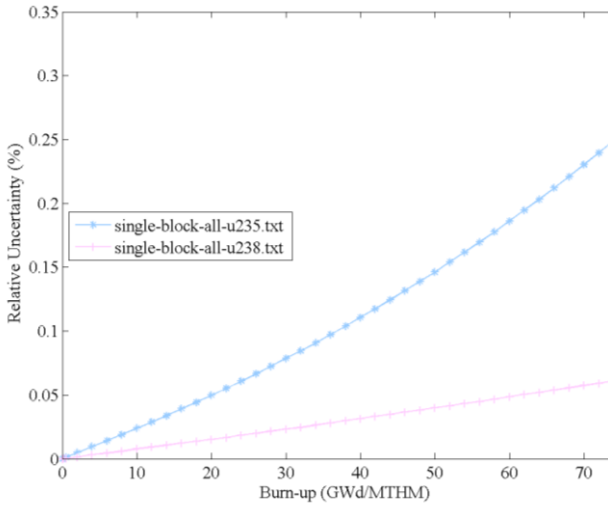

Figure 82. U relative uncertainty – XS and yield perturbed in the single block

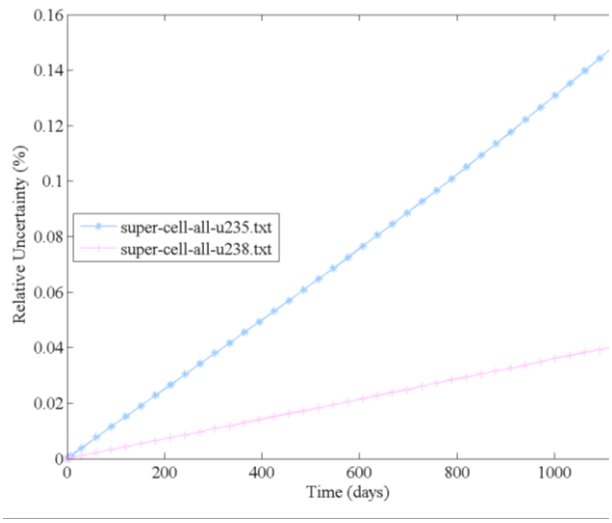

Figure 83. U relative uncertainty – XS and yield perturbed in the super cell

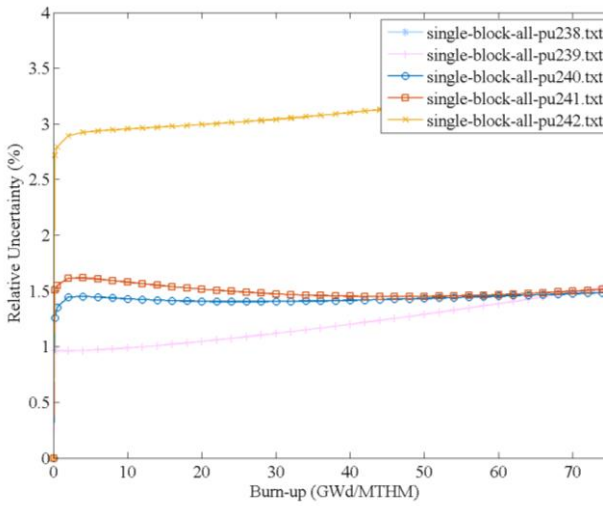

Figure 84. Pu relative uncertainty – XS and yield perturbed in the single block

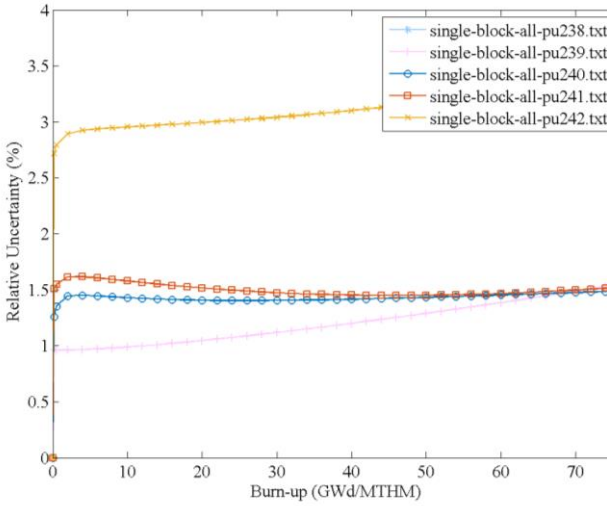

Figure 85. Pu relative uncertainty – XS and yield perturbed in the super cell

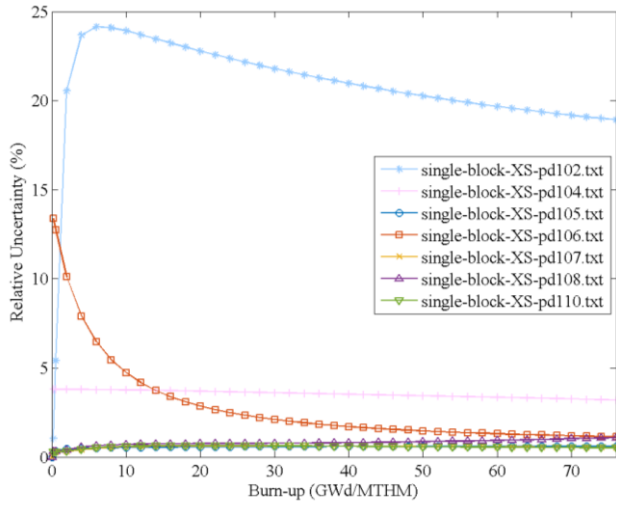

Figure 86. Pd relative uncertainty – XS perturbed in the single block

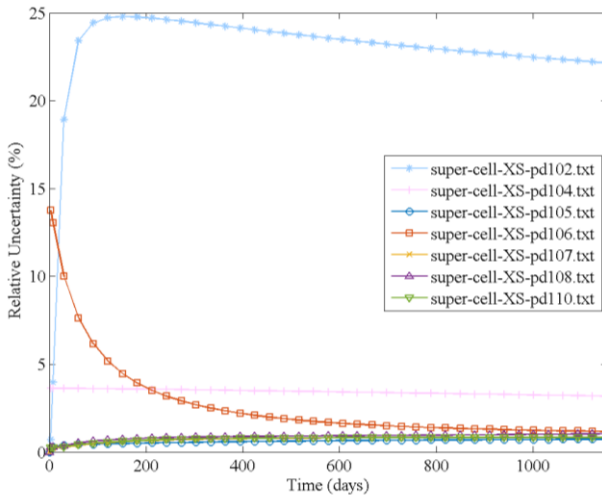

Figure 87. Pd relative uncertainty – XS perturbed in the super cell

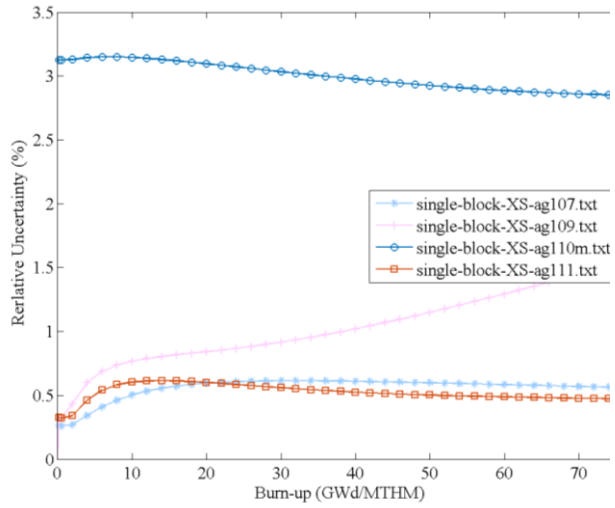

Figure 88. Ag relative uncertainty – XS perturbed in the single block

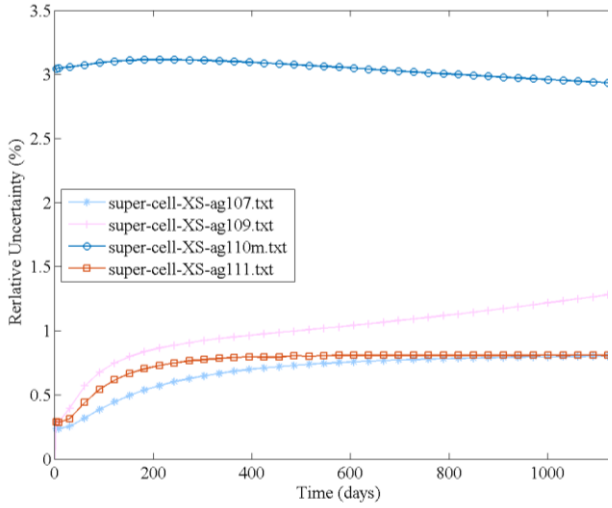

Figure 89. Ag relative uncertainty – XS perturbed in the super cell

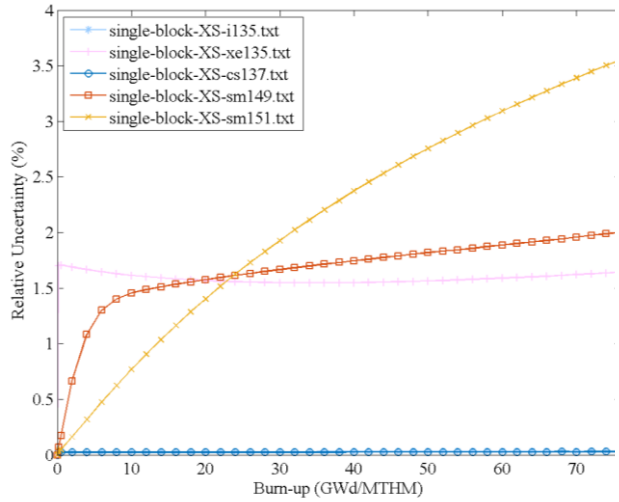

Figure 90. Poisons relative uncertainty – XS perturbed in the single block

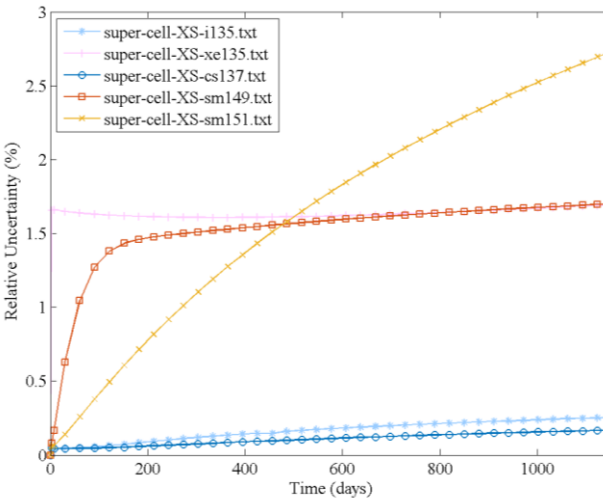

Figure 91. Poisons relative uncertainty – XS perturbed in the super cell

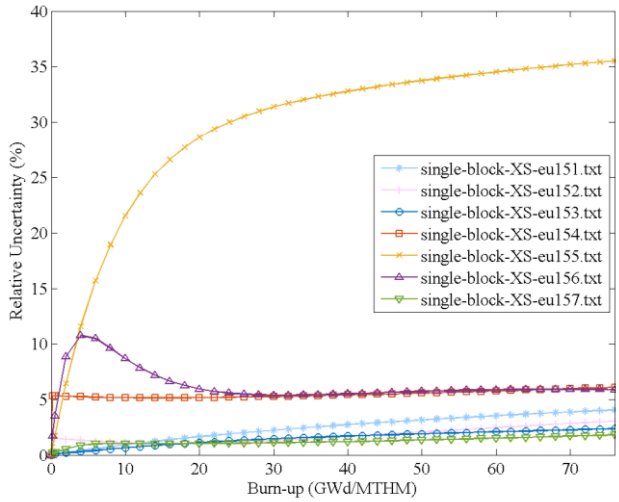

Figure 92. Eu relative uncertainty – XS perturbed in the single block

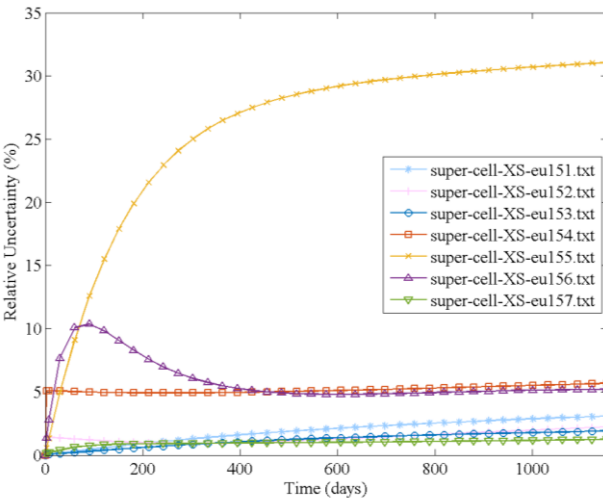

Figure 93. Eu relative uncertainty – XS perturbed in the super cell

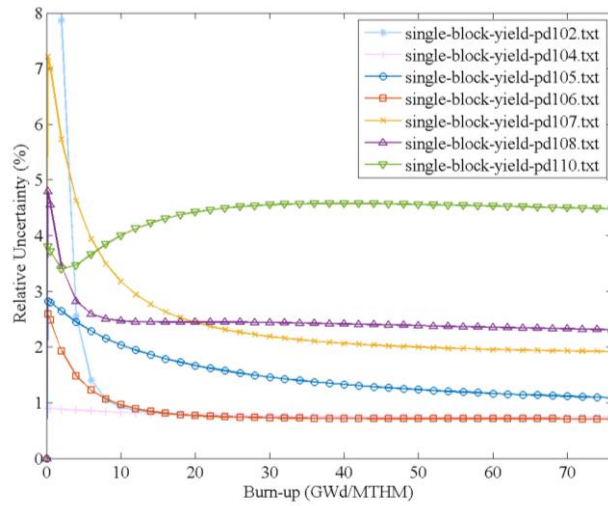

Figure 94. Pd relative uncertainty – Fission Yield perturbed in the single block

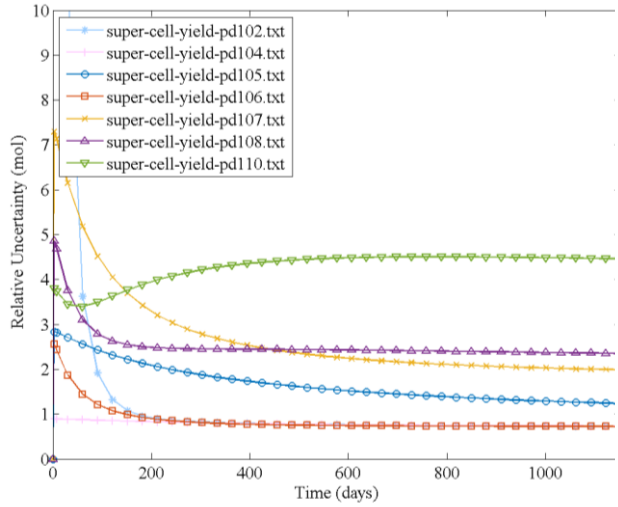

Figure 95. Pd relative uncertainty – Fission Yield perturbed in the super cell

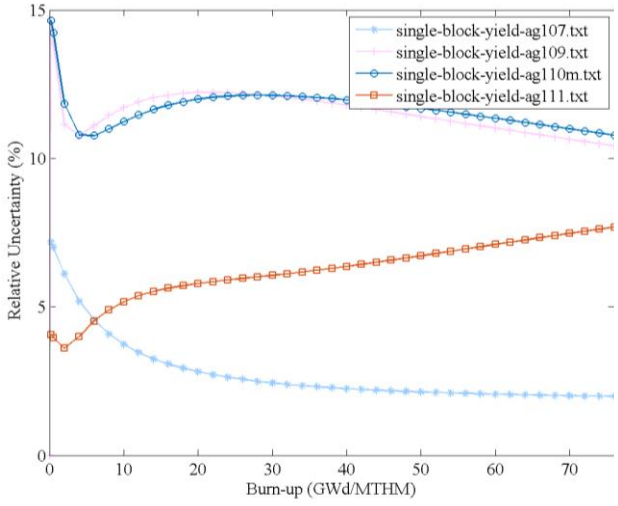

Figure 96. Ag relative uncertainty – Fission Yield perturbed in the single block

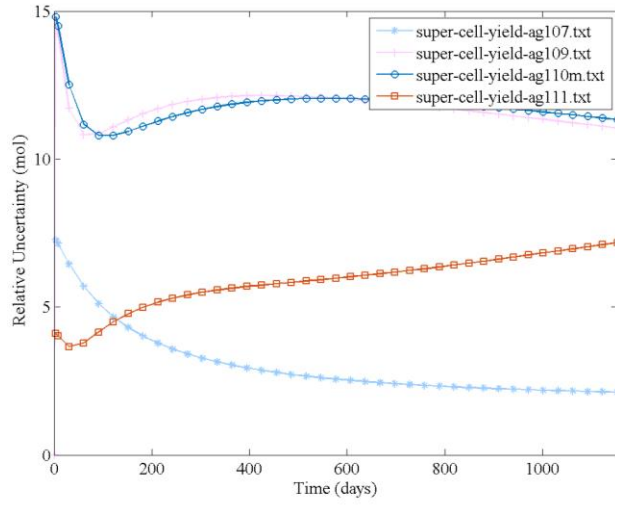

Figure 97. Ag relative uncertainty – Fission Yield perturbed in the super cell

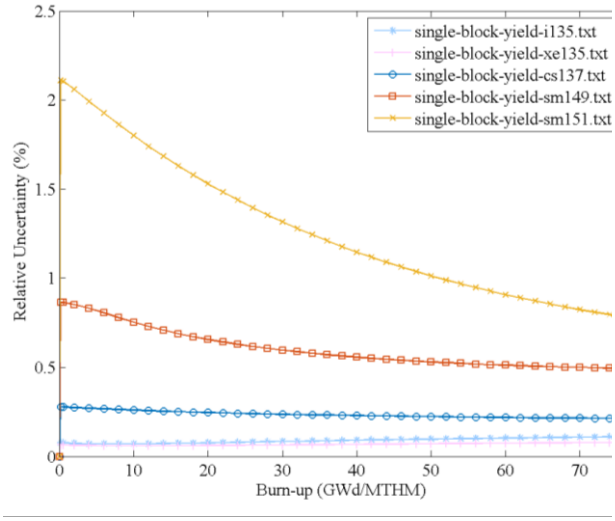

Figure 98. Poisons relative uncertainty – Fission Yield perturbed in the single block

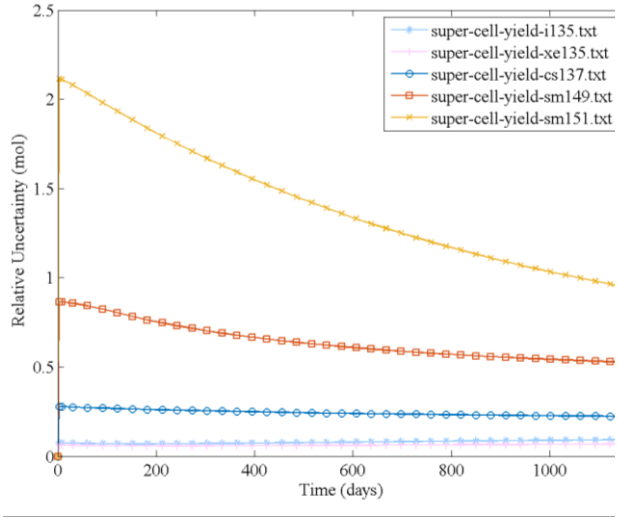

Figure 99. Poisons relative uncertainty – Fission Yield perturbed in the super cell

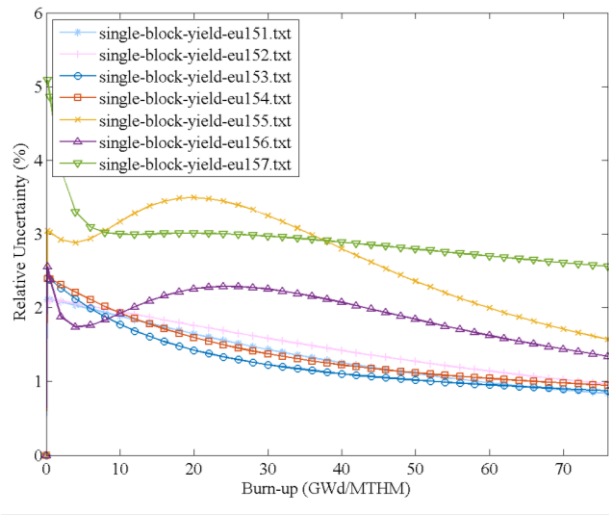

Figure 100. Eu relative uncertainty – Fission Yield perturbed in the single block

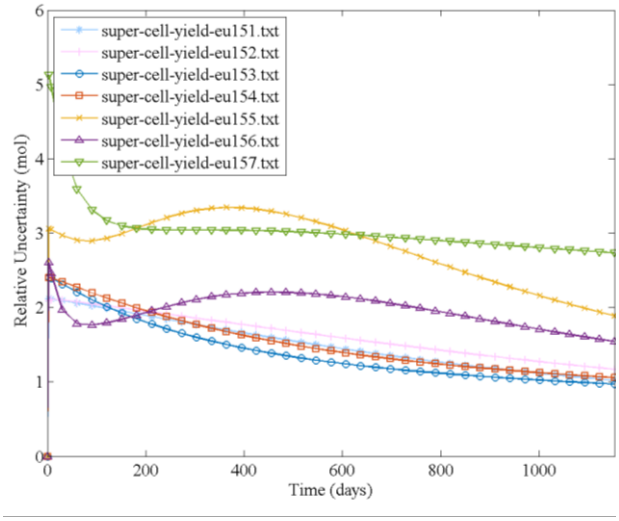

Figure 101. Eu relative uncertainty – Fission Yield perturbed in the super cell

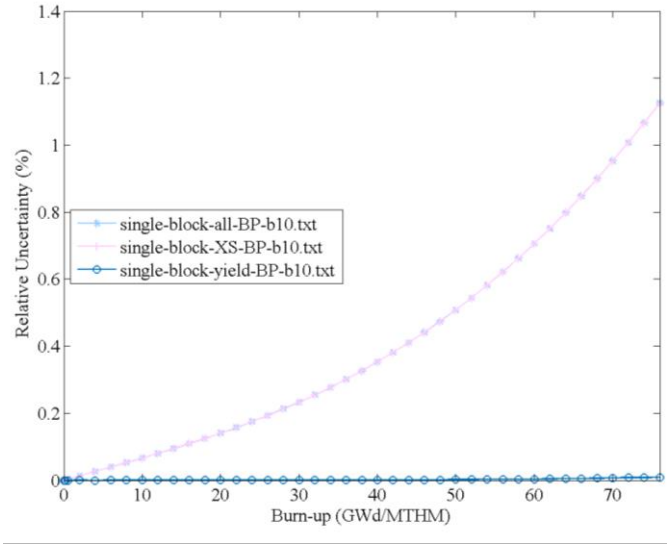

Figure 102. ^{10}B relative uncertainty – Fission Yield and cross section contribution (single block)

Table 30. Relative isotope uncertainties (%) in response to cross section and/or fission yield perturbations in a fuel block

	XS and fission yields combined				*XS*				*Fission Yields*			
	mean	*max*	*BOC*	*EOC*	*mean*	*max*	*BOC*	*EOC*	*mean*	*max*	*BOC*	*EOC*
^{1}h	**17.5**	22.1	21.9	15.3	**17.5**	22.1	21.9	15.3	0.0	0.0	0.0	0.0
^{10}b	**12.6**	14.5	7.5	11.2	**12.6**	14.5	7.5	11.2	0.0	0.0	0.0	0.0
^{11}b	**35.0**	41.4	20.8	41.4	**35.0**	41.4	20.8	41.4	0.0	0.0	0.0	0.0
^{14}n	**0.3**	0.4	0.3	0.4	**0.3**	0.4	0.3	0.4	0.0	0.0	0.0	0.0
^{16}o	**0.0**	0.0	0.0	0.0	0.0	0.0	0.0	0.0	0.0	0.0	0.0	0.0
^{72}ge	**6.9**	8.9	2.7	8.9	0.4	0.5	0.5	0.4	**6.9**	8.9	2.7	8.9
^{73}ge	**11.8**	15.2	15.0	11.0	0.2	0.3	0.3	0.2	**11.8**	15.2	15.0	11.0
^{74}ge	**14.9**	18.1	18.0	14.2	0.1	0.1	0.1	0.1	**14.9**	18.1	18.0	14.2
^{76}ge	**6.3**	6.9	6.9	6.2	0.1	0.1	0.1	0.1	**6.3**	6.9	6.9	6.2
^{75}as	**5.0**	6.1	6.1	4.9	0.0	0.1	0.0	0.1	**5.0**	6.1	6.1	4.8

Table 30 (continued)

^{79}br	**2.8**	3.3	3.3	2.5	0.0	0.0	0.0	0.0	**2.8**	3.3	3.3	2.5
^{76}se	**5.5**	25.9	17.4	5.0	0.5	0.5	0.3	0.5	**5.4**	25.9	17.4	4.9
^{77}se	**4.1**	4.8	4.8	3.8	0.0	0.1	0.0	0.1	**4.1**	4.8	4.8	3.8
^{78}se	**5.5**	5.8	5.7	5.7	0.0	0.0	0.0	0.0	**5.5**	5.8	5.7	5.7
^{80}se	**3.6**	4.2	3.2	4.2	0.0	0.1	0.0	0.1	**3.6**	4.2	3.2	4.2
^{82}se	**3.3**	4.1	2.5	4.1	0.0	0.1	0.0	0.1	**3.3**	4.1	2.5	4.1
^{80}kr	**7.5**	23.8	21.8	5.7	0.5	0.5	0.0	0.5	**7.4**	23.8	21.8	5.6
^{82}kr	**2.0**	9.0	6.5	2.3	0.5	0.5	0.2	0.5	**1.9**	9.0	6.5	2.2
^{83}kr	**0.8**	1.2	0.5	1.2	0.5	0.9	0.0	0.9	**0.6**	0.9	0.5	0.8
^{84}kr	**0.6**	0.7	0.6	0.7	0.2	0.4	0.0	0.4	**0.6**	0.6	0.6	0.5
^{85}kr	**0.4**	0.6	0.2	0.6	0.1	0.1	0.0	0.1	**0.4**	0.6	0.2	0.6
^{86}kr	**0.4**	0.5	0.5	0.4	0.1	0.1	0.0	0.1	**0.4**	0.5	0.5	0.4
^{81}br	**2.3**	2.8	2.0	2.7	0.0	0.0	0.0	0.0	**2.3**	2.8	2.0	2.7
^{85}rb	**0.3**	0.3	0.3	0.3	0.1	0.1	0.0	0.1	**0.3**	0.3	0.3	0.2
^{86}rb	**0.8**	12.7	7.1	0.7	0.6	0.6	0.4	0.6	**0.6**	12.7	7.0	0.4
^{87}rb	**0.3**	0.3	0.3	0.3	0.1	0.1	0.0	0.1	**0.3**	0.3	0.3	0.3
^{84}sr	**14.0**	40.2	32.6	12.2	**12.7**	13.9	4.6	11.6	5.3	40.3	32.3	3.4
^{86}sr	**0.9**	15.4	9.1	0.8	0.5	0.6	0.3	0.6	**0.7**	15.3	9.0	0.5
^{87}sr	**30.3**	41.6	38.4	26.7	0.6	0.6	0.1	0.6	**30.3**	41.6	38.4	26.7
^{88}sr	**0.4**	0.4	0.4	0.4	0.1	0.1	0.0	0.1	**0.4**	0.4	0.4	0.4
^{89}sr	**0.4**	0.5	0.4	0.5	0.1	0.2	0.0	0.2	**0.4**	0.4	0.4	0.4
^{90}sr	**0.7**	0.7	0.7	0.7	0.1	0.1	0.0	0.1	**0.7**	0.7	0.7	0.7

Table 30 (continued)

^{89}y	**0.4**	0.4	0.4	0.4	0.1	0.1	0.0	0.1	**0.4**	0.4	0.4	0.4
^{90}y	**0.7**	0.8	0.8	0.7	0.1	0.1	0.0	0.1	**0.7**	0.8	0.8	0.7
^{91}y	**0.3**	0.4	0.4	0.3	0.1	0.2	0.0	0.2	**0.3**	0.3	0.3	0.3
^{90}zr	**0.7**	1.0	0.8	0.7	0.1	0.1	0.0	0.1	**0.7**	1.0	0.8	0.7
^{91}zr	**0.3**	0.4	0.4	0.3	0.1	0.1	0.0	0.1	**0.3**	0.3	0.3	0.3
^{92}zr	**0.4**	0.4	0.4	0.4	0.1	0.1	0.0	0.1	**0.4**	0.4	0.4	0.4
^{93}zr	**0.3**	0.3	0.3	0.3	0.0	0.1	0.0	0.1	**0.3**	0.3	0.3	0.2
^{94}zr	**0.4**	0.4	0.4	0.4	0.0	0.1	0.0	0.1	**0.4**	0.4	0.4	0.4
^{95}zr	**0.5**	0.5	0.5	0.4	0.0	0.1	0.0	0.1	**0.4**	0.5	0.5	0.4
^{96}zr	**0.8**	0.9	0.9	0.8	0.0	0.0	0.0	0.0	**0.8**	0.9	0.9	0.8
^{93}nb	**21.7**	43.0	35.5	14.7	0.3	0.5	0.2	0.1	**21.7**	43.0	35.5	14.7
^{94}nb	**22.2**	28.2	24.2	23.4	2.5	3.0	0.3	2.0	**22.2**	28.2	24.2	23.5
^{95}nb	**0.5**	0.5	0.5	0.4	0.0	0.1	0.0	0.1	**0.4**	0.5	0.5	0.4
^{92}mo	**8.0**	38.8	37.1	6.2	**7.0**	21.6	21.3	6.2	**2.3**	31.5	29.8	0.1
^{94}mo	**18.4**	37.5	29.6	16.4	**18.3**	21.4	6.6	16.3	0.6	37.5	25.5	0.5
^{95}mo	**0.5**	0.5	0.5	0.5	0.1	0.2	0.0	0.2	**0.5**	0.5	0.5	0.4
^{96}mo	**6.8**	37.3	32.5	5.0	**6.5**	15.0	3.7	5.0	1.0	37.3	31.6	0.5
^{97}mo	**0.4**	0.5	0.5	0.4	0.0	0.1	0.0	0.1	**0.4**	0.5	0.5	0.4
^{98}mo	**0.6**	0.8	0.8	0.6	0.0	0.1	0.0	0.1	**0.6**	0.8	0.8	0.6
^{99}mo	**0.4**	0.5	0.5	0.4	0.0	0.0	0.0	0.0	**0.4**	0.5	0.5	0.4
^{100}mo	**1.2**	1.3	1.2	1.3	0.0	0.0	0.0	0.0	**1.2**	1.3	1.2	1.3
^{98}ru	**15.6**	20.7	20.5	13.1	**15.6**	20.8	20.7	13.2	0.8	2.0	1.7	0.6

Table 30 (continued)

^{99}ru	**0.4**	0.5	0.5	0.4	0.0	0.0	0.0	0.0	**0.4**	0.5	0.5	0.4
^{100}ru	**3.2**	3.6	3.5	3.1	**3.2**	3.3	3.3	3.1	0.4	1.0	0.7	0.4
^{101}ru	**0.5**	0.6	0.5	0.6	0.2	0.3	0.0	0.3	**0.5**	0.5	0.5	0.5
^{102}ru	**0.5**	0.6	0.6	0.5	0.2	0.3	0.0	0.3	**0.5**	0.6	0.6	0.4
^{103}ru	**0.8**	0.9	0.8	0.9	0.1	0.2	0.0	0.2	**0.8**	0.8	0.8	0.8
^{104}ru	**0.6**	0.8	0.8	0.6	0.2	0.2	0.0	0.2	**0.6**	0.8	0.8	0.5
^{105}ru	**1.2**	2.8	2.6	1.0	0.3	0.4	0.1	0.3	**1.1**	2.8	2.6	0.9
^{99}tc	**0.5**	0.5	0.5	0.5	0.1	0.3	0.0	0.3	**0.4**	0.5	0.5	0.4
^{103}rh	**0.9**	1.2	0.8	1.2	0.5	1.0	0.0	1.0	**0.7**	0.8	0.8	0.7
^{105}rh	**1.3**	2.8	2.7	1.1	0.6	0.6	0.4	0.6	**1.1**	2.8	2.6	0.9
^{106}rh	**1.7**	13.4	11.2	1.1	**1.4**	13.1	10.9	0.7	0.7	2.5	2.0	0.7
^{102}pd	**21.2**	35.8	29.0	19.0	**21.1**	24.1	8.9	19.0	0.8	35.9	24.5	0.7
^{104}pd	**3.6**	3.9	3.9	3.3	**3.5**	3.8	3.8	3.2	0.7	0.8	0.8	0.7
^{105}pd	**1.5**	2.8	2.7	1.2	0.5	0.6	0.3	0.6	**1.4**	2.8	2.7	1.1
^{106}pd	**2.4**	13.7	12.3	1.3	**2.2**	13.4	12.0	1.1	0.7	2.5	2.3	0.7
^{107}pd	**2.3**	7.2	6.6	1.9	0.5	0.6	0.2	0.5	**2.3**	7.2	6.6	1.9
^{108}pd	**2.6**	4.8	4.3	2.5	0.8	1.0	0.3	1.0	**2.4**	4.8	4.2	2.3
^{110}pd	**4.4**	4.6	3.6	4.5	0.5	0.6	0.3	0.5	**4.4**	4.5	3.6	4.4
^{107}ag	**2.5**	7.1	6.7	2.0	0.5	0.6	0.2	0.5	**2.5**	7.1	6.7	2.0
^{109}ag	**11.6**	14.5	13.1	10.6	1.0	1.5	0.3	1.5	**11.5**	14.5	13.1	10.5
^{111}ag	**6.4**	7.7	3.8	7.7	0.5	0.6	0.3	0.4	**6.3**	7.6	3.8	7.6
^{106}cd	**6.7**	41.9	18.5	6.1	**6.6**	41.2	18.3	6.1	0.1	0.6	0.2	0.1

Table 30 (continued)

^{108}cd	**21.4**	25.4	25.2	20.3	**17.6**	18.2	15.4	17.1	**12.1**	20.8	19.7	10.7
^{110}cd	**12.2**	15.3	14.3	11.6	3.0	3.1	3.1	2.9	**11.6**	14.6	13.5	11.1
^{111}cd	**5.5**	6.4	3.9	6.3	0.5	0.5	0.3	0.5	**5.5**	6.3	3.9	6.2
^{112}cd	**2.4**	3.3	3.2	2.3	0.4	0.4	0.4	0.4	**2.4**	3.3	3.2	2.3
^{113}cd	**3.0**	3.2	1.7	3.2	**1.9**	2.1	0.5	2.1	**2.1**	2.2	1.5	2.2
^{114}cd	**1.6**	3.2	2.8	1.8	0.3	0.4	0.4	0.3	**1.5**	3.2	2.8	1.7
^{116}cd	**4.5**	4.9	4.5	4.9	0.2	0.3	0.2	0.3	**4.5**	4.9	4.5	4.9
^{113}in	**2.0**	2.4	1.6	2.4	0.7	1.0	0.3	1.0	**1.8**	1.9	1.5	1.9
^{115}in	**3.1**	4.2	4.1	3.1	**1.1**	1.8	0.3	1.8	**2.7**	4.2	4.1	2.4
^{112}sn	**15.5**	22.1	21.9	11.8	**15.4**	22.2	22.0	11.6	1.6	1.7	1.5	1.5
^{114}sn	**2.7**	8.9	7.3	2.5	**2.0**	8.8	7.1	1.5	**1.6**	1.8	1.6	1.8
^{115}sn	**2.8**	4.2	4.1	2.4	0.3	0.3	0.3	0.2	**2.8**	4.2	4.1	2.4
^{116}sn	**3.6**	5.0	5.0	2.9	2.1	2.8	2.8	1.6	**3.0**	4.1	4.1	2.5
^{117}sn	**5.5**	7.0	3.1	6.9	0.2	0.2	0.2	0.2	**5.6**	7.0	3.1	7.0
^{118}sn	**4.8**	5.6	5.5	4.9	0.3	0.4	0.4	0.2	**4.8**	5.6	5.5	4.9
^{119}sn	**4.7**	6.0	6.0	4.4	0.2	0.3	0.3	0.2	**4.7**	6.0	5.9	4.4
^{120}sn	**5.6**	6.7	6.6	5.6	0.2	0.3	0.3	0.2	**5.5**	6.7	6.6	5.5
^{122}sn	**5.5**	7.1	7.0	5.4	0.2	0.3	0.2	0.2	**5.5**	7.1	7.0	5.4
^{124}sn	**6.2**	7.0	6.9	6.5	0.2	0.2	0.2	0.2	**6.2**	7.0	6.9	6.5
^{125}sn	**7.7**	9.1	3.2	9.1	0.3	0.3	0.0	0.3	**7.6**	9.1	3.2	9.0
^{126}sn	**3.9**	6.2	6.1	3.2	0.2	0.2	0.1	0.2	**3.9**	6.2	6.1	3.2
^{120}te	**41.9**	43.1	43.1	39.5	0.8	1.1	1.1	0.8	**41.9**	43.1	43.1	39.6

Table 30 (continued)

^{122}te	**4.7**	11.3	7.8	4.4	0.5	0.5	0.4	0.5	**4.6**	11.3	7.8	4.3
^{123}te	**5.3**	37.8	29.0	4.5	1.0	1.0	0.5	1.0	**5.1**	37.8	29.0	4.3
^{124}te	**7.6**	19.2	15.9	7.0	0.5	1.1	0.9	0.6	**7.6**	19.2	15.9	7.0
^{125}te	**1.8**	2.5	2.2	2.3	0.2	0.2	0.2	0.2	**1.8**	2.5	2.2	2.3
^{126}te	**29.6**	47.0	44.1	25.6	0.0	0.1	0.0	0.1	**29.6**	47.0	44.1	25.6
^{128}te	**3.5**	4.3	2.8	4.2	0.1	0.1	0.0	0.1	**3.5**	4.3	2.8	4.2
^{130}te	**2.1**	2.3	2.0	2.3	0.0	0.0	0.0	0.0	**2.1**	2.3	2.0	2.3
^{132}te	**0.5**	0.6	0.3	0.6	0.0	0.0	0.0	0.0	**0.5**	0.6	0.3	0.6
^{121}sb	**4.6**	6.0	5.9	4.4	0.2	0.3	0.3	0.2	**4.5**	5.9	5.8	4.4
^{123}sb	**7.9**	10.7	10.5	7.3	0.2	0.3	0.3	0.2	**7.9**	10.7	10.6	7.3
^{124}sb	**7.6**	24.3	19.0	7.1	0.5	0.6	0.5	0.6	**7.5**	24.2	18.9	7.1
^{125}sb	**2.1**	2.7	2.0	2.7	0.2	0.2	0.2	0.2	**2.1**	2.7	2.0	2.7
^{126}sb	**25.5**	36.5	36.1	23.2	0.1	0.2	0.0	0.2	**25.5**	36.5	36.1	23.1
^{127}i	**2.2**	2.5	2.2	2.5	0.3	0.5	0.0	0.5	**2.2**	2.4	2.2	2.4
^{129}i	**1.1**	1.5	0.8	1.4	0.1	0.2	0.0	0.2	**1.1**	1.5	0.8	1.4
^{130}i	**6.4**	13.3	10.0	6.7	**6.2**	6.5	2.5	6.5	1.3	13.2	9.0	1.4
^{131}i	**0.2**	0.3	0.3	0.2	0.0	0.0	0.0	0.0	**0.2**	0.3	0.3	0.2
^{135}i	**0.0**	0.1	0.0	0.1	0.0	0.0	0.0	0.0	**0.0**	0.1	0.0	0.1
^{126}xe	**17.2**	41.1	31.1	15.0	**16.7**	20.3	8.9	14.5	2.2	41.0	26.0	2.2
^{128}xe	**8.2**	13.8	10.1	8.2	**8.2**	8.3	7.0	8.1	2.1	12.0	5.8	2.2
^{129}xe	**8.2**	8.2	5.6	8.2	**8.2**	8.2	4.1	8.2	2.0	4.3	3.0	2.1
^{130}xe	**6.2**	13.6	11.0	6.5	**6.0**	6.4	1.8	6.4	1.3	13.5	10.4	1.2

Table 30 (continued)

^{131}xe	**2.0**	3.6	0.3	3.5	**1.9**	3.6	0.0	3.5	0.2	0.3	0.3	0.2
^{132}xe	**1.0**	1.6	0.3	1.5	**0.9**	1.5	0.0	1.5	0.2	0.4	0.3	0.2
133xe	**0.3**	0.3	0.3	0.3	0.0	0.0	0.0	0.0	**0.3**	0.3	0.3	0.3
^{135}xe	**1.5**	1.7	1.7	1.6	**1.5**	1.7	1.7	1.6	0.0	0.0	0.0	0.0
^{136}xe	**0.8**	0.8	0.8	0.8	**0.7**	0.7	0.7	0.7	0.2	0.2	0.2	0.2
^{139}la	**0.4**	0.5	0.4	0.5	0.0	0.0	0.0	0.0	**0.4**	0.5	0.4	0.5
^{140}la	**0.3**	0.5	0.4	0.3	0.0	0.0	0.0	0.0	**0.3**	0.5	0.4	0.3
^{134}ba	**5.5**	5.6	5.3	5.3	**5.5**	5.6	5.3	5.4	0.3	1.0	0.6	0.3
^{135}ba	**6.2**	30.2	23.9	5.5	**5.2**	5.6	0.3	5.5	2.0	30.2	23.9	0.3
^{136}ba	**7.7**	33.2	26.3	6.6	**3.8**	4.5	0.3	4.5	**6.6**	33.2	26.3	5.0
^{137}ba	**0.4**	9.9	5.2	0.3	0.0	0.0	0.0	0.0	**0.4**	9.9	5.2	0.3
^{138}ba	**0.3**	0.3	0.3	0.3	0.0	0.0	0.0	0.0	**0.3**	0.3	0.3	0.3
^{140}ba	**0.3**	0.3	0.3	0.3	0.0	0.0	0.0	0.0	**0.3**	0.3	0.3	0.3
^{140}ce	**0.3**	0.8	0.5	0.3	0.0	0.0	0.0	0.0	**0.3**	0.8	0.5	0.3
^{141}ce	**0.5**	0.5	0.5	0.5	0.0	0.0	0.0	0.0	**0.5**	0.5	0.5	0.5
^{142}ce	**0.3**	0.4	0.4	0.3	0.0	0.0	0.0	0.0	**0.3**	0.4	0.4	0.3
^{143}ce	**0.2**	0.3	0.3	0.3	0.0	0.1	0.0	0.1	**0.2**	0.3	0.3	0.2
^{144}ce	**0.2**	0.2	0.2	0.2	0.0	0.1	0.0	0.1	**0.2**	0.2	0.2	0.2
^{133}cs	**0.5**	0.7	0.3	0.7	**0.3**	0.6	0.0	0.6	**0.3**	0.3	0.3	0.3
^{134}cs	**5.4**	5.6	5.5	5.2	**5.4**	5.6	5.5	5.2	0.3	0.5	0.4	0.3
^{135}cs	**1.6**	1.6	1.6	1.5	**1.5**	1.6	1.5	1.5	0.0	0.0	0.0	0.0
^{136}cs	**7.0**	26.6	22.0	6.1	**4.6**	5.1	0.9	5.1	**5.2**	26.6	21.9	3.4

Table 30 (continued)

^{137}cs	**0.2**	0.2	0.2	0.2	0.0	0.0	0.0	0.0	**0.2**	0.2	0.2	0.2
^{141}pr	**0.5**	0.5	0.5	0.5	0.0	0.0	0.0	0.0	**0.5**	0.5	0.5	0.5
^{142}pr	**7.0**	7.1	6.6	7.1	**6.9**	7.0	6.5	7.0	0.5	0.5	0.5	0.5
^{143}pr	**0.2**	0.3	0.3	0.3	0.0	0.1	0.0	0.1	**0.2**	0.3	0.3	0.2
^{142}nd	**7.0**	7.1	6.6	7.1	**6.9**	7.0	6.5	7.0	0.5	0.5	0.5	0.5
^{143}nd	**0.6**	1.1	0.3	1.1	**0.5**	1.1	0.0	1.0	**0.2**	0.3	0.3	0.2
^{144}nd	**1.0**	1.2	0.4	1.2	**0.9**	1.2	0.3	1.2	0.2	0.2	0.2	0.2
^{145}nd	**0.7**	1.1	0.4	1.1	**0.5**	1.0	0.0	0.9	**0.4**	0.4	0.4	0.4
^{146}nd	**0.6**	1.0	0.3	1.0	**0.6**	1.0	0.0	1.0	0.2	0.3	0.3	0.2
^{147}nd	**0.6**	0.8	0.7	0.6	0.1	0.1	0.0	0.1	**0.6**	0.8	0.7	0.6
^{148}nd	**0.7**	0.7	0.7	0.7	0.1	0.1	0.0	0.1	**0.7**	0.7	0.7	0.7
^{150}nd	**1.5**	1.9	1.9	1.3	0.0	0.0	0.0	0.0	**1.5**	1.9	1.9	1.3
^{144}sm	**38.4**	76.7	58.4	43.9	**38.4**	76.9	58.7	43.8	0.6	6.0	2.5	0.6
^{147}sm	**1.2**	1.7	0.8	1.7	**0.9**	1.6	0.0	1.6	**0.7**	0.8	0.8	0.6
^{148}sm	**3.8**	4.8	4.8	3.0	**3.8**	4.8	4.8	3.0	0.7	0.8	0.8	0.6
^{149}sm	**1.8**	2.0	0.9	2.0	**1.7**	2.0	0.3	1.9	0.5	0.8	0.8	0.5
^{150}sm	**1.0**	2.2	1.7	1.2	**0.7**	2.0	1.5	1.1	**0.6**	0.8	0.8	0.5
^{151}sm	**2.5**	3.5	2.0	3.5	**2.2**	3.5	0.0	3.5	**1.2**	2.1	2.0	0.8
^{152}sm	**1.5**	2.1	1.1	2.1	**1.2**	1.9	0.1	1.9	**0.8**	1.1	1.0	0.7
^{153}sm	**1.5**	2.4	2.3	1.5	**1.2**	1.3	0.1	1.3	**1.0**	2.3	2.3	0.7
^{147}pm	**1.4**	2.1	0.8	2.0	**1.2**	2.0	0.0	1.9	0.7	0.8	0.8	0.6
^{148}pm	**3.8**	4.8	4.8	3.1	**3.8**	4.8	4.8	3.0	0.6	0.8	0.8	0.6

Table 30 (continued)

^{149}pm	**0.8**	0.8	0.8	0.8	**0.5**	0.6	0.0	0.6	**0.5**	0.8	0.8	0.4
^{151}pm	**1.2**	2.1	2.0	0.9	0.1	0.1	0.0	0.1	**1.2**	2.1	2.0	0.9
^{151}eu	**2.9**	4.0	2.1	4.0	**2.5**	4.0	0.1	4.0	**1.3**	2.1	2.1	0.8
^{152}eu	**2.3**	3.0	2.5	3.0	**1.8**	3.0	1.4	2.9	**1.4**	2.1	2.0	0.9
^{153}eu	**1.9**	2.4	2.3	2.3	**1.5**	2.3	0.1	2.3	**1.2**	2.4	2.3	0.8
^{154}eu	**5.6**	6.1	5.8	6.1	**5.4**	6.0	5.3	6.0	1.3	2.3	2.3	0.9
^{155}eu	**31.3**	35.8	4.5	35.7	**30.8**	35.5	2.9	35.4	2.6	3.4	2.9	1.6
^{156}eu	**6.3**	10.8	5.4	5.9	**6.2**	10.7	4.7	5.8	1.9	2.5	2.2	1.3
^{157}eu	**3.0**	5.0	4.6	2.9	1.2	1.8	0.3	1.7	**2.8**	5.0	4.6	2.5
^{159}tb	**2.8**	4.5	4.2	2.8	0.9	1.5	0.3	1.5	**2.7**	4.5	4.2	2.4
^{160}tb	**2.9**	5.7	4.6	2.9	1.1	1.5	0.6	1.5	**2.7**	5.8	4.7	2.4
^{160}dy	**2.9**	7.6	5.4	2.9	0.9	1.2	0.7	1.2	**2.7**	7.7	5.5	2.5
^{161}dy	**3.6**	3.9	2.6	3.2	0.6	0.7	0.6	0.6	**3.5**	3.9	2.6	3.1
^{162}dy	**8.9**	14.3	12.1	6.8	0.7	1.6	1.3	0.5	**8.8**	14.3	12.1	6.7
^{163}dy	**10.5**	15.6	13.5	8.0	0.7	2.2	1.7	0.6	**10.5**	15.5	13.5	8.0
^{164}dy	**10.4**	14.3	12.7	7.9	0.9	3.5	2.7	1.0	**10.3**	14.3	12.7	7.8
^{152}gd	**2.2**	2.7	2.6	2.6	**1.6**	2.5	1.4	2.4	**1.5**	2.2	2.1	1.1
^{154}gd	**5.4**	5.8	5.8	5.7	**5.2**	5.6	5.3	5.5	1.4	2.3	2.3	1.0
^{155}gd	**27.7**	30.9	3.9	30.5	**27.2**	30.6	2.0	30.3	2.6	3.3	3.0	1.6
^{156}gd	**6.4**	9.9	4.5	5.3	**6.3**	9.8	3.5	5.1	1.9	2.5	2.3	1.7
^{157}gd	**5.8**	6.6	5.1	6.5	**5.0**	6.1	1.0	6.1	2.5	5.1	4.8	2.0
^{158}gd	**3.9**	8.2	6.8	3.8	1.1	1.7	0.7	1.6	**3.7**	8.2	6.9	3.4

Table 30 (continued)

^{160}gd	**10.4**	17.8	16.1	10.3	0.6	0.6	0.4	0.5	**10.4**	17.8	16.1	10.3
^{165}ho	**9.2**	12.9	11.2	7.6	0.7	3.7	3.0	0.4	**9.2**	11.9	10.4	7.5
^{166}er	**6.4**	14.2	12.2	5.7	0.8	4.6	3.9	0.6	**6.3**	13.2	11.3	5.6
^{167}er	**12.7**	14.0	11.3	10.5	1.1	4.4	4.0	0.9	**12.6**	14.0	10.8	10.5
^{230}th	**15.1**	19.6	19.5	10.2	**15.1**	19.6	19.5	10.2	0.0	0.0	0.0	0.0
^{231}pa	**0.1**	0.3	0.0	0.3	**0.1**	0.3	0.0	0.3	0.0	0.0	0.0	0.0
^{233}pa	**2.0**	2.6	0.6	2.6	**2.0**	2.6	0.6	2.6	0.0	0.0	0.0	0.0
^{232}th	**0.3**	0.3	0.2	0.3	**0.3**	0.3	0.2	0.3	0.0	0.0	0.0	0.0
^{232}u	**3.5**	8.6	0.2	8.3	**3.5**	8.6	0.2	8.3	0.0	0.0	0.0	0.0
^{233}u	**5.0**	21.3	20.7	3.2	**5.0**	21.3	20.7	3.2	0.0	0.0	0.0	0.0
^{234}u	**12.9**	19.6	19.5	6.8	**12.9**	19.6	19.5	6.8	0.0	0.0	0.0	0.0
^{235}u	**0.1***	0.2	0.0	0.2	**0.1**	0.2	0.0	0.2	0.0	0.0	0.0	0.0
^{236}u	**1.2**	1.2	1.2	1.2	**1.2**	1.2	1.2	1.2	0.0	0.0	0.0	0.0
^{238}u	**0.0***	0.0	0.0	0.0	**0.0**	0.0	0.0	0.0	0.0	0.0	0.0	0.0
^{237}np	**4.2**	18.0	12.6	4.1	**4.2**	18.0	12.6	4.1	0.0	0.0	0.0	0.0
^{238}pu	**5.5**	20.0	15.3	4.7	**5.5**	20.0	15.3	4.7	0.0	0.0	0.0	0.0
^{239}pu	**1.2**	1.5	0.9	1.5	**1.2**	1.5	0.9	1.5	0.0	0.0	0.0	0.0
^{240}pu	**1.4**	1.4	1.3	1.4	**1.4**	1.4	1.3	1.4	0.0	0.0	0.0	0.0
^{241}pu	**1.4**	1.6	1.5	1.5	**1.4**	1.6	1.5	1.5	0.0	0.0	0.0	0.0
^{242}pu	**3.1**	3.4	2.8	3.4	**3.1**	3.4	2.8	3.4	0.0	0.0	0.0	0.0
^{241}am	**2.0**	2.8	1.5	2.7	**2.0**	2.8	1.5	2.7	0.0	0.0	0.0	0.0
^{242}am	**3.9**	5.1	5.1	3.0	**3.9**	5.1	5.1	3.0	0.0	0.0	0.0	0.0

Table 30 (continued)

^{243}am	**11.5**	12.2	12.1	10.9	**11.5**	12.2	12.1	10.9	0.0	0.0	0.0	0.0
^{242}cm	**4.1**	5.1	5.0	3.2	**4.1**	5.1	5.0	3.2	0.0	0.0	0.0	0.0
^{243}cm	**12.0**	12.2	5.6	11.9	**12.0**	12.2	5.6	11.9	0.0	0.0	0.0	0.0
^{244}cm	**12.0**	12.6	8.2	11.4	**12.0**	12.6	8.2	11.4	0.0	0.0	0.0	0.0
$^{10}b_{BP}$†	**0.4**	1.1	0.0	1.0	**0.4**	1.1	0.0	1.0	0.0	0.0	0.0	0.0

*for U-238: total uncertainty due to cross sections and fission yields: 0.03% (mean) and 0.06% (EOC)

* for U-235: total uncertainty due to cross sections and fission yields: 0.12 % (mean) and 0.26% (EOC)

†*B-10BP is the B-10* in the burnable poison region

Table 31. Comparison of the isotope uncertainty (%) in the single block and super cell in response to cross section and fission yield perturbations

Isotope	*SB*	*SC*	*Isotope*	*SB*	*SC*	*Isotope*	*SB*	*SC*
^{1}h	17.5	19.7	^{110}pd	4.4	4.3	^{137}cs	0.2	0.2
^{10}b	12.6	14.0	^{107}ag	2.5	2.9	^{141}pr	0.5	0.5
^{11}b	35.0	30.8	^{109}ag	11.6	11.8	^{142}pr	7.0	6.1
^{14}n	0.3	0.3	^{111}ag	6.4	6.1	^{143}pr	0.2	0.3
^{16}o	0.0	0.0	^{106}cd	6.7	6.6	^{142}nd	7.0	6.1
^{72}ge	6.9	6.0	^{108}cd	21.4	22.6	^{143}nd	0.6	0.5
^{73}ge	11.8	12.3	^{110}cd	12.2	12.2	^{144}nd	1.0	0.7
^{74}ge	14.9	15.4	^{111}cd	5.5	5.3	^{145}nd	0.7	0.5
^{76}ge	6.3	6.3	^{112}cd	2.4	2.4	^{146}nd	0.6	0.5
^{75}as	5.0	5.2	^{113}cd	3.0	2.8	^{147}nd	0.6	0.7
^{79}br	2.8	2.9	^{114}cd	1.6	1.5	^{148}nd	0.7	0.7
^{76}se	5.5	5.9	^{116}cd	4.5	4.3	^{150}nd	1.5	1.6

Table 31 (continued)

^{77}se	4.1	4.3	^{113}in	2.0	1.9	^{144}sm	38.4	33.4
^{78}se	5.5	5.4	^{115}in	3.1	3.2	^{147}sm	1.2	0.9
^{80}se	3.6	3.4	^{112}sn	15.5	18.7	^{148}sm	3.8	3.9
^{82}se	3.3	3.0	^{114}sn	2.7	2.7	^{149}sm	1.8	1.6
^{80}kr	7.5	8.5	^{115}sn	2.8	3.0	^{150}sm	1.0	0.9
^{82}kr	2.0	2.0	^{116}sn	3.6	3.9	^{151}sm	2.5	2.2
^{83}kr	0.8	0.7	^{117}sn	5.5	4.8	^{152}sm	1.5	1.3
^{84}kr	0.6	0.6	^{118}sn	4.8	4.8	^{153}sm	1.5	1.6
^{85}kr	0.4	0.3	^{119}sn	4.7	4.9	^{147}pm	1.4	1.1
^{86}kr	0.4	0.4	^{120}sn	5.6	5.6	^{148}pm	3.8	4.0
^{81}br	2.3	2.2	^{122}sn	5.5	5.6	^{149}pm	0.8	0.8
^{85}rb	0.3	0.3	^{124}sn	6.2	6.1	^{151}pm	1.2	1.4
^{86}rb	0.8	0.9	^{125}sn	7.7	6.9	^{151}eu	2.9	2.5
^{87}rb	0.3	0.3	^{126}sn	3.9	4.2	^{152}eu	2.3	2.1
^{84}sr	14.0	16.0	^{120}te	41.9	42.5	^{153}eu	1.9	1.8
^{86}sr	0.9	1.0	^{122}te	4.7	4.9	^{154}eu	5.6	5.4
^{87}sr	30.3	31.0	^{123}te	5.3	6.0	^{155}eu	31.3	27.5
^{88}sr	0.4	0.4	^{124}te	7.6	8.0	^{156}eu	6.3	5.9
^{89}sr	0.4	0.4	^{125}te	1.8	1.6	^{157}eu	3.0	3.0
^{90}sr	0.7	0.7	^{126}te	29.6	31.2	^{159}tb	2.8	2.8
^{89}y	0.4	0.4	^{128}te	3.5	3.2	^{160}tb	2.9	3.0
^{90}y	0.7	0.7	^{130}te	2.1	2.0	^{160}dy	2.9	2.9

Table 31 (continued)

^{91}y	0.3	0.3	^{132}te	0.5	0.5	^{161}dy	3.6	3.8
^{90}zr	0.7	0.7	^{121}sb	4.6	4.7	^{162}dy	8.9	9.5
^{91}zr	0.3	0.3	^{123}sb	7.9	8.2	^{163}dy	10.5	11.4
^{92}zr	0.4	0.4	^{124}sb	7.6	7.8	^{164}dy	10.4	11.4
^{93}zr	0.3	0.3	^{125}sb	2.1	1.9	^{152}gd	2.2	2.0
^{94}zr	0.4	0.4	^{126}sb	25.5	26.8	^{154}gd	5.4	5.2
^{95}zr	0.5	0.5	^{127}i	2.2	2.2	^{155}gd	27.7	24.9
^{96}zr	0.8	0.8	^{129}i	1.1	1.0	^{156}gd	6.4	6.2
^{93}nb	21.7	18.3	^{130}i	6.4	7.0	^{157}gd	5.8	5.6
^{94}nb	22.2	22.2	^{131}i	0.2	0.3	^{158}gd	3.9	3.9
^{95}nb	0.5	0.5	^{135}i	0.1	0.2	^{160}gd	10.4	10.4
^{92}mo	8.0	8.6	^{124}xe	43.5	42.1	^{165}ho	9.2	9.6
^{94}mo	18.4	20.9	^{126}xe	17.2	19.8	^{166}er	6.4	6.7
^{95}mo	0.5	0.5	^{128}xe	8.2	8.2	^{167}er	12.7	13.4
^{96}mo	6.8	6.5	^{129}xe	8.2	8.1	^{230}th	15.1	17.2
^{97}mo	0.4	0.4	^{130}xe	6.2	6.8	^{231}pa	0.1	0.1
^{98}mo	0.6	0.7	^{131}xe	2.0	1.3	^{233}pa	2.0	2.0
^{99}mo	0.4	0.4	^{132}xe	1.0	0.7	^{232}th	0.3	0.2
^{100}mo	1.2	1.2	^{133}xe	0.3	0.3	^{232}u	3.5	1.8
^{96}ru	41.4	39.7	^{135}xe	1.5	1.6	^{233}u	5.0	5.3
^{98}ru	15.6	18.3	^{136}xe	0.8	0.8	^{234}u	12.9	15.4
^{99}ru	0.4	0.4	^{139}la	0.4	0.4	^{235}u	0.1	0.1

Table 31 (continued)

^{100}ru	3.2	3.3	^{140}la	0.3	0.3	^{236}u	1.2	1.2
^{101}ru	0.5	0.5	^{134}ba	5.5	5.4	^{238}u	0.0	0.0
^{102}ru	0.5	0.5	^{135}ba	6.2	6.3	^{237}np	4.2	4.3
^{103}ru	0.8	0.8	^{136}ba	7.7	8.1	^{238}pu	5.5	5.7
^{104}ru	0.6	0.6	^{137}ba	0.4	0.4	^{239}pu	1.2	1.1
^{105}ru	1.2	1.4	^{138}ba	0.3	0.3	^{240}pu	1.4	1.4
^{99}tc	0.5	0.4	^{140}ba	0.3	0.3	^{241}pu	1.4	1.5
^{103}rh	0.9	0.8	^{140}ce	0.3	0.3	^{242}pu	3.1	2.7
^{105}rh	1.3	1.4	^{141}ce	0.5	0.5	^{241}am	2.0	2.0
^{106}rh	1.7	1.7	^{142}ce	0.3	0.4	^{242}am	3.9	4.1
^{102}pd	21.2	23.5	^{143}ce	0.2	0.3	^{243}am	11.5	11.5
^{104}pd	3.6	3.5	^{144}ce	0.2	0.2	^{242}cm	4.1	4.3
^{105}pd	1.5	1.7	^{133}cs	0.5	0.4	^{243}cm	12.0	11.6
^{106}pd	2.4	2.4	^{134}cs	5.4	5.3	^{244}cm	12.0	12.0
^{107}pd	2.3	2.6	^{135}cs	1.6	1.6	$^{10}b_{BP}$	0.4	0.3
^{108}pd	2.6	2.6	^{136}cs	7.0	7.3			

6.9 Conclusion

This chapter estimated the uncertainties in nuclide inventories over burnup calculations. The uncertainty quantification was performed with SAMPLER/T-NEWT with a typical MHTGR-350 fuel block and a one-region super cell. The results proved the cross section uncertainties contribute primarily to the actinides' number density uncertainties and in some cases to the fission products' number density uncertainties. The fission yields dominate in general the fission products' number density uncertainties. In a fuel block, the cycle-averaged uncertainty response to cross section and fission yield perturbations over the ~80.0 GWd/MTHM cycle is 0.12

% for ^{235}U; 0.03% for ^{238}U; 1.22 % for ^{239}Pu; 1.43 % for ^{240}Pu; 1.49% for ^{241}Pu; 1.58 % for ^{135}Xe; 1.81 % for ^{149}Sm and 0.44 % for ^{10}B (burnable poison). The fuel block model versus the super cell model shows in average 12 % differences in the predicted uncertainties. This 12 % discrepancy is entirely explained by the spectrum difference within the fuel block compared to the super cell. No trend can be attributed to a softer or harder spectrum: the analysis must be done isotope-per-isotope. For instance, the cycle-averaged uncertainties predicted after perturbation of the cross sections and fission yields in the super cell model decrease for the ^{235}U (total uncertainty 0.08%), ^{238}U (0.02%), ^{239}Pu (1.14%), ^{10}B (0.38 %) and ^{147}Sm (1.67 %). Those uncertainties increase for the ^{240}Pu (1.48 %), ^{241}Pu (1.52 %) and ^{135}Xe (1.64 %).

CHAPTER 7

IMPLEMENTATION OF A SENSITIVITY AND UNCERTAINTY ANALYSIS SEQUENCE WITH PHISICS/RAVEN

This chapter evaluates the manufacturing uncertainties predicted in the VHTRC experiment with the RAVEN/PHISICS sequence. This analysis proposes to develop the following aspects:

- Elaborating the RAVEN/PHISICS coupling features;
- Enumerating the RAVEN/PHISICS capabilities;
- Validating the uncertainty estimates provided by RAVEN/PHISICS;
- Assessing the VHTCR uncertainty results;
- Reviewing the cross section perturbation status in RAVEN/PHISICS.

7.1 RAVEN/PHISICS/(RELAP5-3D) coupling

Section 2.6.8 clarified that an interface is necessary to explore the RAVEN capabilities on an external code. To address the objective of this chapter, a PHISICS interface was produced to perturb the neutron cross sections, the nuclide number densities, the decay constants, the fission yields, the energy emitted per fission and the energy emitted per decay. Separate libraries contain all of those parameters within PHSICS. The PHISICS Parsers substitute the RAVEN-perturbed values into the PHISICS libraries, except for the cross sections. For the cross sections, the covariance relative to the perturbed cross sections are expressed as multivariate variables in the RAVEN input. RAVEN uses three types of cross section “modifiers” (additive, multiplicative or absolute) to generate scaling factors which are applied to a specific nuclide/reaction and in an energy group g with respect to the covariance. As the cross section sections depraved from scaling factors are set to the nominal values, a Parser replacing the nominal values by the perturbed values is not necessary. An “XML file creator” that builds the scaling factor file is required instead.

Three modules compose the PHISICS suite (section 2.6.5), among which the MRTAU sequence fulfills the depletion analysis abilities. The PHISICS interface was constructed so that

RAVEN/MRTAU can function in “standalone” mode. RAVEN/MRTAU can for example replicate the Bateman equations and provide sensitivity coefficients relative to the decay constants in a decay chain. Another interface enabled RAVEN/PHISICS/RELAP5-3D simulations. The RAVEN/MRTAU and RAVEN/PHISICS/RELAP5-3D capabilities are not demonstrated in this work. Figure 103 charts the workflow of the PHISICS/RAVEN sequence. Figure 104 overviews the data handling in RAVEN/PHISICS/RELAP5-3D.

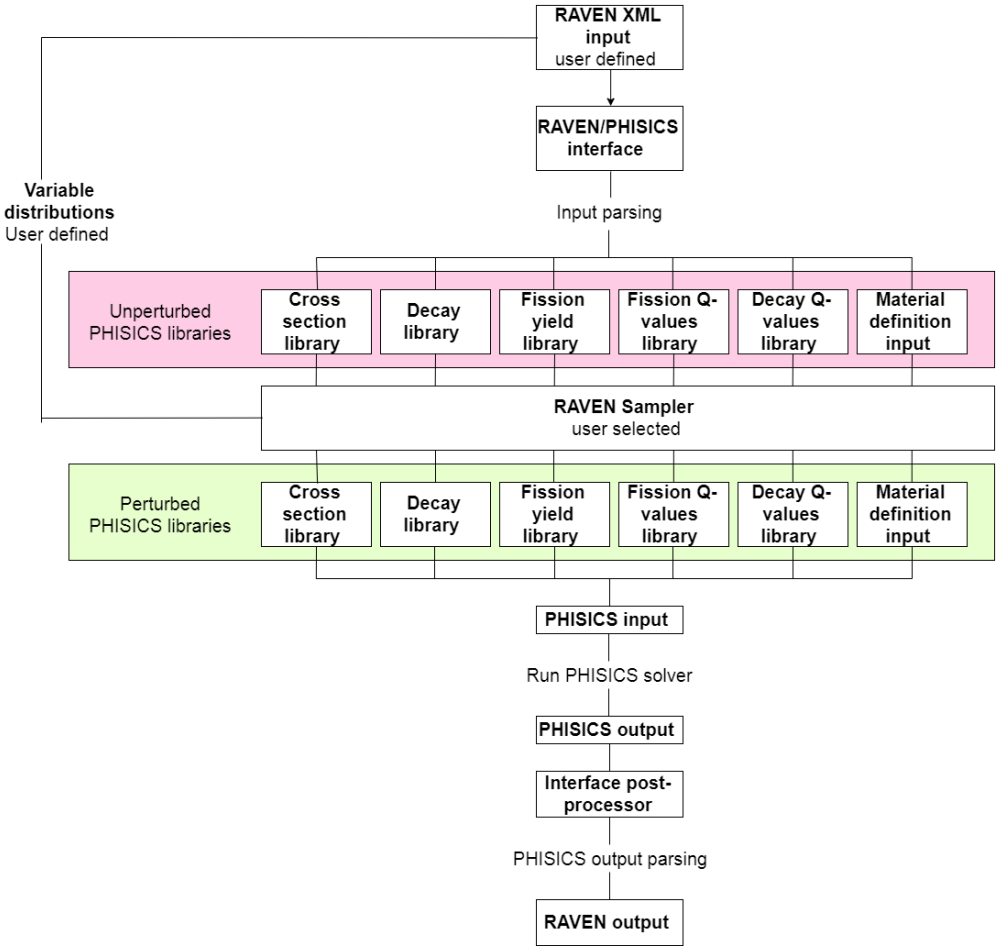

Figure 103. Workflow of the sequence RAVEN/PHISICS

7.2 Application of the RAVEN/PHISICS capabilities on the VHTRC model

7.2.1 Description of the model

The section 2.1.3 overviews VHTRC core. This chapter utilizes the methodology from CHAPTER 5 for the generation of the nominal cross sections in PHISICS. T-NEWT generates

the lattice cell cross sections. Disadvantage factors correct the spatial self-shielding from the lattice cell homogenization. PHISICS computes the transport solution with the flux-weighted, smeared out cross sections originating from T-NEWT. A lattice cell generates two to three sets of cross sections:

- The central block provides the fuel block's cross sections for the PHISICS VHTRC core;
- The northernmost block (graphite) constitutes the reflector;
- The side block (
- Figure **105**, right) models optionally the "minor" blocks found in the VHTRC core.

The VHTRC cores embed of 4.0 %-enriched (primarily) blocks in the central rings of the core. The outer fuel rings include 2.0 %-enriched blocks or half-populated fuel blocks. The blocks from the outer layer of the VHTRC core are designated as the "minor" fuel blocks. In the lattice cells proposed, the medium surrounding the heterogeneous block is representative of the VHTRC HP core.

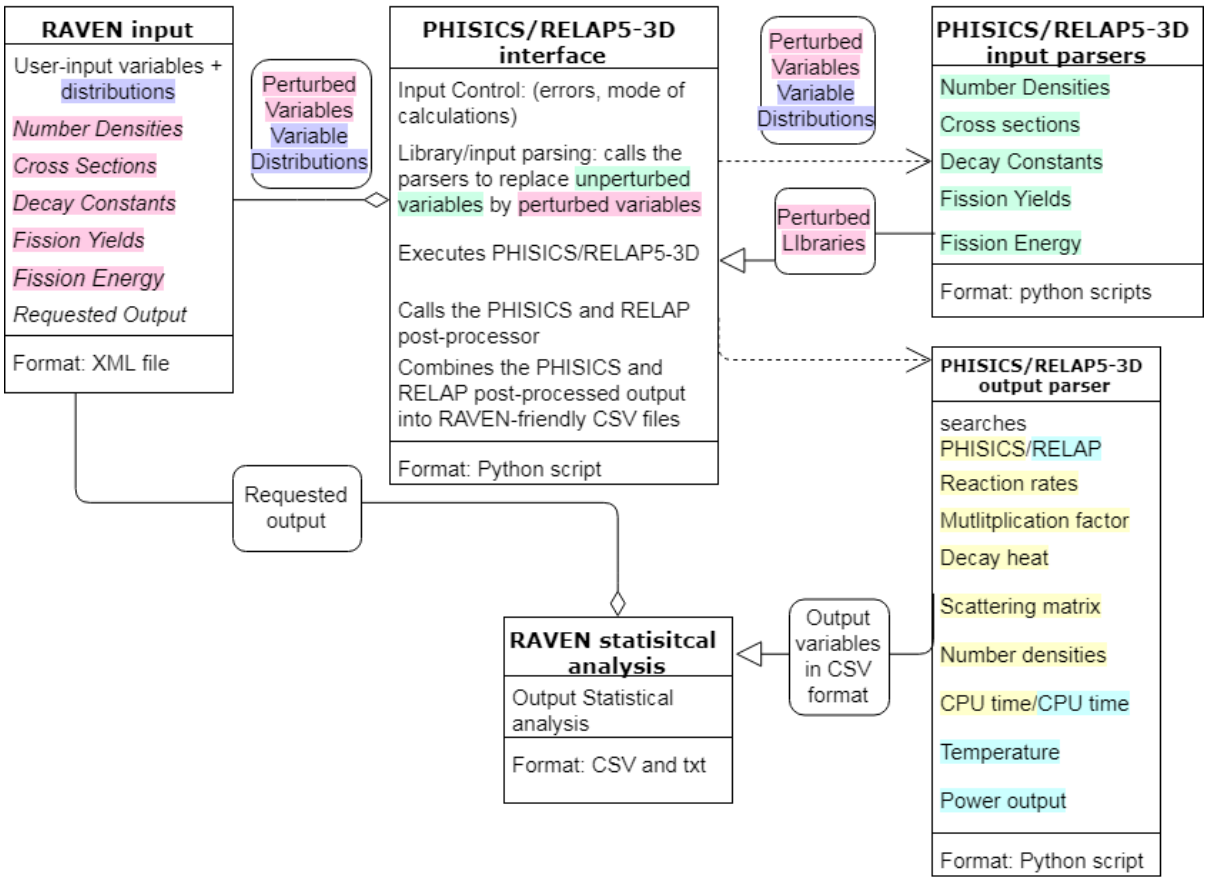

Figure 104. Data handling in RAVEN/PHISICS/RELAP5-3D

The lattice cell VHTRC HC-I (Figure 105, left) is executed twice in T-NEWT, once for the fuel and once for the reflector. At each run, the T-NEWT homogenization block indicates the mixtures homogenized together. A sub-sequent Python script prior the PHISICS core calculation generates the disadvantage factors from the mixture numbers and the corresponding scalar fluxes.

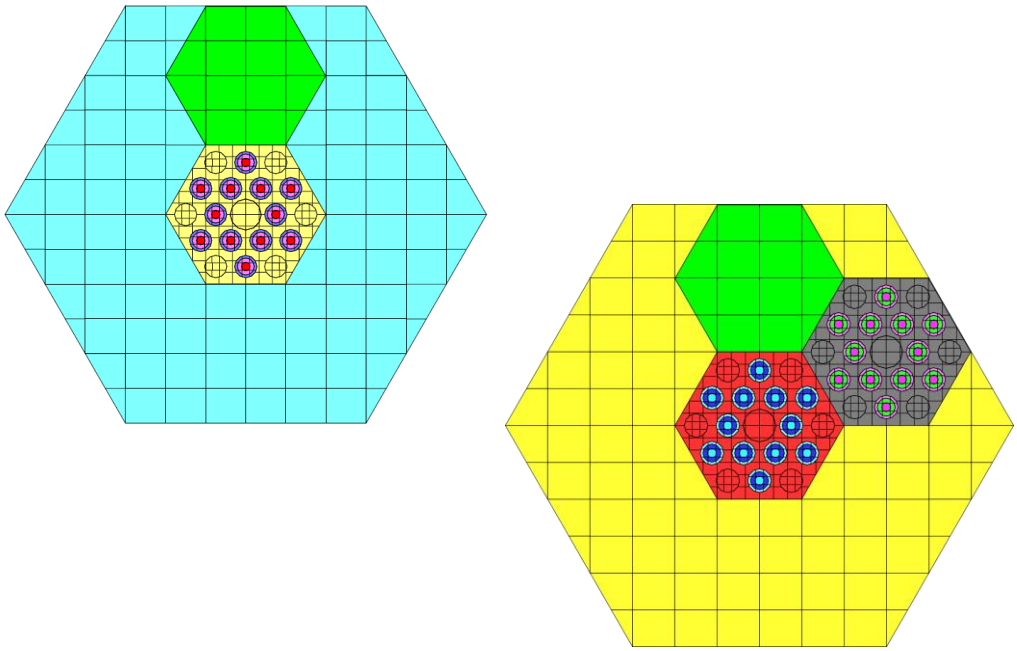

Figure 105. VHTRC lattice model for the HC-I core (left) and the HP core (right)

Figure 4 shows the VHTRC model built in PHISICS consists in five fuel rings. In Figure 4**,** The VHTRC core shape is perfectly hexagonal but PHISICS does not have the capability to model trapezoidal geometries. The PHISICS model also disregards the absorber blanket surrounding the core and assumes vacuum boundary conditions. Hence, the VHTRC system in PHISICS ignores the effects of back scattering from the blanket and the background. The PHISIC input does not substantiate the control rod lying in the top part of the reflector because no specifications were provided in the references. Graphite fills the electric heater channels, the control rod insertion holes and the BF_3 counter slots. Figure 106 depicts the core shape modeled in PHISICS. The actual VHTRC core contains 51 graphite blocks radially (42 fuel block plus 18 halves), while the PHISICS core (Figure 106) encompasses 49 blocks. Hence, the configuration in PHISICS is slightly under-reflected. The lattice cells model the graphite reflector as plain blocks and disregard the coolant gap in the one-, six- and nineteen-holed blocks. Figure 106 represents radially the core but the actual shape is representative of the VHTRC: a 3-D core, made of 72.0 fuel column in each half.

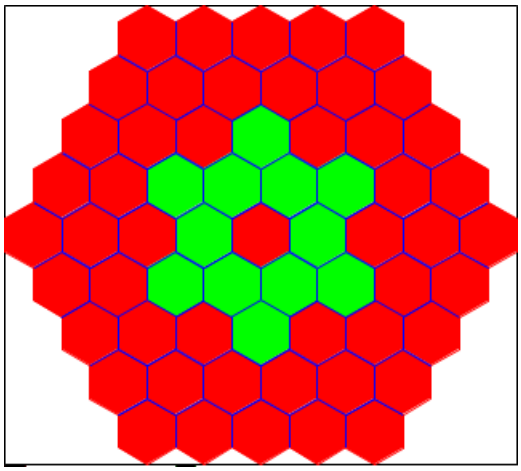

Figure 106. VHTRC HC core shape in PHISICS

7.2.2 Manufacturing Uncertainties Reported in the Experiment

7.2.2.1 Effective multiplication factor

This section overviews the uncertainties derived in the VHTRC experimental reports [65], [66]. The k_{eff} uncertainties reported from the experiment range from 0.00002 (HP core, 25.5 °C) to 0.00035 (HP core, 199.6 °C). Those uncertainties are the standard deviations of the corrected area ratios $f_j(A_p/A_c) = -\rho/\beta$ (see section 2.1.3) of the four detectors scattered in the VHTRC. The reports disregarded the following sources of uncertainties:

- The experiment was not replicated to evaluate the measurement precision;
- The experimental report does not specify the uncertainty arising from the precision of the detectors and the background noise of the experiment;
- Four-group nuclear constants and an empirical extrapolation between the experimental temperatures demonstrated the f_j factors. No uncertainties from cross sections were propagated to f_j;
- The least-square fitting did not contribute to the uncertainty [67];
- The coverage factor relative to the evaluated uncertainties was not provided;

Additionally, the final eigenvalues reported were the experimental values plus a correction factor. “Loading irregularities” (i.e. modeling uncertainties) justified the k_{eff} correction factor. Exhaustively, the loading irregularities include the reactivity effects caused by:

- The gap between the two assemblies;

- The tips of the control rods and safety rods poking in the fuel region even in withdrawn positions;
- The substitution of the BF_3 counters by graphite rods;
- The substitution of the electric heaters by graphite rods;
- The substitution of void holes by graphite rods;
- Dry out of moisture induced by increased temperatures;
- The substitution of the thermocouples and guide tubes by graphite rods.

The reports did not mention the nature of the methodologies (experimental or numerical) to determine the magnitude of the loading irregularities. The approach used to quantify most of the irregularities is referred to as "compensation methods" without additional explanation. The critical position of the CR before the temperature raise and after the temperature drop at 200 °C evaluated the magnitude of the dry-out effect. Overall, those effects could be described as "model corrections relevant for numerical design". The loading irregularities appear in two different types: the "all or nothing" type and the continuous type. Continuous distributions cannot model the "all or nothing" type because a VHTRC element substitutes another. For instance, graphite replaces the BF_3 counters. Physically, a quantity of N_g graphite atoms substitute without uncertainty a quantity N_i of isotopes *i*. The process is purely artificial. A smooth distribution can model the second type of loading irregularities. For instance, the moisture in the graphite elements or the gap between the blocks.

In the experiment, the individual reactivity contributions from each loading irregularity was added to the nominal value of the system's effective multiplication factor. A new uncertainty value complements the corrected effective multiplication factor to account for the loading irregularities' uncertainty contributions.

In a second step of the analysis, the MVP-II code [68] and the JENDL-3.3 library predicted the contribution of each uncertain parameter, aside from the loading irregularities. At the time, the code could not achieve perturbation-theory-based or sampling-based calculations. A "one-by-one" approach perturbed the input parameters instead. For each input parameter, the input uncertainty was summed to the nominal quantity, so MVP-II simulated two "perturbations". For instance, the specifications suggested an uncertainty of ± 0.5 ppm of equivalent boron in the coatings. One perturbation was performed with the nominal boron concentration in the coatings minus 0.5 ppm and a second one with impurities in the coatings set as nominal value plus 0.5

ppm. The contribution to the k_{eff} uncertainty materialized as the maximum of $|k_{eff}(perturbed) - k_{eff}(nominal)|$. In RAVEN/PHISICS, the perturbed variables oscillate around a normal distribution, so statistically 99.73 % of the values allocated to a variable are bounded between $\mu \pm 3\sigma$.

Table 32 summarizes the output uncertainties in the multiplication factor in the VHTRC experiment after corrections for loading irregularities and the uncertainties calculated with MVP-II.

Table 32. Uncertainties in k_{eff} reported in the VHTRC experiment and VHTRC simulation ([65])

	HP 25.5 °C	*HP 71.2 °C*	*HP 100.9 °C*	*HP 150.5 °C*	*HP 199.6 °C*	*HC-1 8.0 °C*	*HC-2 200.3 °C*
Experiment	0.00030	0.00034	0.00041	0.00052	0.00065	0.00031	0.00056
MVP-II code	0.00323	0.00333	0.00350	0.00354	0.00368	0.00339	0.00309

The uncertainties predicted numerically are about ten times larger than the uncertainties predicted by the experimentalists. Three hypotheses can explain this:

- the experimentalists under-evaluated the uncertainties, which could be verified by a repetition of the experiments, or
- the code over-estimated the uncertainties; which means either the approach chosen to estimate the uncertainties is incorrect or the input uncertainties were over-estimated, or
- all of the above.

The uncertainties derived in the MVP-II code constituted the final uncertainties because they represent the maximum uncertainties between the experimental prediction and the simulations. No data were provided on the measurement precision or repeatability.

7.2.2.2 Reactivity coefficient

Like the multiplication factor, experimental and numerical approaches evaluate the reactivity coefficient. The final uncertainty is the maximum uncertainty between the experimental estimate and the numerical prediction. In the experiment, the uncertainties on the temperature coefficient are based on “the uncertainty of the subcriticality determination and the temperature measurements” (from [66]). The uncertainty on the temperature measurements is combined from

the thermocouples' precision evaluated at ± 1 °C and the standard deviation of the temperatures measured. The "subcriticality determination" refers probably to the method used to measure the sub-critical state. The experimental report estimated the contribution of the BF_3 counters to the temperature coefficient α_T to be "not large". The reference [66] calculates α_T with Equation 7-1:

$$\alpha_T = \frac{1}{T_2 - T_1} \frac{(k_{eff}(T_2) - k_{eff}(T1)}{k_{eff}(T_2) k_{eff}(T_1)} + C \qquad \text{Equation 7-1}$$

C is a correction factor accounting for the thermal expansion of the graphite. It equals -1.0 × 10^{-5} % Δk/k ± 0.00000 (no uncertainty) in the temperature range [300 K; 500 K]. Note that the formula (1.2) provided in [65] disagrees with the formula provided in equation (3) in [66]. The temperature coefficient in Equation 7-1 is rewritten:

$$\alpha_T = \gamma + C \qquad \text{Equation 7-2}$$

The theoretical uncertainty on the temperature coefficient is:

$$\alpha_T = \sqrt{\delta\gamma^2 + \delta C^2} \qquad \text{Equation 7-3}$$

No uncertainty was defined on the thermal expansion term C, then the theoretical uncertainty is:

$$\delta\alpha_T = |\alpha_T| \sqrt{\left(\frac{\delta\Delta T}{\Delta T}\right)^2 + \left(\frac{\delta\Delta k}{\Delta k}\right)^2 + \left(\frac{\delta k_1}{k_1}\right)^2 + \left(\frac{\delta k_2}{k_2}\right)^2} \qquad \text{Equation 7-4}$$

$$\Delta k = k_{eff}(T_2) - k_{eff}(T_1) \;\; , \delta\Delta k = \sqrt{\delta k_1^2 + \delta k_2^2} \qquad \text{Equation 7-5}$$

$$\Delta T = T_2 - T_1 \;\; , \delta\Delta T = \sqrt{\delta T_1^2 + \delta T_2^2} \qquad \text{Equation 7-6}$$

Equation 7-4 does not account for the dependence of k_{eff} to the temperature. Reference [67] provides a more accurate methodology to derive the uncertainty:

$$\delta\alpha_T = \sqrt{\sum_{i=1}^{N}\left[\frac{\partial\alpha_T}{\partial x_i}\right]^2 u_i^2 + 2\sum_{i=1}^{N-1}\sum_{j=i+1}^{N}\frac{\partial\alpha_T}{\partial x_i}\frac{\partial\alpha_T}{\partial x_j}cov(x_i, x_j)}$$ Equation 7-7

$$\delta\alpha_T = \sqrt{\left[\frac{\partial\alpha_T}{\partial \Delta \mathrm{T}}\right]^2 \delta\Delta T^2 + \left[\frac{\partial\alpha_T}{\partial \Delta \mathrm{k}}\right]^2 \delta\Delta k^2 + 2\frac{\partial\alpha_T}{\partial\Delta T}\frac{\partial\alpha_T}{\partial\Delta k}cov(\Delta T, \Delta k)}$$ Equation 7-8

Table **33** summarizes the values of the temperature coefficient along with experimental uncertainties found in [65]. The uncertainties stem from the measured values in [65] because they seem to descend from [66]. The two papers agree on the measured nominal values. The references do not demonstrate the propagation of uncertainties reported in

Table **33**, so a column derives “revised” uncertainties using Equation 7-4 and the experimental data. The uncertainties on the temperature coefficient were computed from the uncertainties on the experimental multiplication factors and the uncertainties on the temperatures specified in

Table **33**. The "revised" column versus the experimental column overviews the spread of the nominal values and uncertainties one can obtain if different methodologies are applied.

The multiplication factors obtained with the simulations on MVP-II calculate the reactivity coefficients. The reports do not detail the methodology to compute the uncertainty through the simulations. Following the approach adopted for the effective multiplication factor, a "one-by-one" perturbation on an uncertain input parameter was carried out in a systematic way. The uncertain parameter takes two "perturbed" values: the maximum and minimum uncertainty. Table 34 and Table 35 recap for example the uncertainty contribution from the graphite sheath [65].

The report does not justify the uncertainties reported in Table 35 relative to the perturbed and nominal α_T. It is assumed they derive from the uncertainties found on the multiplication factor. A propagation of uncertainties is then performed based on the uncertainties provided on the multiplication factor in Table 34, Equation 7-4, Equation 7-5 and Equation 7-6.

$$\begin{aligned}
&\alpha_T^{25.5\rightarrow 71.2}(pert_{low}) \\
&= |-1.546| \\
&\times 10^{-4}\sqrt{\left(\frac{0.0005}{0.0074}\right)^2+\left(\frac{1.3}{-45.7}\right)^2+\left(\frac{0.00006}{1.0171}\right)^2+\left(\frac{0.00006}{1.0097}\right)^2} \\
&= 0.047\times 10^{-4}\frac{\Delta k}{k}/°C
\end{aligned} \qquad \text{Equation 7-9}$$

Table 33. Summary of the VHTRC temperature coefficient, plus uncertainties

$T_1 \rightarrow T_2$ (°C)	$\delta\Delta k$ $\times 10^{-5}$	$k_1 \pm \delta k_1$	$k_2 \pm \delta k_2$	$\alpha_T \pm \delta\alpha_T$ Revised (10^{-4} $\Delta k/k$)	$\alpha_T \pm \delta\alpha_T$ Measured (10^{-4} $\Delta k/k$)
	0.0005	1.0171±0.000	1.0097±0.000	-	-
25.5→71.2 ±1.3	0	3	4	1.677±0.123	1.488±0.073
	0.0005	1.0171±0.000	1.0045±0.000	-	-
25.5→100.9±1.6	0	3	4	1.636±0.073	1.597±0.055
	0.0005	1.0171±0.000	0.9957±0.000	-	-
25.5→150.5±1.6	8	3	5	1.690±0.051	1.673±0.041
	0.0007	1.0171±0.000	0.9869±0.000	-	-
25.5→199.6±1.8	6	3	7	1.828±0.049	1.078±0.064
	0.0005	1.0097±0.000	1.0045±0.000	-	-
71.2→100.9±1.7	6	4	4	1.726±0.212	1.764±0.155
	0.0006	1.0097±0.000	0.9957±0.000	-	-
71.2→150.5±1.7	4	4	5	1.756±0.088	1.780±0.069
	0.0008	1.0097±0.000	0.9869±0.000	-	-
71.2→199.6±1.9	1	4	5	1.882±0.072	1.786±0.069
100.9→150.5±1.	0.0008	1.0045±0.000	0.9957±0.000	-	-
9	6	4	5	1.777±0.145	1.789±0.120
100.9→199.6±2.	0.0008	1.0045±0.000	0.9869±0.000	-	-
0	0	4	5	1.889±0.095	1.793±0.103
150.5→199.6±2.	0.0008	0.9957±0.000	0.9869±0.000	-	-
0	6	5	5	1.924±0.203	1.796±0.174

The uncertainty calculated in the Table 35 from 25.5 to 71.2 °C is ± 0.018 10^{-4} Δk/k/°C. Otherwise, if the reasoning followed reference [65] consisting in taking the worse possible outcome was applied in the experimental report, the uncertainty on the temperature coefficient should be calculated from the difference of the highest achievable k_{eff} minus the lowest achievable k_{eff}. The index "eff" is removed for clarity. The index 1 and 2 referred to as parameters relative to temperature T_1 and T_2.

$$\begin{cases} {\alpha_T^{25.5\to71.2}}_{pert,low} = \dfrac{1}{T_2 - T_1}\dfrac{k_2 - k_1 + (\delta k_1 + \delta k_2)}{(k_2 + \delta k_2)(k_1 + \delta k_1)} + C \\ {\alpha_T^{25.5\to71.2}}_{pert,high} = \dfrac{1}{T_2 - T_1}\dfrac{k_2 - k_1 - (\delta k_1 + \delta k_2)}{(k_2 - \delta k_2)(k_1 - \delta k_1)} + C \end{cases} \qquad \text{Equation 7-10}$$

Table 34. k_{eff} reported in the experiment for a perturbation in the graphite density of the rod sheath

core	*T (°C)*	*Perturbed (-0.051 g.cm^{-3})*	*Unperturbed (g.cm^{-3})*	*Perturbed (+0.051 g.cm^{-3})*
	25.5	1.01508 ± 0.00006	1.01587 ± 0.00006	1.01688 ± 0.00006
	71.2	1.00785 ± 0.00006	1.00881 ± 0.00006	1.00983 ± 0.00006
HP	100.9	1.00287 ± 0.00006	1.00390 ± 0.00006	1.00477 ± 0.00006
	150.5	0.99460 ± 0.00006	0.99549 ± 0.00006	0.99645 ± 0.00006
	199.6	0.98632 ± 0.00006	0.98717 ± 0.00006	0.98812 ± 0.00006
HC-1	8.0	1.01323 ± 0.00006	1.01428 ± 0.00006	1.01514 ± 0.00006
HC-2	200.3	1.01031 ± 0.00006	1.01134 ± 0.00006	1.01257 ± 0.00006

$$\delta\alpha_T = max\left\{{\alpha_T^{25.5\to71.2}}_{p} - {\alpha_T^{25.5\to71.2}}_{nom}\right\} = 0.051 \times 10^{-4}\frac{\Delta k}{k}/°C \qquad \text{Equation 7-11}$$

The subscript *p* denotes the upper perturbation or lower perturbation from Equation 7-10. This approach does not account for the uncertainty on the temperature. Even without the propagation of the temperature uncertainty, the experimental report underestimates the α_T uncertainty using both methodologies (The analytical methodology with Equation 7-4 or the methodology applied in the experiment and corrected with "the worst case scenario approach" with Equation 7-11).

Table 35. α_T reported in the experiment for a perturbation in the graphite density of the rod sheath

		$\alpha_T(10^{-4}\ \Delta k/k/°C)$		
Temperature difference		*Perturbed*	*Nominal*	*Perturbed*
ΔT (°C)		*(-0.051 g.cm^{-3})*		*(+0.051 g.cm^{-3})*
45.7	(25.5→71.2)	-1.546 ± 0.018	-1.507 ± 0.018	-1.502 ± 0.018
75.4	(25.5→100.9)	-1.591 ± 0.011	-1.557 ± 0.011	-1.572 ± 0.011
125	(25.5→150.5)	-1.623 ± 0.007	-1.612 ± 0.007	-1.613 ± 0.007
174.1	(25.5→199.6)	-1.650 ± 0.005	-1.644 ± 0.005	-1.644 ± 0.005
29.7	(71.2→100.9)	-1.659 ± 0.028	-1.632 ± 0.028	-1.679 ± 0.028
79.3	(71.2→150.5)	-1.667 ± 0.011	-1.673 ± 0.011	-1.677 ± 0.011
128.4	(71.2→199.6)	-1.687 ± 0.007	-1.692 ± 0.007	-1.694 ± 0.007
49.6	(100.9→150.5)	-1.672 ± 0.017	-1.697 ± 0.017	-1.675 ± 0.017
98.7	(100.9→199.6)	-1.695 ± 0.009	-1.710 ± 0.009	-1.699 ± 0.009
49.1	(150.5→199.6)	-1.719 ± 0.018	-1.724 ± 0.018	-1.723 ± 0.018

The propagation may not be rigorous when the contribution of each parameter is reported in the table. The methodology relies on the maximum possible difference achievable to define the uncertainty contribution. The worst possible scenario does not account for the intermediate uncertainties predicted for each contribution. For example, the graphite density of the rod sheath

uncertainty at 25.5 ° to 71.2 °C is the difference between the lower bound perturbation (-1.546 Δk/k/°C) to the nominal value (-1.507 Δk/k/°C) in Table 35, and is equal to 0.039 Δk/k/°C as reported in the reference. If the "worst case scenario" logic is followed, the intermediate uncertainties on the perturbed and nominal α_T values should be accounted for. Assuming the uncertainties reported in the experiment were computed correctly, the lower bound becomes (-1.546 Δk/k/°C – 0.018 Δk/k/°C) and the nominal case becomes (-1.507 Δk/k/°C + 0.018 Δk/k/°C), giving an uncertainty of 0.075 Δk/k/°C instead of 0.039 Δk/k/°C.

Note also that the uncertainty on the temperature was evaluated but the effect of the temperature on the multiplication factor was not estimated. A repetition of the experiment would let the system vary around its temperature range (evaluated to be ±1.5 °C on average for the various experiments) and include another component to the k-eff uncertainty.

7.2.3 Manufacturing Uncertainties in RAVEN/PHISICS Compared to the Experimental Data

7.2.3.1 Effective multiplication factor

The documented data originating from the VHTRC experiment include estimates of manufacturing uncertainties. Table 36 lists the manufacturing data from [65].

Table 36. Uncertainties evaluated in the VHTRC experiment

	Manufacturing uncertainty	*Value ± Uncertainty*
1	^{235}U isotopic abundance of B-2 type kernel (wt. %)	2.000 ± 0.0020
2	^{235}U isotopic abundance of B-4 type kernel (wt. %)	4.000 ± 0.0032
3	Number of coated particles in B-2 fuel type	(2.00×10^4)±2.7%
4	Number of coated particles in B-4 fuel type	(2.04×10^4)±2.2%
5	Graphite density of fuel rod sheath ($g.cm^{-3}$)	1.674 ± 0.051
6	Graphite density of blocks, rods, and end gaps ($g.cm^{-3}$)	1.671 ± 0.001
7	Graphite density of B-2 type fuel compact matrix ($g.cm^{-3}$)	1.710 ± 0.020
8	Graphite density of B-4 type fuel compact matrix ($g.cm^{-3}$)	1.690 ± 0.020
9	Impurities in UO_2 (ppmw-EBC)	0.160 ± 00160
10	Impurities in graph. blocks, rods, end caps, sheaths (ppmw-EBC)	0.070 ± 0.050
11	Impurities in fuel compact matrix (ppmw-EBC)	0.160 ± 0.0160
12	Impurities in coating layers of fuel particles (ppmw-EBC)	0.160 ± 0.0160

The uncertainties from Table 36 are implemented in the RAVEN/PHISICS model with the following assumptions:

- These input uncertainties represent the one standard deviation distributed over a normal distribution.
- These uncertainties are independent to each other, except for the number of particles and the fuel abundance (entry 1, 2, 3 and 4). A first calculation treats the uncertainties 1, 2, 5 – 12. A second random sampling from RAVEN/PHISICS propagates the uncertainties from 3 and 4.

The effect of the variables on the multiplication factor are evaluated individually and globally from these simulations, performed at 8.0°C (HC-I core), 25.5°C, 71.2°C, 100.9°C, 150.5°C (HP cores) and 200.3 °C (HC-II core).

The scalar flux originates from T-NEWT lattice calculations to derive the lattices' disadvantage factors at the core temperatures. Hence, the disadvantage factors are computed before the perturbation of the manufacturing uncertainties. Consequently, they do not account for the neutron flux variations induced by the manufacturing uncertainties. The assumption of "frozen" disadvantage factors seems acceptable for the independent variables presented in Table 36, but *a*

priori less acceptable for the number of particles in the fuel considering the magnitude of the uncertainty. This justifies why the number of BISO particles are perturbed aside from the other parameters. The uncertainties are recombined *a posteriori* into the total uncertainty.

The uncertainty in number densities may introduce "substitution" effects in the cores. For example, a negative perturbation in the graphite matrix triggers a positive perturbation in the gap or a positive perturbation in the outer layer of the BISO particles. The experimental report does not mention how the substitution effects were treated in the numerical simulations. RAVEN/PHISICS deals with the substitution effect through matrices of a multivariate variables. Physically, a change in the number of BISO particles induces an equal change with the opposite sign in the graphite matrix. The reciprocity is not true: a change in the graphite matrix does not induce a change in the number of coated particles. Identically, a change in the ^{235}U abundance compensates an equal change in the ^{238}U concentration. A conservation of the number of isotopes approximates the compensations in the graphite matrix or in the fuel. *N* atoms from the coated particles appearing induces *N* atoms of graphite from the matrix to disappear, and *vice versa*. Figure 107 identifies the relative covariance matrix proposed to account for the number of BISO particle uncertainty ($\sigma = 2.2$ %). An increase of sigma (relative) in the fuel induces an increase of sigma (relative) in the coatings. The correlation coefficient equals -1 between the particles (fuel and coatings) and the graphite matrix. This multivariate matrix does not account for the cross-correlation effects, i.e. the impurities or the matrix density uncertainties. Those effects were accounted for as independent variables in assumptions 1, 2, 5 – 12. It is verified after the RAVEN post-processing that the particle-to-particle isotopes have Pearson coefficients (correlation coefficients) equal to 1. The matrix-to-matrix and particle-to-matrix correlation coefficients are equal respectively to 1 and -1.

Mathematically, the relationship between the ^{235}U and ^{238}U is also purely linear, hence the correlation coefficient equals 1. The covariance between those two isotopes is simply the product of their absolute standard deviations. Figure 108 provides the covariance matrix of the B-4 and B-2 fuel. The cross-correlation effects are not tallied in the total uncertainty and may lead to uncertainty underestimations.

	Non-matrix isotopes				*Matrix isotopes*		
	^{234}U	^{235}U	…	^{11}B	C	^{10}B	^{11}B
^{234}U	4.840E-04	4.840E-04	…	4.840E-04	-9.296E-08	-9.296E-08	-9.296E-08
^{235}U	4.840E-04	4.840E-04	…	4.840E-04	-9.296E-08	-9.296E-08	-9.296E-08
^{238}U	4.840E-04	4.840E-04	…	4.840E-04	-9.296E-08	-9.296E-08	-9.296E-08
.	.	.	…	.	.	.	.
.	.	.	…	.	.	.	.
.	.	.	…	.	.	.	.
^{11}B	4.840E-04	4.840E-04	…	4.840E-04	-9.296E-08	-9.296E-08	-9.296E-08
C	-9.296E-08	-9.296E-08	…	-9.296E-08	9.296E-08	9.296E-08	9.296E-08
^{10}B	-9.296E-08	-9.296E-08	…	-9.296E-08	9.296E-08	9.296E-08	9.296E-08
^{11}B	-9.296E-08	-9.296E-08	…	-9.296E-08	9.296E-08	9.296E-08	9.296E-08

Figure 107. Relative covariance matrix of the B-4 type particles and the graphite matrix

	^{235}U	^{238}U
^{235}U	5.3826E-17	-5.3826E-17
^{238}U	-5.3826E-17	5.3826E-17

	^{235}U	^{238}U
^{235}U	2.1101E-17	-2.1101E-17
^{238}U	-2.1101E-17	2.1101E-17

Figure 108. Relative covariance matrix of the ^{235}U abundance in B-4 fuel (left) and B-2 fuel (right)

PHISICS only accepts homogenized number densities accompanied with the flux-weighted cross sections originating from the lattice cells. The VHTRC core is built from a block basis (Figure 106). Three types of cells (a) B-4 fuel blocks (b) B-2 fuel blocks and (c) reflector blocks load the PHISICS VHTRC core.

Table **37** shows the main data relevant to the volume-averaged homogenization, including the normalized volume coefficient R_i of each region of the VHTRC core. The volume-averaging is performed over one fuel block. The fuel blocks have a 15.005 cm flat-to-flat distance and are axially 72.02 cm long.

Table 37. Volume-averaged number densities of the VHTRC blocks (B-4 and B-4 fuel blocks)

Iso.	*Region*	*B-4 fuel blocks*		*B-2 fuel blocks*	
		R_{B4}	*Number densities* $(at.b^{-1}.cm^{-1})$	R_{B2}	*Number densities* $(at.b^{-1}.cm^{-1})$
^{234}U	Fuel kernels	0.009810	7.3910E-08	0.004881	1.5569E-08
^{235}U			9.1708E-06		2.2968E-06
^{236}U			5.7531E-08		1.8296E-09
^{238}U			2.1719E-04		1.1110E-04
^{16}O			4.5298E-04		2.2717E-04
^{10}B			1.8006E-10		9.0201E-11
^{11}B			7.2473E-10		3.6307E-10
$C^{\dagger}$	First coating	0.009989	5.9100E-04	0.004940	2.9474E-04
^{10}B			2.0906E-11		1.0426E-11
^{11}B			8.4148E-11		4.1966E-11
C	Second coating	0.014935	1.4003E-03	0.007486	7.0194E-04
^{10}B			4.9533E-11		2.4830E-11
^{11}B			1.9938E-10		9.9945E-11

Figure 37 (continued)					
C			7.0076E-03		3.5039E-03
^{1}H			2.6169E-06		1.3085E-06
^{16}O	Matrix	0.082723	1.3085E-06	0.04088	6.5426E-07
^{10}B			2.4795E-10		1.2398E-10
^{11}B			9.9806E-10		4.9904E-10
C			8.7013E-03		4.3506E-03
^{10}B			1.3467E-10		6.7334E-11
^{11}B			5.4208E-10		2.7104E-10
^{1}H	Sheath	0.103679	1.2764E-06	0.05184	6.3820E-07
^{16}O			9.1024E-07		4.5512E-07
^{14}N			1.0102E-06		5.0512E-07
^{15}N			3.6908E-09		1.8454E-09
C			6.0999E-02		7.2087E-02
^{10}B			9.4413E-10		1.1158E-09
^{11}B			3.8002E-09		4.4910E-09
^{1}H	Graphite ††	0.72799	8.9477E-06	0.8603	1.0574E-05
^{16}O			6.3931E-06		7.5552E-06
^{14}N			7.1263E-06		8.4217E-06
^{15}N			2.6034E-08		3.0767E-08
^{4}He	Hollow cyl.	0.038978	9.5886E-07	0.01947	4.7890E-07
^{4}He	Gaps	0.011897	2.9268E-07	0.01018	2.5054E-07

† all the carbon are graphite allotropes

†† Graphite component

RAVEN/PHISICS simulates 250 perturbations of the 3-D VHTRC core surrounded by vacuum boundary conditions in ~ 18 seconds with six-group libraries and ~180 seconds with a 56-group library (half axial symmetry, no radial symmetry). The calculations are achieved with a six-group structure (Table 38) unless mentioned otherwise. Table 39 summarizes the total uncertainty and the individual contributions on the effective multiplication factor. The uncertainties computed by RAVEN are bolded and complemented with the confidence interval (in italic) below. The regular-captioned values come from the experimental report. The relative confidence interval for the uncertainties (one standard deviation) computed with RAVEN covers -8.0 % < σ < 9.6 %. The values relative to the confidence interval are provided in Table 40. Note that misinterpretations of the input uncertainties (range, nature of the distribution) modifies the total uncertainty and then the absolute confidence interval.

Figure 109 sketches the total uncertainties from RAVEN/PHISICS and the experiment. The propagation of uncertainties on the number of BISO particles without substitution effects (i.e. the particles are added/subtracted without modifying accordingly the graphite matrix) was performed on the HC core at 8.0 °C and is worth ± 0.00358 instead of ± 0.00325. The contribution of the ^{235}U abundance without substitution effects (i.e. without replacing the added/subtracted ^{235}U by ^{238}U) was estimated in a separate sampling batch to be ± 0.00033 in the HC core at 8.0 °C, versus ± 0.00018 with the substitution effects. The major discrepancy between the experimental data and the RAVEN/PHISICS sampling is the contribution of the impurities in the graphite. This effect was measured separately in another 250 sampling batch and the uncertainty on the k_{eff} was estimated at ± 0.00072 with a confidence interval of [0.00066; 0.00078], confirming the initial predictions. Table 40 provides the intermediate data to derive the tolerance interval.

Table 38. Upper energy boundaries of the six-group structure, in eV

1	*2*	*3*	*4*	*5*	*6*	
2.000E+07	5.500E+05	5.060E+01	3.763E+01	1.110E+00	4.500E-01	0.00187

Table 39. Uncertainties on k_{eff} in the VHTRC induced by manufacturing uncertainties

Contrib.	*HC-I**	*HP*	*HP*	*HP*	*HP*	*HP*	*HC-II*
	8.0 °C	*25.5 °C*	*71.2 °C*	*100.9 °C*	*150.5 °C*	*199.6 °C*	*200.3 °C*
^{235}U	±0.00016	±0.00034	±0.00038	±0.00044	±0.00019	±0.00027	±0.00026
% wt	**±0.00018**	**±0.00018**	**±0.00018**	**±0.00018**	**±0.00018**	**±0.00019**	**±0.00016**
(B-2 &	*0.00016*	*0.00016*	*0.00016*	*0.00016*	*0.00017*	*0.00017*	*0.00015*
B-4)	*0.00020*	*0.00020*	*0.00020*	*0.00020*	*0.00020*	*0.00020*	*0.0018*
C	±0.00105	±0.00101	±0.00102	±0.00103	±0.00096	±0.00095	±0.00123
sheath	**±0.00083**	**±0.00083**	**±0.00082**	**±0.00081**	**±0.00081**	**±0.00081**	**±0.00081**
	0.00076	*0.00076*	*0.00075*	*0.00075*	*0.00074*	*0.00074*	*0.00074*
	0.00091	*0.00091*	*0.00089*	*0.00089*	*0.00089*	*0.00088*	*0.00088*
C	±0.00038	±0.00044	±0.00033	±0.00032	±0.00033	±0.00041	±0.00042
(blocks	**±0.00019**	**±0.00019**	**±0.00019**	**±0.00019**	**±0.00019**	**±0.00019**	**±0.00017**
&	*0.00017*	*0.00017*	*0.00017*	*0.00017*	*0.00018*	*0.00018*	*0.00015*
Refl.)	*0.00020*	*0.00020*	*0.00021*	*0.00021*	*0.00021*	*0.00021*	*0.00018*
Matrix	±0.00017	±0.00029	±0.00018	±0.00030	±0.00020	±0.00022	±0.00029
(B-4	**±0.00024**	**±0.00024**	**±0.00024**	**±0.00024**	**±0.00024**	**±0.00024**	**±0.00027**
&	*0.00022*	*0.00022*	*0.00022*	*0.00022*	*0.00022*	*0.00022*	*0.00025*
B-2)	*0.00026*	*0.00026*	*0.00026*	*0.00026*	*0.00026*	*0.00026*	*0.00029*
	±0.00018	±0.00018	±0.00006	±0.00024	±0.00003	±0.00006	±0.00009
Impur.	**±0.00008**	**±0.00008**	**±0.00008**	**±0.00008**	**±0.00007**	**±0.00007**	**±0.00007**
(UO_2)	*0.00007*	*0.00007*	*0.00007*	*0.00007*	*0.00007*	*0.00007*	*0.00007*
	0.00008	*0.00008*	*0.00008*	*0.00008*	*0.00008*	*0.00008*	*0.00008*
Impur.	±0.00017	±0.00018	±0.00014	±0.00017	±0.00013	±0.00011	±0.00016
(Matrix)	**±0.00011**	**±0.00011**	**±0.00011**	**±0.00011**	**±0.00011**	**±0.00011**	**±0.00009**
	0.00010	*0.00010*	*0.00010*	*0.00010*	*0.00010*	*0.00010*	*0.00009*
	0.00012	*0.00012*	*0.00012*	*0.00012*	*0.00012*	*0.00012*	*0.00010*

Table 39 (continued)							
Impur.	±0.00101	±0.00102	±0.00096	±0.00101	±0.00097	±0.00095	±0.00087
(Graph.	**±0.00065**	**±0.00065**	**±0.00062**	**±0.00061**	**±0.00060**	**±0.00058**	**±0.00046**
&	*0.00060*	*0.00060*	*0.00057*	*0.00056*	*0.00055*	*0.00054*	*0.00042*
Refl.)	*0.00071*	*0.00071*	*0.00068*	*0.00067*	*0.00066*	*0.00064*	*0.00051*
Impur.	±0.00022	±0.00014	±0.00012	±0.00013	±0.00012	±0.00015	±0.00007
(Coat-	**±0.00003**	**±0.00003**	**±0.00003**	**±0.00003**	**±0.00002**	**±0.00002**	**±0.00002**
ings)	*0.00002*	*0.00002*	*0.00002*	*0.00002*	*0.00002*	*0.00002*	*0.00002*
	0.00003	*0.00003*	*0.00003*	*0.00003*	*0.00003*	*0.00003*	*0.00003*
Sub-Tot.	±0.00156	±0.00159	±0.00154	±0.00160	±0.00144	±0.00146	±0.00162
k_{eff}**	**±0.00112**	**±0.00111**	**±0.00109**	**±0.00109**	**±0.00108**	**±0.00107**	**±0.00100**
	0.00103	*0.00103*	*0.00101*	*0.00100*	*0.00099*	*0.00098*	*0.00092*
	0.00123	*0.00122*	*0.00120*	*0.00119*	*0.00118*	*0.00117*	*0.00110*
# part.***	±0.00299	±0.00279	±0.00295	±0.00295	±0.00319	±0.00331	±0.00280
B-2 &	**±0.00325**	**±0.00326**	**±0.00339**	**±0.00344**	**±0.00350**	**±0.00357**	**±0.00235**
B-4	*0.00299*	*0.00299*	*0.00311*	*0.00316*	*0.00321*	*0.00328*	*0.00216*
	0.00356	*0.00357*	*0.00371*	*0.00377*	*0.00383*	*0.00391*	*0.00257*
Grand to-	±0.00339	±0.00323	±0.00333	±0.00350	±0.00354	±0.00368	±0.00309
tal k_{eff}***	**±0.00343**	**±0.00345**	**±0.00356**	**±0.00361**	**±0.00366**	**±0.00373**	**±0.00255**
	0.00316	*0.00317*	*0.00327*	*0.00332*	*0.00337*	*0.00343*	*0.00234*
	0.00377	*0.00378*	*0.00390*	*0.00395*	*0.00401*	*0.00408*	*0.00280*

* No B-2 type fuel in the HC core

**sub-total without the contribution of the number of particles

***Evaluation with the substitution effects

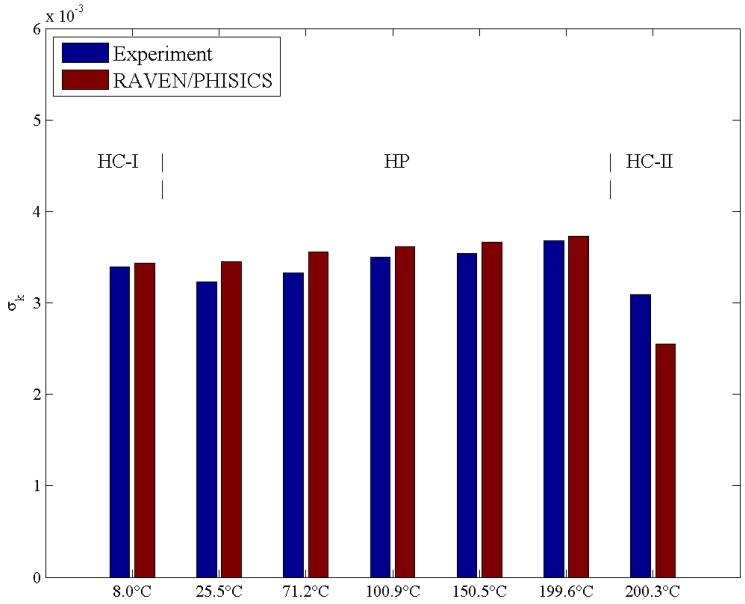

Figure 109. Histogram of propagation of the manufacturing uncertainties to the k_{eff} total uncertainty in RAVEN/PHISICS compared to the experiment

Table 40. Intermediate values relative to the 95% confidence interval

Parameter	*Value*	*Comments*
Number of samples	250	249 degrees of freedom
χ^2 (lower bound)	294.601	$(1-\alpha/2) = 0.975$
χ^2 (upper bound)	207.186	$\alpha/2 = 0.0250$
Lower CI	-8.0 %	Use Equation 3-3: Lower CI = $CI^{\%}_{low}$ - 1
Upper CI	9.6 %	Use Equation 3-3: Upper CI = $CI^{\%}_{up}$ - 1

As a verification process, Table 41 compares the relative standard deviations to the input uncertainties provided in the experimental report, after the 250 sampling. The same seed is conserved from one VHTRC core to another, so the standard deviations relative to the input variables do not vary.

Table 41. Verification of the standard deviations after the RAVEN sampling process (HP core 25.5 °C)

Blocks type	*Region*	*Isotope*	*Relative sigma*	*Expected relative sigma*
Reflector	*Reflector*	*C*†	6.04E-04	6.00E-04
		^{10}B	7.84E-01	7.14E-01
		^{11}B	7.68E-01	7.14E-01
B-4	*Fuel*	*^{235}U*	8.68E-04	8.00E-04
		^{238}U	3.66E-05	3.37E-05
		^{10}B	9.08E-01	1.00E-00
		^{11}B	9.96E-01	1.00E-00
	First coating	*C*	5.94E-04	6.00E-04
		^{10}B	1.01E+00	1.00E-00
		^{11}B	1.15E+00	1.00E-00
	Second coating	*C*	5.87E-04	6.00E-04
		^{10}B	1.11E+00	1.00E-00
		^{11}B	1.11E+00	1.00E-00
	Matrix	*C*	1.20E-02	1.18E-02
		^{10}B	9.97E-01	1.00E-00
		^{11}B	1.08E+00	1.00E-00

Table 41 (continued)

B-4	*Sheath*	*C*	2.99E-02	3.05E-02
		^{10}B	7.29E-01	7.14E-01
		^{11}B	7.33E-01	7.14E-01
	Block comp.	*C*	6.15E-04	6.00E-04
		^{10}B	6.64E-01	7.14E-01
		^{11}B	7.01E-01	7.14E-01
B-2	*Fuel*	^{235}U	1.04E-03	1.00E-03
		^{238}U	2.14E-05	2.06E-05
		^{10}B	9.04E-01	1.00E-00
		^{11}B	1.04E+00	1.00E-00
	First coating	*C*	6.24E-04	6.00E-04
		^{10}B	9.00E-01	1.00E-00
		^{11}B	9.46E-01	1.00E-00
	Second coating	*C*	5.87E-04	6.00E-04
		^{10}B	9.42E-01	1.00E-00
		^{11}B	1.10E+00	1.00E-00
	Matrix	*C*	1.16E-02	3.04E-02
		^{10}B	9.50E-01	1.00E-00
		^{11}B	9.13E-01	1.00E-00

Table 41 (continued)

B-2	*Sheath*	*C*	3.11E-02	3.04E-02
		^{10}B	6.51E-01	7.14E-01
		^{11}B	6.89E-01	7.14E-01
	Block comp.	*C*	5.96E-04	6.00E-4
		^{10}B	6.92E-01	7.14E-01
		^{11}B	7.51E-01	7.14E-01

† All carbon regions are graphite allotropes

The individual contributions specified in Table 39 are computed manually from the individual sensitivities. The input uncertainties are considered independent of each other. The individual variance contribution of a parameter P_i on the k_{eff} uncertainty is:

$$Var(k_{eff}) = \sum_i \left[\frac{\partial k_{eff}}{\partial P_i}\right]^2 Var(P_i) \qquad \text{Equation 7-12}$$

If the parameters are not independent:

$$Var(k_{eff}) = \sum_i \frac{\partial k_{eff}}{\partial P_i}\frac{\partial k_{eff}}{\partial P_j} cov(P_i, P_j) \qquad \text{Equation 7-13}$$

The partial derivative term is the sensitivity of the effective multiplication factor to the parameter P_i. Table 42 shows the sensitivities in the core HC-I (8.0°C) and the core HC-II (200.3 °C). The material indices refer to the region they belong to. Isotopes with an identical material index are part of the same T-NEWT mixture. Hence, the table lists the individual contribution of each isotope in each mixture exhaustively. Table 43 maps the material indices to the T-NEWT mixtures. It is verified that the sum of the products between the squared sensitivities and the input parameters' variance equals the sub-total uncertainty on k_{eff} in Table 39 (contribution without the number of BISO particle uncertainty).

Table 42. k_{eff} Sensitivity coefficients in cores HC-I and HC-II

Statistical parameters	*Mat. index*	*8.0 °C* ***Sensitivity B-4 blocks (at.b^{-1}cm^{-1})*** *Var Pi*	*200.3 °C* ***Sensitivity B-4 block (at.b^{-1}cm^{-1})*** *Var Pi*	***Sensitivity B-2 block (at.b^{-1}cm^{-1})*** *Var Pi*
$\frac{\partial k_{eff}}{\partial^{235}U}$	4	**3.2789E+04**	**1.429E+04**	**5.925E+03**
		5.61E-17	6.33E-17	2.27E-17
$\frac{\partial k_{eff}}{\partial^{238}U}$	4	**-1.680E+04**	**-1.429E+04**	**-5.925E+03**
		5.61E-17	6.33E-17	2.27E-17
$\frac{\partial k_{eff}}{\partial C}$	2	**2.9966E+00**	**2.531E+00**	**2.531E+00**
		2.69E-09	2.56E-09	2.56E-09
$\frac{\partial k_{eff}}{\partial^{10}B}$	2	**-6.1732E+05**	**-3.641E+05**	**-3.641E+05**
		7.96E-19	8.79E-19	8.79E-19
$\frac{\partial k_{eff}}{\partial^{11}B}$	2	**-1.1798E+02**	**5.067E+00**	**5.067E+00**
		1.19E-17	1.34E-17	1.34E-17
$\frac{\partial k_{eff}}{\partial^{10}B}$	4	**-4.5827E+05**	**-3.829E+05**	**-1.270E+05**
		2.96E-20	3.02E-20	2.79E-20
$\frac{\partial k_{eff}}{\partial^{11}B}$	4	**1.5001E+03**	**3.163E+01**	**2.976E+02**
		5.63E-19	5.41E-19	4.62E-19
$\frac{\partial k_{eff}}{\partial C}$	6	**3.0001E+00**	**2.561E+00**	**1.396E+00**
		1.18E-13	1.29E-13	1.35E-13

Table 42 (continued)

$\frac{\partial k_{eff}}{\partial {}^{10}B}$	6	**-4.1926E+05**	**-3.840E+05**	**-1.161E+05**
		4.07E-22	3.36E-22	3.87E-22
$\frac{\partial k_{eff}}{\partial {}^{11}B}$	6	**-4.5965E+03**	**1.200E+03**	**-3.496E+03**
		6.25E-21	8.66E-21	6.95E-21
$\frac{\partial k_{eff}}{\partial C}$	8	**3.3379E+00**	**2.966E+00**	**1.223E+00**
		8.95E-13	6.92E-13	6.80E-13
$\frac{\partial k_{eff}}{\partial {}^{10}B}$	8	**-4.5000E+05**	**-3.897E+05**	**-1.334E+05**
		2.62E-21	2.74E-21	2.58E-21
$\frac{\partial k_{eff}}{\partial {}^{11}B}$	8	**-3.4043E+02**	**1.906E+03**	**5.572E+02**
		4.70E-20	4.23E-20	4.38E-20
$\frac{\partial k_{eff}}{\partial C}$	10	**3.1899E+00**	**3.039E+00**	**9.337E-01**
		5.72E-09	7.08E-09	7.65E-09
$\frac{\partial k_{eff}}{\partial {}^{10}B}$	10	**-4.5776E+05**	**-3.863E+05**	**-1.278E+05**
		6.08E-20	5.37E-20	5.91E-20
$\frac{\partial k_{eff}}{\partial {}^{11}B}$	10	**-2.0396E+02**	**1.005E+02**	**-4.131E+02**
		9.91E-19	8.95E-19	1.08E-18
$\frac{\partial k_{eff}}{\partial C}$	13	**3.0802E+00**	**2.950E+00**	**9.034E-01**
		7.21E-08	6.79E-08	7.38E-08
$\frac{\partial k_{eff}}{\partial {}^{10}B}$	13	**-4.7907E+05**	**-4.053E+05**	**-1.289E+05**
		8.26E-21	1.04E-20	8.51E-21

Table 42 (continued)

$\frac{\partial k_{eff}}{\partial {}^{11}B}$	13	**9.0001E+02**	**1.324E+02**	**5.393E+02**
		1.44E-19	1.61E-19	1.38E-19
$\frac{\partial k_{eff}}{\partial C}$	14	**2.7850E+00**	**2.764E+00**	**8.533E-01**
		1.36E-09	1.41E-09	1.33E-09
$\frac{\partial k_{eff}}{\partial {}^{10}B}$	14	**-5.3422E+05**	**-4.374E+05**	**-1.368E+05**
		4.17E-19	4.59E-19	4.38E-19
$\frac{\partial k_{eff}}{\partial {}^{11}B}$	14	**-2.9352E+01**	**-6.277E+00**	**3.107E+01**
		7.72E-18	7.02E-18	7.72E-18

Table 43. Mixture index mapping

Mixture number	*Region*
2	Graphite reflector
4	Fuel
6	First coating
8	Second coating
10	Graphite matrix
13	Graphite Sheath
14	Graphite component in blocks

It was also attempted to evaluate the effects of the loading irregularities in core HC-II (200.3 °C) even if the experimental report did not specify these input uncertainties. The following uncertainties were modeled:

- The moisture in the matrix, graphite component and reflector with a 50 % relative standard deviation;

- A 5% standard deviation is given to the gap between the blocks;
- The tip of the control rod in the top location can vary ± 1 cm from its nominal position;

The total uncertainty equals ± 0.00020 (far from the estimated value of 0.00785). This estimate did not account for the major loading uncertainties (BF_3 counters, heaters, void holes). The gap contribution from RAVEN is equal to 0.00008 (0.00092 in the experimental report) and the CR contribution 0.00005 (0.00039 in the experimental report). The moisture content was explicitly quantified in the experimental report and a good agreement is found between the experimental output uncertainty (0.00015) and RAVEN/PHISICS (0.00017).

Currently, the uncertainty on the input temperature cannot really be accounted for in RAVEN/PHISICS because the cross sections are generated at a given temperature with the lattice code. The manufacturing uncertainties are perturbed within PHISICS afterwards. To perturb the temperatures in the model, two possibilities are available for future developments. The “discrete” solution would consist in perturbing the temperatures with SAMPLER/NEWT, generating M sets of cross sections at normally-distributed temperatures (M<N, N being the number of perturbations in RAVEN) for the lattices, and using randomly those sets of N libraries in the RAVEN/PHISICS model. The “continuous” solution would consist in using the RAVEN/PHISICS/NEWT version of the sequence, perturbing with RAVEN/NEWT the temperatures to generate the cross sections on-the-fly for each perturbation. This approach is more rigorous but much more computationally expensive, because it would require new self-shielding calculations at each code execution. This approach would also account for the implicit effects, by perturbing the number densities straight from the lattice code, and hence recalculating the disadvantage factors at each perturbation.

7.2.3.2 Systematic Bias versus Statistical Uncertainty in the Manufacturing Process

In section 7.2.3.2, RAVEN/PHISICS propagates the manufacturing input uncertainties obtained from the individual contribution of each input uncertainty. The total uncertainty on the effective multiplication factor results from the simulations. The approach assumed a systematic bias in the manufacturing process, i.e. the input uncertainties was repeated identically over all the blocks within the core. For example, the uncertainty on number of BISO particles in the fuel B-4 was evaluated at 2.2%. In a systematic bias approach, all the compacts contain the same quantity

of coated particles. Such configuration can happen if the compacts are manufactured by batches and an identical bias applies to the number of particles manufactured over the batch.

A second approach would consider these uncertainties as independent random events. Thus, each unit subject to input uncertainties in the core has specific quantities scattered over the normal distribution. For instance, the number of BISO particles in each compact of a given batch would contain a different quantity of BISO particles, distributed over the input uncertainty given by the manufacturer. This approach is more realistic, although it does not account for the worst-case scenario and imposes more computational efforts, because each component (graphite block, compacts, etc.) needs individual treatment.

As shown in section 7.2.2, the uncertainties predicted by the pure experiment are ten times smaller than the uncertainty simulated with the JAERI's MVP-II code. It is proposed in this section to treat the input uncertainties as statistical uncertainties from the manufacturing process.

The modeling of independent normal distributions across the fuel and core components translates in RAVEN into defining each fuel block and material block as individual units. An independent Gaussian (μ,σ) distribution is assigned to each one of them, with an identical mean value μ and the standard deviation σ for a given manufacturing uncertainty. The effect of the number of BISO particles per compact is evaluated for the HC-I core at 8.0 °C. A compact height is 6.25 cm, which means there are about 2,750 compacts over the core. An uncertainty appended or subtracted to a compact involves sixteen isotopes (^{234,235,236,238}U, ^{16}O ^{10}B ^{11}B in the fuel, C, ^{10}B ^{11}B in both coatings and the matrix), i.e. a rigorous modeling would require the definition of 2,750 16-by16 covariance matrices, which represents about 700,000 variables and 2,750 distributions. This would tremendously increase the cost of simulations on both the RAVEN's side, because of the grid generation of the 700,000 variables, and on the PHISICS's side because each compact would have to be modeled explicitly (individual material composition). In the current version of the PHISICS VHTRC model, the fuel blocks are 72.0 cm high fuel columns surrounded by the reflector in each assembly. In the HC-I core, a radial third-symmetry and axial half symmetry are applied, so the twelve 72.0-cm-high fuel blocks are modeled radially with four fuel locations. The model is refined to 8, 12, 16 and 20 independent fuel elements (IFE) (totaling always 72.0 cm in height) each of them characterized by a random distribution of particles. Table 32 gave the uncertainties on the number of particles. Table 44 compares the uncertainty obtained

with RAVEN/PHISICS from the statistical distribution of the number of BISO particles and the systematic bias approach.

Under the statistical scatter approach, the number of particles within the fuel blocks are independent. The total contribution of the number of particles in the (independent) fuel blocks should equals the total contribution of the variances (Equation 7-13).

Table 44. Comparison of k_{eff} uncertainties with a systematic bias approach versus statistical approach

Approach	*HC-I 8.0 °C IFE = 8*	*HC 8.0 °C IFE = 12*	*HC 8.0 °C IFE = 16*	*HC 8.0 °C IFE = 20*
Systematic bias	0.00325	0.00325	0.00325	0.00325
Statistical scatter	0.00126	0.00100	0.00089	0.00080

If the blocks are designed with an equal volume of fuel made of the same fuel type, the individual contributions of the blocks are equal (Equation 7-15): $\sigma_{i,b} = \sigma_b$. The total uncertainty contribution of the number of BISO particles on the k_{eff} is σ_{tot}.

$$\sigma_{tot}^2 = \sum_{i=1}^{N} \sigma_{i,b}^2 \qquad \text{Equation 7-14}$$

$$\sigma_{tot}^2 = N\sigma_b^2 \qquad \text{Equation 7-15}$$

$$\sigma_b = \frac{\sigma_{tot}}{\sqrt{N}} \qquad \text{Equation 7-16}$$

If the total number of independent blocks is N = 1, the uncertainty is equal to the sigma obtained with the manufacturing bias approach σ_{tot} (equal to 0.00325 for the HC-I core at 8.0 °C). Figure 110 collates the values obtained from statistical approach in Table 44 with the theoretical value from Equation 7-15. Naturally, the limit of Equation 7-16 when *N* tends to infinity is 0. Considering the number of compacts in the VHTRC core, the contribution of the number of particles on the total output uncertainty cancels out if the number of particles scattered in the

compacts is independent. If this assumption is accepted, the contribution of the number of particles on the total uncertainty is null and the total uncertainty on the multiplication factor decreases to ~ 0.00100.

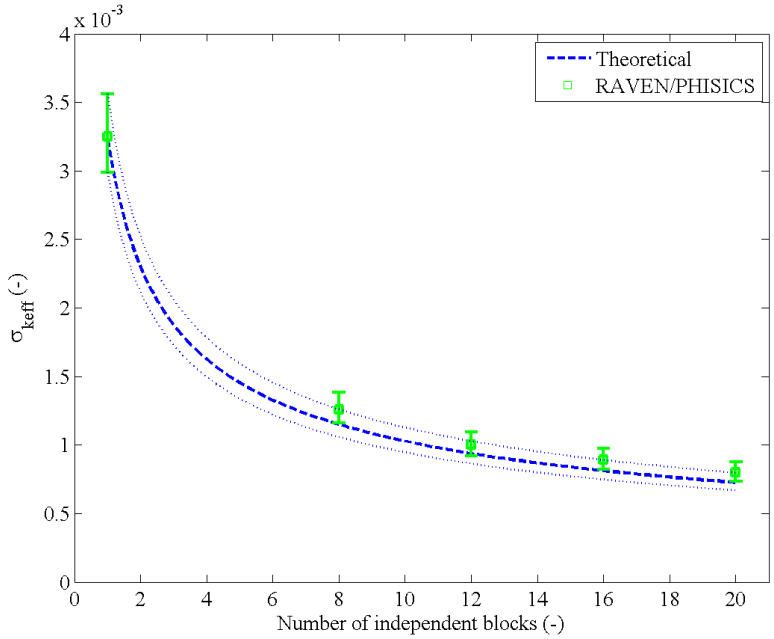

Figure 110. Comparison of k_{eff} uncertainties with a systematic bias approach versus statistical approach. The dotted lines and the vertical lines symbolize the confidence interval [-8.0 %; 9.6 %] from the theoretical approach and RAVEN/PHISICS respectively.

7.2.3.3 Input uncertainty approached as 3-sigmas

The section 7.2.2 assumed that the input uncertainties estimated in the experimental report equal one standard deviation (1σ) from the nominal value. The uncertainty provided by the manufacturer could also be interpreted as the maximum deviation observable from the nominal value. Hence, the uncertainties in Table 36 may be interpreted as the $u_{max} = 3\sigma$ deviation (99.73 % of the values are spread between the upper and lower bounds of the uncertainty). $(\mu, u_{max}/3)$ defines the associated Gaussian distribution, which significantly narrows down the spread of values about the nominal value. This section compares briefly the output uncertainties obtained from $\sigma_{1/3}=\sigma/3$ input uncertainties. Table 45 compares the HC-I and the HC-II core, in

which the number of BISO particles is perturbed. The "particles" category represents the contribution of the number of BISO particles on the total uncertainty. The confidence interval remains -8.0 %; +9.6 % for both 1σ and 3σ predictions.

Table 45. Comparison of the output uncertainty as function of the input uncertainty interpretation (1σ versus 3σ) in RAVEN/PHISICS

Input uncertainty	*HC-I*	*HC-II*
	8.0 °C	*200.3 °C*
Particles	0.00325	0.00235
Particles	0.00108	0.00078

Similarly, as the demonstration in section 7.2.3.2, the results were easily predictable from Equation 7-12. Let σ be defined as described in section 7.2.3.1 and $\sigma_{1/3}=\sigma/3$. If the variables are independent, the results from Table 45 are justified with:

$$Var_{1/3}(k_{eff}) = \sum_i \left[\frac{\partial k_{eff}}{\partial P_i}\right]^2 \sigma_{i,1/3}^2 \qquad \text{Equation 7-17}$$

$$Var_{1/3}(k_{eff}) = \sum_i \left[\frac{\partial k_{eff}}{\partial P_i}\right]^2 \left(\frac{\sigma_i}{3}\right)^2 \qquad \text{Equation 7-18}$$

$$\sigma_{1/3}(k_{eff}) = \frac{1}{3}\sqrt{\sum_i \left[\frac{\partial k_{eff}}{\partial P_i}\right]^2 \sigma_i^2} \qquad \text{Equation 7-19}$$

$$\sigma_{1/3}(k_{eff}) = \frac{1}{3}\sigma \qquad \text{Equation 7-20}$$

7.2.3.4 Uniform distributions

The input uncertainties are interpreted as uniform distributions varying around the nominal value in the HC-I core to estimate the effect of the distribution on the output uncertainty. RAVEN cannot implement multivariate flat distributions, so the uncertainty on the number of parti-

cles cannot be predicted. The other manufacturing uncertainties contributing to the "k_{eff} sub-total" in Table 39 resulted in a ±0.00064 output uncertainty versus ±0.00112 in a normal distribution (1σ) and ±0.00038 ($\sigma_{1/3}$).

7.2.3.5 Effect of the number of groups on the uncertainty

The group structure is raised from six groups to the SCALE 6.2 pre-defined 56-group structure. Table 46 compares the k_{eff} computed from the HC-I, HP and HC-II cores in both 6- and 56-group structures. Figure 111 sketches the results from Table 46 and illustrates that the output uncertainty relative to the eigenvalue tends to be about 10 % lower in 56-group simulations. In Table 46, the category labelled "density" gathers the input uncertainties used to derive the sub-total effect on the k_{eff} in Table 39 (density of graphite, UO_2, impurities). The "particles" category represents the contribution of the number of BISO particles on the total uncertainty. The "total" category combines the contribution of the "density" and the "particle" categories.

Table 46. VHTRC manufacturing obtain from RAVEN/PHISICS compared between a 6-group to a 56-group structure

# of Grps.	*Input uncertainty*	*HC-I 8.0 °C*	*HP 25.5°C*	*HP 71.2 °C*	*HP 100.9 °C*	*HP 150.5 °C*	*HP 199.6 °C*	*HC-II 200.3 °C*
6	Particles	0.00325	0.00326	0.00339	0.00344	0.00350	0.00357	0.00235
	Density	0.00112	0.00111	0.00109	0.00109	0.00108	0.00107	0.00100
	Total	**0.00343**	**0.00345**	**0.00356**	**0.00361**	**0.00366**	**0.00373**	**0.00255**
56	Particles	0.00293	0.00294	0.00307	0.00311	0.00318	0.00325	0.00205
	Density	0.00123	0.00123	0.00121	0.00120	0.00119	0.00118	0.00111
	Total	**0.00318**	**0.00319**	**0.00330**	**0.00333**	**0.00339**	**0.00346**	**0.00233**

7.2.3.6 Summary of the output uncertainties collected on k_{eff}

The interpretation of the input uncertainties may lead to widely different results. For instance, the treatment of independent lattice effects in section 7.2.3.2 yields to a negligible contribution of the number of BISO particles per compact, which is evaluated as the main uncertainty contributor in the experimental report. If in the meantime, the other manufacturing uncertainties

are treated as maximal values, the standard deviations used for each contributor in section 7.2.3.1 (graphite density, ^{235}U abundance etc.) predicts a total uncertainty equal to ±0.00031 in the HC-I core (one third of the "sub-total contribution to k_{eff}" in Table 39) while the original approach predicted ±0.00325. In other words, the interpretation of the same input uncertainties on the same experiment may vary the output uncertainties by a factor 10.

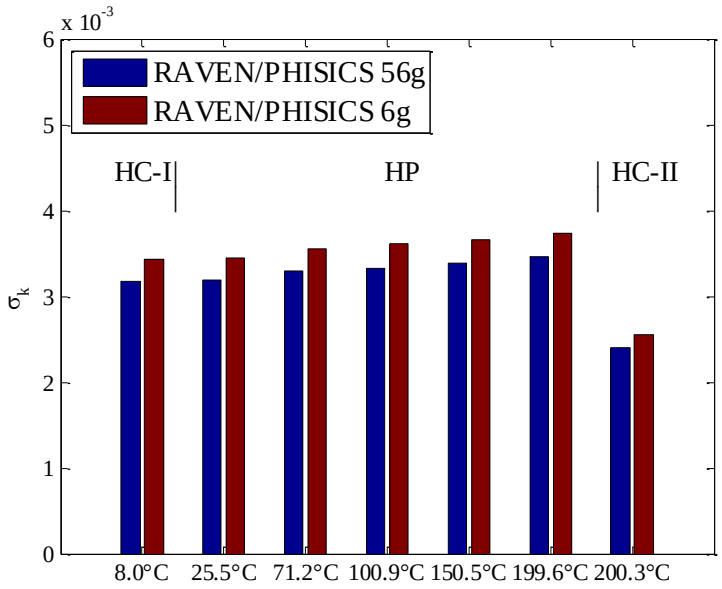

Figure 111. Eigenvalue uncertainty resulting from the manufacturing uncertainties: comparison between 6-group and 56-group simulations

7.2.3.7 Temperature Coefficient α_T

The reactivity coefficient uncertainties stem from the eigenvalue uncertainties. RAVEN/PHISICS evaluates the α_T uncertainties following the methodologies proposed in section 7.2.2. Equation 7-1 provides the nominal values and Equation 7-4, Equation 7-5 and Equation 7-6 propagate the uncertainties from the eigenvalues, although RAVEN/PHISICS cannot directly account for temperature variation because the cross sections provided to PHISICS by T-NEWT are generated at a temperature given *a priori*. The propagation of uncertainties from Equation 7-4 assumed that Δk_{eff} does not change with respect to ΔT (but k_{eff} varies as a function of T). Table 47 summarizes the temperature coefficients obtained with the corresponding uncertainties.

Table 47. Propagation of the k_{eff} uncertainties to the temperature coefficient obtained from RAVEN/PHISICS

T_1 (°C)	T_2 (°C)	$\delta\Delta T$ (°C)	$\delta\Delta k$	$k_1 \pm \delta k_1$	$k_2 \pm \delta k_2$	$\alpha_T \pm \delta\alpha_T$ Revised (10^{-4} $\Delta k/k$)
25.5	71.2	1.3	0.00496	1.02271±0.00345	1.00812±0.00356	-3.19±1.086
25.5	100.9	1.6	0.00496	1.02271±0.00345	1.00238±0.00361	-2.73±0.670
25.5	150.5	1.6	0.00503	1.02271±0.00345	0.99407±0.00366	-2.35±0.413
25.5	199.6	1.8	0.00508	1.02271±0.00345	0.98609±0.00373	-2.18±0.303
71.2	100.9	1.7	0.00507	1.00812±0.00356	1.00238±0.00361	-2.01±1.778
71.2	150.5	1.7	0.00511	1.00812±0.00356	0.99407±0.00366	-1.86±0.678
71.2	199.6	1.9	0.00516	1.00812±0.00356	0.98609±0.00373	-1.82±0.427
100.9	150.5	1.9	0.00514	1.00238±0.00361	0.99407±0.00366	-1.78±1.102
100.9	199.6	2.0	0.00519	1.00238±0.00361	0.98609±0.00373	-1.77±0.564
150.5	199.6	2.0	0.00523	0.99407±0.00366	0.98609±0.00373	-1.75±1.151

Figure 112 shows four temperature coefficients along with differently calculated uncertainties. The first temperature coefficient (α_{P6}) comes from the PHISICS solution in a six-group structure. The uncertainties are propagated from the k_{eff} uncertainties summarized in Table 39. Note that the uncertainties from the experimental report and the uncertainties computed from RAVEN are close. Hence the use of the experimental report's uncertainties or the RAVEN's uncertainties makes little difference. The second temperature coefficient (α_{P56}) comes from the PHISICS solution in a 56-group structure. The third temperature coefficient (α_R) originates from

Table **33**. It represents the temperature coefficient calculated from the experiment and revised with uncertainty propagation from Equation 7-4. The last temperature coefficient (α_E) comes straight from the experimental report.

It is important to emphasize that the large uncertainty from the PHISICS k_{eff} and propagated to α_{P6} does not involve PHISICS or RAVEN. The large input uncertainty involving k_{eff} (σ~0.00350) stems from the assumptions and propagates into large output uncertainties. It was demonstrated in section 7.2.3.2 that the assumptions made on the input uncertainties influence widely the output uncertainty. For the calculation of (α_R) and (α_E) however, the input uncertainty (i.e. the k_{eff} uncertainty) was extracted from the experimental report. The k_{eff} uncertainty evaluated to σ~0.00040 ("experiment" row, Table 32). In other words, the experimentalists decided to not choose the worst-case k_{eff} uncertainty derived with the MVP-II code, but rather experimental uncertainty. The implementation of the k_{eff} uncertainty predicted from MVP-II to derive α_E or α_R would yield to an uncertainty band comparable to α_{P6}, derived with RAVENN/PHISICS.

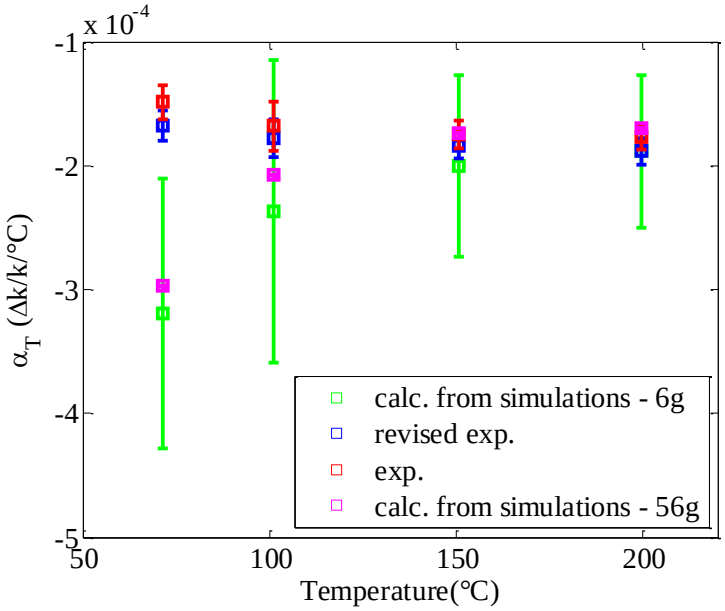

Figure 112. Comparison of the uncertainty on the temperature coefficient from the experiment, the revised values and RAVEN/PHISICS in both 6- and 56-group structures

7.3 Future Work: Introduction to Cross Section Perturbation with RAVEN/PHISICS

7.3.1 Cross section perturbation in SAMPLER

As described in CHAPTER 6, the SCALE 6.2 suite stands as an alternative for uncertainty and sensitivity calculations. In SCALE 6.2, the infinitely-dilute cross sections and the Bondarenko self-shielding factors are tabulated. The SCALE 6.2 covariance are a combination of the ENDF/B-VII.1 covariance data and ORNL-developed low-fidelity covariance data. The covariance serve as a backbone in SCALE 6.2 to generate the tabulated group-wise perturbation factors relative to a given nuclide/reaction.

$$Q_{x,g} = 1 + \frac{\Delta\sigma_{x,g}}{\sigma_{x,g}} \qquad \text{Equation 7-21}$$

The SCALE suite stores a set of 1,000 perturbation factors to avoid the time-consuming cross section sampling step at each perturbation. The perturbation factors are applied to the problem-independent cross-sections before the self-shielding calculations to account for the implicit effects in the uncertainty propagation. To obtain consistent self-shielded cross sections, the Bondarenko factors and the continuous-energy cross sections (details in section 2.5) are needed inside and outside the resolved range, respectively. The Bondarenko factors depend on the background cross section and the temperature for a given energy group and a given nuclide/reaction. They must be consistent with the perturbed infinitely-dilute cross sections. In the SAMPLER sequence, the same perturbation factor $Q_{x,g}$ can be used to obtain the perturbed background cross sections [31]. Those perturbed background cross sections yield to the perturbed Bondarenko factors through tables. $Q_{x,g}$ is also relevant for the CE data cross sections in the resolved energy range.

7.3.2 Cross Section Perturbation in PHISICS

New capabilities were implemented in PHISICS to achieve cross section perturbations. PHISICS cannot generate cross sections and an additional lattice code must deliver the microscopic cross sections, so group-wise “scaling factors” relative to a given nuclide/reaction were

integrated to the code. The scaling factors modify the self-shielded cross sections from the microscopic library. They can be relative (i.e. identical to the perturbation factors in SAMPLER, see Equation 7-21) absolute or additive. Absolute scaling factors replace the cross section value by the new user-defined value and additive scaling factors summates a user-defined perturbation to the nominal cross section.

Because PHISICS receives self-shielded cross sections as an input, the application and implementation of the scaling factors on the Bondarenko factors (or equivalent) and the CE cross section data is moot. The appropriate Bondarenko factors correct the infinitely-dilute cross sections in the lattice step. However, the uncertainty propagation does not account for the implicit effects. As opposed to SAMPLER, the perturbation factors are not calculated *a priori* but "on the fly". This means that the covariance data are folded into scaling factors at each perturbation.

The cross sections available for perturbation are: (n,γ), (n,α), (n,2n), (n,p), (n,fission), $\bar{\nu}$ and the total scattering. Regardless of the self-shielding factors, the cross sections require rebalancing after perturbation to obtain an adequate absorption, scattering and total cross sections. Currently, the inelastic scattering is available for perturbation but the lattice code (i.e. T-NEWT) does not provide explicitly the break-down of elastic and inelastic scattering contributions. The cross-correlations between cross sections are not available in the current version of PHISICS. The cross-correlations mainly concern the elastic-to-inelastic scattering cross sections, the elastic-to-(n,2n) cross sections, the elastic-to-capture cross sections.

In each group *g*, let's denote an elemental cross section Σ_g. The corresponding perturbed cross section Σ'_g is:

$$\Sigma'_g = \left(s_{m,g}\Sigma_g + s_{+,g}\right)s_{a(corr),g} + s_{a,g} \qquad \text{Equation 7-22}$$

The scaling factors can be multiplicative (associated with the factor $s_{m,g}$), additive (associated with the factor $s_{+,g}$) or absolute (associated with the factors $s_{a(corr),g}$ and $s_{a,g}$). The scaling factor options are mutually exclusive for a given nuclide/reaction in a given group. For example, a perturbation cannot be both multiplicative and additive. Hence, two out three scaling factors take neutral element values in the calculation of the perturbation:

Based on the perturbed cross sections, the nominal values are replaced by the perturbed data and the absorption cross section is first re-calculated. The total cross section is then re-balanced as the sum of the absorption cross section and the total scattering cross section. The nu*fission cross section must also be computed accordingly to the perturbed values.

Table 48. Definition of the perturbation factor coefficients

	Multiplicative	*Additive*	*Absolute*
$s_{m,g}$	Perturbed	1	1
$s_{+,g}$	0	Perturbed	0
$s_{a,g}$	0	0	Perturbed
$s_{a,corr,g}$	1	1	0

7.4 Covariance library collapsing

The covariance libraries are stored in few-group structures (typically 15 to 50 groups). The SCALE 6.2 covariance library contains 56-energy groups. The COMMARA-2.0 covariance library, initiated by the Brookhaven National Laboratory and the Los Alamos National Laboratory, contains covariance data for 110 materials in 33 groups [69]. CHAPTER 5 demonstrated the cooperative use of T-NEWT (section 2.6.2) and PHISICS (section 2.6.5), the former accomplishing the cross section generation task, the latter achieving the transport solution. In the version 6.2 and the previous versions, T-NEWT only allows few-group structures hinged to its 252-group structure. A correct interaction between the cross sections and the covariance requires identical group-structures. The stiff collapsing scheme in T-NEWT raises a conflict because the energy boundaries vary from the COMMARA-2.0 MG covariance data to the SCALE fine-group structure. The structures of the cross sections must adapt to the covariance data library because the SCALE boundaries do no match with the COMMARA-2.0 boundaries as shown in Figure 113.

Section 2.5 described the self-shielding treatment of cross sections in the SCALE 6.2 code. The tabulated Bondarenko factors and the lattice cell calculations transform the MG problem-independent libraries into problem-specific cross section libraries. The covariance data defined in the libraries (ENDF/B, COMMARA or others) are associated to infinitely-dilute cross sections. Previous studies suggest enhanced methods to collapse the covariance data relative to the MG infinitely-dilute cross sections and self-shielded cross sections. If the self-shielded cross-

sections characterize the system, reference [70] recommends collapsing the covariance matrix with respect to the sensitivities of the broad-group cross sections to the fine-group cross sections. Let the indices *G* and *G'* be relative to the broad groups and the indices *g* and *g'* be relative to the fine groups:

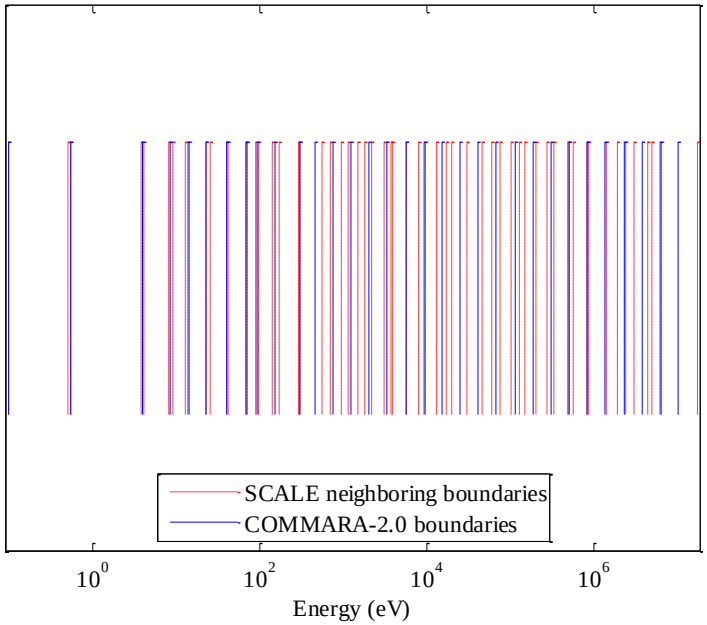

Figure 113. Difference in the SCALE neutron energy boundaries and the COMMARA-2.0 co-variance library

$$cov(\sigma_G, \sigma_{G'}) = \sum_{g} \sum_{g'} \left(\frac{\partial \sigma_G}{\partial \sigma_g}\right)\left(\frac{\partial \sigma_{G'}}{\partial \sigma_{g'}}\right) cov(\sigma_g, \sigma_{g'}) \qquad \text{Equation 7-23}$$

A covariance condensation method is also proposed in the PUFF-IV code [71]. Let $cov(\sigma_I, \sigma_J)$ be the covariance between the cross sections σ in the energy ranges I and J and let Φ be the scalar flux:

$$cov(\sigma_I, \sigma_J) = \frac{1}{\Phi_I \Phi_J} \int_I \int_J \Phi(E)\Phi(E')cov(\sigma, \sigma)dEdE' \qquad \text{Equation 7-24}$$

Equation 2-13 becomes, in MG format:

$$cov(x_I, y_J) = \frac{1}{\Phi_I \Phi_J} \sum_{g \in I} \sum_{g' \in J} \phi_g \phi_{g'} cov(\sigma_g, \sigma_{g'}) \qquad \text{Equation 7-25}$$

In the current state (December 2018), one of the methodologies must be implemented either in PHISICS or as an external tool to collapse the covariance data into the energy group format provided to PHISICS. After the collapsing process, the PHISICS routines that pre-processes the perturbation factors must be verified following a rigorous verification and validation process. Currently, PHISICS computes properly the perturbation factor with respect to the covariance data, but the application of the perturbation factors on the cross sections overestimates the scattering perturbations, which means further corrections must be implemented in the post-processing of the perturbation factors within PHISICS.

7.5 Conclusion

The RAVEN/PHISICS coupled sequence was developed for uncertainty and sensitivity analysis of nuclear systems. This chapter demonstrated the theoretical capabilities of the sequence and the architecture of the interactions between RAVEN and PHISICS *via* a RAVEN interface.

Manufacturing uncertainties were predicted from the VHTRC experiment with RAVEN-PHISICS and compared to the experimental report. Satisfying results from RAVEN/PHISICS were obtained compared to the uncertainties from the experiment. The effects of a 6-group structure compared to a 56-group structure provided k_{eff} uncertainties varying by 10 % of the total uncertainty.

This chapter also investigated in-depth the nature and magnitude of the manufacturing uncertainties utilized in the VHTRC experiment. Aside from assessing the RAVEN/PHISICS capabilities, two additional components were appended, from (a) the experimentalist and (b) from the analyst point of view. (a) Some of the input uncertainties may have been disregarded from the experimental point of view, coming from but not only least-square fitting approach, the determination of the detector's correction factors, the precision of the experiment, the determination of the loading uncertainties, the propagation of uncertainties to the temperature coefficient. The

repeatability of the experiment was not estimated. The k_{eff} uncertainty derived from the experiment represents then a minimum uncertainty associated with the nominal experimental results. (b) From the analyst side, caution is required regarding the approach of the input manufacturing uncertainties because of the non-specificity of the input uncertainties. For example, interpreting a graphite density uncertainty at ±0.51 $g.cm^{-3}$ may be read as "the graphite density varies over a normal distribution described by a 0.51 $g.cm^{-3}$ standard deviation", or this uncertainty may be deduced as "the maximum achievable values of the graphite density is 0.51 $g.cm^{-3}$ over a flat distribution". The repeatability of a given uncertainty within the lattice elements of the core conditions the output uncertainty, especially for widely repeated elements. For instance, the number of BISO particles within a compact is given at ± 2.2 %. This data may indicate that all the compacts have the same number of BISO particles, and this unique value can range 2.2 % around the nominal value, or it can suggest the number of BISO particles in each compact may deviate independently 2.2 % about the nominal value. The former statement results in large eigenvalue uncertainties because the effect is reproduced in each lattice in the entire core while in the latter statement, the independence of each compact yields to a null output uncertainty. Overall, the magnitude of the input uncertainties interpreted from the experimental report may yield to over 100 % differences in the output uncertainty predicted depending on how the input uncertainties are interpreted.

CHAPTER 8

IMPLEMENTATION OF AN AUTOMATIC FEW-GROUP-STRUCTURE SEARCH ENGINE USING THE SURROGATE CAPABILITIES OF RAVEN

8.1 Energy-group collapsing

In thermal systems, the fission neutrons slowdown from fission energies of several MeV to the thermal energies neighboring 1 eV. The treatment of the large magnitude of the neutron energy requires thousands of discretized energy bins which are impractical in industrial-sized reactor analysis. The transport solution on a core level involves the generation of self-shielded cross sections from a lattice cell, in a condensed group structure. The nature of the systems (i.e. the moderator, coolant, geometry, fuel, temperature of operation etc.) is of essence in the neutronics response. Hence, the definition of the few-group energy boundaries depends on the problem simulated. The establishment of optimized few-group structures is necessary to obtain accurate simulations and computational predictions.

The years of experience, operation and academic investigation on the LWRs showed the adequacy of the two-group energy format for transport solutions. The non-LWR designs suffer from a general lack of feedback. Neutron moderation in a medium other than water is associated with a lower moderating power. The number of collisions necessary to thermalize the neutrons increases. Thus, the worsening of the moderating power magnifies the importance of energy resonances. A two-group energy discretization does not suit most of the reactor designs, including the HTGRs.

The brute force approach of testing each group structure in transport calculations was considered. The number of combinations without repetitions (N) from G fine groups down to g broad groups is:

$$N = \frac{(G-1)!}{(g-1)!\,(G-g)!} \qquad \text{Equation 8-1}$$

The SCALE 6.2 suite offers 56, 238 and 252 bins of predefined neutron energies. Figure 114 gives the number of broad-group structures available from 252 energy groups. For a two-group structure, only one boundary must be chosen, leading to 251 possible cases. For a three-group structures, 31,375 combinations exist. An expert opinion to settle the thermal cut-off can lower down the study into reasonable numbers. If the number of broad groups is greater than three, the "brute force" method faces an unmanageable number of combinations. Methodologies were developed in the literature to acquire, if not optimal, suitable structures for transport and coupled transient calculations.

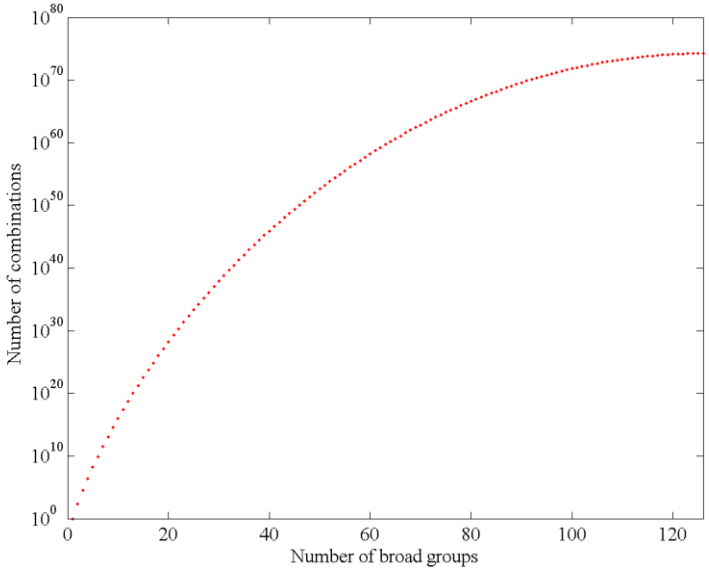

Figure 114. Number of possible energy-group combinations from a 252-group structure

A method called YGROUP [72] uses the forward and adjoint fluxes to automatically search a flat distribution of the adjoint flux. The algorithm begins with a two-group structure and splits the most contributing group until the importance function profile is satisfyingly flat. The automatic feature of the program is an advantage, preventing from arbitrary user's decisions.

However, it converges to an unknown number of broad groups, which reduces the flexibility of the approach. The results presented are only based on the effective multiplication factor. Cancellation of errors may appear if an integral value such as the k_{eff} is selected as figure of merit. The methodology relies also on the definition of the adjoint flux which is not always accessible. Some of the results also proved large discrepancies (up to 1%) on the multiplication factor.

A second method based on the opposite approach was developed [73]. It merges the energy groups together from the fine mesh until the desired number of groups is obtained. The importance function from the adjoint flux indicates which fine groups are collapsed together. This approach, unlike the first one, achieves a greater control over the coarse mesh, but the sensitivity of a group to the user-defined figure of merit(s) might increase during the successive collapsing. Since the groups that were collapsed cannot be broken back down, the methodology is blind to any rebalancing of the adjoint flux profile in a previously-collapsed group.

A third methodology takes advantage of the few combinations existing in a two-group search [74]. An optimized cut-off boundary is defined in a first step at different axial locations of core. The algorithm conserves the energy boundary providing the optimized results for the all axial levels and introduces a new energy boundary. An identical search is performed on the third energy-group cut-off. This method has the advantage to define the reference solution with the same code as the test cases, which prevents code-to-code discrepancies in the mathematical solution. It also investigates the effects relative to the burnup, the fuel temperature and the moderator temperature on the group structure optimization. However, the first boundary only relies on one figure of merit (the k-effective). The second energy boundary depends on the void coefficient as goal function. This iterative approach is not pushed further than three groups and hence may face the same limitations as the backward approach which consists in collapsing groups of higher sensitivity. As new groups are created, potential new sensitivities can appear in previously-defined groups. This methodology remains relatively “brute-force” and is limited to few broad groups (~4).

A fourth approach starts at a two-group basis but does not investigate all the span of possibilities at each added boundary. The boundaries tested relate to the major resonance isotopes established from an expert-judgment basis. The multiplication factor and the spatial power distribution define the figure of merits [75]. This approach allows the development of structures from two to twelve groups, but does not rely on a numerical, systematic approach.

The Particle Swarm Optimization (PSO) [76] is a numerical methodology that have been applied to the energy-group optimization problem [77]. The cooperative contribution of "low-intelligence" solutions are collected identically to animal swarming. The applicant solutions are called *particles*. They are defined as a point of dimension N, in an N-dimensional input space. At the end of an iteration, a particle memorizes two information:

- the best result it has achieved ("cognitive" component);
- the best result achieved by its neighbor in a local PSO approach, or the best result achieved by the swarm in a global PSO strategy ("social" component).

A uniform normalized random number is assigned to both the cognitive and the social component to give a stochastic characteristic to the particle. The particles are allocated new positions (i.e. input space values) based on their own experience, the swarm feedback and a stochastically-made decision until meeting a goal function. This tool provides a systematic and automatic approach, but it was implemented in a way that only infinite homogeneous lattices relative to the core model may be used.

It is intended to develop a sequence capable of searching mechanically a group structure. The cross sections must be prepared with heterogeneous lattice cells to model the full core's transport calculations, and the collapsed structure must be searched with artificial intelligence algorithms (i.e. Reduced Order Models (ROM)). The methodology must adapt to any fuel (single heterogeneous or doubly-heterogeneous), any spectrum, temperature and geometry, and does not have to require any assumption although it should be able to accept additional user-defined constraints.

The approach proposed in this chapter combines the lattice code NEWT, the nodal code PHISICS and the uncertainty analysis code RAVEN in a calculation flow (see section 8.2). Section 2.6.8.2 emphasized the adaptive sampling techniques utilized to explore the input space (i.e. the energy boundaries). This chapter contains an explicit application of the methodology on an HTTR (section 2.1.2). The RAVEN/NEWT/PHISICS sequence compares the performances of group structures found in the literature along with the goal functions selected for the adaptive sampling to the results obtained with the ROM. Section 8.7 details the computational performances of the sequence.

8.2 RAVEN/NEWT/PHISICS Algorithm

The algorithm is constructed around the software NEWT, PHISICS and RAVEN coupled together through a Python interface. The sequence NEWT/PHISICS/RAVEN performs automatically the successive steps:

- generation of self-shielded, microscopic cross sections "on-the-fly" in a broad-group structure defined by RAVEN;
- calculation of the problem-dependent transport solution;
- collapsing of the fine-group reference's scalar flux into the broad-group structure defined by RAVEN;
- comparison of the broad-group structure to the collapsed reference based on a given figure of merit.

The T-XSEC (section 2.6.3) code performs the cross section preparation (file ft44f001). T-XSEC also provides the mixing table (file ft92f001) required by NEWT for the transport calculations. As explained in section 2.6.3, manual corrections must be added in the mixing table file if the system is in double heterogeneous state. The NEWT's capabilities were described in 2.6.2. NEWT collapses the fine-group cross sections into a RAVEN-defined structure. The SCALE 6.2 252-group structure is chosen as the reference fine-group structure. RAVEN receives *G* input variables, in which *G* is number of collapsed groups desired by the user. The RAVEN interface transfers the variables to the parsers. At this stage, the variables are weight functions uniformly and continuously defined from 1 to 252. A parser normalizes the variables and transforms them into a NEWT-formatted group structure. The RAVEN interface transmits those variables to the NEWT input file and executes NEWT.

Mathematically, the group structure is defined following this process: let v_g be the value of the continuous uniform variable sampled by RAVEN, g = 1, …, G. The normalized weights w_g associated to each group are:

$$w_g = \frac{v_g}{\sum_{g=1}^{G} v_g} G_F \qquad \text{Equation 8-2}$$

The total number of fine groups equals 252 but is generalized to G_F in the derivation. The algorithm verifies first that the first group (the fastest one) incorporates at least the first eight

groups from the 252-group structure. In the SCALE 252-group structure, the upper energy of the ninth group is 6.434 MeV. Beyond this threshold, the neutron flux may equal zero which causes errors in the transport codes' (PHISICS) iteration scheme. By collapsing at the least the first eight groups, the resulting broad-group structure avoids subsequent errors in the transport code. If the normalized weight relative to the first group is smaller than eight, the RAVEN parser computes a Minimum Acceptable Weight (MAW) and rebalances the normalized weights accordingly. If $w_1 < 8$ then:

$$MAW = \frac{8}{G_F} \sum_{g=1}^{G} v_g \qquad \text{Equation 8-3}$$

The new normalized weights are:

$$w_g = \frac{v_g}{MAW + \sum_{g=2}^{G} v_g} G_F \qquad \text{Equation 8-4}$$

With this approach, w_1 will still be slightly lower than 8 as the new sum of the weights (the coefficient in the denominator of the Equation 8-4) is larger than original denominator in Equation 8-2. To improve the routine, an iterative scheme would repeat the process until w_1 reaches a weight equal to 8 (or slightly more). In the current state, no iteration was implemented, which does not induce problems in the routine because (a) the 7th group does not necessarily have a scalar flux equal to zero so collapsing the first seven groups is usually enough, and (b) the next algorithm described below usually rounds up the weights with the highest decimal part.

The sum of the final set of variables w_g must equal the number of groups collapsed in the NEWT input, G_F. The weights originating from Equation 8-2 or Equation 8-4 are floating points, while NEWT only tolerates integers. A Python method within the RAVEN/NEWT parser rounds up or down the bin values to turn them into integers. Figure 115 depicts the algorithm. The idea is to separate the integer part and the decimal part of each weight and to calculate the sum of the integer part. If the sum is equal to G_F (which is rarely the case), the algorithm truncates the weights to their integer parts and transfers them straight to the NEWT input. Otherwise, if the sum of the integer parts is lower than G_F, the algorithm rounds up the integer part with the highest associated decimal part until the sum of the integers equals G_F. If the sum of the integer parts is higher than G_F (which is rarely the case), the mirror process applies: the integer part with the

lowest associated decimal part is rounded down, until the sum of the integer parts is narrowed down to G_F. An exception routine intervenes if the integer value is equal to one, to prevent to round it down to zero because NEWT errors out if a group collapses into zero group.

The resulting structure obtained is under the form of "number of groups to be collapsed from the fine library into group g". For example, if the algorithm provides a three-group structure "79 29 144", the first 79 groups of the 252 library will be collapsed together to constitute the group 1 of the broad-group structure, then the 29 following groups (80 through 108) will constitute the broad-group two, and the groups 109 through 252 will constitute the last bin of the broad-group structure.

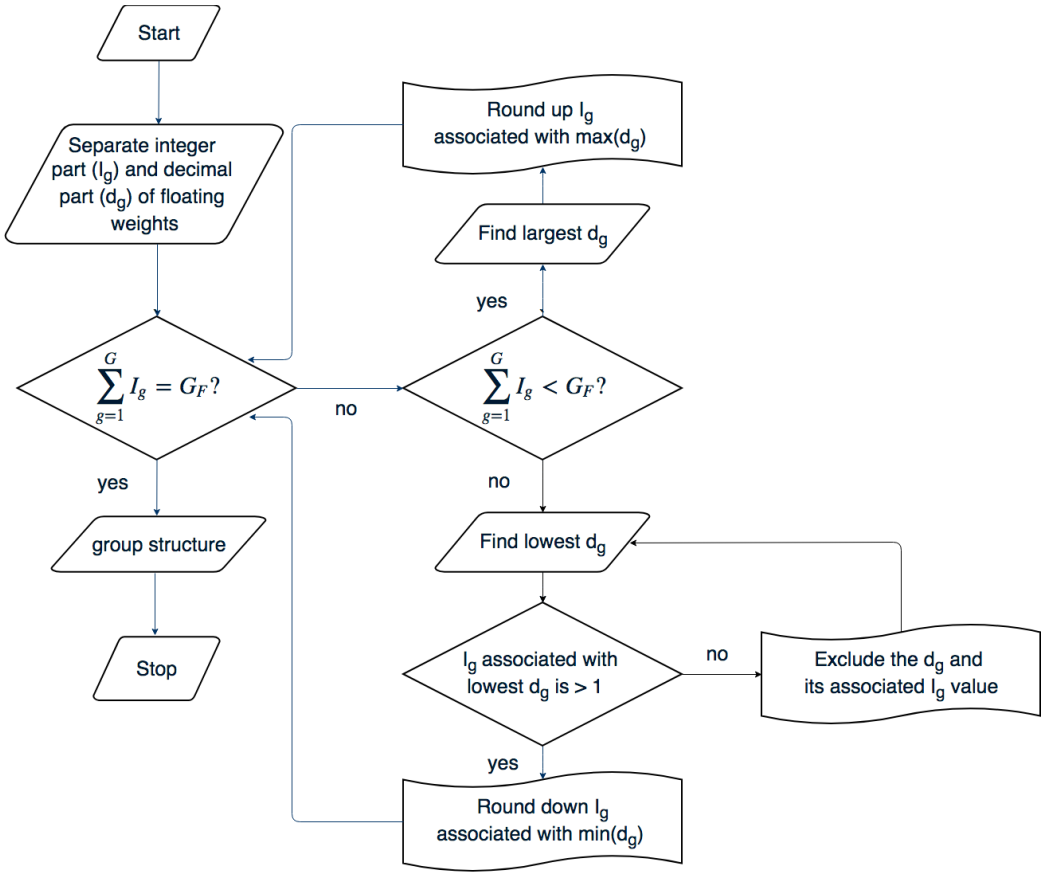

Figure 115. Treatment of the floating weights of energy bins in the RAVEN/NEWT interface

The RAVEN parser passes this structure to the NEWT input file and the RAVEN interface executes NEWT to engage the collapsing process. The NEWT execution results in the generation of microscopic, self-shielded, collapsed cross section libraries in G-energy groups (file ft30f001). The libraries prepared by SCALE do not include the flux disadvantage factors, and hence impose further corrections to account for spatial shielding. A Python method incorporated in the RAVEN/NEWT OPP parses the scalar fluxes relative to each mixture defined in NEWT and computes the disadvantage factors. PHISICS receives those disadvantage factors through the RAVEN/NEWT/PHISICS interface to use correctly the microscopic cross sections in a homogenized fashion.

The disadvantage factors account for the spatial self-shielding within a given material after the homogenization process. They also account for the lattice cell environment, which means that the materials excluded from the homogenized mixture still have a contribution to the homogenized cross sections. To carry out the calculation of those coefficients, the scalar flux relative to each material homogenized together in the NEWT problem must be collected. The disadvantage factor of mixture *m* (m=1, …, M) in group *g* (g=1, …, G) is denoted d^m_g. It is computed as the ratio of the scalar flux in mixture *m* in group *g* to the sum of the normalized volume-weighted scalar fluxes within the homogenized mixture:

$$d_g^m = \frac{\Phi_g^m}{\frac{\sum_{m=1}^{M} \Phi_g^m V^m}{V}} \qquad \text{Equation 8-5}$$

Φ^m_g is the flux in mixture *m* in energy group *g*;
V^m is the volume of mixture *M*;
V is the total volume of the materials homogenized.

The RAVEN/PHISICS interface drives the disadvantage factors and the microscopic libraries to PHISICS to perform the core-wise transport calculations in the broad-group structure. The PHISICS/RAVEN parsers can optionally perturb the PHISICS-related inputs, if the user desires to measure more complex relationships between the group structures and the reactor physics input data. Such analysis is beyond the scope of this study. The interface executes PHISICS and the system's transport solution, which is compared to a reference simulation performed in a preliminary step with PHISICS, using a NEWT 252-group microscopic library. The reference

fine-group structure is integrated with respect to the energy to obtain the coarse-group nuclear data to compare rigorously with the broad-group structure sampled. Another post-processing Python script achieves this step. The group structure changes at each perturbation, hence, the OPP repeats the collapsing of the reference fine-group structure at each perturbation. The neutron flux in a given broad structure g is collapsed following Equation 8-6:

$$\Phi_g = \frac{1}{E_{Bu} - E_{Bl}} \sum_{b=Bu}^{Bl} \Phi_{gF}(E_{F,g} - E_{F,g+1}) \qquad \text{Equation 8-6}$$

Φ_F is the flux in the fine-group structure;
$E_{F,g}$ is an upper energy boundary in the fine-group system;
E_{Bu} corresponds to the upper energy of the broad-group considered;
E_{Bl} corresponds to the lower energy of the broad-group considered.
In the version 6.2.2 of SCALE and before, the coarse-group structure has to be a sub-set of the 252-group structure.

The multiplication factor and the normalized group-wise neutron flux define the goal functions to perform the ROM training. The coarse and fine structure results are compared with the same code (PHISICS), avoiding code-to-code bias in the mathematical solution and user-input discrepancies. New few-group structures based on the previous simulations are further sampled considering the ROM training. Figure 116 illustrates a flowchart of the sequence**.**

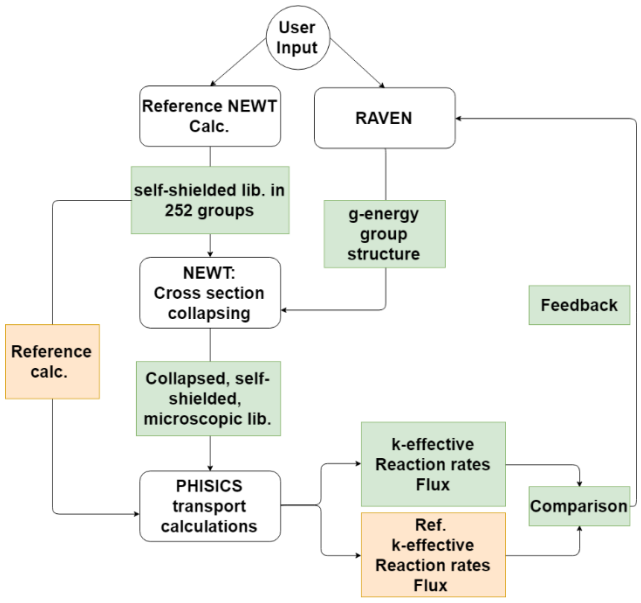

Figure 116. Flowchart of the sequence RAVEN/NEWT/PHISICS

Figure 117 shows the capabilities added to the RAVEN/PHISICS standalone interface (Figure 103) to construct the RAVEN/NEWT/PHISICS interface.

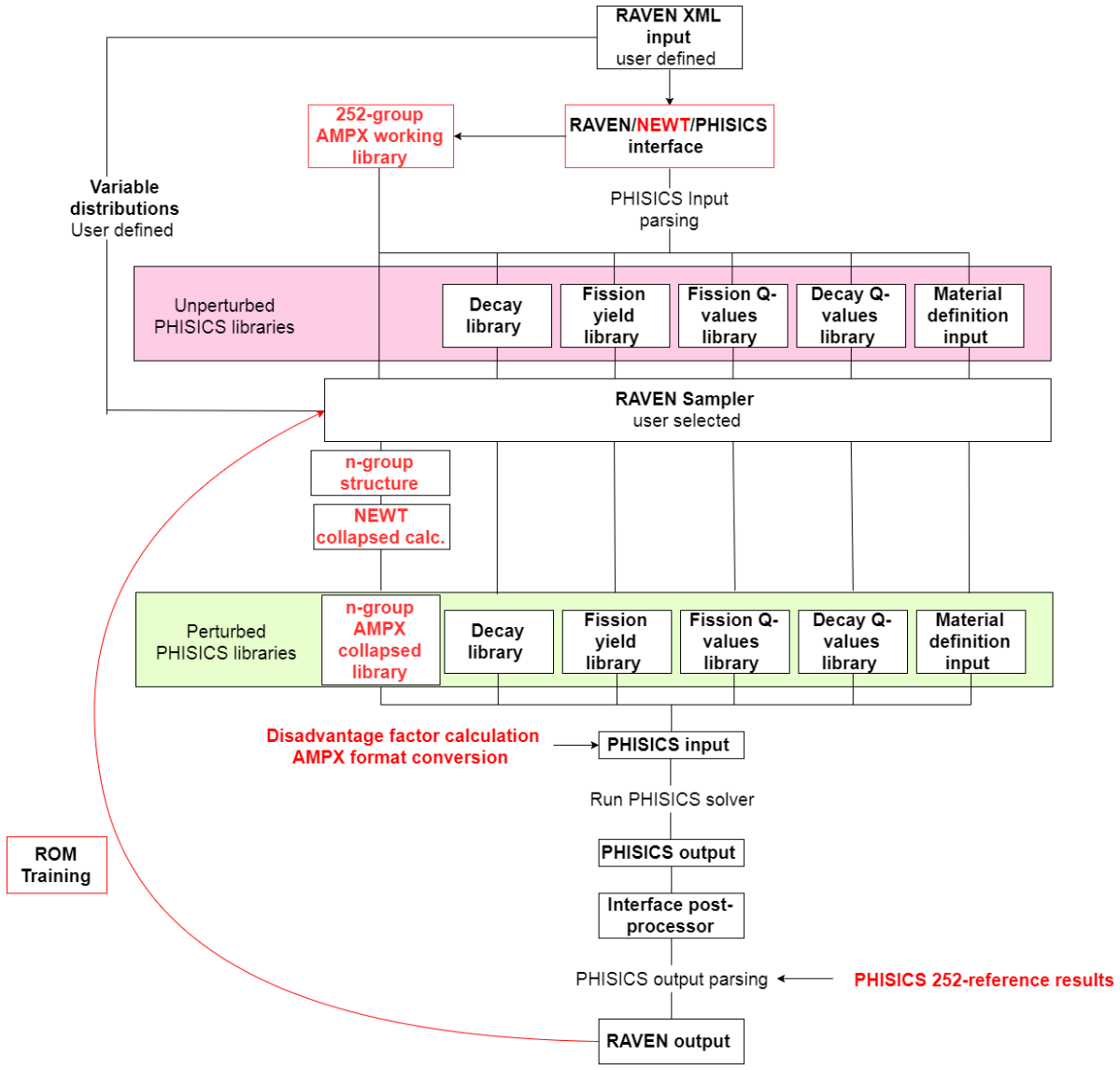

Figure 117. Workflow of the sequence RAVEN/NEWT/PHISICS, with emphasis on the capabilities added from the RAVEN/PHISICS interface

The libraries and input files necessary on a step-by-step basis are summarized below, including the preliminary steps.

The preliminary files required are:

- A mixing table (file ft92f001) for each lattice used in the PHISICS core. The SCALE T-XSEC 1-D transport code generates this file;

- A master library (file ft04f001) containing the microscopic cross sections using KENO (possibility to use the T-XSEC ft44f001 file);

The preliminary files must be generated only once and placed in the temporary folders of each NEWT sub-sequent calculations. This approach is optimal because the spectral calculations are not repeated in the sampling process which relieves the computational load. Once the preliminary libraries are collected, PHISICS generates a fine-group reference solution to obtain the reference fine-group spectrum and multiplication factor.

- Using the NEWT lattices and the preliminary libraries (ft92f001 and ft04f001), the cross sections are artificially collapsed into 244 groups. The first 8 groups are collapsed together to avoid scalar fluxes equal to zero at high energies;
- The SCALE module *AmpxMGConverter* transforms the collapsed microscopic cross section (file ft30f001) from the newest AMPX format into the old AMPX format, which is currently the accepted format in PHISICS;
- The NEWT output files in ASCII format are parsed to derive the disadvantage factors for each lattice cell.
- From this point on, the RAVEN/NEWT/PHISICS calculations can be performed.

On the RAVEN side, the user must implement:

- The RAVEN input deck that defines the number of groups the libraries will be collapsed into and the convergence criteria. The interface automatically handles the implementation of NEWT-formatted collapsed structure in the NEWT input mock-up, the conversion of the AMPX libraries, the calculation of the disadvantage factors and the PHISICS core calculations.
- A “decision” python script compares the post-processed data from PHISICS broad-group solution and PHISICS reference calculations.

8.3 Description of the HTTR Model

The applicability of the sequence presented in section 8.2 is demonstrated through an example. Lattices representative of the HTTR model (presented in section 2.1.2) are selected for this purpose. Reference [78] introduced a two-dimensional model of the HTTR to evaluate the accuracy of transport codes for reactor calculations. The HTTR being axially heterogeneous, the

benchmark proposes a list of simplifications in the model to convert the 3-D HTTR into a suitable 2-D benchmark. This section does not aim to obtain matching results with the one demonstrated in [78], but rather to develop lattice models representative of the HTTR. Hence, the simplifications (a), (f), (g) and (h) justified in [78] were adjusted, while the simplifications (b), (c), (d), (e) and (f) were conserved:

(a) The number of fuel enrichments are reduced to one (against twelve in the actual HTTR and seven in [78]). The one enrichment considered is the volume-averaged enrichment in the actual HTTR, equal to 6.0% ;
(b) The HTTR has two different types of fuel blocks made of 31 or 33 pins. To model a symmetric core, only 33-pin blocks are modeled. The BPs' atomic number density is axially averaged, and the number density in the BP rods on the three corners is identical;
(c) Gaps between blocks in the active region of the core, dowels at the top of the BP rods, handling holes at the top of the fuel rods and neutron shielding pins were neglected in the lattice models;
(d) For symmetry purposes, the control rods are fully withdrawn;
(e) The full shape of the core is hexagonal and not dodecagonal;
(f) A homogeneous medium surrounds the lattice cell. The homogeneous medium is representative of the two-dimensional HTTR core composition. Figure 118 represents the three lattice models generated with NEWT;
(g) The fuel is kept doubly-heterogeneous;
(h) Impurities in the graphite components were conserved as they are in the original benchmark.

The outer region surrounding the lattice is a homogeneous medium made of a volume-averaged mixture of the full two-dimensional HTTR core. It provides a coupling between the different lattice cells. It is only modeled to provide a common spectrum background to the central cells. Table 49 provides the atomic composition of the outer region of the lattice cells.

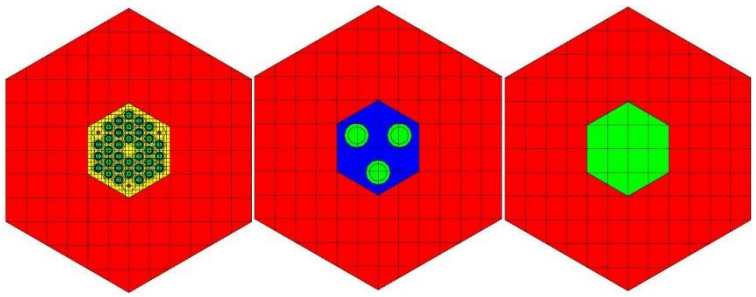

Figure 118. HTTR lattices (left) Fuel; (center) control rods fully withdrawn; (right) reflector

Table 49. Composition of the homogenized region of the lattice cells

Isotope	*Number Density* $(at.b^{-1}.cm^{-1})$
He-4	1.1469E-06
C-graphite	8.3462E-02
B-10	7.7295E-07
B-11	1.1628E-06
O-16	9.9381E-05
U-234	2.2452E-08
U-235	2.9391E-06
U-238	4.6262E-05
Si-Nat	4.5929E-05

The homogenized self-shielded microscopic cross sections are collapsed and implemented in PHISICS. Those cross sections are only representative of the central block of the lattices. The fuel in the grains, the coatings and the matrix are defined at 1130.0 K, the control rod blocks, the reflector blocks, the structural graphite in the fuel blocks and the outer region of the lattice cells made of homogeneous medium are defined at 1080.0 K. The helium coolant is at 853.0 K, as prescribed in [78]. The fuel pin radius is 4.1 cm, and the pin pitch in the fuel block is 5.15 cm. In the control rod lattices, the block center to the rod center distance is 10.8 cm.

The angular discretization (number of polar angles and azimuthal angles) in the NEWT lattices does not affect the flux-weighted cross sections and the disadvantage factors, so the angular discretization can remain poor (three polar angles and three azimuthal angles) in the reference 252-group calculations and broad-group models. The same statement is valid for the k-infinity's convergence limit: the convergence criterion on the multiplication factor are reduced to accelerate the lattice calculations. However, a loose spatial grid (for example 3 × 3) in the NEWT lattice may predict erroneously the neutron fluxes. The bias in the neutron flux predictions propagates through the disadvantage factors and introduces errors in the PHISICS neutron flux and multiplication factor. The effects of a grid refinement in the lattice cells tend to be more sensitive in fine-group structures than broad-group structures. To avoid discrepancies between the reference fine-group structure and the broad-group structures, the grids of the NEWT lattice cells must be sufficiently refined. It is chosen to work with 12 × 12 grids for each lattice cell.

Figure 119 represents the PHISICS full core model built with the NEWT lattice cells. The slots numbered "1", "2" and "3" are the control rod blocks, the fuel blocks and the reflector blocks, respectively.

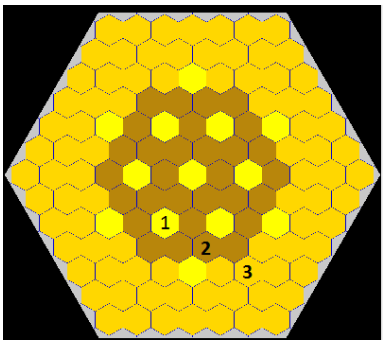

Figure 119. HTTR core modelled in PHISICS

8.4 Group Structures Relative to HTGRs in the Literature

The RAVEN/NEWT/PHISICS sequence is demonstrated in a six-group configuration. The literature proposes several six-group structures developed for general HTGR applications. The structures listed below serve as reference.

- The structure from reference [78] constitutes the *structure 1*. This six-group structure was created for the development of HTTR benchmark model but was not optimized. The structure was originally utilized in HTTR application specifically [79].
- The *structures 2*; *3*; *4*; *5*; *6*; *7*; *8* and *9* from reference [75] were developed for general HTGR purposes and not specifically for the HTTR. A pebble-bed modular reactor was used to demonstrate the group structures.
- Two structures were developed for transport calculations of the Fort Saint Vrain (*structure 10*) and THTR (*structure 11*) reactors [80].

Table 50 specifies the energy boundaries of the group configurations 1 through 11.

Table 50. Upper energy boundaries of the reference structures in six-group format

	Group Upper boundaries (eV)					
	1	*2*	*3*	*4*	*5*	*6*
Struct. 1	2.000E+07	1.830E+05	9.610E+02	2.380E+00	6.500E-01	1.050E-01
Struct. 2	1.690E+07	1.430E+05	2.040E+03	2.380E+00	4.300E-01	1.200E-01
Struct. 3	1.690E+07	5.250E+04	2.380E+00	1.600E+00	4.300E-01	1.200E-01
Struct. 4	1.690E+07	1.830E+05	2.380E+00	1.600E+00	4.300E-01	1.200E-01
Struct. 5	1.690E+07	1.830E+05	9.611E+02	2.380E+00	6.500E-01	3.500E-01
Struct. 6	1.690E+07	5.250E+04	4.540E+02	2.380E+00	4.300E-01	1.800E-01
Struct. 7	1.690E+07	5.250E+04	4.540E+02	1.860E+00	4.300E-01	1.800E-01
Struct. 8	1.690E+07	1.830E+05	2.040E+03	2.380E+00	4.300E-01	1.200E-01
Struct. 9	1.690E+07	1.830E+05	2.040E+03	2.380E+00	4.300E-01	1.800E-01
Struct. 10	1.500E+07	1.830E+05	1.760E+01	2.380E+00	4.140E-01	1.000E-01
Struct. 11	2.000E+07	7.485E+02	1.760E+01	1.900E+00	3.700E-01	3.000E-01

The uppermost energy boundary in SCALE is defined at 2.000E+07 eV. The upper boundaries from the *structures 1* through *11* are reported as they are in the source, but the SCALE uppermost energy must be used in the comparison scheme. This detail has no importance as the reaction rates only have non-zero values from energies below 8.000E+06 eV or below.

The reference normalized flux is integrated from the 252-group structure into the broad-group structure considered at each sample. The reference collapsed flux (referred to as *structure 0*) is defined as the averaged surface under the flux curve within the groups that are collapsed together. Equation 8-6 computes it. The normalized neutron fluxes relative to the *structure 1* (Figure 120) and the *structure 10* (Figure 121) shows a poor agreements to the *structure 0*, with relative differences peaking at -47% and +157% in group 6 and 2 respectively. The *structure 11* (Figure 122) has a relative difference with the *structure 0* of about 350 % (group 1) and 50% (group 2). The best-performing structure among *structure 2* through *9* is the *structure 5* (Figure 123) in which only group 1 and 5 have a relative difference to the *structure 0* higher than 10%.

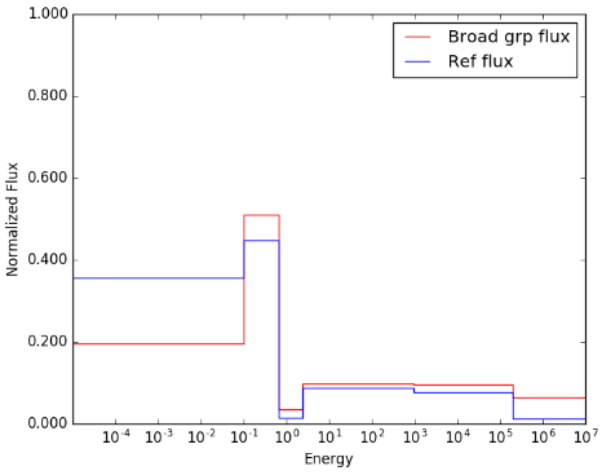

Figure 120. Normalized neutron flux in the PHISICS HTTR core (*structure 1*)

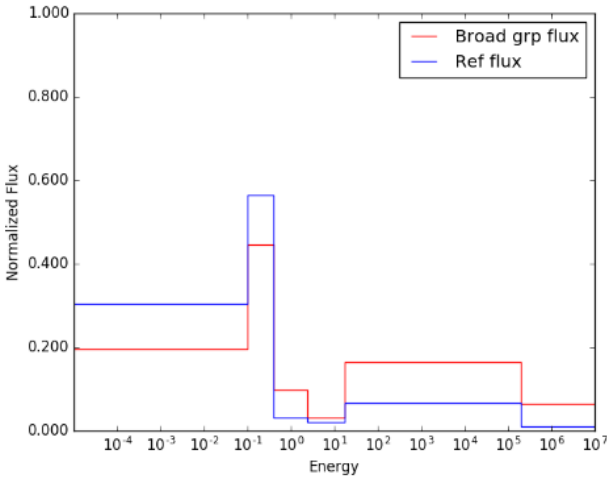

Figure 121. Normalized neutron flux in the PHISICS HTTR core (*structure 10*)

An evaluation was also performed at 300 K for *structure 1* (Figure 124) and *structure 5* (Figure 125). The comparison of the eleven structures proposed in the literature gives an overview of the potential performances of six-group structures in HTGR systems along with temperature effects. As observed in Figure 120 versus Figure 124, the *structure 1* performs differently at high temperatures compared to room temperature. Hence, the structures must be adapted to the system considered.

Those configurations are used as a benchmark to evaluate the performances of the solutions obtained with a RAVEN-created surrogate model. Table 51 summarizes the differences in the k_{inf} between the PHISICS 252-group and the PHISICS six-group simulations.

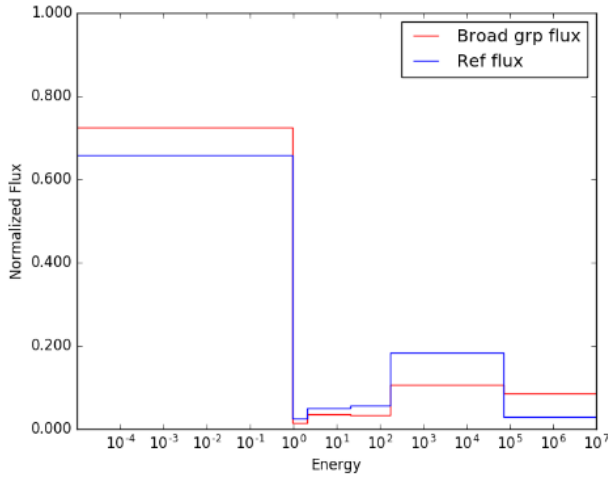

Figure 122. Normalized neutron flux in the PHISICS HTTR core (*structure 11*)

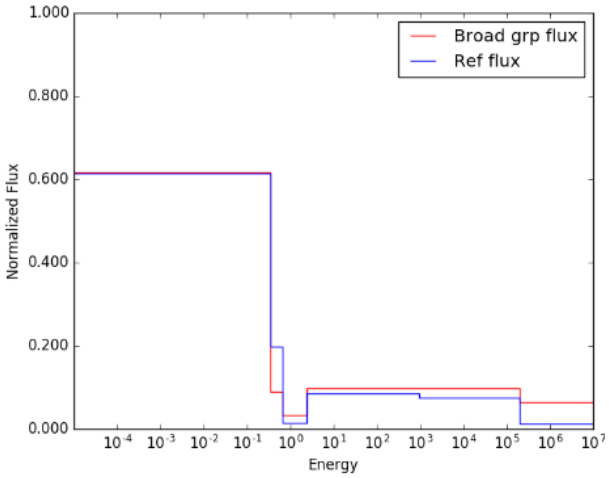

Figure 123. Normalized neutron flux in the PHISICS HTTR core (*structure 5*)

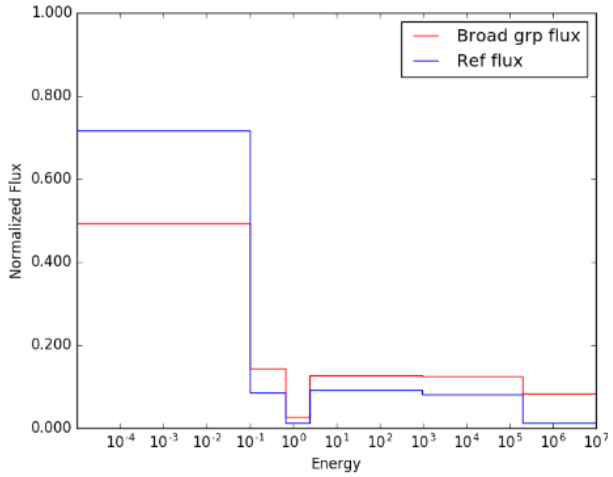

Figure 124. Normalized neutron flux in the PHISICS HTTR core (*structure 1,* 300 K)

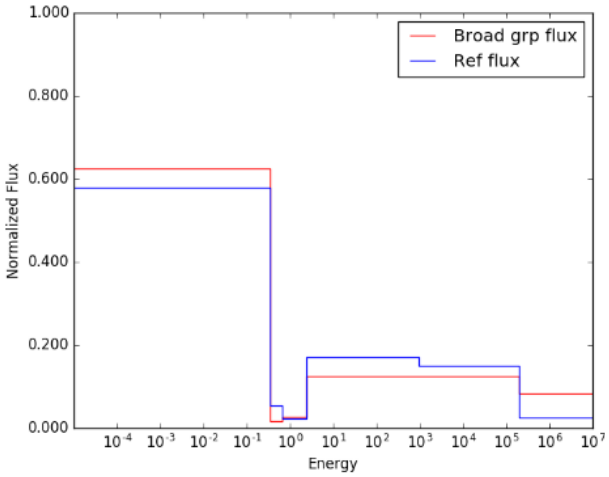

Figure 125. Normalized neutron flux in the PHISICS HTTR core (*structure 5,* 300 K)

Table 51. Comparison of the infinite multiplication factor between the broad-group and the fine-group structures

Structure number	*k-inf difference*
Structure 1	0.00278
Structure 2	0.00333
Structure 3	0.00417
Structure 4	0.00470
Structure 5	0.00230
Structure 6	0.00286
Structure 7	0.00299
Structure 8	0.00323
Structure 9	0.00303
Structure 10	0.00436
Structure 11	0.00172

8.5 Constrains imposed on the PHISICS output

The section 2.6.8.2 explained the construction of the ROM is based on a training system. The data classification relies on a user-defined set of constrains imposed on the simulation outcome. RAVEN then generates a set of input values and NEWT/PHISICS simulates the system's response. The outcome is compared to goal functions to classify the group-structure (i.e. input space) into a "success" or "failure" category. The multiplication factor and the group-wise scalar fluxes are chosen as goal functions imposed on the simulation output phase to establish the classification. The multiplication factor is an integral value and is hence the simplest neutronics constrain. The effective multiplication factor is merely a global response of the system. It represents

a necessary condition but not sufficient to categorize the input space. The group-wise scalar flux is chosen as an energy-based constrain. Therefore, the total number of criteria to be simultaneously met is equal to G+1, among which G criteria are explicitly correlated because the neutron flux is normalized.

The following "passing" criteria from the PHISICS simulations must meet altogether:

- k_{inf} criterion: The infinite multiplication factor in the six-group structure is within 0.00200 of the reference 252-group one, in absolute value:

$$-0.00200 \;<\; (k_{inf}^{broad} - k_{inf}^{fine}) \;<\; 0.00200 \qquad \text{Equation 8-7}$$

- group flux criteria: at least two-third of the group fluxes or the two major group fluxes must be within "passing" limits. The two major group fluxes are the two largest group-wise flux values of the normalized neutron flux;
- major flux criterion: If the normalized neutron flux in an energy group is larger than or equal to 0.5, the normalized flux must be within 10% of the *structure 0* (referred to as $\Phi^{(0)}$) to be labelled "passing":

$$0.90\ \Phi_g^{(0)} < \frac{\Phi_g^{\text{broad}}}{\Phi_g^{(0)}} \;<\; 1.10\ \Phi_g^{(0)} \qquad \text{Equation 8-8}$$

- minor flux criterion: if the normalized neutron flux in an energy group is lower than 0.5, the normalized flux must be within 20% of the *structure 0* to be labelled "passing":

$$0.80\ \Phi_g^{(0)} < \frac{\Phi_g^{\text{broad}}}{\Phi_g^{(0)}} \;<\; 1.20\ \Phi_g^{(0)} \qquad \text{Equation 8-9}$$

- exclusion criterion: If any of the relative differences between the broad structure and the *structure 0* is higher than 100% or lower than 50%, the group structure is classified as "failure", unless the normalized flux is lower than $\Phi^{lim} = 0.1$;

As an illustration of the screening system, the reference group structures plotted in section 8.4 are analysed one by one.

- Structure 1 (Figure 120) exceeds the k_{inf} criterion. Additionally, only group 2, 3 and 5 are within 20% of the group flux criterion.
- Structure 10 (Figure 121) exceeds the k_{inf} criterion. Additionally, none of the groups meet the group flux criterion. Groups 2, 5 and 6 exceed the exclusion criterion.
- Structure 11 (Figure 122) exceeds the k_{inf} criterion. Only group 6 meets the flux criterion.
- Structure 5 (Figure 123) exceeds the k_{inf} criterion. Only group 6 and 3 meet the flux criterion, and group 5 exceeds the exclusion criterion.

The screening system is user-defined and input-space-dependent, i.e. the goal functions are not defined in an absolute fashion and can adapt to the number of energy groups desired. .

8.6 Results

The limit surface search starts with 250 Monte Carlo samplings as an initial survey of the input space (section 2.6.8.3). This primary phase trains the surrogate model. The adaptive sampling comes in a second phase to continue the training and test the ROM. The adaptive sampling component embeds 200 samples in a five-nearest neighbor approach. The limit surface predicted by the surrogate model in RAVEN consists in 1022 structures. RAVEN does not automatically verify the structures predicted by the ROM with NEWT/PHISICS. However, the structures proposed by the ROM were post-tested manually in NEWT/PHISICS. The manual post-processing section is not mandatory in actual applications, it is merely a cross-checking analysis to evaluate the reliability of results provided by the surrogate model.

Within the eleven configurations from the literature detailed in section 8.4, only the structure 11 passes the k_{inf} test. The average difference (in absolute value) between infinite multiplication factors originating from the broad-group and the *structures 0* equals 0.00310. The 1022 limit surfaces are collected from the surrogate model, implemented in NEWT to obtain the microscopic cross sections, and used to run 1022 PHISICS HTTR core models. The average multiplication factors associated with the limit surface are averaged and compared in absolute value to the reference fine-group solution. The difference found was 0.00197, 623 structures passed the multiplication factor test. This average difference is naturally close to the k_{inf} criterion defined in

section 8.5. The best-performing eigenvalue has an absolute difference to the reference of +0.00096. Figure 126 sketches a sample of the group-wise scalar fluxes in the structures proposed by the surrogate model. They correspond respectively to the limit surface 112, 446, 470, 861, 983 and 999. Table 52 indicates the energy boundaries relative to structures (a) through (f) in Figure 126. Δk_{eff} denotes the absolute difference in the multiplication factor with the reference fine-group structure. The structures presented show a very good agreement with the reference, as well as a multiplication factor lower than 0.00200 (passing criteria defined in the goal function).

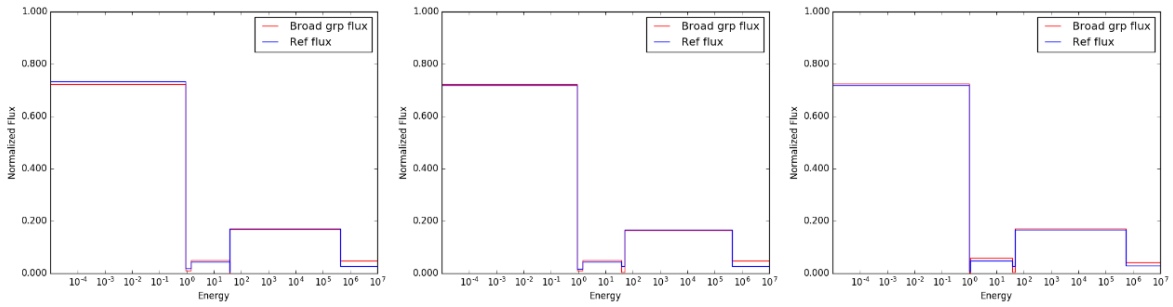

Group structures (a) (b) (c)

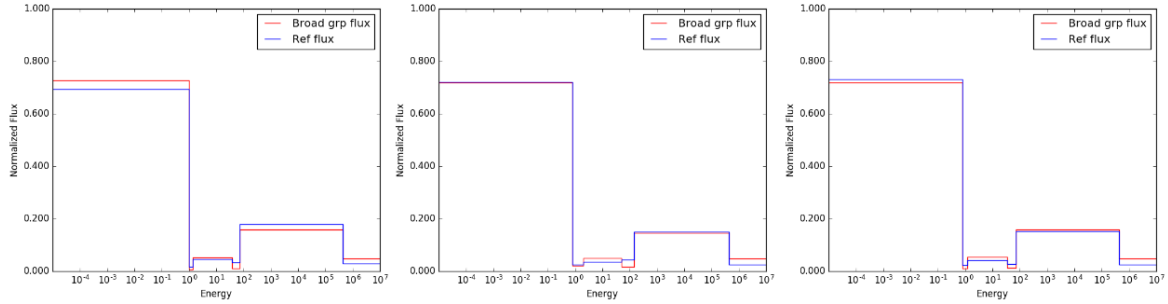

Group structures (e) (f) (g)

Figure 126. A sample of scalar fluxes in group structures proposed by the surrogate model

A failure test is implemented to assess the limit surfaces found by the surrogate. The neutron flux having at least one of the two major group-wise flux greater than a factor 1.5 of the reference flux or lower than a factor 0.5 of the reference flux were considered “failure”. Out of the 1022 limit surfaces, 176 (~17.2%) did not pass the “failure test” (so 88.8 % of the structure were satisfying). Note that all the group structures from the literature fail this test as well, even the best-performing *structure 5* because of group 2.

The sequence shows as expected increasing performance as the conditions are refined. The use of 350 Monte Carlo training runs, and 350 adaptive sampling runs with a seven-neighbor approach provides 40 successful group structures. The average multiplication factor of the 40 limit surfaces has an absolute difference 0.00186 with the fine-group structure, and 100% of the structures pass the “failure test”.

Table 52. Energies boundaries of structures (a) through (f) calculated by the ROM

Struct.	*Group Upper boundaries (eV)*						*Δ k_{eff}*
	1	*2*	*3*	*4*	*5*	*6*	
(a)	2.000E+7	6.000E+5	6.750E+1	6.500E+1	2.770E+0	1.070E+0	1.720E-3
(b)	2.000E+7	5.730E+5	9.000E+1	6.100E+1	2.300E+0	1.010E+0	1.580E-3
(c)	2.000E+7	5.500E+5	5.060E+1	3.763E+1	1.110E+0	4.500E-1	1.870E-3
(d)	2.000E+7	4.920E+5	9.000E+1	4.400E+1	1.940E+0	8.000E-1	1.410E-3
(e)	2.000E+7	4.920E+5	1.175E+2	4.400E+1	1.940E+0	8.000E-1	1.270E-3
(f)	2.000E+7	1.000E+5	1.120E+2	3.763E+1	1.770E+0	9.250E-1	1.620E-3

8.7 Performances of the Sequence

The computational performances of the sequence depend majorly on two external criteria and two internal criteria. The external components depend on the physical model. Only model approximations accelerate the external criteria. The internal criteria rely on the simulation settings and remain model-independent.

The number of broad groups represents the first external criterion. It corresponds to the size of the input space, it controls the number of variables to sample within RAVEN. RAVEN creates a G-dimensional grid prior to the beginning of the calculations which remains relatively cost-effective below fifteen groups (~ few minutes in less than ten groups, a few hours until fifteen groups) but rapidly increases as the number of structures and convergence (i.e. the grid refinement) increases. In a six-group problem, the grid was built in 1010 seconds with 1 node and 8 processors, and a convergence set to 1.0e-6 (more information on the convergence in section 2.6.8.3).

The number and type of lattices required by PHISICS core constitutes the second external parameter. In the current version of the sequence, the lattices are executed sequentially: the number of lattices and the lattice types increase drastically the computational time. For example, if NEWT collapses the cross section of three lattices in seven, three and one minutes respectively, the broad-group generation time for one sample would be eleven minutes. If the sequence were to be parallelized, only the type of the lattice considered would be the driver in the computational time, so the generation time would be as long as the longest-running lattice. In the 2-D HTTR problem, the fuel lattice takes about three minutes to be completed. The reflector lattice and control rod lattices require about fifteen seconds, using 1 node and 8 processors.

The tightness of the constraints constitutes the first internal criterion. If the user requires constricted success conditions to define the limit surface, the number of samplings needed will increase and so will the computational cost of the simulations. Increasing the number of goal functions has an equivalent effect on the computational time.

The number of samples establishes the second internal criteria. The definition “forced samplings” allows additional user-imposed adaptive samplings despite the convergence configuration. Imposing samplings refines both the limit surface found by the algorithm and quality of the surrogate model.

The other steps in the sequence remain relatively negligible. The conversion of the collapsed libraries into the SCALE 6.1 AMPX format is instantaneous even if the libraries are loaded with several materials and isotopes. The PHISICS calculations are also of secondary effect but can become more prevalent depending on the broad-group structure and the user’s model (especially in a three-dimensional configuration). In the case of the HTTR in one-third symmetry, the transport iterations complete in a few seconds with 1 node and 8 processors. The RAVEN post-processing of the PHISICS output for statistical analysis requires less than a minute as well. The parsing of the NEWT output for disadvantage factor calculations is also immediate (~ two seconds).

For the 2-D HTTR core in a five-neighbor approach, results were obtained in 24 hours with 1 node and 8 processors, by sampling 450 group structures. The simulation in a seven-neighbor approach and 600 samplings took about 32 hours.

8.8 Conclusions

The RAVEN/NEWT/PHISICS sequence can perform automatic energy-group searches on problem-specific core calculations. The sequence relies on NEWT to generate "on the fly" the cross sections. PHISICS uses the self-shielded microscopic cross section to obtain the transport solution. The multiplication factor and group-wise scalar fluxes are compared to a reference flux collapsed from the 252-group SCALE 6.2 structure into the broad-group structure under investigation. The comparison is confronted to constraints, which RAVEN utilizes to cast a limit surface between acceptable group structures and unsatisfying structures. Two sampling stages occur to define the limit surface: a Monte Carlo sampling phase to explore the input space stochastically and an adaptive sampling phase to generate more data points around the limit surface region(s). The limit surface search functionality within RAVEN builds a surrogate model.

This methodology is innovative and resulted in the development of an interface RAVEN/NEWT/PHISICS as a by-product. The RAVEN interface lets the energy-group search be automatic. The PHISICS broad-group solutions are compared to a PHISICS fine-group reference to avoid code-to-code discrepancies in the transport calculation. In the current version of the interface, the sequence handles multi-lattice cores and tolerates cross sections at different temperatures to construct the core. The sequence also accepts PHISICS-based perturbations, which means parametric studies may be carried out on the energy-group structure.

The methodology depends on the pre-defined SCALE 6.2.0 fine-group structure. The broad-group configurations predicted by the limit surface search must be a sub-set of the 252-group structure already existing. The sequence requires the user to define *a priori* the number of groups desired. The implementation of the constraints remains iterative and depends on the user's experience. The algorithm cannot output configurations in an optimized number of groups.

The sequence was tested on a two-dimensional HTTR core constructed with three lattices (fuel, CR and reflector) to establish a six-group structure. Satisfying results were obtained using a five- and seven-nearest neighbor algorithm.

CHAPTER 9

CONCLUSIONS AND FUTURE WORK

The contribution of the Uncertainty Analysis Modeling in Light Water Reactors triggered the need for similar activities regarding High Temperature Gas-cooled Reactors (HTGR). The International Atomic Energy Agency responded to this interest in 2012 by initiating a Coordinated Research Program to stimulate the development of uncertainty quantification methods in gas-cooled systems. As the Best Estimate Plus Uncertainty (BEPU) methods started competing with the conservative approach, the gaps in this field regarding HTGR applications was primarily logistic: nuclear codes and data analysis tools existed but lacked coordination and development to enable uncertainty analysis. This analysis concentrated on the construction and verification of new tools, sequences and code capabilities appropriate for HTGR neutronics, multi-physics and uncertainty predictions. The work emphasized on the treatment of cross sections and neutron flux spectrum within typical HTGRs.

The thesis addressed a four-fold approach. (a) An emphasis directed towards the generation of rigorously self-shielded cross sections in few- or fine-group energy formats. The coupling of nuclear codes or uncertainty software was encouraged. This step required a comprehensive understanding of the self-shielding methodologies applied in pebble-bed and prismatic reactors in the nuclear codes. A sequence KENO/XSDRN/NEWT, three codes embedded in the SCALE suite, was implemented through an automatic sequence to generate cross sections in doubly-heterogeneous lattice cells. This sequence collects the cross section data at each burnup step of depletion calculations to perturb the libraries in a second stage with the GRS code XSUSA. T-NEWT followed by PHISICS/RELAP5-3D unveiled a sequence capable of condensing doubly-heterogeneous fuel's cross sections within lattice cells for the subsequent multi-physics applications. The sequential application of these three codes proved that the nature and topology of MHTGR lattice cells may induce ~4 to 7% radial perturbations within the core power density in coupled neutronics/thermal hydraulics calculations. These investigations, however, disregarded the neutronics/TH feedback and transient evaluations.

(b) The work focused on testing sequences excelling at uncertainty quantification. SAMPLER/NEWT, developed by ORNL, derived uncertainties relative to nuclide inventories over depletion calculations. The two codes proved the uncertainties attributed to an isotope depend on (1) exclusively cross section uncertainties if the isotope is an actinide and (2) primarily fission yields uncertainties if the isotope is a fission product. The range of uncertainties depend on the isotope that is analyzed, e.g. the uncertainty at the end of a MHTGR cycle was estimated at 0.26 % for the ^{235}U and 1.64% for the ^{135}Xe. SAMPLER/NEWT could not estimate the effects of the decay constants on the isotope inventory uncertainty. The neutron spectrum influences the output uncertainty on the nuclide inventory by about 12% in thermal systems.

(c) The RAVEN software, in collaboration with the codes manipulated in phase (a), unlocked new uncertainty quantification capabilities and induced the development of several new features in PHISICS as a by-product: handling of disadvantage factors, region-specific isotopic treatments from the cross section libraries and scaling factor implementation for cross section perturbation. The coordinating capabilities between RAVEN and the nuclear codes required the development of code interfaces, parsers and output post-processor within RAVEN. Phase (c) utilized the cross section methods derived in part (a) to investigate uncertainties on prismatic-type gas cooled reactors. RAVEN/PHISICS simulated the VHTRC experiment and predicted satisfactory abilities to reproduce the eigenvalue uncertainties documented in the VHTRC experimental report. The framework, however, challenges the so-called uncertainty validation. The results obtained from uncertainty quantifications, including those confronted to the VHTRC experimental report with RAVEN, can be contested. It was attempted to approach the input uncertainties from different angles to account for the non-specificity of the input uncertainty data. The objective overall aimed to investigate the range of the output uncertainties relative to the VHTRC model. It was proposed for instance to consider the distributions (uniformity versus normality), the magnitude of the input uncertainties (maximum versus standard deviation) and the independence of the lattice cells' uncertainties. The results proved that the analyst's interpretation regarding the non-specificity of the input uncertainties yields to up to a ten-fold increase in the output uncertainties predicted for the VHTRC (from ±0.00038 to ±0.00325 on the k_{eff} in the HC-I core for instance). The validation process relays a dual challenge: assessing the experimentalist's output uncertainties and interpreting properly the manufacturer's input uncertainties. RAVEN/PHISICS treated the scope of manufacturing uncertainty evaluations in depth, but the capabilities of cross section

perturbation remained rudimentary. Thus, phase (c) fell short on thorough verifications of the PHISICS scaling factors. Future developments call for an implementation of cross correlations between nuclide-reactions, the differentiation between elastic and inelastic scattering in the cross section perturbation factors, and advanced code-to-code verification(s).

Phase (d) was a supplement analysis exploring the RAVEN's adaptive sampling capabilities. The part of the work addressed modeling uncertainties *via* group structure development in HTGRs. The method employed RAVEN/NEWT/PHISICS to construct Reduced Order Models. It explores the limit surface search algorithm to highlight "eligible" energy group structures based on user-defined constraints. The method applies to any type of reactors including HTGRs. Six-group structures were proposed for an HTTR system. This novel approach is automatic and presents the advantage to rely on only one code (PHISICS) for the constraint comparison although the methodology remains immature. A smarter sampling strategy would compare the running time versus the performances of the group structures to evaluate an optimal number of groups as opposed to the current approach that sets a fixed number of groups at the beginning of the sampling. Additional efforts regarding the verification of mixed cores and temperature gradients is also encouraged. Future developments could address an autonomic constraint implementation accounting for the system's characteristics.

REFERENCES

[1] F. Reitsma, et al., "**The IAEA Coordinated Research Program on HTGR Uncertainty Analysis: Phase I Status and Initial Results**", Proceedings of HTR 2014, Weihai, China (2014).

[2] J. Ortensi, et al., "**Prismatic Coupled Neutronics/Thermal Fluids Transient Benchmark of the MHTGR-350 MW Core Design: Benchmark Definition**", OECD Nuclear Energy Agency NEA/NSC/DOC (2013) DRAFT (03/01/2013).

[3] Shigeaki Nakagawa, Kuniyoshi Takamatsu, Yukio Tachibana, Nariaki Sakaba, Tatsuo Iyoku "**Safety Demonstration Tests using High Temperature Engineering Test Reactor**", Nuclear Engineering and Design 233 (2004) 301–308.

[4] D. A. Copinger, D. L. Moses "**Fort Saint Vrain Gas-Cooled Reactor Operational Experience**", Oak Ridge National Laboratory, NUREG/CR-6839.

[5] Shinji Kubo, Hayato Nakajima, Seiji Kasahara, Syunichi Higashi, Tomoo Masaki, Hiroyoshi Abe, Kaoru Onuki, "**A Demonstration Study on a Closed-Cycle Hydrogen Production by the Thermochemical Water-Splitting Iodine-Sulfur Process**", Nuclear Engineering and Design 233 (2004) 347–354.

[6] S. Dardour, S. Nisan, F. Charbit, "**Utilization of Waste Heat from GT-MHR and PBMR Reactors for Nuclear Desalination**", Desalination, 205 (2007), pp 254-268.

[7] A.J. Neylan, D.V. Graf, A.C. Millunzi "**The Modular High-Temperature Gas-cooled Reactor in the U.S**" Nuclear Engineering and Design 109 (1988) 99-105.

[8] S. Saito, T. Tanaka, Y. Sudo "**Present Status of the High Temperature Engineering Test Reactor (HTTR)**", Nuclear Engineering and Design 132 (1991) 85-93.

[9] J. Ortensi et al., "**Deterministic Modeling of the High Temperature Test Reactor**", INL/EXT-10-18969 (2010).

[10] NEA, 2013, "**International Handbook of Evaluated Reactor Physics Benchmark Experiments**", NEA/NSC/DOC, NEA No. 7140.

[11] Y. Kaneko, S. Ohkubo and F. Akino, "**Effect of Delayed-Neutron Mode on the Determination of the Prompt-Neutron Decay Constant in Pulsed-Neutron Measurements**", Nucl. Sci. Eng., 50, 173-176 (1973).

[12] T. Yamane, H. Yasuda, F. Akino & Y. Kaneko "**Measurement of Overall Temperature Coefficient of Reactivity of VHTRC-1 Core by Pulsed Neutron Method**" Journal of Nuclear Science and Technology, 27:2, 122-132 (1990).

[13] R.N. Morris, D.A. Petti, D.A Powers, B.E. Boyack, "**TRISO-Coated Particle Fuel Phenomenon Identification and Ranking Tables (PIRTs) for Fission Product Transport Due to Manufacturing, Operations and Accidents**", NUREG-6844 Volume 1 (2004), pp 132-166.

[14] I.J. Van Rooyen et al., "**Progress in Solving the Elusive Ag Transport Mechanism in TRISO Particles: 'What Is New**'" Proceedings of the HTR 2014 Weihai, China, 2014 Paper HTR 2014-31261.

[15] K. Ivanov, et al., "**Benchmark for Uncertainty Analysis in Modelling for Design, Operation and Safety Analysis of LWRs**, **Vol. I: Specification and Support Data for the Neutronics Cases (Phase I)**", Version 2.0, OECD Nuclear Energy Agency NEA/NSC/DOC (2013), (May 2013).

[16] W. P. Poenitz and J. F. Whalon Applied Physics Division, "**Total Neutron Cross Section Measurements in the Energy Region from 47 keV to 20 MeV**", ANL-NDM-80 (1983) , pp 5-7.

[17] A.D. Carlson, "**the Neutron Cross Section Standards, Evaluations and Applications**", (2011), Metrologia 48 S328.

[18] H. H. Saleh, T, T.A. Parish, S. Raman, N. Shinohara "**Measurements of Delayed Neutron Decay Constants and Fission Yields from U^{235}, Np^{237}, Am^{241}, Am^{243}**", Nuclear Science and Engineering 125, 51-60 (1997).

[19] S. Okajima, T. Sakurai, F.G Lebrat, V.Z Averlant, M. Martini, "**Summary on International Benchmark Experiments for Effective Delayed Neutron Fraction β_{eff}**", Progress in Nuclear Energy, Vol. 41, No, 1-4 pp 285-301 (2002).

[20] The International Atomic Energy Agency, "**Compilation and Evaluation of Fission Yield Nuclear Data**" Final Report of the CRP (1991-1996), TECDOC-1168.

[21] M.B. Chadwick et al., "**ENDF/B-VII.0 Next Generation Evaluated Nuclear Data Library for Nuclear Science and Technology**", Nuclear Data Sheets107 (2006) 2931-3060.

[22] D. L. Smith "**Evaluated Nuclear Data Covariances: The Journey from ENDF/B-VII.0 to ENDF/B-VII.1**" Nuclear Data Sheets 112 (2011) 3037–3053.

[23] P. Talou, P.G. Young, and T. Kawano "**Quantification of Uncertainties for Evaluated Neutron-Induced Reactions on Actinides in the Fast Energy Range**" Nuclear Data Sheets, Vol 112, issue 12, pp 3054-3074 (2011).

[24] S. Hoblit et al. "**Neutron Cross Section Covariances for Structural Materials and Fission Products**", Nuclear Data Sheets Vol 112, issue 12 (2011) 3075-3097

[25] M. Herman et al. "**COMMARA-2.0 Neutron Cross Section Covariance Library**" BNL-94830-2011 (2011).

[26] H. J. Park, H. J. Shim, C. H. Kim "**Uncertainty Propagation Analysis for PWR Burnup Pin Cell Benchmark by Monte Carlo Code McCard**" Science and Technology of Nuclear Installations Volume 2012, Article ID 616253 (2012).

[27] M. L. Williams, D. Wiarda, G. Arbanas, and B. L. Broadhead "**SCALE Nuclear Data Covariance Library**" Sect. 10.2 in SCALE: a Modular Code System for Performing Standardized Computer Analyses for Licensing Evaluations, ORNL, TM-2005/39,Version 6.2, Oak Ridge National Laboratory (2011).

[28] S. F. Mughabghab, "**Atlas of Neutron Resonances: Resonance Parameters and Thermal Cross Sections**", Elsevier, Amsterdam (2006).

[29] E. E Lewis, W.F Milller Jr. "**Computational Methods of Neutron Transport**" ANS Scientific Publications (1993) La Grange Park, Illinois, 401.

[30] M. L. Williams, "**Resonance Self-Shielding Methodologies in SCALE 6**" Oak Ridge National Laboratory, Nuclear Science and Tchnology Division (2010).

[31] B.T. Rearden, M.A. Jessee, "**SCALE Code System**" ORNL/TM2005/39, Reactor and Nuclear Systems Divisions (2016) (page 2476).

[32] Y. Kim, W. S. Park, "**Reactivity-Equivalent Physical Transformation for Elimination of Double-Heterogenity**", 2005, 93. 959-960.

[33] Y. Kim, K. S. Kim, J. M. Noh, "**Reactivity-Equivalent Physical Transformation for Homogenization of Double-Heterogeneous Fuels**", Korean Atomic Energy Institute, Transactions of Korean Nuclear Society Autumn Meeting, 2005.

[34] W. Wiarda et al., "AMPX-6 : a Nuclear Code System for Processing ENDF/B", ORNL/TM-2016-43 (2016).

[35] C. Rabiti, A. Alfonsi, A. Epiney, "**New Simulation Schemes and Capabilities for the PHISICS/RELAP5-3D Coupled Suite**", Nuclear Science and Engineering, Vol. 182 No. 1, pp. 104-118 (2016).

[36] G. Strydom et al., "**Comparison of the PHISICS/RELAP5-3D Ring and Block Model Results for Phase I of the OECD/NEA MHTGR-350 Benchmark**", Nuclear Technology, Vol. 193, pp. 15-35 (2015).

[37] M. L. Williams, G. Ilas, M. A. Jessee, B. T. Rearden, D. Wiarda, W. Zwermann, L. Gallner, M. Klein, B. Krzykacz–Hausmann, and A. Pautz, "**A Statistical Sampling Method for Uncertainty Analysis with SCALE and XSUSA**," Nuclear Technology, 183, 515–526 (2013).

[38] C. Rabiti et al, "**RAVEN User's Manual**" INL/EXT-15-34123.

[39] A. Alfonsi et al., "**Improving Limit Surface Search Algorithms in RAVEN Using Acceleration Schemes**" INL/EXT-15-36100 (2015).

[40] C. Frepoli, "**An Overview of Westinghouse Realistic Large Break LOCA Evaluation Model**", science and Technology Installations, Vol 2008 article ID-498737.

[41] E. Ivanov, A. Sargeni, F. Dubois, "**Best Estimate Plus Uncertainty (BEPU): Why it Is still not Widely Used**", BEPU2018-309, ANS BEPU International conference, Real Collegio, Lucca, Italy (2018).

[42] Saltelli, A., K. Chan, and E. M. Scott, editors, "**Sensitivity Analysis**", John Wiley &Sons, Ltd 2000 (2000).

[43] B. Iooss, P. Lemaitre, "**A Review on Global Sensitivity Analysis methods**", EDF R&D (2014).

[44] D. G. Cacuci, M. Ionescu-Bujor "**A Comparative Review of Sensitivity and Uncertainty Analysis of Large Scale Systems - II Statistical Methods**", Nuclear science and Engineering, 147, No. 3, pp 204-217 (2004).

[45] M. Ionescu-Bujor, D.G. Cacuci "**A Comparative Review of Sensitivity and Uncertainty Analysis of Large Scale Systems - II Deterministic Methods**", Nuclear science and Engineering, 147, No. 3, pp 183-203 (2004).

[46] L. L. Briggs, "**Uncertainty Quantification Approaches for advanced reactor analysis**", ANL-GenIV-110 (2008).

[47] D. Rochman et al. "**Nuclear data Uncertainty Propagation: Perturbation vs. Monte Carlo**", Annals of Nuclear Energy 38 (2011) 942–952.

[48] W. Zwermann et al. "**Nuclear Data Uncertainty and Sensitivity Analysis with XSUSA for Fuel Assembly Depletion Calculations**", Nuclear Engineering and Technology, Vol. 46 No 3 (2014).

[49] O. Buss et al. "**NUDUNA - Nuclear Data Uncertainty Analysis**", International Conference on Nuclear Criticality 2011, Edinburgh (2011).

[50] A.J. Koning, D. Rochman "**Towards Sustainable Nuclear Energy: Putting Nuclear Physics to Work**", Annals of Nuclear Energy 35 (2008) 2024–2030.

[51] H. Glaeser, "**GRS Method for Uncertainty and Sensitivity Evaluation of the Code Results and Applications**" Science and Technology of Nuclear Installations, Vol (2008) ID 798901.

[52] S. Greenland et al., "**Statistical Tests, P-Values, Confidence Intervals, and Power: a Guide to Misinterpretations**", European Journal of Epidemiology, 2016; 31:7 350 (2016).

[53] K. Ivanov et al. "**Benchmark for Uncertainty Analysis in Modeling (UAM) for the Design, Operation and Safety Analysis of LWRs**" NEA/NSC/DOC(2013),Nuclear Energy Agency (2013)

[54] R. Bratton, M. Avramova, K. Ivanov "**OECD/NEA Benchmark for Uncertainty Analysis in Modeling (UAM) for LWRS – Summary and Discussion of Neutronics Cases**" Nuclear Engineering and Technology, Vol.46 No 3 pp 313-342 (2014).

[55] M.L Williams et al. "**SCALE Nuclear Data Covariance Library**" Sect. M19 in SCALE: a Modular Code System for Performing Standardized Computer Analyses for Licensing Evaluations, ORNL, TM-2005/39,Version 6.1, Oak Ridge National Laboratory (2011).

[56] A. Aures, W. Zwermann, P. Rouxelin, K. Velkov, "**Uncertainty and Sensitivity Analysis for an OECD/NEA HTGR Benchmark with XSUSA**", PHYSOR 2014, Kyoto, Japan.

[57] F. Bostelmann et al. "**The IAEA Coordinated Research Program on HTR Uncertainty Analysis: Phase I Status and Ex I-1 Prismatic Reference Results**" Nuclear Engineering and Design 306 (2016) 77–88.

[58] A. T. Ardakani, M. B. Ghofrani, A. O. Ezzati "**Stochastic Arranging of CFPs in HTTR and Criticality Benchmark Considering Different Modeling of CFPs**" Nuclear Engineering and Design 271 348-351 (2014)

[59] F. Bostelmann, W. Zwermann, K. Velkov, "**Nuclear Data Uncertainty Analysis of the MHTGR-350 – Exercise I-1 a/b and 2a**", IAEA CRP on HTRG UAM: RCM-3, Idaho Falls, May 9-12 2016

[60] G. Strydom, F. Bostelmann, "**IAEA Coordinated Research Project on HTGR Physics, Thermal-Hydraulics, and Depletion Uncertainty Analysis. Prismatic HTGR Benchmark Definition: Phase I**", INL/EXT-15-34868 (2015).

[61] P. Rouxelin, G. Strydom, K.Ivanov, "**IAEA CRP on HTGR Uncertainties in Modeling: Assessment of Phase I Lattice to Core Model Uncertainties**", INL/EXT-15-36306 (2016).

[62] J. Ortensi, "**Supercell Depletion Studies for Prismatic High Temperature Reactor**", INL/CON-12-24395, (2012).

[63] B. Tyobeka, K. Ivanov, A. Pautz, "**Utilization of Two-Dimensional Deterministic Transport Methods for Analysis of Pebble-Bed Reactors**", Annals of Nuclear Energy 34, 396-405, pp 401, (2007).

[64] S. Goluoglu, M. L. Williams **"Modeling Doubly Heterogeneous Systems in SCALE**" Trans. Am. Nucl. Soc. 93, 767 (2005).

[65] T. Yamane, Y. Kitamura, Y. Eguchi. "**Temperature Effects on Reactivity in VHTRC-1 Core**" NEA/NCS/DOC (2006).

[66] T. Yamane, H. Yasuda, F. Akino & Y. Kaneko "**Measurement of Overall Temperature Coefficient of Reactivity of VHTRC-1 Core by Pulsed Neutron Method**" Journal of Nuclear Science and Technology, 27:2, 122-132 (1990).

[67] G. Poullot , D. Doutriaux, J. Anno, "**ICSBEP Guide to the Expression of Uncertainties**".

[68] Y. Nagaya, L. Okumura, T. Mori, M. Nakagawa, "**MVP/GMVP II General Purpose Monte Carlo Codes for Neutron and Photon Transport Calculations Based on Continuous Energy and Multigroup Methods**", JAERI 1348, Japan Atomic Energy Research Institute (2005).

[69] M. Herman et al., "**COMMARA-2.0 Neutron Cross Section Covariance Library**", BNL-94830-2011 (2011)

[70] G. Chiba, M. Tsuji, T. Narabayashi, "**Resonance Self-Shielding Effect in Uncertainty Quantification of Fission Reactor Neutronics Parameters**", Nuclear Engineering and Technology, Vol. 46 No.3 (2014)

[71] D. Wiarda, M. E. Dunn, "**PUFF-IV: a Code for Processing EDNF Uncertainty Data into Multigroup Covariance Matrices**" ORNL/TM-2006/147 (2006).

[72] C. Yi and G. Sjoden, "**Computationally Optimized Multi-Group Cross Section Data Collapsing using the YGROUP Code**", Proc. Int. Conf. on the Physics of Reactors (PHYSOR 2010). May 9–14. [CD-ROM].

[73] A. Moghrabi, D.R. Novog, "**Optimization Approach of Energy Group Structure for the Canadian Pressure Tube Supercritical Water Reactor**" The 37th Annual Conference of the Canadian Nuclear Society, Niagara Falls, Ontario, Canada.

[74] A. Moghrabi, D.R. Novog, "**Determination of the Optimal Few-Energy Group Structure for the Canadian Super Critical Water-Cooled Reactor**", Annals of Nuclear Energy 115 (2018) 27–38

[75] J.S Han, K.N. Ivanov, S. Levine, "**Sensitivity Study on the Energy-Group structure for High Temperature Reactor Analysis**", Master Thesis (Pennsylvania State University).

[76] F. Marini, B. Walczak (2015), "**Particle Swarm Optimization. A Tutorial**", Chemometrics and Intelligence Laboratory Systems 149 (2015)153-165.

[77] P. Mosca, C. Mounier, R. Sanchez & G. Arnaud (2011) "**An Adaptive Mesh Constructor for Multigroup Library Generation for Transport Codes**", Nuclear Science and Engineering, 167:1, 40-60, DOI: 10.13182/NSE10/10.

[78] Z. Zhang et al. (2011), "**Simplified Two and Three Dimensional HTTR Benchmark**", Annals of Nuclear Energy 38 (2011) 1172-1185.

[79] I. Murata et al. (1994) "**Evaluation of Local Power Distribution with Fine-Mesh Core Model for High Temperature Engineering Test Reactor (HTTR)**", Journal of Nuclear Science and Technology, 31:1, 62-72.

[80] L. Massimo (1976) "**Physics of High-Temperature Reactors**", Pergamon Press.